Titre: Title:	Estimation and Validation of Post-Peak Behavior of Hard Rocks
Auteur: Author:	Arash Khosravi
Date:	2016
Type:	Mémoire ou thèse / Dissertation or Thesis
Référence: Citation:	Khosravi, A. (2016). Estimation and Validation of Post-Peak Behavior of Hard Rocks [Thèse de doctorat, École Polytechnique de Montréal]. PolyPublie. https://publications.polymtl.ca/2257/

UNIVERSITÉ DE MONTRÉAL

ESTIMATION AND VALIDATION OF POST-PEAK BEHAVIOUR OF HARD ROCKS

ARASH KHOSRAVI

DÉPARTEMENT DES GÉNIES CIVIL, GÉOLOGIQUE ET DES MINES (CGM)

ÉCOLE POLYTECHNIQUE DE MONTRÉAL

THÈSE PRÉSENTÉE EN VUE DE L'OBTENTION

DU DIPLÔME DE PHILOSOPHIAE DOCTOR

(GÉNIE MINÉRAL)

AOÛT 2016

UNIVERSITÉ DE MONTRÉAL

ÉCOLE POLYTECHNIQUE DE MONTRÉAL

Cette thèse intitulée :

ESTIMATION AND VALIDATION OF POST-PEAK BEHAVIOUR OF HARD ROCKS

présentée par : KHOSRAVI Arash

en vue de l'obtention du diplôme de : Philosophiae Doctor

a été dûment acceptée par le jury d'examen constitué de :

M. LI Li, Doctorat, président

M. SIMON Richard, Ph. D., membre et directeur de recherche

M. BELEM Tikou, Ph. D., membre

M. HASSANI Ferri, Ph. D., membre externe

DEDICATION

I dedicate this work to

my beloved wife Nooshin and my son Arya.

ACKNOWLEDGEMENTS

First of all, I would like to thank my supervisor, Professor Richard Simon for giving me the opportunities to study at École Polytechnique de Montréal for my Ph.D. I would also like to thank my committee members Prof. Li Li from École Polytechnique de Montréal and Prof. Tikou Belem from UQAT, and my external examiner Prof. Ferri Hassani from McGill University for the time they have dedicated to reviewing my dissertation.

I would like to express my gratitude to Raglan mine (Glencore group) for providing the rock samples used in this study. Without the rock samples it was not possible to fulfill this research successfully.

I would also like to express my special thanks the technicians of the laboratories Rock and Soil Mechanics at École Polytechnique Mr. André Ducharme and Mr. Etienne Bélanger and Mr. Samuel Chénier for their technical support, encouragement and helps. I have learned a lot from these gentlemen.

I would like to acknowledge and thank Prof. Patrice Rivard and the technicians Mr. Danick Charbonneau and Mrs. Ghislaine Luc for their supports to conduct a big part of my laboratory tests at University of Sherbrooke and also for any progress in my thesis.

I would also like to thank Prof. Ferri Hassani and Mr. Pejman Nekoovaght for their support and opportunity in preparing my first rock samples at the rock mechanics laboratory at McGill University.

I have a lot of things from friends in the department of mining engineering at Ecole Polytechnique of Montreal. This help and friendship is appreciated and acknowledged.

Finally, I would like to express my deepest gratitude to my lovely wife Nooshin and my son Arya for their endless love and support, without which, this life and thesis would not be possible.

RÉSUMÉ

Travailler en profondeur sous terre peut générer des situations dangereuses. Des précautions particulières doivent être prises lors de la phase de conception et d'exploitation. La rupture fragile du massif rocheux (coup de terrain) est l'un des instabilités qui peut se produire dans les roches dures ayant une faible porosité à cause de la concentration de contrainte élevée. Il est important de prévoir le comportement du massif rocheux lié à la phase post-pic lors de ruptures. La compréhension du comportement post-pic et le comportement en cisaillement d'un plan de rupture induite sous une condition de limite de chargement particulier est cruciale pour réduire les risques. Jusqu'ici, de nombreuses recherches ont été menées sur la surveillance sismique des excavations souterraines en situation potentielle de coups de terrain. Par ailleurs, quelques méthodes de prévision des coups de terrain ont été proposées basée sur les mathématiques logiques. La solution analytique est également l'une des approches fiables basées sur les travaux expérimentaux dans lesquels les propriétés mécaniques de la roche intacte et des fractures sont prises en compte.

L'objectif principal de cette thèse est de prédire la courbe post-pic de roches dures en utilisant des essais de compression triaxiale et de cisaillement direct et la caractérisation des fractures en utilisant le modèle CSDS (Simon, 1999) et l'approche proposée par Simon et al. (2003). Les résultats de la caractérisation de la surface de rupture montrent que comment les différents modes de chargement affectent les paramètres de rugosité des fractures. Les résultats indiquent également la variation de la rugosité de la surface de rupture avec la contrainte de confinement appliquée. La rugosité sur chaque surface de rupture indique la variation de la rugosité dans les échantillons en fonction de la distribution des contraintes.

La variation de la rugosité de la surface de rupture à la traction induite par l'essai Brésilien dévoile un effet combiné de la direction de chargement, la taille du grain, et le rapport L/D sur la valeur de la rugosité. Il est démontré que les profils de rugosité parallèles et perpendiculaires à la direction de chargement ont une variation de la rugosité distincte. Une nouvelle méthode de chargement appelée « chargement en dommage-contrôlé cyclique » proposée permet d'obtenir la courbe post-pic des roches dures, en utilisant une procédure spécifique. Les courbes complètes de contrainte-déformation de deux roches dures ont été obtenues par cette méthode.

Les résultats montrent que l'énergie élastique accumulée dans les échantillons en utilisant cette nouvelle procédure est moindre et comment la procédure influe sur la configuration de fracturation. Une approche existante basée sur le modèle constitutif CSDS pour les joints de roche a également été vérifiée afin d'estimer le comportement post-pic de roches dures. Il est démontré que cette approche est capable d'estimer les propriétés du modèle requis en utilisant les essais de compression triaxiale et de cisaillement direct et la caractérisation de la surface de rupture.

ABSTRACT

Working in deep underground opening is often accompanied by hazardous situations. Special care must be taken in the design and operation phase. Brittle fracturing of the rock mass (rockburst) is one of instabilities that occurs in hard rocks with low porosity due to high stress concentration. It is important to predict the rockburst behaviour that corresponds to the post-peak phase. Understanding of the post-peak behaviour and the shear behaviour of an induced failure plane under a particular loading boundary condition is a critical issue in order to prevent risks. To date, many researches have been conducted on the seismic monitoring of deep underground openings. Also, a few rockburst prediction methods have been proposed based on logical mathematics. Analytical solution is also one of the reliable approaches based on the experimental works in which the mechanical properties of both intact rock and fracture surface are taken into account.

The main objective of this thesis was to predict the post-peak curve of hard rocks using triaxial and direct shear tests and rock surface characterization by using the CSDS model (Simon, 1999) and the proposed approach by Simon et al. (2003). The results of fracture surface characterization show how different loading modes affect the roughness parameters of the fractures. The results also indicate the variation of the fracture roughness with the applied confining stress. The roughness on each fracture surface indicates the roughness variation in the samples due to the stress distribution.

Roughness variation of the tensile fractures induced by Brazilian tests reveals a combined effect of the loading direction, grain size, and the L/D ratio on the roughness value. It is shown that the roughness profiles parallel and perpendicular to the loading direction have a unique roughness variation. A new proposed damage-controlled cyclic method is used to obtain the post-peak curve of hard rocks using a specific procedure. The complete stress-strain curves of two hard rocks were obtained by this method.

The results show that the elastic energy accumulated in the specimens using this new procedure is lower and that the procedure influences the fracturing pattern. An existing approach based on the CSDS constitutive model for rock joints was also verified in order to estimate the post-peak behaviour of hard rocks. It is shown that this approach is able to estimate the required model properties using triaxial compression and direct shear tests and the surface characterization.

TABLE OF CONTENTS

LIST OF TABLES

LIST OF FIGURES

List of symbols and abbreviations

CSDS	Complete Stress Displacement Surface
L/D	Length-to-Diameter
2DRP	2D Roughness Profilometry
BIM	Brittleness Index Modified
JRC	Joint Roughness Coefficient
τ_p	Peak shear strength
τ_r	Residual shear strength
τ	Shear stress on the failure plane
σ_n	Normal Stress
σ_T	Ultimate compressive strength
σ_n	Normal Stress
σ_1	Major principal stress
σ_3	Minor principal stress
$\Delta\varepsilon_t$	Axial strain component induced by the shear displacement (u) on the failure plane
$\Delta\varepsilon_n$	Axial strain component induced by the normal displacement (v) of the failure plane
$\Delta\varepsilon_e$	Axial strain component due to the rock matrix compaction
ε	Total axial strain
E	Elastic modulus
E′	Post-peak modulus
ϕ_o	Angle of friction of intact rock
β	Angle of failure plane
ϕ_r	Residual friction angle

V_m	rock joint closure
v	normal displacement
u	shear displacement
B_0	Ratio of residual to peak strength
a_s	Shear area ratio
i	Angle of asperity
i_0	Initial angle of asperity
ϕ_u	Angle of friction
a, b, c,d and *e*	The CSDS model parameters (joint shear behaviour)
β_1, β_2, β_3	The CSDS model parameters (joint dilation behaviour)
u_p	Peak shear displacement
u_r	Residual shear displacement
S_r	Shear strength (Mohr-Coulomb)
S_0	Cohesion
RMS	Root mean square
A_i	Average inclination angle of asperity
Z_2	The RMS of the first derivative of the roughness profile
R_p	Roughness profile index
D	Fractal dimension
$i_{o\ max}$	Maximum asperity angle
$i_{o\ ave}$	Average asperity angle

CHAPTER 1 INTRUDUCTION

Strainbursts occur in deep mines when the post-peak stiffness of failed rock is higher than the stiffness of surrounding layers. The accumulated energy is released suddenly with damage risk to whole mining stope or underground opening as well as workers and equipment. Rockburst can be easily triggered and/or accelerated by seismic waves induced by mining activities. The occurrence of rockbursts is associated with many factors such as geological structures of rock mass, depth, stress conditions, rock mass strength, excavation method, excavation size and rock blasting. The stress state increases as the depth increases, thus, the rock mass instabilities and other safety issues matter.

Many researches have been carried out to predict and prevent rockburst. In the last four decades considerable achievements have been made in rockburst phenomenon based on rock mechanics knowledge. The potential of bursting has been evaluated by measuring the brittleness of rock. Brittleness indices are based on strain energy accumulation and mechanical properties of rock in the loading phase. These indices can be used to estimate the risk of any violent instability.

Since rockburst phenomenon is related to mechanical behaviour of rock mass in the post-peak phase, the knowledge of the post-peak behaviour of rocks is required. Determination of the post-peak behaviour of brittle rocks in the laboratory is difficult and needs specific procedures to be achieved. Predominantly, the sharp and sudden strength drop is the result obtained at the peak strength. To identify the post-peak phase of an intact rock, modern stiff servo-controlled pressing machines are used. However, even modern technology does not guarantee to acquire the post-peak curve of brittle hard rocks.

Martin (1993) and Martin and Chandler (1994) proposed a damage controlled method to obtain the post-peak curve of rocks under compression experimentally. Fairhurst and Hudson (1999) suggested an alternative control technique by a testing procedure to obtain a complete stress-strain curve. Simon et al. (2003) proposed an indirect analytical approach based on the results of triaxial compression tests and a constitutive model for rock joint- the CSDS model (complete stress-displacement surface) - to estimate the post-peak behaviour of brittle rocks. In this proposed approach, the model properties (as rock mechanical parameters) were obtained from literature on medium rocks using curve-fitting method. This is nonetheless important to validate this approach based on laboratory tests on hard rocks. However, there are still many other factors

that should be considered to estimate the post-peak behaviour of intact rocks. One of these factors is the influence of the created fractures in uniaxial and triaxial loading modes.

The post-peak behaviour of intact rock is controlled by the fracture created at the peak strength. These fractures control the post-peak mechanical behaviour of the rock mass. The mechanical behaviour of the created fractures plays an important role in the severity of the process regarding the applied boundary condition in the post-peak. By characterizing the fracture surface created in triaxial and uniaxial loading modes, the roughness parameter and physical properties of the surface can be quantified. Subsequently, a closer insight into the post-peak behaviour of an intact rock subjected to the compression can be provided. The effect of different loading modes on the roughness also needs to be studied further.

1.1 **Introduction**

As technology allows for the exploitation of deeper orebodies with higher extraction ratios, mining engineers will most likely have to deal with instability problems. One of the most important, costly and harmful instability problems in Canadian deep mines is rockburst. Rockburst is a violent and suddenly brittle failure of rock in the surrounding rock mass due to the high stress state and huge amount of released energy. Since rockburst occurs suddenly and violently, it can cause injuries including death to workers, damage to equipment and even substantial disruption and economic loss of underground resources. Rockburst is a seismic event that can be easily triggered and/or accelerated by seismic waves induced by mining activities.

Rockbursts are regularly classified in two main types: fault-slip burst and strain-burst (e.g. Johnston, 1988). Fault-slip burst occurs where an underground opening approaches a fault or a main geological discontinuity. In this case, normal load on the fault surface can decrease and the induced shear stress exceeds the shear strength and the failure can thus occur violently. Strain-burst takes place in a few manners such as exfoliation, buckling, pillar burst in which rock ejection and fall are dominant mechanisms. In particular cases, the combination of two types of rockbursts can be observed where a seismic event causes sufficiently high dynamic stress near an underground opening due to remote fault-slip (Kaiser et al., 1995).

In both types of rockbursts, the dominant phenomenon is movement of a discontinuity. The discontinuity controls the post-peak mechanical behaviour of intact rock. Many constitutive

models were established to estimate the mechanical behaviour of a joint subjected to a certain boundary condition, such as Patton (1966), Ladany-Archambault (1970), Barton et al. (1973; 1985), Saeb-Amadei (1992), and Simon (1999). These proposed models showed linear and non-linear behaviours of rock joints in stress-shear and normal strain curves for peak and/or post-peak regions. These researches, among several others, not only indicated the importance of discontinuity shear behaviour in rock engineering, but also demonstrated the influence of discontinuity surface characterization in complex problems related to the field of geotechnics, rock mechanics, mining and petroleum engineering.

Additionally, many studies have been conducted to characterize and correlate the joint surface roughness with the joint mechanical behaviour using 2D and 3D roughness profiling devices (e.g. Mayers, 1962; Barton and Choubey, 1977; El-Soudani, 1978; Tse and Cruden, 1979; Maerz et al., 1990; Yu and Vayssade 1991; Poon et al., 1992; Kulatilake et al., 1995; Belem et al., 2000; Grasselli, 2001; Yang et al., 2001; Kim et al., 2009; Tatone and Grasselli, 2010; and Jang et al., 2014). Fracture roughness has been quantitatively characterized based on several morphological approaches, including empirical (Barton and Choubey, 1977), statistical (Reeves, 1985; Maerz et al., 1990) and fractal approaches (Seidel and Haberfield, 1995; Zhou and Xie, 2003; Babadagli and Develi, 2003).

The effect of loading boundary conditions on morphology of induced fracture has been lately investigated. The effect of different loading modes on the roughness has been studied on rocklike materials (Amitrano and Schmittbuhl, 2002; Seredin et al., 2013). Tang and Kou (1998) investigated the effect of loading modes on a pre-flawed sample using numerical code RFPA^{2D} (Rock Fracture Propagation Analysis). Bobet and Enstein (1998) studied the effect of the loading modes on the crack initiation and propagation by applying uniaxial tensile, uniaxial and triaxial compression tests on samples with a unique pattern of flaws. Feng et al. (2014) carried out an investigation on the fracture surface morphology originated from the Brazilian tests.

Since the strain-type rockburst can be investigated on intact rock using compressive loading, the shear mechanical behaviour of the created joint plays an important role in the severity of post-peak behaviour regarding to the applied boundary condition. To predict rockburst in mines, many attempts were made based on different approaches. Crack growth mechanisms, seismicity, strain energy accumulation, artificial neural networks, numerical modeling, Gaussian process, and

fuzzy modeling are the methods used to predict the rockburst (e.g., Dyskin and Germanovich, 1993; Beer and Mendecki, 1998; Haijun et al., 2003; Wiles, 2005; Su et al., 2009; Adoko et al., 2013 and Dong et al., 2013). These models are based on statistical and mathematical methods in which the mechanical properties of rock mass are not well considered. Aubertin and Gill (1988), Aubertin et al. (1994) and Wang and Park (2001) proposed the brittleness indices to evaluate severity of the brittleness. These indices are based on strain energy accumulation and mechanical properties of rock in loading phase.

Since rockburst phenomenon is related to the energy release in the post-peak phase of intact rock, the post-failure was studied by many researchers using laboratory tests (Cook, 1965; Rummel and Fairhurst, 1970; Wawersik and Fairhurst, 1970; Salamon, 1974; Gill et al., 1993; Aubertin and Simon, 1997; Ray et al., 1999; Xiao et al., 2010). Martin (1993) and Martin and Chandler (1994) proposed a damaged controlled procedure to obtain post-peak behaviour of granite, limestone and potash specimens. Fairhurst and Hudson (1999) suggested an alternative control technique by a testing procedure in which the axial and circumferential strain control along with a computed feedback control were used to obtain a complete stress-strain curve. Simon et al. (2003) also proposed an indirect analytical approach based on triaxial compression tests to predict the post-peak behaviour of hard rock. They used a constitutive model for rock joint- the CSDS model (complete stress-displacement surface) - to estimate the uniaxial post-peak behaviour using a complete stress-strain curve of triaxial tests. The model parameters were obtained from literature on medium strength rocks. This is nonetheless important to validate this approach based on laboratory tests on hard rocks.

The first purpose of this thesis is to validate the proposed indirect approach proposed by Simon et al. (2003) which can be used to predict the post-peak behaviour of rock and the rock burst proneness in underground excavations. This approach can be developed by focusing on the fracture surface quantification. The secondary motivation for this thesis is to perform uniaxial, triaxial and direct shear tests on hard rocks to obtain the CSDS model properties and also to characterize the roughness properties of the created joints considering the loading directions. This indirect approach gives a good estimation of the severity of brittle failure based on the post-peak stress-strain curve. Mining engineers can then use these results for optimized designing of mine layout (i.e. room and pillar mining method) based on the regional stress field (surrounding rock mass stiffness) and the optimum production rate. These results can also be applied in oil well

drilling engineering to predict the wellbore instability in deep wells. Also, the roughness characteristics of rock joints can be better estimated considering different loading conditions.

For these purposes, a comprehensive laboratory tests (over 300 tests) were conducted on hard rock specimens, including gabbro, microgabbro and basalt. The created joint surfaces using modified splitting, Brazilian, uniaxial and triaxial compression tests were then characterized using 2D and 3D profilometry devices. The variation of the roughness parameters along the roughness profiles parallel and perpendicular to the loading axis was investigated for different rock types considering grains size. The influence of length-to–diameter ratio (L/D) on roughness parameters obtained from the created joints was also studied. The results specifically show that how the joint surface parameters are affected by different loading condition, grain size and the shape of specimens (L/D ratio). An applied loading procedure was proposed in order to obtain the post-peak curve of samples subjected to uniaxial and triaxial compression. The required properties for the proposed approach based on the CSDS model were also obtained using uniaxial, triaxial and direct shear tests on hard rocks. The results of this study imply that the proposed approach can be used to predict the post-peak behaviour of hard rock using the results of direct shear and triaxial compression tests along with the results of the surface characterization.

This thesis contains the following parts: Chapter 1 presents the research problem and objective with a glance of the methodology. Chapter 2 reviews the literature related to rockburst mechanisms, joint roughness and mechanical shear behaviour models of joints, which are interconnected in order to control the post-failure behaviour of rocks. In Chapter 3, the main focus is on the fracture surface characterization. A new surface roughness quantification (2DRP) method is proposed. The fracture surfaces created using modified splitting method, uniaxial, and triaxial compression tests are investigated using 2DRP method; the results of this study is compared with a 3D roughness profilometry device. This Chapter also addresses the joint roughness characterization based on different loading conditions for three rock types. Chapter 4 illustrates the roughness parameters of fracture surfaces created by tension using the Brazilian tests. The results show the influence of the shape effect and loading direction on the joint roughness parameters. The effect of L/D ratio on the roughness parameters is also presented for three rock types. Chapter 5 presents an experimental procedure to obtain the post-failure curve of brittle hard rocks through the damage-controlling method. Chapter 6 provides the results of the

post-peak stress-strain curves for uniaxial, triaxial and direct shear tests using the proposed approach and based on the CSDS model. These results indicate that how the proposed approach can be used for prediction of the post-peak behaviour of intact rock with respect to the fracture surfaces obtained by different loading modes. Chapters 3 to 6 are presented in the form of paper manuscripts that have been submitted to peer-reviewed journals; because of this paper format, there will be overlaps and repetitions between the chapters. The interpretation of results shown in these chapters is context dependent and, in some cases, may include engineering judgment of the author. Chapter 7 discusses these findings. The last chapter includes a conclusion and recommendations for the future works.

1.2 **Problem statement**

In practice, the post-peak behaviour of intact rock can be evaluated using direct and indirect approaches. Simon et al. (2003) proposed an indirect analytical approach based on the results of triaxial compression tests to predict the post-peak behaviour of hard rock. A constitutive model for rock joint- the CSDS model (complete stress-displacement surface) – was used to estimate the uniaxial post-peak behaviour of brittle rocks using a complete stress-strain curve of triaxial tests. The model properties were obtained from the test results of the literature on medium strength rocks. There is no validation on the application of this approach for hard rocks based on the laboratory tests.

This dissertation deals with the validation of this approach based on comprehensive laboratory tests on hard rocks to predict the post-peak stiffness of rock. The goal of this thesis is to estimate and adjust the model properties using triaxial, uniaxial, and direct shear tests on hard rocks. In addition, this approach can be developed by focusing on surface quantification of the fractures created by uniaxial, triaxial and direct shear tests. The created joint surfaces using indirect tension, modified splitting, shear, uniaxial and triaxial compression tests are characterized using 2D and 3D profilometry devices. The variation of the roughness parameters along the roughness profiles parallel and perpendicular to the loading axis is also investigated for different rock types considering the grain size and the length-to-diameter (L/D) ratio. The required properties for the proposed approach and the CSDS model are adjusted based on the roughness properties of the created joints considering the loading directions.

1.3 **Thesis objective**

The main objective of this thesis was to investigate and to validate the proposed approach (Simon et al. 2003) for estimation the post-peak behaviour of hard rock using the CSDS model with respect to the fracture surface characterization. These objectives can be divided into sub-sections:

1- Conduct a review of the past and current methods for joint surface characterization and the joint shear models as well as the prediction of the post-peak behaviour of rock.

2- Carry out comprehensive laboratory tests, including modified splitting, Brazilian, uniaxial and triaxial compression; and direct shear tests for different rock types considering the effect of grain size, the loading direction and the L/D ratio with the following capabilities:

- Propose a new 2D roughness profilommetry method (2DRP) which is simple and appropriate for the joint with the length of maximum 100 mm.
- Validate a new roughness profilommetry technique (2DRP) using 3D profilommetry devices.
- Create fractures in different loading modes in terms of tension or shear by splitting, uniaxial and triaxial compression tests. This process is pursued with characterizing the fracture surfaces based on the different loading modes in terms of the roughness parameter on three hard rocks.
- Evaluate the roughness anisotropy in tensile fractures considering the loading direction and length of the sample as well as the effect of grain size and stress distribution in the samples.

3- Perform the uniaxial compression tests on hard rocks by a new damage-controlled cyclic procedure in order to obtain the post-peak curve.

4- Evaluate and validate the proposed approach for prediction of the post-peak behaviour of intact hard rocks and develop the CSDS model parameters considering the induced fracture characterization and the results of laboratory tests.

1.4 Relevance of the thesis

Rockburst is one of the most important instability problems in hard rock mining, civil construction and oil well drilling caused by overstressing and violent release of strain energy stored in the system. This phenomenon usually occurs suddenly, which causes major damages and injuries in underground structures. Many studies have been carried out to predict rockburst occurrence, but few studies paid attention to the rock behaviour in the post-failure stage, which is very important in terms of optimized mining design and required support.

The prediction of post-peak behaviour of hard rock will improve the determination of the load-bearing capacity of the failed rock in order to optimized fulfill of the mining design projects. It may also be possible to select the pillar slenderness based on the regional stress field (boundary stiffness) and the optimum production rate.

This thesis provides a development of the proposed approach (Simon et al. 2003) for the optimum design of deep underground openings based on the post-peak behaviour of hard rocks. The post-peak curve of hard rocks is predicted considering the influence of various factors. The effect of fracture surface characterization in the post-peak curve estimation is also studied. The results of this study also show the effect of the loading direction and L/D ratio on the roughness parameters of the fracture surfaces.

1.5 Contribution

The current research will contribute to predict the behaviour of strain-type rockburst induced by overstressing condition. It may help to better achieve a deep insight of elastic energy release observed in the walls of underground openings. This research may lead to the following benefits:

- Proposition of a new 2D profilommetry technique in order to characterize fracture surfaces.
- Determination of the mechanical behaviour of rock joints created using different loading modes.
- Development of a procedure to obtain uniaxial post-peak curve for very hard rock when using a non-stiff pressing machine.

- Optimization of the pre-existing analytical approach in predicting the post-peak curve of intact rocks.
- Significant cost saving by an improved prediction of the post-peak behaviour of hard rocks.
- Significant risk reduction due to strain-burst phenomenon and improved pillar design and production rates following a better estimation of the post-peak behaviour of intact hard rocks.

The scientific contribution of this project is a thesis that includes the following four manuscripts submitted to peer reviewed journals:

1) Khosravi, A., Simon, R., Falaknaz, N. Morphological evaluation of fractures created by different loading modes focusing on the modified splitting technique. *Canadian Geotechnical Journal*. Submitted in June 2016.

2) Khosravi, A., Simon, R., Rivard, P. The shape effect on the morphology of fracture surface induced by the Brazilian test. *Int. Jrnl. of Rock Mech. and Min. Sci.* Submitted in February 2016.

3) Khosravi, A., Simon, R., Effect of the pre-peak loading condition on the post-peak behaviour of the brittle rocks. *Int. Jrnl. Of Rock Mech. and Min. Sci.* Submitted in June 2016.

4) Khosravi, A., Simon, R. Post-peak behaviour of hard and brittle rocks: Estimation and verification using the CSDS model for rock joints. *International Journal of Geomechanics*. Submitted in June 2016.

Four other conference papers were also published in the proceeding in the course of this doctoral work (Khosravi et al., 2014; Khosravi and Simon, 2014, 2015, 2016).

It is worth noting that the four manuscripts included in this thesis (Chapters 3 to 6) are based on those initially submitted to journals and may be corrected (as requested by the reviewers and editors) later. These corrections are not included here and the final papers may thus differ from the versions in the thesis.

1.6 **Outline of the thesis**

Chapter 1 contains the research approach, objectives and the relevance of the thesis. Chapter 2 presents a literature review of the main subjects such as: rockburst definitions, rockburst types

and mechanisms, joint shear behaviour, joint shear models and roughness characterization and parameters.

Chapter 3 introduces a new technique of roughness profilommetry, which has been verified using a 3D profilommetry apparatus (ATOS II). Fracture surface obtained by different loading modes including uniaxial, triaxial and modified splitting tests were characterized in terms of roughness parameters. Three rock types were considered for this investigation. The effect of loading direction on the roughness variation was also studied. The trajectory of the fracture created by the modified splitting was investigated microscopically.

Chapter 4 presents the main results of the fracture characterization created by the Brazilian tests on the samples with different length to diameter (L/D) ratio. The fracture patterns were studied in terms of the L/D ratio. The roughness profiles perpendicular and parallel to the loading direction were also obtained for different L/D ratio for three different rock types. The scale effect on the fracture roughness was also evaluated. Special attention has been also paid on the roughness anisotropy in terms of the loading direction.

Chapter 5 contains a procedure by which the post-peak curve of a hard brittle rock can be obtained by applying a damage-control approach. The results are presented in terms of stress-strain curve for the uniaxial compressive tests. The fracture patterns obtained using this method was studied in this chapter. The influence of the brittleness and energy release concept is addressed by looking at the fracturing pattern on the broken specimens. The results of this method were also validated using BIM (Brittleness Index Modified) and energy concept method. In addition, the brittleness indices were classified for different rock types.

Chapter 6 includes the results of uniaxial, triaxial compression and direct shear tests conducted to estimate the post-peak behaviour of hard rocks. The CSDS model properties were obtained for each test using the proposed approach. Then, the model properties were compared in different tests to obtain fitted model parameters. The uniaxial and triaxial tests were also conducted to characterize the fracture surfaces created in different loading modes. The model properties were then modified based on the fracture surface characterization and the results of the different rock tests. The post-peak stress-strain curve of hard rocks in uniaxial compression was further obtained based on the results of direct shear test, uniaxial and triaxial compression tests and the fracture surface characterization.

Chapter 7 includes a summary and general discussion on the results obtained in this investigation. Chapter 8 contains a conclusion and recommendations for future studies.

CHAPTER 2 THEORETICAL BACKGROUND- ROCKBURST AND ROCK JOINT MECHANICAL BEHAVIOUR

2.1 Introduction

Underground mines are prone to various dangers. The most feared of these threats have always occurred unexpectedly with violence. Explosions or disturbance of unstable equilibrium, including rockbursts, coal bumps, and rock-fall are examples of these types of events (Salamon, 1993).

One of the most destructive problems associated with underground deep mines is rockburst. Many scholars consider rockburst as a seismic event. A seismic event can trigger rockburst phenomenon, in which, the rockburst emits seismic waves that can lead to other seismic activities. Depending on high or low seismic frequencies, the severity of the consequences can be low or high, respectively. The occurrence of rockbursts is associated with many factors such as the geological structures of rock mass, depth, the stress conditions, the rock mass strength, the excavation method, the excavation size and the rock blasting. As the stress state increases with depth, the rock mass instabilities and other safety issues matter. Rock burst has been reported since the 18th century. In the early 1900's, rockburst was observed as "air blast" in Coeur d'Alene district and the first injury as fatality was reported in 1914 (Whyatt et al., 2002).

The first recorded rockburst in British coal mine was at Stafford in 1938 (Jiang et al., 2010). Kolar gold mine (India) is one of the earliest mines reached to great depth and encountered rockburst problem at moderate depth (500 m) at the end of 19th century (Morrison, 1942). According to mining history, rockbursts have occurred at all depths and mines with different rock types (Blake, 1972; Blake & Hedley, 2003). It should be mentioned that rockburst occurrence in shallow depth and surface mines (Vermont, U.S.A.) are scarce in comparison with deep hard rock mines. Normally, the seismic events would be observed in the high-stressed regions whether at depth or not. There are many active mines in Canada, in which, relatively notable rockbursts have occurred and led to injuries or loss of a part of ore deposit. For example, a rockburst phenomenon was reported in Director Fluorspar mine in Newfoundland at depth of 150 m (Blake and Hedley, 2003). This problem has been observed in other countries too (e.g. South Africa, Germany, Poland, Russia, Australia, Japan and china) and was studied by many scholars. In the last four

decades, many research strived to alleviate the problems comprehensively (Cook, 1963, 1966, 1978; Salamon, 1970, 1983, 1984, 1993; Petukhov, 1972; Heunis, 1980; Kidyinski, 1981; Blake, 1972 & 2003; Lippmann, 1990; Ortlepp, 1978, 1994, 2000, 2001; Vardoulakis, 1984; Ryder, 1986, 1988; Hedley, 1987; Singh, 1987, 1988, 1989; McMahon, 1988; Gill & Aubertin, 1993; Kaiser et al., 1995; Linkov, 1996; Wu et al., 1997; Frid, 1997, 2000, 2001; Tang, 2000; Wang et al., 2001, 2010; Whyatt, 2000, 2002; Chen et al., 2003; Lee et al., 2004; Mitri, 1993,2007; Jian et al., 2009). Many researches have been done to predict and prevent rock burst while the miners encountered the rockburst problems. In South Africa (Salamon, 1993) and in recent years in Canada (Kaiser et al., 1995), considerable achievements have been made in rockburst phenomenon based on rock mechanics knowledge.

Since rockburst is considered as a time-dependent phenomenon, the prevention methods can be categorized as before, during and after extraction. By considering the mine depth and stress state of the region, the burst-prone area can be determined. Mining layout, mining rate (sequence), ground support and mining method can be modified in the design phase to prevent rockburst. Kaiser et al. (1995) have carried out a comprehensive study about supporting methods in the burst-prone areas in Canadian mines. Different types of ground support used in Canadian mines have been discussed and analysed. De-stress blasting and water infusion are the methods performed during mining. Backfilling of the mined-out area with different methods is another rockburst prevention method, which is applied after extracting each stope.

2.2 **Rockburst definition**

When an underground opening is excavated, the stress state is changed. As a consequence, the potential energy of the whole system is also changed by mining out of the underground opening. Jaeger and Cook (1979) have shown that one half of the potential energy change can be stored as elastic strain energy and the rest must be released. This released energy can be in the form of rockbursts

Rockburst is a particular expression of underground excavation instability. It accompanies violent fracturing and explosive displacement of rock into the mine opening.

Cook (1963, 1966) addressed rock burst as the excess potential energy changes in rock that leads to brittle fracturing. Hoek and Brown (1980) described rockburst as a product of explosive brittle

fracturing in deep hard rock mines with respect to extreme state of the existing stresses. According to Kaiser et al. (1995, 1997), rockburst is a seismic event that concerns damages to mine opening directly with a sudden and violent manner. Rockburst occurs in all kinds of mining or civil underground openings. Vardoulakis (1984) introduced rockburst in coal mines as a surface instability. Linkov (1996) also allocated rockburst to a local pillar edge fracturing. As a result of rapid convergence and oscillation of the underground excavation wall, periphery slabbing parallel to the maximum principal stress direction and finally failure of the rock occur. Based on slabbing, rockburst can be accounted as a surface buckling phenomenon that can happen at a tiny time (Ortlepp, 1978; Bardet, 1989). These phenomena happen when one productive layer takes place between two layers with lower stiffness.

According to an energy point of view, the magnitude of energy changes as a result of mining activities. Some amount of the energy consume in the transient period to the new state and a part of that is stored in the rock mass in the adjacent of underground opening. In fact, rockburst is a part of the stored strain energy, which is released in rock mass suddenly and violently (Blake, 1972 and Salamon, 1983). This definition is the most common scientifically used one in the research centres such as U.S Bureau of Mines (U.S.B.M.).

Since the geological structures are influenced by pre-mining and mining activities, the strain energy produced by the structural displacements (micro or macro) causes the seismic events (Cook, 1983). Basically most seismic events have no negative side effects to miners and potential harm or damage to underground openings. Only a severe release of energy leads a big seismic event. According to Cook (1966), “all rockbursts are seismic events but not all seismic events become rockbursts”. The emitted seismic energy must have a sufficient magnitude to be able to fracture the different volume of rock and to lead a rockburst (McMahon, 1988). It is observed that the rockburst occurs when the seismicity builds up and follows by dramatic seismicity drop. The longer travel time between seismicity build-up and drop, causes the greater amount of energy release, which can increase the hazardous damage (rockburst).

2.3 **Rockburst types and mechanisms**

Bath (1984) concluded that the rockburst mechanism was associated with the mine geometry, stress pattern and fracture orientation in the region. A rockburst in the fractured zone occurs due to:

1. Collapse of fractured zone;
2. Weak and inadequate support;
3. Geological disturbances;
4. Other disturbances in the mining area (mining layout, mining method); and,
5. The disturbances originated from the surrounding solid rock.

Different research proposed distinctive classifications for rockburst types. Joughin and Jaeger (1983) addressed two types of rockburst, in which, the fractures or discontinuities are main sources, including where the fault or discontinuities move and where the fractures are exposed on the opening faces.

Brummer and Rorke (1990) categorized three types of rockbursts in South African gold mines, including crush rockburst, pillar foundation failure and shear slip rockburst. In the other researches, rockbursts are divided into two types; The first type (Type I) is directly related to an advancing mine face that is so-called strainbursts; The second type (Type II) is one involving induced movement along pre-existing fault planes that is called fault-slip rockburst (Johnstone, 1988; and Yi and Kaiser, 1993).

Type I is directly associated with the working face fracturing and is a function of excavation rate. In this case, the source of stress redistribution is located near the active working face. The opening geometry and the surrounding rock mass stiffness are the most important parameters involved in the fracturing process. Shear stress increases due to different stiffness of rock masses. Also, any increase in the stresses at immediate roof and floor of the working face can increase shear stress on the surrounding rock mass. In such a condition, mining may be followed by a dynamic event and the damages due to the amount of energy emitted in the brittle strata. This phenomenon can be seen in all types of underground openings with different mining methods.

Type II occurs less often than type I. In this case, the rockburst occurs when the pre-existing geological structure (mainly faults) is affected by the stress field. As a consequence, a brittle

fracturing zone in the working face and roof is formed. The condition of critical burst can be achieved by studying the geological and deformational properties of rock mass. It is worth noting that pillar-bursts often occur with a combination of the two mechanisms.

By comparing two types, type I involves the higher rate of released energy and the larger affected area of rock masses due to the fracturing process. Type II is triggered by mining activities close to the pre-existing major discontinuities. The amount of released energy at a time unit is higher in type I than type II while the affected areas in type II are extensive.

2.3.1 Fault-slip burst

As mentioned before, rockburst occurs due to a rapid energy release from rock mass. In the fault-slip bursts, the energy releases by slip along the geological discontinuities such as faults, dykes, joints and bedding plane, when such discontinuities exist in the vicinity of underground opening. These discontinuities can either be persistent or interrupted by rock bridging, opened, closed or filled. All kind of discontinuities would have shear movement when the condition is satisfied. Such events are controlled by the shear stresses and cohesion along the plane. The stress changes may increase the shear stress or reduce the applied normal stress on a discontinuity. It also changes the coefficient of the internal friction (which drops slightly after slip is initiated), cohesion (which affects the shear strength and shear stress level) and the dilation angle. Therefore, it can provoke a violent slip.

Joughin and Jaeger (1983) classified all fractures in an underground gold mine (South Africa) into three types. The strikes of these fractures were almost parallel to the stope faces as shown in Figure 2-1. These three types are expressed as follows:

- *Fracture type 1*: These fractures are inclined created in the relatively high distance ahead from the stope face with no shear displacements. When the stope span is increased, energy release rate grows up and the fractures form with inclination of 80-100^{o}. Actually, these kinds of fractures represent the maximum principal stress direction.
- *Fracture type 2*: These types of fractures are accompanied with displacement with an aperture of few millimetres and an inclination of 60-75^{o}. These fractures form an en-echelon fracture in the vicinity of a fault.

- *Fracture type 3*: These types of fractures are low inclined (20-40^{o}). They are very close to the stope face with no shear displacement. They are created as a result of stress changes in the opening periphery. All three types of fractures may tend to move inside the mine space violently as a rockburst.

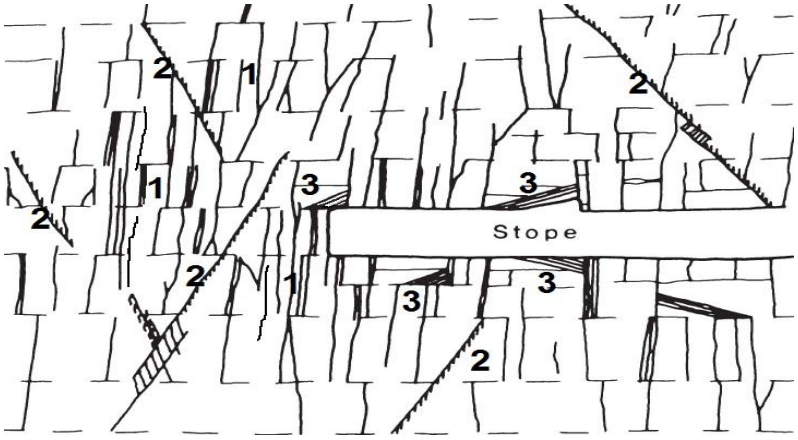

Figure 2-1: Different types of fractures as a consequence of mining (McMahon, 1988).

The slip behaviour of the discontinuity depends on three factors: normal stress on the slip surface, surface roughness and stiffness and deformation modulus of surrounding rock mass. The normal stress has a dominant effect on the slip behaviour. When the normal stress decreases beyond a critical stress level (as an unloading process-increase in differential stress), the other type of fault-slip burst (stick-slip) occurs in combination with the existing shear stress (Zou et al., 1989). The surface roughness along discontinuities influences the slip behaviour. Energy gradually builds up during the stick period and releases suddenly at the time of slip. Salamon (1974) developed a stiffness approach to fault-slip rockbursts. Figure 2-2 shows the load-deformation obtained using the direct shear tests on the samples with a planar discontinuity.

When the post-failure stiffness of rock (k_p') exceeds the stiffness of testing machine (loading system-k_{ls}), the stored energy is released and the violent failure occurs (Fig. 2-2a). If the stiffness equilibrium is satisfied (rock sample stiffness is less than loading system stiffness), there is no dynamic phenomenon and the failure will be occurred smoothly and gradually (Fig. 2-2b).

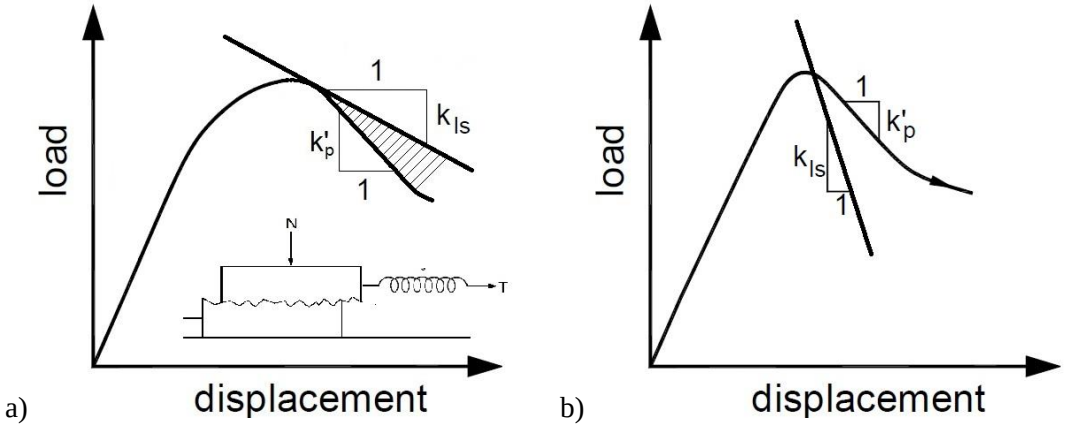

Figure 2-2: A stiffness approach related to load-displacement curve: a) Violent failure due to stored energy release; b) gradual failure (k_{ls} is loading system stiffness; k'_p the rock post-peak stiffness) (After Salamon, 1974).

2.3.2 Strain-burst

Cook (1987) concluded that the phenomenon of violent failure of the rock surface can be divided into two parts: Cracking of the stope wall along with implosion and collapsing of the wall rock. Strain-burst is as well as a compression where the loading machine stiffness is lower than the rock stiffness (Cook, 1965; Gill et al., 1993). Figure 2-3 schematically presents the loading system stiffness in the uniaxial compression test, which is similar to the strain-burst phenomenon.

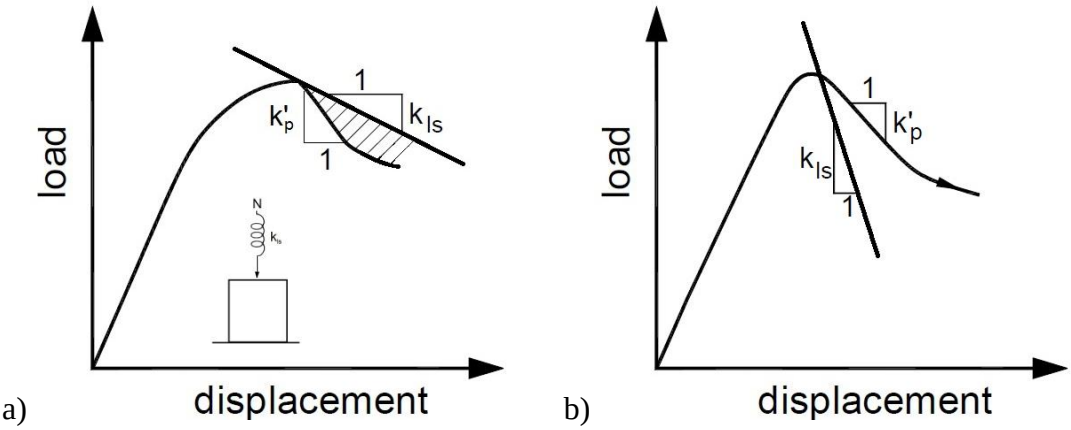

Figure 2-3: The role of loading system stiffness in uniaxial compression test: a) energy accumulation and violent failure; b) gradual failure (After Cook, 1965).

As it is illustrated, when the loading system stiffness (k_{ls}) - in absolute value- is smaller than the rock post-peak stiffness (k_p'), some amount of strain energy is accumulated in the whole system (hatched area in Figure 2-3a). If the amount of stored energy exceeds a critical value, a big portion of energy is released violently in the form of a fracture. Reversely, when the loading system stiffness is high, gradual failure would occur (Figure 2-3b).

Generally, all types of rockbursts occur due to high magnitudes of the accumulated energy in the stressed region of rock mass. In strain-burst, a stress-induced failure is formed in underground excavations due to the energy release. From a geological point of view, the strain-burst most likely occurs in more massive rock types, which have a high degree of brittleness (Aubertin and Gill, 1988). The failures are mainly classified in two modes: tension and tension shearing.

According to observations, rock bursts (strain burst) are particularly influenced by the geological factors rather than the stress state. In steeply dipping sedimentary layers, the strain burst is the common failure mechanism in rock walls fragmented and buckled skin of opening sidewalls may be formed due to severe cleavages parallel to bedding plane and brittle nature in the media.

2.3.2.1 Exfoliation and slabbing

In some cases, strain-burst is exposed by the rock mass lamination with different thicknesses as can be seen in Figure 2-4. This phenomenon is due to three main reasons: the governing stresses state, the rock mass brittleness and the mineralogical properties. In the worst case, the laminating process will lead to rockburst when the stress state exceeds the rock mass strength. The slab thickness depends on the stress state, pre-existing joints, rock mass grain size and rock mechanical properties such as the tensile strength (Muehlhaus, 1990).

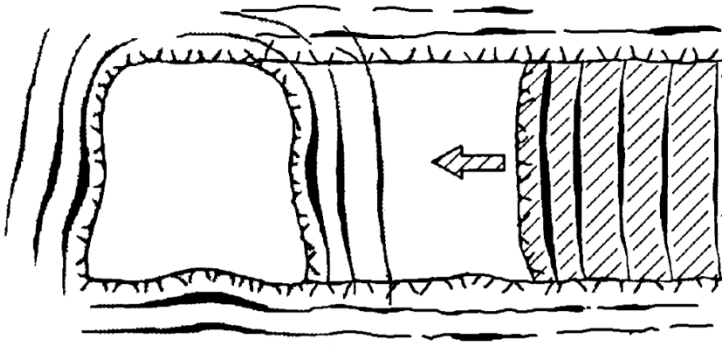

Figure 2-4: Slabbing of the face and sidewall of underground excavation (Muehlhaus, 1990).

Wawersik and Fairhurst (1970) performed the uniaxial tests to study the effect of confining pressure in the slabbing thickness. It was observed that the fractures were formed with inclination of 12-18° to the vertical at the early stages of the test. Then, the shear fractures were formed at inclination of 30º to the vertical toward the interior of the specimens (Figure 2-5).

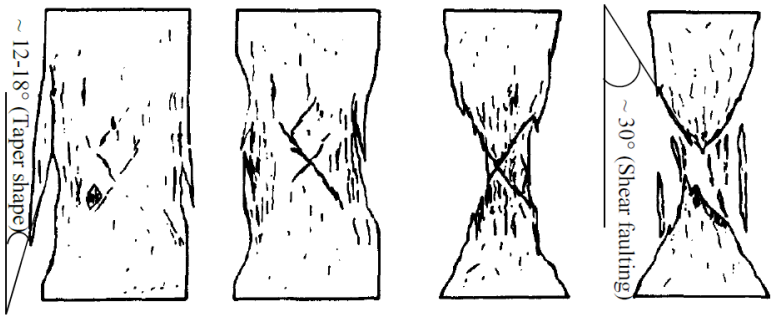

Figure 2-5: Slabbing process during uniaxial compression with respect to influence of confinement (Wawersik and Fairhurst. 1970).

2.3.2.2 Pillar burst

Pillar burst is a seismic event as a result of damage to the load-bearing capacity of a pillar. A big seismic event shakes the surrounding rock mass and can cause significant damage or chain pillars failure. In some cases, it seems that two mechanisms, strain and slip burst, are combined in the pillar burst (Yi and Kaiser, 1993). It is generally addressed that the pillar burst occurs under a strain-burst mechanism, unless a geological discontinuity was pre-existed and placed in the middle of the pillar. These kinds of induced fractures can be activated as the slip burst.

The most important factor in the pillar design is its slenderness. According to Holland (1964), pillars with slenderness ratio (Width/Height) more than 10 are virtually indestructible and can withstand high stresses. In the ratio of 2.5 slabbing and spalling of the pillar wall is triggered (Martin and Maybee, 2000) continued by failure at the ratio of 1. As pillar is deteriorated, the areal size reduces and pillar slenders by spalling the sidewall rocks. This process looks like a simple uniaxial compression test. Wawersik and Fairhurst (1970) studied the behaviour of rock fracturing using uniaxial compression tests.

2.4 **Rockburst origin**

The factors influencing rockburst occurrence are very complex and numerous, which play a crucial role in the results validation. These factors include tectonic, stress state, mining-induced stress, geological structure, mining layout, extraction sequence, engineering measure, release of stored energy and the energy release rate. Another rock burst source is the changes generated by seismic events due to differences in the geological features.

Singh (1988) proposed three main sources and conditions for rockburst occurrence as follows:

1. Ultimate stress conditions: favourable rock characteristics, gravity loading, mining induced stresses, stresses due to previous temperature and loading conditions, stresses due to faulting, folding, metamorphism.
2. Instability conditions: a sudden stress change with significant magnitude, discontinuous of rock mass, rocks in the strain softening state, some support system on the verge of collapse and the geological discontinuities.
3. Source with sufficient energy: mining induced stresses, gravitational forces and tectonic forces.

When in situ rock stresses increase to a certain level, an overloading takes place on the remaining rock structures. As a result, the plastic deformation and fracturing occurs. High horizontal stress, tectonic activity and the brittle rock material are the other reasons of being prone to rockburst. The brittleness is an original reason for dynamic fracturing, but it is not the only condition for rockburst occurrence. This concept has been studied micro- and macroscopically by many authors (e.g. Martin, 1993; Lajtai, 1971, 1974; Nemat-Nasser & Horii, 1982; Eberhardt, 1998; Hajiabdolmajid, 2001).

Since, the fault-slip burst occurs in pre-existing discontinuities generated tectonically, hence, the brittle fracturing mechanism is not the dominant phenomenon in slipping process on discontinuities. However, the strain-burst originates from brittle fracturing due to the essence of rock mass tolerability in the highly stress state. Basically, the conditions of loading are different in nature. In the laboratory, achieving to the natural loading condition is hardly possible. However, the initiation of cracking in laboratory tests indicated that the cracking is independent of the loading conditions and dependent to the material properties (Martin, 1993).

2.4.1 Brittle Fracturing

Theory of brittle fracturing has been established by Griffith (1920). In this theory, the equilibrium state of a deformed elastic solid body would be satisfied when the system can pass from the unbroken to the broken condition by a process involving a continuous decrease in the potential energy. The amount of consumed energy exceeds the required work to form new surface by elongation of pre-existed Griffith crack.

The behaviour at the tip of the crack is assumed homogenous linear elastic. Single crack extension occurs when the surface energy is gathered through the rupturing. Subsequently, the equilibrium in the system is satisfied if the total potential energy is equal to the sum of the elastic strain energy and the surface energy in the free faces of the crack. By increasing the applied stress intensity at the tip of favourably oriented crack, the associated potential energy increases in the crack and extension will occur (Griffith, 1920; Murrell and Digby, 1970; Cotterell, 1971; Lajtai, 1974; Eberhardt, 1998).

If a long elliptical crack under a compressive condition is assumed, the crack may be closed before the tensile stress at the tip is high enough for the crack propagation. After the crack is closed, the frictional resistance caused by the contact pressure between the crack faces must be overcome before the crack initiation. To consider the frictional movement of two surfaces of the crack, McClintock and Walsh (1962) suggested a modification in which the normal and frictional stresses acting across the surface of crack were taken into account. In Figure 2-6, the Griffith theory and the modified theory by McClintock and Walsh are compared schematically.

2.4.1.1 Crack initiation and geometry

The crack geometry plays a very important role in developing stresses in the crack tip. The researchers considered three types of cracks, including: inclined ellipse, inclined zero-width ellipse and axial ellipse. In crystalline materials, the grain boundaries are assumed as the stress concentrators and the crack length depends on materials grain size (Simmons and Richter, 1976; Kranz, 1983). Grain size is the elementary and critical factor in the crack length. A finer-grained material corresponds to the higher crack density and heterogeneity of the local stress field. This heterogeneity influences the crack propagation so that the prediction of crack length is difficult

due to the cracking termination at the stages earlier than those predicted in coarser grained materials (Fredrich et al., 1990).

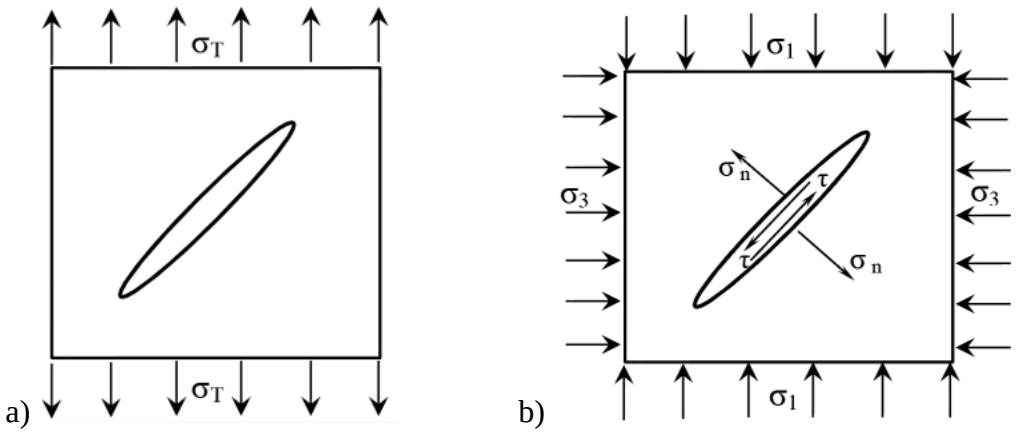

Figure 2-6: Loading conditions and induced stresses on two dimensional model of a single crack: a) Griffith model (Griffith, 1920); b) McClintock and Walsh model (McClintock and Walsh, 1962).

If the applied stress level on the materials exceeds the threshold strength, cracks initiate. When the number of cracks increases, the progressive stress begins to propagate. The crack propagation will occur in either stable or unstable manners. Several researches have been conducted on the brittle fracturing to characterize cracking stages focusing of the crack damage threshold (Martin and Chandler, 1994; Eberhardt et al., 1998; and Aubertin et al., 1998).

2.4.1.2 Crack propagation

The studies demonstrated that a crack parallel to the uniaxial tensile load is extended less than a crack perpendicular to the load due to stress concentration at the tip of long axis. In compression, the crack is developed along the loading direction due to tangential stress concentration on the elliptical boundary of crack (Lajtai, 1971). In the crack propagation stage, cracks are developed and a shear belt, mainly in tips, is formed at the micro-crack and propagated in an unstable manner along the loading direction. When a single flaw is subjected to a compression load, two cracks are created, including: wing (tensile) and secondary cracks (shear) (Figure 2-7).

Two neighbor cracks can be coalesced by the tensile or shear failure under compression in different patterns depending on cracks array and position (Reyes and Einstein, 1990; Bobet and Einstein, 1998; Wong and Chau, 1998; Wong et al., 2002; Wong and Einstein, 2009; Park and

Bobet, 2010). The pattern of the cracks coalescence is influenced by the crack angle, bridge angle (angle of line between two neighbor cracks) and frictional coefficient of the crack surface (Wong and Chau, 1998).

Brittle fracturing is a result of coalescence of numerous pre-existed and/or stress induced flaws, which will form the fracture path. Normally, the first induced flaws in the uniaxial compression are in the loading direction while the pre-existed flaws may be inclined. Fracturing is a product of the cracks coalescence with different patterns, which depends on different factors such as: grain size, grain cementation, loading conditions, pre-existing flaws (Wong and Einstein, 2009).

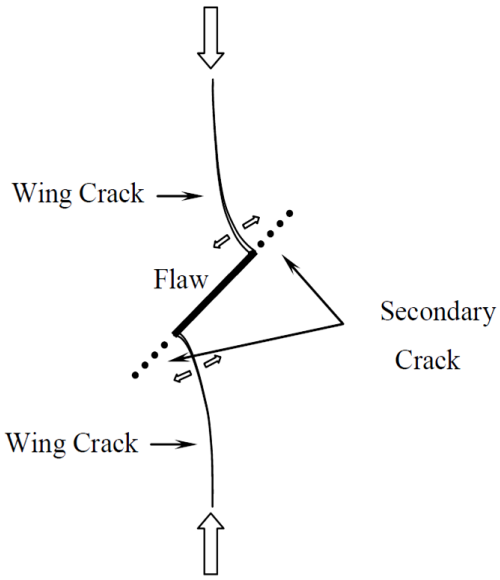

Figure 2-7: Wing and secondary cracks emanated from a single flaw (After Bobet & Einstein, 1998; Park and Bobet, 2010).

2.4.2 Brittle fracturing process

Numerous studies have been carried out to investigate the rock fracturing process in micro scale. The fracturing process is revealed through compression tests of a cylindrical sample. The full process can be seen in three stages of the stress-strain curves, including: pre-peak (pre-failure), peak (maximum strength) and post-peak (post failure) (Hajiabdolmajid, 2001).

2.4.2.1 Pre-peak stage in uniaxial compression

In the case of axial compression, rock materials behave mainly elastically during the loading phase in major part of the pre-peak range. All elastic properties of rock are derived in this state.

At the onset of loading, the pre-existing cracks are closed, (markedly in non-crystalline rocks) and then reopened when the loading increases. The important phenomenon observed in this stage is dilatancy or volume increase which is typical in the brittle rocks. In fact, the dilatant behaviour of brittle rocks is associated with the initiation and propagation of cracks (Martin and Chandler, 1994; Eberhardt et al., 1998; and Aubertin et al., 1998). Martin (1993) and Martin and Chandler (1994) carried out the compression tests and divided the pre-peak stress-strain curve into different parts in terms of cracks (pre-existing and stress-induced cracks) behaviour with the loading process. Martin concluded that the dilatancy starts at a load between 30 to 40% of the unconfined compressive strength. In this case, non-linearity of the stress-lateral strain curve could be the sign of the crack initiation and dilatancy

Figure 2-8 shows axial stress versus axial and volumetric strain curve and also the effect of the axial strain on the dilatancy at different stages in terms of the cracking process. The threshold of each cracking stage differs based on different experiments (Martin and Chandler, 1994; Eberhardt et al., 1998; and Aubertin et al., 1998).

According to Martin (1993), a crack experimentally starts propagating when the direct path of stress-lateral strain curve is deviated (stage IV) as shown in Figure 2-8. At this point, the crack propagation is considered stable. The stable crack propagation continues up to a critical point corresponding to the loading rate and the rock mechanical properties. After this point, the crack propagation will continue even though the loading is stopped or remained constant.

2.4.2.2 Peak stage in uniaxial compression

The rock peak strength depends on the confinement stress, the size of specimens and the loading rate (Marin, 1993). Micro-cracks formed in the pre-peak phase are increased numerously while the load increases. The extension of tensile and shear micro-cracks causes the micro-cracks coalescence throughout the specimen. At this point, the crack growth is led to the failure initiation by sliding along the macro-cracks. The stress-lateral strain curve will have a reversal slope. Therefore, the failure occurs when the loading magnitude exceeds the specimen peak strength. According to Xia and Zhou (2010), the number of tensile micro-cracks is almost twice of the shear micro-cracks at the peak strength.

2.4.2.3 Post-peak stage in uniaxial compression

Since rock materials in the post-peak zone around underground openings are still able to carry considerable amount of loads, understanding the post-peak behaviour would be interesting and important. The macro-shear fractures are created as a result of the loading progress in the post-peak and caused a significant stress drop. This phenomenon is called "strain softening" behaviour. The loading process leads to the last stage called residual strength due to the shear fracture and the stress drop. The residual strength is mainly related to the resistance developed on the failure plane during displacement. When the failure plane consists of multiple fracture surfaces, the residual strength represents the combination effects of the different fracture orientations, degree of interlocking, surface irregularities and degree of pulverising.

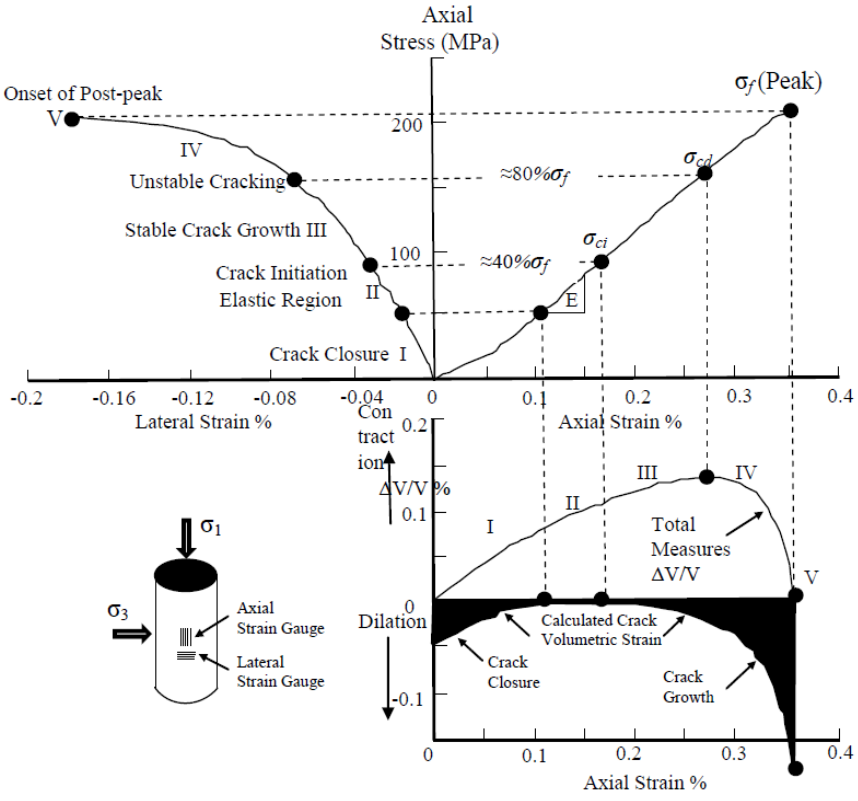

Figure 2-8: The stress-strain curve resulted from uniaxial compression test of Lac de Bonnet granite that shows the crack initiation until peak strength (After Martin and Chandler, 1994).

The post-peak behaviour strongly depends on the fracture plane angle and also the morphology of the fracture surface. The surface morphology (roughness) of the created fracture is dependent on the crack coalescence manner and the loading boundary conditions. The fracture surface

characteristics include asperity angle, roughness waviness, asperity amplitude and fracture aperture. A few experimental procedures have been developed (Wawersik and Fairhurst, 1970; Martin and Chandler, 1994; Fairhurst and Hudson, 1999 among others) to obtain the post-peak curve of hard rocks from the laboratory tests. Three experimental methods were proposed to obtain the post-peak curve of medium to hard rocks, are concisely described in the following:

- *Wawersik and Fairhurst method*

Wawersik and Fairhurst (1970) used a stiff servo-controlled pressing machine to investigate the post-peak behaviour of brittle rocks. A stiff frame was heated first. The loading was started while the load increased by circulating cold water through the supporting column. The loading rate was about 10^{-5} psi/sec. The post-peak curve was controlled by stabilizing jacks to stiffen the system with respect to the rock specimen. They concluded that rock under the uniaxial compression reveals two different classes of stress-strain characteristics, including: class I and class II (Figure 2-9).

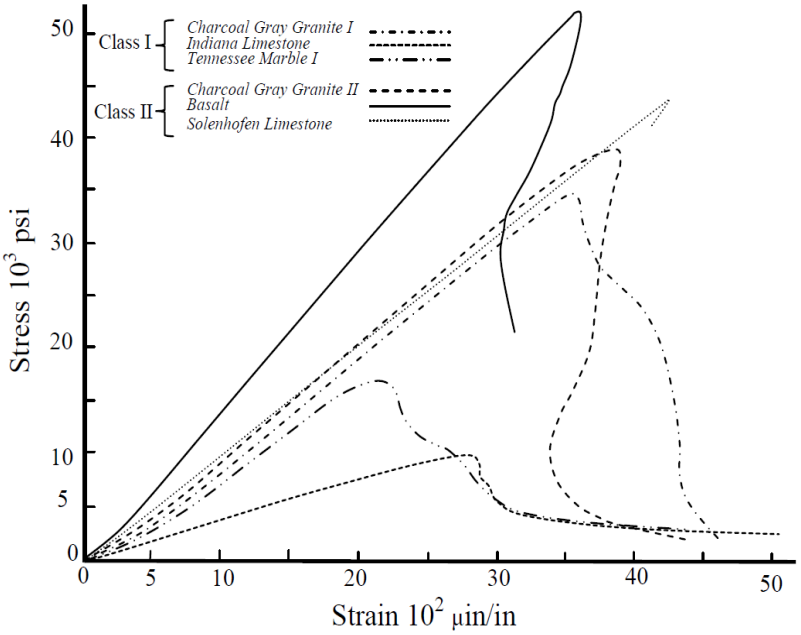

Figure 2-9: Stress-strain curves for two classes of rock behaviour during uniaxial compression test (After Wawersik & Fairhurst, 1970).

In class I, the fractures are propagated in a stable manner and the load-carrying capability is incrementally and monotonically decreased. In this mode, a local fracturing (cleavage failure) is predominantly parallel to the applied stress. In class II, the failure would not be stable so that the

self-sustaining, unstable and uncontrollable fracturing occurs. In this mode of failure, both local and macroscopic shear failures (faulting) occur.

- *Martin and Chandler method*

The damage-controlled loading method was proposed by Martin and Chandler (1994) in order to obtain a complete stress-strain curve. A stiff and servo-controlled testing machine was used to apply the confining pressure and the axial stress with a rate of 0.75 MPa/sec. The axial stress was then increased with the axial strain rate control equivalent to 0.75 MPa/sec until approximately 75% of the expected ultimate strength of the specimen was reached. The load-unload cycles were conducted at 40 MPa increments. The load-unload cycles were carried out at 0.063 mm increments of circumferential deformation using axial-strain control (Fig. 2-10). This method took approximately 8 hours to be completed. Since the unstable cracking in the brittle materials began at approximately 70-80% of their peak strength, the cyclic loading lead to a releasing of a portion of the accumulated energy of the system in the damage-controlled loading method (Martin 1993).

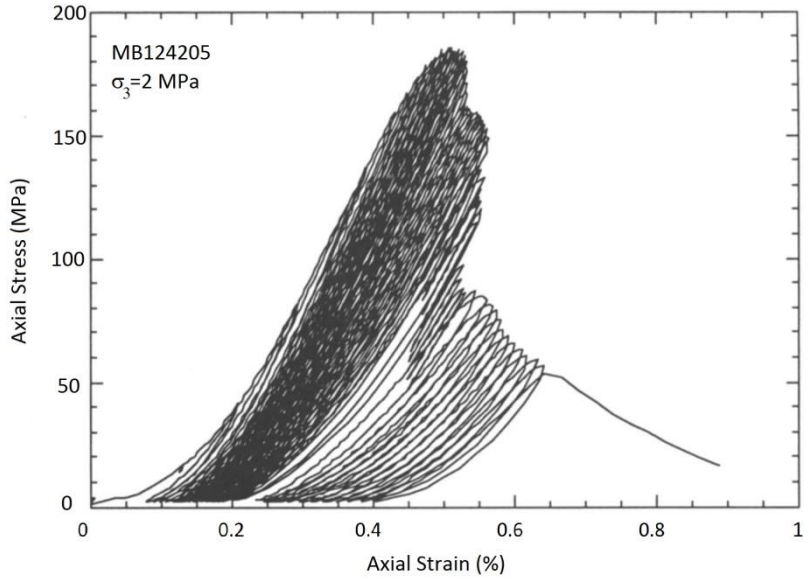

Figure 2-10: Damaged-controlled loading method showing post-peak behaviour of class II (After Martin and Chandler, 1994).

- *Fairhurst and Hudson method*

A complete stress-strain curve cannot only be obtained by using a proper stiff and servo-controlled loading machine. The testing procedure also plays a very important role as second factor that influences the successful complete uniaxial compression test. Since the result of axial force is uncontrolled failure at the compressive strength, Fairhurst and Hudson (1999) proposed an alternative controlled testing procedure in which the axial and circumferential strain control or computed feedback control were used to obtain the complete stress-strain curve. In order to improve the stiffness of the testing machine and to reduce the elastic energy accumulation in the system, the spacers and rotating support were not recommended to locate in the loading setup.

In this method, the loading was started with an axial strain rate of 0.001 mm/mm/s and continued at this rate until 70% of the expected strength was obtained. The strain control mode was then switched to the circumferential control at the rate of 0.0001 mm/mm/s. With this low rate, the applied load was dropped gradually to 50% of the peak load. Once obtained, the strain loading was switched back and maintained at 0.001 mm/mm/s axial strain rate until the residual strength of the sample was obtained. In this method, the load reduction took long time during which many microscopic fractures might occur in the sample. Due to this lengthy load reduction procedure, many microscopic fractures may occur during the testing process. It has been suggested in this method that the control variable (force and displacement or both) could be applied based on the rate of acoustic emission.

2.5 **Rockburst prediction methods: brittleness indices**

In deep underground mines, the confining stresses are increased with depth. Any stress changes in surrounding rock release the stored elastic energy rapidly. Rockburst occurs when the energy releases intensively and suddenly. Many researchers have studied the rockburst phenomenon and proposed different kinds of empirical and traditional methods. These methods enable us to know the loaded rock mass behaviour and to forecast and control rockburst occurrence as quickly and effectively as possible. There are different methods, techniques, criteria and indices for evaluating the rockburst. Among them, stress and energy concepts are two main approaches that can be used to predict the rockburst. Accordingly, rock strengths (laboratory and in situ) have been used in the prediction relationships. In the energy approach, the elastic energy stored in rock mass and energy consumed in the fracturing process are studied.

The brittleness index represents the severity of strength loss after failure and the ability of a material to withstand the inelastic deformations before failure. Many Brittleness indices are defined to predict the rockburst. Some brittleness indices have been obtained using a stress-strain curve while the others were calculated from the mechanical properties of rocks. The area under the stress-strain curve corresponds to the elastic energy accumulated in the system. In the following, some of these indices are described:

- ***Energy concept indices***

  Strain-energy storage index (W_{et})

Neyman et al. (1972) presented a rockburst indicator, W_{et}, as follows:

$$W_{et} = \frac{E_r}{E_a} \qquad (2\text{-}1)$$

where, E_r is the recovered elastic energy in the unloading phase corresponds to the area under the unloading curve and E_a is the dissipated energy related to the area between the loading and unloading curves (Figure 2-11). The higher the value of the indicator, the higher is rockburst susceptibility. As shown in Figure 2-11, the load is applied up to 80-90% of the uniaxial compressive strength. The rock burst susceptibility can be classified according to the strain-energy storage index as presented in Table 2.1.

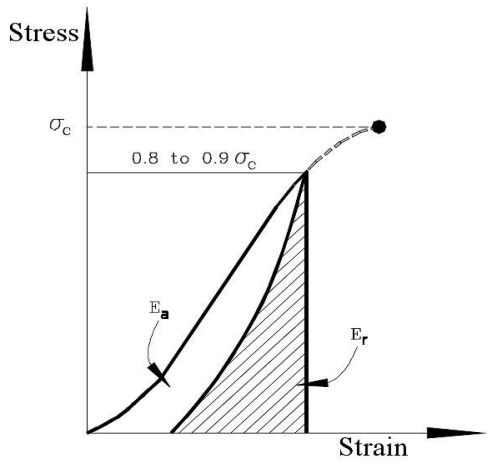

Figure 2-11: W_{et} calculation method (After Kidybinski, 1981).

Table 2.1. W_{et} classification results (Peng, 1986).

W_{et}	Description
< 2.0	not susceptible
$2.0 < W_{et} < 5.0$	slightly susceptible
$W_{et} > 5.0$	severely susceptible

Rockburst indicator for several coal seams can be obtained based on the average of rockburst indicator (W_{et}) for each layer by considering their thicknesses. Kidybinski (1981) introduced two different methods to calculate in situ W_{et}. In the first method, two horizontal parallel boreholes are drilled in the non-fractured and new exposed coal rib. Then, the deformation of one borehole is measured by pressurizing the other. In the second method, the rebound test is performed by L type rebound hammer.

Index Modified (BIM)

Gill and Aubertin (1988) also proposed an index called Brittle Index Modified (BIM) as a modified version of the W_{et} index. This index can be obtained using the uniaxial compression curve. Based on Figure 2-12, BIM can be defined as the area under loading curve (A_2) to the area under the line passes through the peak strength and parallel to the deformation modulus of rock taken at 50% of peak strength (A_1):

$$\text{BIM} = \frac{A_2}{A_1} \geq 1.0 \qquad (2\text{-}2)$$

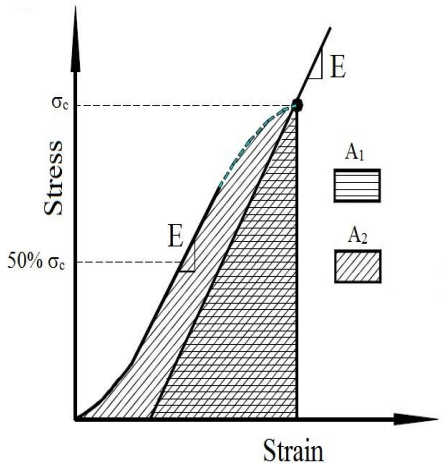

Figure 2-12: Brittleness Index Modified (After Gill and Aubertin, 1988).

The smaller the value of BIM, the higher is rockburst proneness. Based on experiments on most of brittle rocks, BIM would be close to unity. The rockburst potential classification is expressed by Aubertin et al. (1994a) as seen in Table 2.2.

Table 2.2. BIM assessment (Aubertin et al., 1994a).

BIM	Bursting Susceptibility
1.0~1.2	High
1.2~1.5	Moderate
> 1.5	Low

- ***Indices based on the rock mechanical properties***

- *Qiao Brittleness Index*

Qiao and Tian (1998) proposed a simple equation based on Ramsay's theory (1967). This index was obtained using experimental studies on the mechanical strengths of rock.

$$B_{Qiao} = \frac{\sigma_C}{\sigma_t} \qquad (2\text{-}3)$$

Where σ_C and σ_t are the uniaxial compressive and tensile strength, respectively. According to this index, the rockburst occurrence can be classified into four groups as shown in Table 2.3. Wang and Park (2001) applied this brittle index in Linglong gold mine (China) and observed an appropriate conformity.

Table 2.3. Rockburst classification by Qiao index (1998).

B_{Qiao}	Rockburst Severity
> 40	No rockburst
40~26.7	Weak rockburst
26.7~14.5	Strong rockburst
< 14.5	Violent rockburst

- *Altindag Brittleness Index*

Ramsay (1967) reported that the rock brittleness is highly related to rock mechanical properties. He observed that the brittleness increases when the difference between the

compressive and tensile strength increases. Altindag (2010) proposed an empirical equation based upon Ramsay hypothesis and the rock penetration as follows:

$$B_3 = \frac{\sigma_c \times \sigma_t}{2} \quad (2\text{-}4)$$

Where, σ_C is the compressive strength and σ_t is the absolute value of uniaxial tensile strength. Altindag (2010) presented another index and classified the brittleness as categorized by table 2.4:

$$B_4 = \sqrt{\frac{\sigma_c \times \sigma_t}{2}} \quad (2\text{-}5)$$

Table 2.4. Classification of brittle fracturing by Altindag index B_4 (2010).

Altindag Brittleness	Description
0~10	Low Brittleness
10~15	Moderately Brittle
15~20	Brittle
20~25	Very Brittle
> 25	Extremely Brittle

2.6 **Rock joint mechanical behaviour models**

Rockburst is divided into two main types namely Fault-slip burst and Strain-burst. Generally, fault-slip burst occurs in the presence of pre-existed fault or other discontinuities induced by stress distribution due to mining activities.

Fault-slip rockburst is mobilized when the normal load is decreased and the shear stress distributed on the fault exceeds the shear strength. Shear mobilization of a discontinuity depends on many factors such as: roughness, rock/joint inherent mechanical strength and discontinuity aperture (unmated, mated or filled).

In strain-burst, a discontinuity is created due to the governing stress conditions. Uniaxial compression tests performed by Wawersik and Fairhurst (1970) indicated that two types of fracturing happen when the load exceeds the critical magnitude. The tensile failure would occur close to the boundaries and almost parallel to the stress direction, while a shear fracture is followed by the tensile fractures towards the core of the sample with an angle to the stress direction. Therefore it can be implied that the main fracturing mode is the shear fracturing in strain burst.

Basically, the mechanical behaviour of a single fracture depends on the fracture if it is filled or unfilled. In a filled fracture, the shear behaviour would be a function of the physical and mineralogical properties of filling materials. The mechanical properties of fracture wall have less importance. However, these properties play crucial roles in the mechanical behaviour of the unfilled fractures.

Two approaches can be considered to describe the mechanical properties of the rock fractures as: a) the theoretical approach; and b) the empirical approach. There are various unfilled joint behaviour models such as: Patton (1966), Ladanyi and Archambault (1970), Barton (1971), Barton and Choubey (1977), Bandis et al. (1981), Barton et al. (1985), Fortin et al. (1988), Amadei and Saeb (1990), Saeb and Amadei (1992), Huang et al. (1993), Haberfield and Jahnston (1994), Simon (1999), Homand et al. (2001), Grasselli and Egger (2003), Lee et al. (2006) and Asadollahi and Tonon (2010). According to relevance, some of these approaches are described in the following sections. All of these mechanical behaviour models are used to predict three following issues:

1. Shear strength of non-planar rock fractures based on their dilatant behaviour.
2. Degradation of fracture asperities.
3. Dilatancy behaviour of regular or irregular fractures subjected to the direct shear loading.

2.6.1 Patton's model

Patton (1966) proposed a developed version of the Coulomb law as a bi-linear model for rock joints with a non-planar surface, based on mechanics of sliding over the asperity. Patton involved the asperity inclination in the Coulomb's equation. Two failure modes were introduced including: sliding over the asperities and shearing through the asperities as presented in Figure 2-13. Joint sliding can be initiated if the shear stress exceeds the shear resistance over the asperities as follows:

$$\tau = \sigma_n \, tan(\phi_b + i_o) \qquad (2\text{-}6)$$

where, τ is the shear resistance of the joint; σ_n denotes the normal force on the joint; ϕ_b is the friction angle along the contact surface of asperities; and i_o is the inclination angle of asperities. The asperities will be sheared off when the shear load exceeds the shear strength after a

displacement. Consequently, the shear strength relationship would be the same as Coulomb's equation:

$$\tau = c + \sigma_n \, tan\phi_r \qquad (2\text{-}7)$$

Based on the laboratory tests, Patton (1966) showed that the magnitude of internal friction angle is fairly close to the residual friction angle (ϕ_r). Patton noticed that a curved failure envelope can show the gradual shear of asperities from the larger amplitude to the lower one.

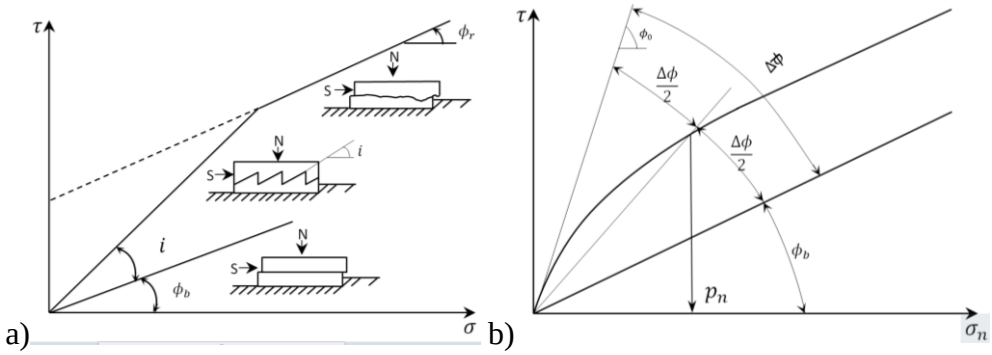

Figure 2-13: a) Patton's shear strength bi-linear criterion (1966). b) Non-linear criterion developed by Maksimovic (1996).

Patton (1966) proposed a conservative estimation of the peak shear strength in the field using the residual friction angle obtained from the laboratory direct shear tests. Also, inclination angle of asperities obtained from the large-scale waviness was added to the angle of friction. Moreover, Patton's bilinear model is valid for the saw-tooth regular joints.

Since rock joints are irregular, a different combination of sliding mechanisms and shearing through asperities can be responsible for the rock joint strength at each normal load level. Therefore, Maksimovic (1996) developed a non-linear failure envelope to take into account the natural profiles behaviour based on their dilation as a function of normal load as follows:

$$\tau = \sigma_n \, tan(\phi + \frac{\Delta\phi}{1+\frac{\sigma_n}{p_n}}) \qquad (2\text{-}8)$$

where, $\Delta\phi$ is the joint roughness angle that reflects the maximum dilatancy ; p_n is the median angle pressure equal to the value of the normal stress at which the contribution of dilation and the breakage of asperities is equal to one half the angle of dilatancy at zero normal stress ($\Delta\phi/2$). This criterion is limited to three shear tests on the identical surfaces from a morphological point of view and also uncertain parameter determination technique in the laboratory.

2.6.2 Ladanyi-Archambault's (LADAR) model

Ladanyi and Archambault (1970) developed a constitutive criterion (LADAR) to model the non-linear shear behaviour of joints. The transition from dilation at low normal stress levels to the shearing through asperities was theoretically and experimentally studied. The following relationship was proposed to calculate the peak shear strength:

$$\tau_p = \frac{\sigma_n(1-\mathrm{a}_s)(\dot{\mathrm{v}}+tan\phi_u)+\mathrm{a}_s s_r}{1-(1-\mathrm{a}_s)\dot{\mathrm{v}}tan\phi_u} \qquad (2\text{-}9)$$

where, τ_p is the peak shear strength of a rock joint; a_s is the shear area ratio (the sum of areas of failed asperities to the total sample area); $\dot{\mathrm{v}}$ is the dilation rate at the peak shear strength; ϕ_u is the friction angle; and s_r is the shear strength of intact rock.

For an irregular rock surface, a_s and $\dot{\mathrm{v}}$ may be expected to continuously vary with the normal stress. Therefore, at very low normal stress no asperities are sheared off ($a_s = 0$) and the rate of dilation is the maximum ($\dot{\mathrm{v}} = \tan i$). In this case, Equation 2-9 can be written same as the Patton's model (Equation 2-6). In a high normal stress, the shear area ratio (a_s) becomes unity (for planar joints) and the equation 2-8 reduces to:

$$\tau_p = s_r \qquad (2\text{-}10)$$

The shear strength of asperities (intact rock) (s_r) has been derived from the equation of the parabola proposed by Fairhurst (1964): as follows:

$$s_r = c_o \frac{\sqrt{(1+N)}-1}{N}\left(1 + N\frac{\sigma_n}{C_o}\right)^{1/2} \qquad (2\text{-}11)$$

where, C_o is the uniaxial compressive strength of rock and N is the ratio of the uniaxial compressive strength to the uniaxial tensile strength of rock material adjacent to the discontinuity$|C_o/T_o|$. Ladanyi and Archambault carried out shear tests on the prepared rough surfaces and proposed the following empirical relationships for a_s and $\dot{\mathrm{v}}$:

$$\dot{\mathrm{v}} = \left(1 - \frac{\sigma_n}{\sigma_T}\right)^{k_2} tan\, i_o \qquad (2\text{-}12)$$

$$\mathrm{a}_s = 1 - \left(1 - \frac{\sigma_n}{\sigma_T}\right)^{k_1} \qquad (2\text{-}13)$$

where, σ_T is the transition pressure beyond which the shearing through asperities is the dominant mechanism (brittle-ductile transition); and i_o is the maximum dilation angle at zero normal stress. Goodman (1976) considered k_1 and k_2 as 1.5 and 4 using the uniaxial compression strength.

Although, the LADAR model is based on the shear tests on the regular saw-teeth surfaces, it takes into account some influenced factors that are not considered in the Patton's model. For instance, this model takes the intact shearing through asperities into account. Also, the influence of normal stress on the dilation is considered; and moreover, the concept of progressive failure accounts for the criterion (Dight and Chiu, 1981).

Some of the joint parameters required for the LADAR model, such as a_s, are difficult to be obtained for practical engineering applications due to the irregularity of rock joints (Wang, 1992).

The LADAR has been modified by Saeb (1990) in which two modes of failures (sliding on the asperities and shear of asperities) were taken into account as follows:

$$\tau_p = \sigma_n \tan(\phi_\mu + i)(1 - a_s) + a_s s_r \qquad (2\text{-}14)$$

where

$$i = \text{arc}\tan \dot{v} = arctan\left[\left(1 - \frac{\sigma_n}{\sigma_T}\right)^{k_2} tani_o\right] \qquad (2\text{-}15)$$

2.6.3 Barton et al.'s model

Barton (1973) took into account the geometry of joint asperity using two parameters as: Joint Roughness Coefficient (JRC) and Joint Compressive Strength (JCS). He proposed an empirical model for the shear process as follows:

$$\tau = \sigma_n tan\left(JRC\ log_{10}\left(\frac{JCS}{\sigma_n}\right) + \phi_r\right) \qquad (2\text{-}16)$$

where, $JRC\ log_{10}\left(\frac{JCS}{\sigma_n}\right)$ is the rate of dilation at the peak shear stress derived from a curve-fitting procedure; and ϕ_r is the residual friction angle. In this model, the residual friction angle can be assumed same as the friction angle ($\phi_r = \phi_b$) for unweathered rock fractures.

In order to simplify the rock fracture properties, Barton (1971) proposed a rough estimation of JRC and JCS. He represented a sliding scale of roughness (JRC), which varies from approximately 0 to 20 from smoothest to roughest rock surfaces. At low stress levels, JCS can be

considered equal to the unconfined compression strength (C_o) for unweathered rocks. It is decreased to $C_o/4$ in the case of weathered fractures.

Barton et al. (1985) modified the first model to consider the stress dependency of the shear strength. Therefore, the progressive degradation of joint roughness during the shear process is represented by the mobilized joint roughness coefficient ($JRC_{mobilized}$ or JRC_m). The failure condition for the shear failure at peak is given by:

$$\tau_p = \sigma_n tan\left(JRC_m\ log_{10}\left(\frac{JCS}{|\sigma_n|}\right) + \phi_r\right) \quad (2\text{-}17)$$

Where,

$$JRC_m = \frac{\arctan(\tau_m/\sigma_n) - \phi_r}{log(JCS/\sigma_n)} \quad (2\text{-}18)$$

According to this investigation, the dimensionless ratio of JRC_m/JRC_p (which corresponds to the ratio of shear /peak shear displacement- u/u_p) increases during the shear process as follows:

$$\frac{JRC_m}{JRC_p} = \frac{arc\ \tan(\tau_m/\sigma_n) - \phi_r}{\phi_{p-}\phi_r} \quad (2\text{-}19)$$

$$\phi_p = arctan\left(\frac{\tau_p}{\sigma_n}\right) \quad (2\text{-}20)$$

Figure 2-14 shows the shear stress-displacement behaviour with respect to Eq. 2-19. Since the estimation of the parameters is relatively easy, the Barton et al.'s model is widely used in the rock joint behaviour study.

This model is not able to predict the post-peak roughness mobilization of fracture. In addition, the negative dilatancy (compression) cannot be predicted. Another limitation of the Barton's model is that the peak shear displacement is considered independent of the normal stress, which is not consistent with the experimental observations. The Barton's model suggested a zero mobilized JRC after 100 times of peak shear displacement (Figure 2-15). This assumption is not applicable for a sawed fracture ($JRC_{mobilized}$=0) (Asadollahi et al., 2010). Moreover, in the mobilized Barton's model (1985), the post-peak shear strength (based on the definition of $\frac{\mathrm{JRC_{mobilized}}}{\mathrm{JRC_{peak}}}$) for planar (JRC≤5) and non-planar (JRC>5) fractures is considered identical.

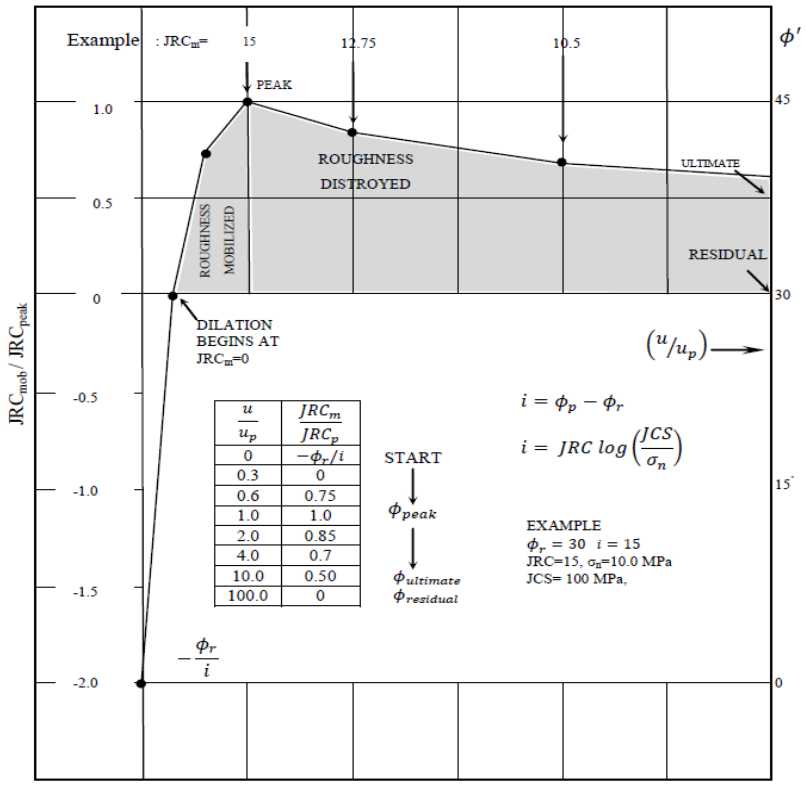

$\frac{u}{u_p}$	$\frac{JRC_m}{JRC_p}$
0	$-\phi_r/i$
0.3	0
0.6	0.75
1.0	1.0
2.0	0.85
4.0	0.7
10.0	0.50
100.0	0

Figure 2-14: Dimensionless model for shear stress-displacement modeling (Barton et al., 1985).

Asadollahi and Tonon (2009) modified the Barton's model to more precisely predict the peak shear displacement, dilation and post-peak shear strength. Figure 2-15 shows the post-peak shear strength calculated by two empirical models (Barton et al., 1985; Asadollahi, 2009).

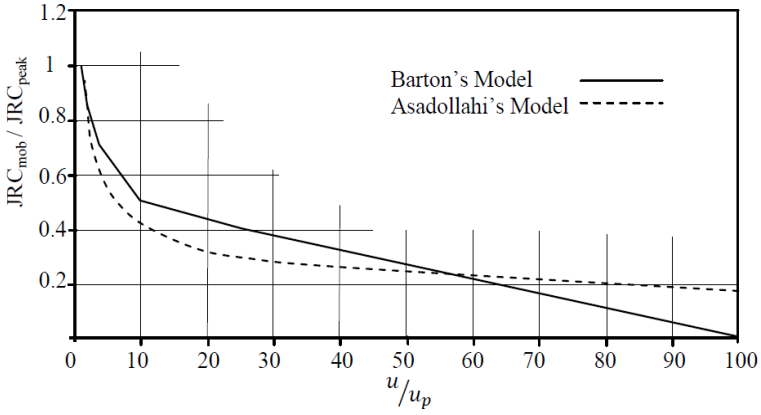

Figure 2-15: Comparison between Asadollahi's and Barton's model for post-peak shear strength (Asadollahi, 2009).

As can be seen in Figure 2-15, the post-peak behaviour of shear strength in the new model is non-linear from the peak point towards the residual strength. Due to lack of experimental data (long shear displacement), the comparison between residual part of the model and experimental data is not possible. However, the existing experimental data indicates how the models are close to the reality.

2.6.4 Saeb and Amadei's model

Saeb and Amadei (1992) proposed a graphical and mathematical constitutive model to predict the effect of boundary conditions on the shear behaviour of a dilatant rock joint. The boundary conditions applied on the joint surface can be in two forms, including: the upper block of joint surface freely moves to be dilated; and the dilatancy of the bottom block is constrained (controlled by stiffness of rock mass). In the second type of boundaries, sliding of the joint surfaces increases the normal stress across the joint planes. In this case, the joint shear behaviour is modified. In fact, the model would predict the shear response of a dilatant rock joint and the changes of the normal deformability during the shearing process.

Since the constant or variable normal stiffness are more likely to exist in the nature rather than constant normal stress, the new model determines the normal displacement and the joint behaviour in shear. Basically, closure of a rock joint under normal stress shows a hyperbolic behaviour until it would be fully closed (V_m). Bandis et al. (1981) proposed a hyperbolic model to describe the normal load (σ_n)-normal displacement (v) behaviour of a rock joint as:

$$\sigma_n = \frac{v\, k_{ni}\, V_m}{V_m + v} \tag{2-21}$$

$$v = \frac{\sigma_n\, V_m}{k_{ni}\, V_m - \sigma_n} \tag{2-22}$$

Where, k_{ni} is the initial normal stiffness of the joint. If the normal stress level changes, the tangent normal stiffness k_{nn} would be equal to:

$$k_{nn} = \frac{\partial \sigma_n}{\partial v} = k_{ni} \left(\frac{k_{ni}\, V_m - \sigma_n}{k_{ni}\, V_m} \right)^2 \tag{2-23}$$

Graphical Model

Saeb and Amadei used a series of idealized joint curves derived by Goodman and Boyle (1985) as shown in Figure 2-16. As can be seen in this figure, the hyperbolic behaviour of joint closure is influenced by the normal stress. Figure 2-16b shows a series of shear stress - shear displacement curves for a joint tested under constant normal stresses (From A to 20A- A is an arbitrary number). It is observed that there is no change in the normal displacement after the peak shear strength for each constant normal stress test. Figure 2-16c represents the dilatancy curves obtained from the shear tests.

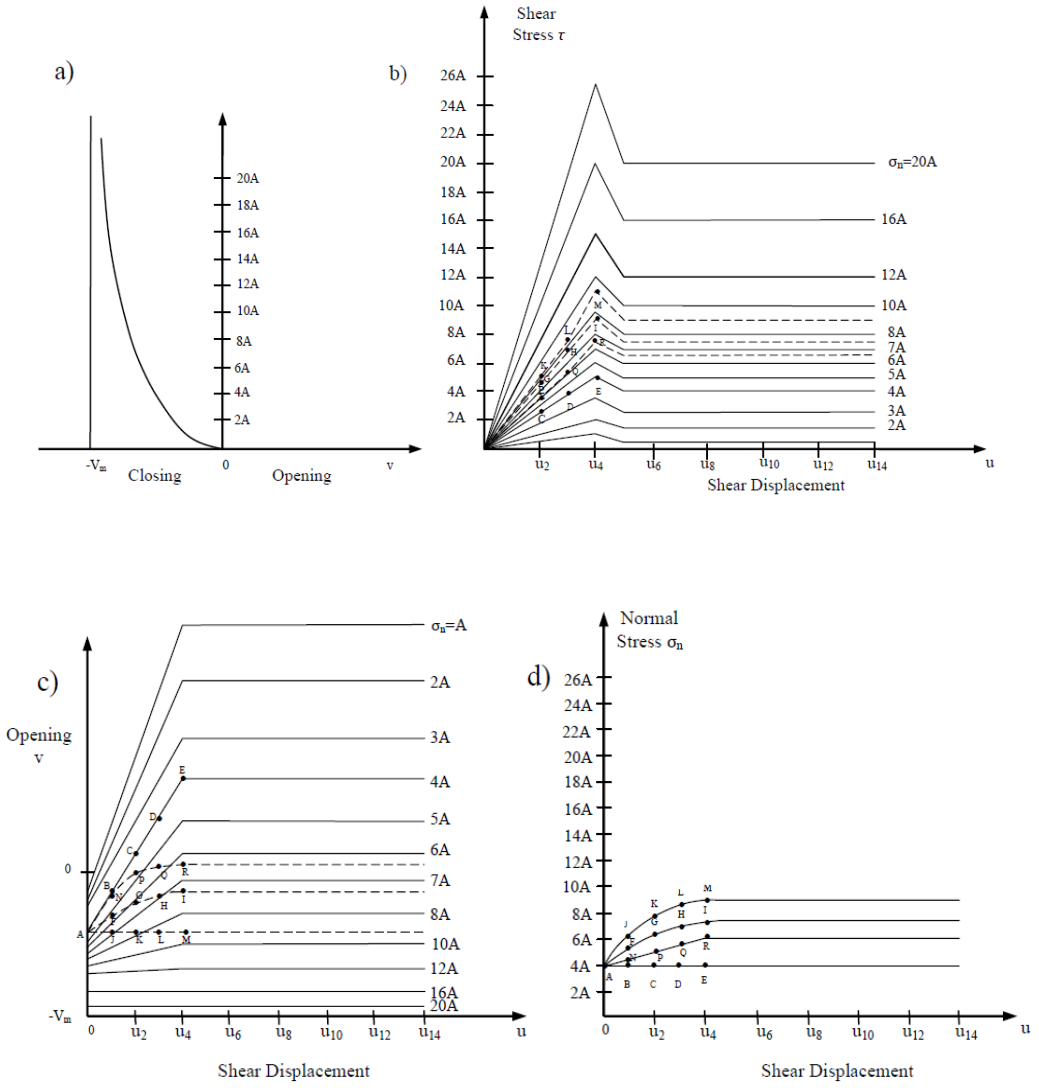

Figure 2-16: Joint response curves for normal stress between 0 and 20A (Saeb and Amadei, 1992).

These figures can be used to extract the variation of the joint normal stress when the joint normal displacement is changed. In Figure 2-17, the effect of shear displacement is considered in the normal stress-normal displacement curve by assuming u_o as zero shear displacement and u_4 as the shear displacement at peak shear strength.

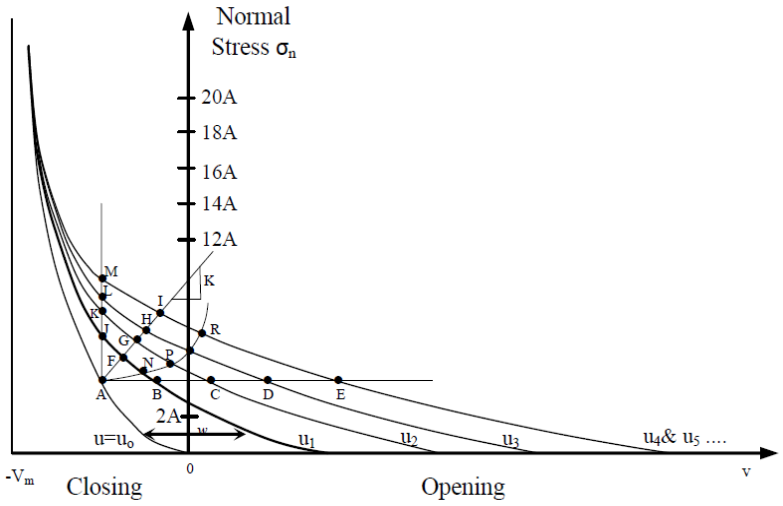

Figure 2-17: Normal stress -normal displacement curves at different shear displacement levels (Saeb and Amadei, 1992).

All curves $u = u_i$ (i =1 to 4) become closer to the curve $u = u_0$ as σ_n increases (the joint dilatancy decreases as the joint normal stress increases). According to Figures 2-17 and 2-16b, the shear strength of a joint can be predicted in different boundary conditions. These boundary conditions are illustrated in Figure 2-16 by four paths. The path AFGHI illustrated shearing under constant normal stiffness K. The path ABCDE is representative of the joint loading condition under constant normal stress (K=0). In unlimited normal stiffness in which there is no change in the joint normal displacement, the path AJKLM should be followed. The path ANPQR can be representative of the increasing applied normal stiffness. All four above-mentioned paths can be used to predict the shear stress- displacement curve. Figure 2-16d shows the normal stress - displacement curves plotted by using these paths.

Mathematical Model: Incremental formulation of joint behaviour

If the total normal displacement v of the joint is a function of the shear displacement u and the normal stress σ_n, the following equations can be extracted (Saeb and Amadei, 1992):

$$\mathrm{v} = u\left(1 - \frac{\sigma_n}{\sigma_T}\right)^{k_2} \tan i_0 + \frac{\sigma_n\, V_m}{k_{ni}\, V_m - \sigma_n} \tag{2-24}$$

$$\mathrm{v} - w = \frac{\sigma_n\, V_m}{k_{ni}\, V_m - \sigma_n} \quad \text{or} \quad \sigma_n = \frac{(\mathrm{v}-w)\, k_{ni}\, V_m}{V_m + (\mathrm{v}-w)} \tag{2-25}$$

Where, w is equal to the first term of the right-hand side of equation 2-24. In fact, w is the increase of the joint aperture created in the shearing process as shown in Figure 2-16a. If it is assumed that the maximum closure V_m is a reasonable estimation of the initial aperture of joint in its mated position, then the value of w at $\sigma_n = 0$ (i.e. $w = u \tan i_o$) represents the additional initial aperture of the unmated joint created through the dilatancy. The maximum additional aperture is equal to $u_r \tan i_o$ when $u = u_r$. Equation 2-25 represents a mathematical expression for the curves $u = u_i$ (i=1, 4). If the joint is non-dilatant ($\tan i_o = 0$), the value of w would be equal to zero. In this case, the normal stress-displacement behaviour is identical for all values of the shear displacement, as expected. An incremental formulation is obtained by differentiating of Equation 2-26 (Saeb and Amadei, 1992):

$$d\sigma_n = \frac{dv - \left(1 - \frac{\sigma_n}{\sigma_T}\right)^{k_2} \tan i_o\, du}{\frac{-uk_2}{\sigma_T}\left(1 - \frac{\sigma_n}{\sigma_T}\right)^{k_2 - 1} \tan i_o + \frac{k_{ni}\, V_m{}^2}{(k_{ni} V_m - \sigma_n)^2}} \tag{2-26}$$

According to Equation 2-26, the normal stress depends on the normal and shear displacements which can be written by:

$$d\sigma_n = k_{nn} d\mathrm{v} + k_{ns} du \tag{2-27}$$

Where, k_{nn} and k_{ns} are two normal stiffness coefficients in normal and shear displacements of the joint, respectively:

$$k_{nn} = \frac{\partial \sigma_n}{\partial \mathrm{v}} = \frac{1}{\frac{-uk_2}{\sigma_T}\left(1 - \frac{\sigma_n}{\sigma_T}\right)^{k_2 - 1} \tan i_0 + \frac{k_{ni}\, V_m{}^2}{(k_{ni} V_m - \sigma_n)^2}} \tag{2-28}$$

$$k_{ns} = \frac{\partial \sigma_n}{\partial u} = \frac{-\left(1 - \frac{\sigma_n}{\sigma_T}\right)^{k_2} \tan i_0}{\frac{-uk_2}{\sigma_T}\left(1 - \frac{\sigma_n}{\sigma_T}\right)^{k_2 - 1} \tan i_0 + \frac{k_{ni}\, V_m{}^2}{(k_{ni} V_m - \sigma_n)^2}} \tag{2-29}$$

Equation 2-28 provides an analytical expression for the joint tangent normal stiffness when the joint has been sheared by a certain amount of u. This equation reduces to Equation 2-23 when the joint is in the mated position (u = 0). Equations 2-26 to 2-29 are valid when $u \leq u_r$ and $\sigma_n / \sigma_T < 1$.

On the other hand, when $u > u_r$ and $\sigma_n / \sigma_T < 1$, k_{ns} vanishes and k_{nn} is equal to its value at $u = u_r$. Finally, when $\sigma_n / \sigma_T \geq 1$, k_{ns} also vanishes, but k_{nn} is given by equation 2-21. Another equation, similar to equation 2-27, can be expressed for the shear stress τ when it depends on v and u. Then:

$$d\tau = k_{sn} dv + k_{ss} du \qquad (2\text{-}30)$$

Where, $k_{sn} = \partial\tau/\partial v$ and $k_{ss} = \partial\tau/\partial u$ are two shear stiffness coefficients. It has been common practice to assume that $k_{sn} = 0$, $k_{ss} = k_s$ and shear stiffness of the pre-peak region of the shear stress-displacement curve equal to unity. However, this assumption is not necessary and the closed-form solutions can be derived (Saeb and Amadei, 1992).

Equation 2-30 has been developed for two models recommended by Goodman (1976): constant stiffness and constant displacement models. In these two models, three different shear stiffnesses were established for three regions of the shear stress-displacement curve: Pre-peak, peak and post-peak (refer to Saeb and Amadei, 1992). Different peak shear strengths can be derived based on different joint mechanical behaviour models. For example, if the modified LADAR (Eq. 2-14) and Mohr-Coulomb criterion for intact rock strength ($s_r = s_0 + \sigma_n \tan\phi_0$) are considered and τ_p is given by Equation 2-14 and τ_r is determined by substituting Equation 2-13 into the Goodman's model, therefore:

$$\tau_r = \tau_p \left(B_0 + \frac{1-B_0}{\sigma_T}\sigma_n\right) \qquad when \quad \sigma_n < \sigma_T \qquad (2\text{-}31)$$

Thus:

$$\frac{\partial\tau_p}{\partial\sigma_n} = (1 - a_s)\tan(\phi_\mu + i) - \frac{\sigma_n}{\sigma_T}\frac{(1-a_s)k_2}{cos^2(\phi_\mu+i)} \times \frac{1}{1+\left(1-\frac{\sigma_n}{\sigma_T}\right)^{2k_2} tan^2 i_0} \tan i_0 \left(1 - \frac{\sigma_n}{\sigma_T}\right)^{k_2-1} -$$

$$\frac{\sigma_n}{\sigma_T} k_1 \tan(\phi_\mu + i)\left(1 - \frac{\sigma_n}{\sigma_T}\right)^{k_1-1} + \frac{s_r}{\sigma_T} k_1 \left(1 - \frac{\sigma_n}{\sigma_T}\right)^{k_1-1} + a_s \tan\phi_0 \qquad (2\text{-}32)$$

Consequently, the rock joint deformability can be written in the matrix form with combination of Equations 2-27 and 2-30 as:

$$\begin{Bmatrix} d\sigma_n \\ d\tau \end{Bmatrix} = \begin{bmatrix} k_{nn} & k_{ns} \\ k_{sn} & k_{ss} \end{bmatrix} \begin{Bmatrix} dv \\ du \end{Bmatrix} \qquad (2\text{-}33)$$

The 2×2 above matrix is the material tangent stiffness and is, in general, non-symmetric.

Under applied constant or variable normal stiffness boundary conditions, a rock joint behaves differently in a shear process that can be predicted. Hence, the variation of the normal stress and displacement would be related as follows:

$$d\sigma_n = Kd\mathrm{v} \qquad (2\text{-}34)$$

Where, K is the applied stiffness, which can be constant or vary with σ_n. By substituting Equation 2-34 into Equation 2-27, two relationships can be obtained for the normal stress and normal displacement along the shear displacement, with respect to the applied stiffness (K).

$$d\sigma_n = \frac{K.k_{ns}}{K-k_{nn}} du \qquad (2\text{-}35)$$

And

$$d\mathrm{v} = \frac{k_{ns}}{K-k_{nn}} du \qquad (2\text{-}36)$$

To relate the changes in the shear stress and displacement, Equation 2-30 is used and the following equation can be derived:

$$d\tau = \left(\frac{k_{sn}k_{ns}}{K-k_{nn}} + k_{ss}\right) du \qquad (2\text{-}37)$$

For a non-dilatant joint, these equations are simplified, because the shear displacement response is independent of the applied stiffness K ($\tan i=0$, $k_{ns}=0$, $d\sigma_n=dv=0$ and $d\tau=k_{ss}du$). When K vanishes, the condition is the same as the joint under a constant normal stress boundary conditions. When $K = \infty$, it corresponds to the constant displacement boundary conditions applied in the rock joint.

The main drawback of the Saeb and Amadei's model is that it is limited to monotonic loading and is not able to predict the joint unloading behaviour. Also, this model doesn't consider the surface roughness degradation. The effect of cyclic loading on the joint normal and shear behaviour has been taken into account by the model proposed by Souley et al. (1995) as an extension of Saeb and Amadei'smodel.

2.6.5 The CSDS model

In order to evaluate the rockburst potential in underground excavation near a geological discontinuity, Simon (1999) developed a constitutive model called CSDS (for Complete Stress-

Displacement Surface) based on a statistical approach proposed by Chapuis (1990) for granular materials to relate deformation to the transportation of the internal structure. This model is able to predict the post-peak behaviour of rock joint under in situ conditions. It is noteworthy to mention that the post-peak behaviour of a rock joint is very important to assess the modes of possible failure (gradual or violent).

The CSDS model contains of two basic set of equations; the first set defines the shear stress (τ)-shear displacement (u) relationship; while the second set expresses the normal displacement (v) - shear displacement (u).

- *Shear stress- shear displacement relationship (τ-u)*

The τ-u relationship is an exponential function of shear displacement:

$$\tau = F(u) = a + b\ exp(-cu) - d\ exp(-eu) \qquad (2\text{-}38)$$

Where, τ is the shear stress (MPa); u is the shear displacement (mm); and a to e are model parameters that must satisfy the imposed conditions: $c < e$, and $a, b, c, d, e > 0$. By considering some assumptions for shear condition in different shear displacements, the following relationships are concluded for each mentioned above parameters:

$$a = \tau_r \qquad (2\text{-}39)$$

$$b = d - a \qquad (2\text{-}40)$$

$$c = {}^{5}/_{u_r} \qquad (2\text{-}41)$$

$$\frac{deu_r}{5(d-\tau_r)} - exp\left[u_p\left(e - \frac{5}{u_r}\right)\right] = 0 \qquad (2\text{-}42)$$

$$d = \frac{\tau_p - \tau_r\left[1 - exp\left(-\frac{5u_p}{u_r}\right)\right]}{exp\left(-\frac{5u_p}{u_r}\right) - exp(-eu_p)} \qquad (2\text{-}43)$$

Where, τ_r and τ_p are the residual and peak strength, respectively; u_p and u_r are the peak displacement and the displacement at the onset of τ_r. To determine the values of d and e, Eq.s 2-42 and 2-43 must be simultaneously solved by standard iterative method with respect to the condition of $c < e$.

To evaluate the residual shear strength, the Coulomb criterion at residual state is used:

$$\tau_r = \sigma_n \tan \phi_r \qquad (2\text{-}44)$$

The modified LADAR criterion (Saeb, 1990) is used to evaluate the peak shear strength (Eq.s 2-11 to 2-15). Also, the following Mohr-Coulomb based strength criterion for intact rock (Saeb, 1990) is used for the shearing of the rock asperities:

$$S_r = S_0 + \sigma_n \tan \phi_0 \qquad (2\text{-}45)$$

Where, S_0 and $\tan \phi_0$ are the rock cohesion and friction angle, respectively. Finally, the CSDS model can be expressed by:

$$\tau = \tau_r + [d - \tau_r] exp\left(-\frac{5u}{u_r}\right) - dexp(-eu) \qquad (2\text{-}46)$$

As can be seen in Figure 2-18, the model has a good correlation with data. Simon (1999) concluded a correlation factor of 0.90 for the performed tests in comparison with the correlation factor of 0.739 obtained by Saeb and Amadei (1992). The new model can closely predict the joint behaviour under constant normal stress, markedly in the post-peak region.

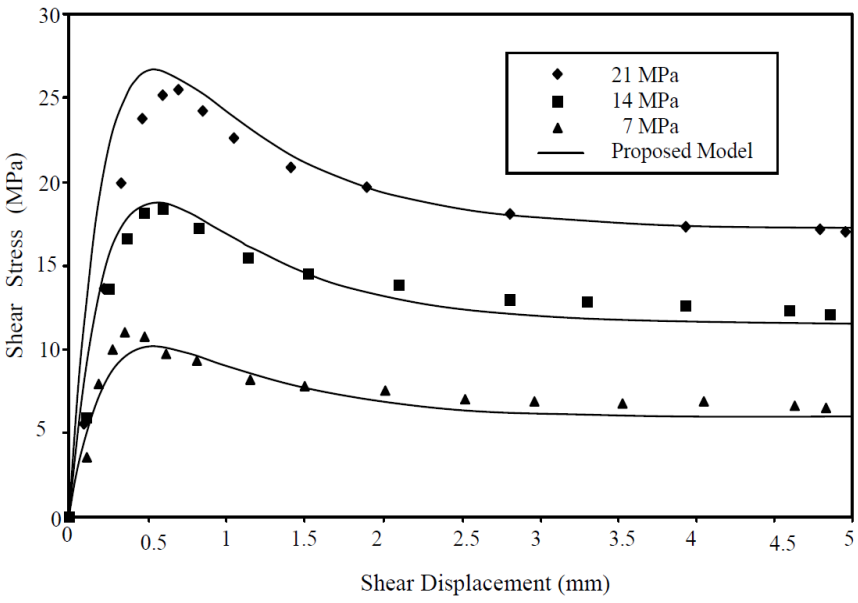

Figure 2-18: Comparison between the CSDS model and the actual shear test results for rock joint replica made by cement under different constant normal stresses (After Simon, 1999).

- *Normal displacement-shear displacement relationship*

To predict the normal displacement-shear displacement, Simon (1999) also introduced a parameters-dependent equation as follows:

$$\mathrm{v} = \beta_1 + \beta_2 \exp(-\beta_3 u) - \beta_4 \exp(-\beta_5 u) \quad (2\text{-}47)$$

Where v is the normal displacement, u is the shear displacement and β_1 to β_5 are model parameters. A simpler equation was proposed due to difficulty in relating all mentioned parameters in the relationship to physical parameters in order to be easily obtained by standard laboratory tests:

$$\mathrm{v} = \beta_1 - \beta_2 \exp(-\beta_3 u) \quad (2\text{-}48)$$

$$\beta_1 = u_r \left(1 - \frac{\sigma_n}{\sigma_T}\right)^{k_2} \tan i_0 + \frac{\sigma_n \, V_m}{k_{ni} \, V_m - \sigma_n} \quad (2\text{-}49)$$

$$\beta_2 = \beta_1 - \frac{\sigma_n \, V_m}{k_{ni} \, V_m - \sigma_n} \quad (2\text{-}50)$$

$$\beta_3 \cong \frac{1.5}{u_r} \quad (2\text{-}51)$$

By substitution equations 2-48 to 2-51 into equation 2-48, the normal displacement can be written as:

$$\mathrm{v} = \left[u_r \left(1 - \frac{\sigma_n}{\sigma_T}\right)^{k_2} \tan i_0 + \frac{\sigma_n \, V_m}{k_{ni} \, V_m - \sigma_n}\right]\left[1 - exp\left(-\frac{1.5u}{u_r}\right)\right] + \left(\frac{\sigma_n \, V_m}{k_{ni} \, V_m - \sigma_n}\right) exp\left(-\frac{1.5u}{u_r}\right) = \left[u_r \left(1 - \frac{\sigma_n}{\sigma_T}\right)^{k_2} \tan i_0\right]\left[1 - exp\left(-\frac{1.5u}{u_r}\right)\right] + \frac{\sigma_n \, V_m}{k_{ni} \, V_m - \sigma_n} \quad (2\text{-}52)$$

To express above equation with an incremental form, equation 2-25 can be used in which:

$$k_{nn} = \frac{\partial \sigma_n}{\partial \mathrm{v}} = \frac{1}{\frac{k_2 u_r}{\sigma_T}\left(1 - \frac{\sigma_n}{\sigma_T}\right)^{k_2 - 1} \tan i_0 + \frac{k_{ni} \, {V_m}^2}{\left(k_{ni} \, V_m - \sigma_n\right)^2}} \quad (2\text{-}53)$$

And

$$k_{ns} = \frac{\partial \sigma_n}{\partial u} = \frac{1.5(k_{ni} \, V_m - \sigma_n)\left(1 - \frac{\sigma_n}{\sigma_T}\right)\left[(k_{ni} \, V_m - \sigma_n)\left[u_r \left(1 - \frac{\sigma_n}{\sigma_T}\right)^{k_2} \tan i_0 - \mathrm{v}\right] + \sigma_n \, V_m\right]}{u_r \left[k_2[V_m \sigma_n - \mathrm{v}(k_{ni} \, V_m - \sigma_n)] - (V_m + \mathrm{v})(k_{ni} \, V_m - \sigma_n)\left(1 - \frac{\sigma_n}{\sigma_T}\right)\right]} \quad (2\text{-}54)$$

The CSDS model was applied into a geometrical approach to estimate scale effects (Deng et al., 2004) in rock joint behaviour based on measurements of the asperity angles of the joint surface. In addition, this model was adapted to take into account the presence of water pressure on the joint behaviour and to assess its hydro-mechanical behaviour (Tremblay et al., 2007).

The CSDS model was verified based on test results taken from the literature. This model is able to predict the post-peak behaviour of intact rock. However, the major difficulty in using of the proposed model is determination of different parameters of the model and the failure plane angle. The CSDS model is constituted based on monotonic loading and it is not able to predict the cyclic loading conditions. The model is also limited to shear behaviour of rock joints and faults. The influence of fracture surface roughness was neglected in the CSDS model. The morphological characteristics of the joint roughness will be more discussed in the next part.

2.7 **Rock joint roughness**

Shearing over discontinuities is often a predominant process in the rock mass under compression. In this phase, the normal pressure and the frictional force subjected to the induced interface can play important roles. The frictional force applied on the interface is divided into three parts: 1) the normal force on the horizontal projected interface; 2) the forces which deform the interlocked asperities; 3) the forces as results of dilatancy. The shearing behaviour of discontinuity interface is influenced by geometrical conditions of the asperities. The shape and orientation of the asperities are two general parameters affecting on the discontinuities shear behaviour.

2.7.1 Roughness

Roughness is referred to the spatial distribution of the asperity peaks and valleys. In the field of rock mechanics, roughness can be generally categorized into small (unevenness) and large scale (waviness) (Fig. 2-19). Immediate shear strength of a rock joint in a laboratory shear test is mostly influenced by the unevenness, while the role of waviness is to control the initial direction of the shear and normal displacements along the discontinuity plane. Based on the literature, the shear behaviour of two different rock types with identical interface characterizations won't be identical. As the strength of the asperities decreases, the geometry of them may have a marginal impact on the shear strength of the discontinuity.

Maximum vertical displacement of a rock joint, known as dilatancy, is strongly affected by the spatial distribution of the asperities and the stiffness of the joint surface and the loading system. Fracture surface dilation can be measured as an important parameter affecting the shear behaviour of fracture. Maximum dilation angle, in constant normal load (CNL), is measured at peak shear strength of a fracture. This parameter is attributed to the asperity angle in first and

second order of asperities (Fig. 2-19) (Patton, 1966; Ladanyi and Archambault, 1970; Barton, 1973).

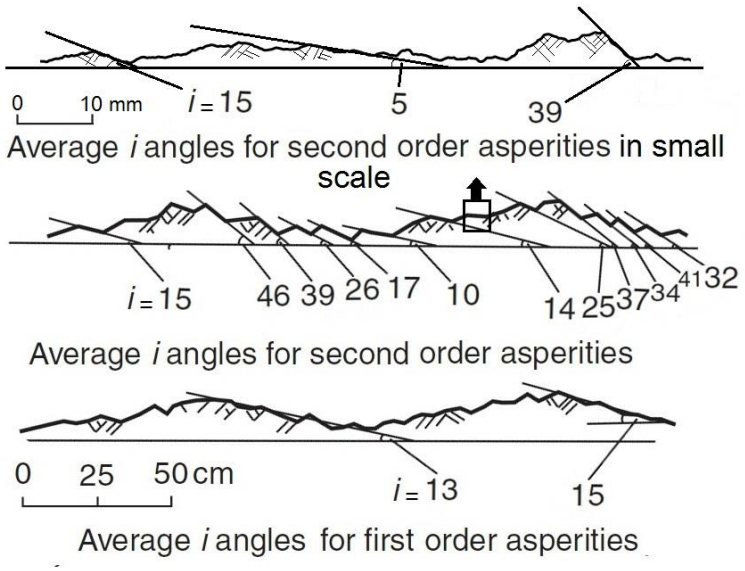

Figure 2-19: First and second order of asperities (Modified after Patton 1966).

2.7.2 Roughness parameter

To predict the shear behaviour of a discontinuity, the roughness profiles must be obtained, simplified and characterized as a numerical parameter. It is always possible to characterize two roughness profiles with the identical parameter but with different spatial status. In the last four decades, huge numbers of roughness parameters have been proposed to characterize and quantify the rough surface in 2D and 3D in the field of metallurgical, mechanical, geotechnical and rock engineering. These roughness parameters are mainly classified into three categories: the statistical methods are based on roughness amplitude, slope and spatial geometry; Joint Roughness coefficient (JRC) as an empirical method proposed by Barton and Choubey (1977); and the fractal approaches which are based on fractal dimension calculated from the geometry of the roughness profile.

2.7.2.1 Statistical roughness parameter

These roughness parameters have been developed to evaluate and characterize discontinuity surfaces based on a statistical concept of the surface geometry. The statistical parameters are a

function of roughness amplitude, wavelength and slope. Here are some of these 2D parameters with a concise definition. (Myers, 1962; El-Soudani, 1978; Tatone and Grasselli, 2010):

- *Maximum elevation* corresponds to the maximum possible aperture during the shearing process.
- *Standard deviation* and variance indicate the height scattering, which reflects the intensity of roughness.
- *Center line average (CLA)* defines the mean value of the amplitude.
- *Root mean square (RMS)* represents the standard deviation of the height distribution.
- *The RMS of the first derivative of the profile (Z_2)* characterizes a profile based on its average slope.
- *The RMS of the second derivative of the profile (Z_3)*.
- *The percentage excess of distance* measured along the profile where the slope is positive over the distance where the slope is negative (Z_4).
- *Maximum peak to valley roughness height (R_{max})* indicate the thickness of shearing band by measuring the vertical distance between the highest peak and lowest valley of the profile.
- *Levelling depth (R_c)* characterize the distance between the highest peak and the centerline.
- *10- points height (R_z)* represents the average distance between the five highest peaks and five lowest valleys.
- *Skewness* measures the symmetry of the profile line about the centerline.
- *Kurtosis* returns the distribution of heights from the centerline.
- *Average spacing (A_r)* indicates the average spacing between each adjacent peak.
- *Bearing length ratio (t_p)* is the length of the profile that positive amplitude over a preselected vertical distance from the centerline.
- *Roughness profile index (R_p)* is the ratio of the true length of the profile over the projected length of the profile in the surface plane in terms of sampling spans (intervals).
- *Average inclination angle of asperities (A_i)* measure the average of slopes between the adjacent points on the profile.
- *2D directional roughness* ($\theta^*_{max}/(C+1)_{2D}$) characterizes the distribution of the inclination of each line of a 2D roughness profile.

- *Mean square value (MSV)* and some stochastic parameters such as *Autocorrelation function* (ACF), *Structure Function* (SF), *Cross-covariance function* (CCF) and *Power spectral density function* ($PSDF$).

There are also some 3D parameters, which have been derived from the above-mentioned 2D parameters (Belem et al., 2000; Tatone and Grasselli, 2010):

- *Surface angularity* (θ_s) corresponds to micro-average angle in 2D.
- *Surface parameter* ($Z_{2\ surface}$) is the generalized Z_2 by replacing the slope with the gradient normal of the surface height.
- *Surface roughness coefficient* (R_s) is the same as roughness profile index in 2D with calculation of the surface with the help of surface triangulation.
- *3D directional roughness* ($\theta^*_{max}/(C+1)$) characterizes the distribution of the apparent dip of each triangular face of a surface in the desired direction.

2.7.2.2 Empirical roughness parameter

The only parameter defined in this category is the Joint Roughness Coefficient (*JRC*). *JRC* is the most common used roughness parameter in applied rock mechanics that has been obtained by back-calculation of a large number of direct shear tests on natural discontinuities. *JRC* is originally obtained by making a visual comparison between the provided roughness profile and the 10 standard *JRC* profiles (Barton, 1973; Barton and Choubey, 1977). Lack of objectivity and huge errors between *JRC* values conjectured by several engineers on the same profile (Beer et al., 2002) gave rise to correlate the *JRC* with some of other roughness parameters (Tse and Cruden, 1979; Maerz et al., 1990).

2.7.2.3 Fractal roughness parameter

The fractal dimension (D) shows the degree of chaos of an object (here a topological object) as a mathematical model. A rough surface can be explained by the fractal dimension as an irregular shape of natural objects (Mandelbrot, 1989). A linear roughness profile is defined as Euclidian two-space and it may have a fractal dimension between 1 and 2, however, the fractal dimension for a surface may be between 2 and 3. Fractal objects are classified into two categories: self-similar and self-affine. A surface is self-similar when two portions of that surface in different

scales are statistically identical. Otherwise two surfaces are self-affine. Fractal methods are divided into some categories:

- *Divider method* measures the length of roughness profile in terms of divider spans with different scales. In modified divider method the span's length are identical. Divider method can give a correct dimension for self-similar fractals.
- *Box counting method* is also applicable to self-similar shapes. Rectangular or square grids –in several sizes- are used as span counting elements for the surface covered by the roughness profiles.
- *Variogram method* has been used to estimate the fractal dimension of natural topography, which is the mean squared increment of points along a curve.
- *Spectral Method* is based on a time series, which can be represented by sum of sine waves having different frequencies, amplitude and phase at each frequency.
- *Roughness-length method* depends on the standard deviation of the roughness profile height in terms of the sampling span length.
- *Line scaling method* is a correlation between the standard deviation of the points on the roughness profile and the span size selected.

2.8 **Selection of a roughness parameter**

A roughness parameter is selected to give a quantified understanding of a discontinuity. These parameters are mainly used to compare two rough interfaces or to identify the intensity of roughness. To determine the mechanical behaviour of discontinuities, the role of roughness parameters has been proven for a long time in the field of rock mechanics. Therefore, a proper parameter can be used to predict the shear behaviour of discontinuities. Some researchers believe that at least two roughness parameters should be considered at roughness quantification (Odling, 1994; and Hong et al., 2008).

Hong et al. (2008) calculated CLA, RMS, Z_2, R_L and A_i of different artificial roughness profiles with different amplitudes and frequencies comprised of unevenness and waviness. Z_2, R_p and A_i identify both amplitude and frequency effect, however, CLA and RMS identify only the amplitude effect. They concluded that Z_2, R_p and A_i can distinguish the superposition effect (mixing unevenness in the waviness). On the other hand, CLA and RMS of the profiles with the same

amplitude but different frequencies are the same, which seems to be wrong. Consequently, at least two types of roughness parameters are required to characterize one roughness profile.

2.9 Correlation between JRC and other roughness parameters

In order to avoid the subjective determination of *JRC* from the 10 typical roughness profiles, several researchers obtained good correlations between 2D statistical roughness parameters (i.e. Z_2, R_p, SF and $\theta^*_{max}/(C+1)_{2D}$) and the standardized *JRC* (Tse and Cruden, 1979; Yu and Yayssade, 1991; Yang et al., 2001; Kim and Lee, 2009; Tatone and Grasselli, 2010 and Jang et al., 2014). Several relationships are briefly listed in Table 2.5 to correlate *JRC* and Z_2 at sampling span of 0.5 mm and 1 mm.

As can be seen, the correlation coefficient between *JRC* and the roughness parameters (Z_2 and R_p) decreases with the sampling span. It indicates the roughness parameter scale dependency. The linearity of the relationship has been subjected to modifications by other researchers after Tse and Cruden (1979) (Yu and Vayssade, 1991; Kim and Lee. 2009: Tatone and Grasselli, 2010; and Jang et al., 2014) and some Power-law and Logarithmic equations emerged in the sampling span of 0.5 mm and 1 mm (Table 2.5).

Correlation between *JRC* and the fractal dimension (*D*) has been carried out by determining the fractal dimension of the ten standard roughness profiles. Some of these relationships are listing in Table 2.6.

It is worth noting that the calculation of the *JRC* value, as a scale free parameter with the help of other scale dependent parameters, does not always lead to an accurate calculation. Other reasons can also lead to an inaccurate calculation of *JRC*, such as the sampling span, the misapplication of roughness parameters and limitations of roughness measurement technology (Yu and Vayssade, 1991, Kulatilake et al., 1995, Fardin et al., 2001 and Hong et al., 2008).

Table 2.5: Relationships between JRC and Z_2, R_p and $\theta^*_{max}/(C+1)_{2D}$.

Author	Relationship	Sampling Span	R^2
Tse and Cruden [1979]	$JRC = 32.2 + 32.47 \log Z_2$	1.27 mm	0.986
Yu and Vayssade [1991]	$JRC = 61.79\, Z_2 - 3.47$	0.5 mm	0.973
	$JRC = 64.22\, Z_2 - 2.31$	1 mm	0.983
Yang et al. [2001]	$JRC = 32.69 + 32.98 \log Z_2$	0.5 mm	0.993
Kim and Lee [2009]	$JRC = 63.4351\, Z_2 - 2.10976$	1 mm	0.974
Tatone and Grasselli [2010]	$JRC = 51.85\, {Z_2}^{0.60} - 10.37$	0.5 mm	0.96
	$JRC = 55.03\, {Z_2}^{0.74} - 6.10$	1 mm	0.977
Jang et al.[2014]	$JRC = 51.16\, {Z_2}^{0.531} - 11.44$	0.5 mm	0.972
Maerz et al. [1990]	$JRC = 411(R_p - 1)$	≈ 0.6 mm	0.984
Yu and Vayssade [1991]	$JRC = 92.07(R_p - 1)^{0.5} - 3.28$	0.5 mm	0.974
	$JRC = 95.23(R_p - 1)^{0.5} - 2.62$	1 mm	0.982
Kim and Lee [2009]	$JRC = 323.013 R_p - 319.788$	1 mm	0.898
Tatone and Grasselli [2010]	$JRC = \left(3.36 \times 10^{-2} + \frac{1.27 \times 10^{-3}}{\ln(R_p)}\right)^{-1}$	0.5 mm	0.972
	$JRC = \left(3.38 \times 10^{-2} + \frac{1.07 \times 10^{-3}}{\ln(R_p)}\right)^{-1}$	1 mm	0.972
Tse and Cruden [1979]	$JRC = 37.28 + 16.58 \log SF$	-	-
Tatone and Grasselli [2010]	$JRC = 3.95(\theta^*_{max}/(C+1)_{2D})^{-0.7} - 7.98$	0.5 mm	-
	$JRC = 2.40(\theta^*_{max}/(C+1)_{2D})^{-0.85} - 4.42$	1 mm	-

Table 2.6: Relationships between JRC and D.

Author	Relationship
Turk et al. (1987)	$JRC = -1138.6 + 1141.6D$
Carr and Warriner (1987)	$JRC = -1022.55 + 1023.92D$
Maerz and Franklin (1990)	$JRC = 1870(D - 1)$
Xie and Pariseau (1994)	$JRC = 85.2671(D-1)^{0.5679}$
Wakabayashi & Fukushige(1992)	$JRC = \sqrt{\frac{D-1}{4.413 \times 10^{-5}}}$
Lee et al (1990)	$JRC = -0.878 + 37.784\left(\frac{D-1}{0.015}\right) - 16.93\left(\frac{D-1}{0.015}\right)^2$

2.10 **Roughness measurement techniques**

There are mainly two main roughness measuring techniques in terms of having contacts to the rough surface. Most of the following methods give 2D roughness profiles. In many cases the 2D roughness profiles are easier to see and to interpret than a 3D rough surface:

1) Mechanical contact profilommeters

These series of methods are known as linear profiling methods in which the vertical distance of the rough surface is measured from a reference line. The measurement is conducted based on the specified sampling span. These methods are as follows:

- *Stylus profilommeter* (Weissbach, 1978)

This kind of profilommeter is one of the most widely used instruments for 2D scanning of the rough surfaces. A stylus moves over a rough surface and the topography of the surface is displayed in the desired direction. Different sizes of the profilommeters have been used in the laboratory. However, their application in the field has also been proven and they can be used in the field with some modifications in shape and size.

- *Profile comb* (Barton and Choubey, 1977)

Profile comb is a very simple instrument for measuring small and large scale components of a limited length of roughness. A roughness profile can be obtained as quickly as possible in comparison with other methods; however, the accuracy of the roughness profile is definitely less than that recorded by stylus profilommeter. Therefore, the *JRC* value can be estimated by comparing the 2D profile and the ten standard roughness profile (ISRM 1978).

- *Straight edge and rulers* (Piteau, 1970)

Straight edge is the simplest tools to measure the large scale waviness of a rough surface. A large area of a surface can be measured; however, the measurement accuracy is considerably low. In this method, a straight edge is placed in the rough surface along the direction of sliding. Then, the distance between the edge and the surface is measured along the length of the edge.

- *Shadow profilommetry* (Maerz et al., 1990)

This method is a kind of photo-analysis technique in which the shadow created by placing a straight edge on a rough surface is captured and digitized. A 2D roughness profile can be made by taking a photograph of the shadow and processing it.

- *Compass and disc-clinometer* (ISRM 1978)

It is applicable in the field to measure roughness on the sliding direction. By using different sizes of the disc and measuring reading the compass, scattering of the poles can be plotted as a pole clusters. Maximum local dip angle, sliding direction and also dilation of the discontinuity can be estimated from the pole clusters.

- *Equilateral tripod or connected pins* (Rasouli and Harrison 2001)

In this method, the orientation of the unit normal vector on an equilateral tripod is measured. Similar to compass and disc-clinometer method, the measurement are recorded on the polar plot for further interpretation.

2) Non-contact profilometers- optical based

The main drawback of the contact methods is low accuracy and being time-consuming particularly for the large area. They are not also able to use in inaccessible and remote locations. By using non-contact roughness measuring methods, the fracture surface characterization process can be conducted quickly with high accuracy on a large area:

- *Photogrammetry* (Wichens et al. 1971)

This method is based on taking two or more 2D photos from different points (referred as standpoints) of a remote surface and making 3D image in place by processing the projecting rays, which intersect at a point. Distance between the standpoints and the scene should be based on a specified regulation. The close-range photogrammetry covers the distances up to 1 km.

- *Light Technique* (Tatone and Grasselli, 2009)

By projecting a single line of light onto a surface and capture the projected line by a CCD camera, the surface can be digitized. An improvement has been made by projecting several lines at the same time to digitize a surface in less time. The imaging distance for this technology is limited to 2 m. ATOS (Advanced TOpometric Sensor) is the known instrument that uses this technique.

- *Laser ranging* (Huang et al. 1992)

In laser ranging, the distance between the source of laser and the surface is measured based on the speed of laser and the time takes to return. The knowledge of laser ranging has been established in 3D laser scanner or profilommeter, which is widely using in the laboratories. The

distance between 3D laser profilommeter and the surface is less than 30 cm. For the higher range of distance, LiDAR (Light Detection and Ranging) systems have been emerged. More resolution for a longer distance and larger area can be achieved by the recent feature of LiDAR, which make its applicability broader in comparison with terrestrial photogrammetric systems.

2.11 **Roughness scale dependency**

Scale dependency of discontinuity roughness has been recognized among many studies carried out on the shear strength of discontinuities. These studies have been focused on the shear behaviour of discontinuities in the laboratory and field (Pratt et al., 1974; Muralha and Pinto Da Cunha, 1990) and also the shear strength of the samples replicated in various sizes (Bandis et al., 1981; Ohnishi and Yoshinala, 1995; Castelli et al., 2001; Leal-Gomes, 2003). Modification of the roughness parameters defined for the joint roughness in different scales indicated neutral, positive, negative or a combination of those scale effects on the joint shear behaviour in 2D and 3D (Bandis et al., 1981; Maerz and Franklin, 1990; Cravero et al., 2001; Fardin et al., 2001, 2004; Fardin, 2008 and Tatone and Grasselli, 2013). Despite of the variation of surface topography in different lengths of the sample, effect of asperity strength and boundary condition should also be taken into consideration. Barton and Choubey (1977) presented an increase in the *JRC* value of smaller sample blocks compared to the bigger blocks by back-analyzing of their tilt tests. The roughness characterization methods have been used for the surfaces in the size of 0.9 cm to 4000 cm^2. Tatone and Grasselli (2013) believe that the confliction between the findings of scale effect on the roughness parameters could be due to the resolution of surface measurement. Lanaro et al. (1999), Fardin (2001) and Tatone and Grasselli (2013) showed the scale dependency of discontinuity through the calculation of fractal roughness parameters. Lanaro et al. (1999) indicated that the variation of the roughness parameter (the standard deviation of the asperity height) follows a power law relationship until a certain scale beyond which this relationship is not exponential any more. This scale point was named “stationary threshold”. Fardin et al. (2001) has also indicated the stationary threshold for the sampling span. To simply describe the stationary threshold, it is assumed that the average angle of asperities as a roughness parameter decreases when the sampling span size exceeds a certain length. Therefore, the roughness profile transforms to a flat surface, meaning that the scale effect will be meaningful before the threshold

is reached. In other words, the length of the rock joint should be longer than the stationary threshold for further study free of scale effect.

There are limited experimental relationships to correct the scale effect on the joint roughness parameter. The most widely relationship was proposed by Barton and Bandis (1982) to correct the scale effect the JRC as:

$$JRC_n = JRC_0 \left(\frac{L_n}{L_o}\right)^{-0.02\, JRC_0} \qquad (2\text{-}55)$$

Where JRC_n and L_n represent the values of roughness and length for the joint size of interest; and JRC_0 and L_0 refer the values of roughness and length for the 10 cm length of the roughness profiles. By inspiring the methodology applied by Barton and Bandis (1982), a relationship has been proposed to represent the scale effect on the maximum asperity angle (i_{0-max}) as one of the statistical roughness parameters (Deng et al., 2004). Assuming a strong relationship between the asperity angle and the shear strength of rock joint, a correlation has been made in terms of different span size. The following equation was proposed in order to model the scale effect of i_{0-max}:

$$i_{0-max}(l_n) = i_{0-max}(l_0) \left(\frac{l_n}{l_o}\right)^{-\alpha\, i_{0-max}(l_0)} \qquad (2\text{-}56)$$

where l_0 is the basic joint length (from laboratory measurement), l_n is the length involved, $i_{0-max}(l_0)$ is the value of i_{0-max} for l= *lo*, and so as $i_{0-max}(l_n))$ for $l = l_n$. Parameter α is obtained by fitting the converted curve i_{0-max}– l (measurement) to Eq. 2-56. Lanaro et al. (1999), Fardin et al. (2001) and Tatone and Grasselli (2013) showed the scale dependency of the roughness parameters, however, no experimental relationships were proposed.

2.12 **Summary and conclusion**

Strain-burst occurs in the rock mass as a result of a violent release of stored energy. This phenomenon can be observed as rock-fall from roof, rock ejection from the wall in underground excavations, buckling of the wall and working face and pillar crush. Rock mass fails when the accumulated energy exceeds rock compressive strength at peak strength point. To know the severity of fracturing, it is necessary to know the mechanism of strain-burst and the amount of accumulated energy.

At bursting, the created fracture surfaces control the post-failure process. The knowledge of the post-failure behaviour can help to better understand rockburst mechanism and also to control it. The post-peak mechanism is interconnected to the shear behaviour of the fractures. Therefore, the rock joints mechanical models can be used to predict the joint behaviour in pre- and post-failure part of the stress-strain curve.

Patton (1966) proposed a bi-linear model for non-planar rock joint based on sliding over the asperities. The asperities' teeth were oriented at an angle with respect to the mean plane of the Joint. In "low" compressive stresses, the model behaviour is characterized by dilatancy and the overriding of asperities. This model can predict the mechanical behaviour of a simple joint with regular asperities. Since different combinations of sliding mechanisms or shearing through asperities are observed for rock joint strength, a nonlinear failure envelope must be used for real rock joints.

The shear strength model proposed by Ladanyi & Archambault (1970) considers both the sliding and shearing mechanisms through the asperities. As a consequence, this model is appropriate for predicting the shear behaviour of natural joints. Moreover, the influence of normal stress on the dilation has been taken into account. This model can predict the peak shear strength of joint. Ladanyi & Archambault considered progressive roughness degradation as shear area ratio.

Barton (1973) took into account the geometry of joint asperity as a parameter that controls the shear and normal displacement behaviour at peak shear strength. In this model, the peak shear displacement is independent of normal stress, which is not consistent with experimental observations. In addition, the negative dilatancy is not taken into account. Barton et al. (1985) modified the original model to express degradation of the joint roughness ($JRC_{mobilized}$). This model is not able to predict the post-peak roughness mobilization of fracture.

The nonlinear analytical (mathematically and graphically) model proposed by Saeb and Amadei (1992) considers the effect of the surrounding rock mass stiffness and any reinforcement system intersecting the joint. Two conditions, including constant normal load and constant displacement are considered. This model can predict the joint shear and normal displacement behaviour in pre- and post-peak. This model is not able to predict the effect of cyclic loading on joint normal and shear behaviour. The surface roughness degradation is also neglected.

The CSDS model proposed by Simon (1999) is composed of two basic set of equations in which two behaviours of the shear stress-shear displacement and the shear displacement- normal displacement can be predicted. Two major loading conditions including, constant normal load and constant normal stiffness, can be modeled by the CSDS. This model is able to predict the pre- and post-peak shear behaviour of a joint. In comparison with the Saeb & Amadei's model, it demonstrated a good agreement with the experimental results. However, the model was verified based on the experimental data included in the literature. In addition, the CSDS model does not consider the cyclic loading conditions.

In conclusion, in order to evaluate the post-peak behaviour of intact rock subjected under axial loading, a comprehensive joint behaviour model should be used. This model should be able to consider different loading conditions existed in nature and also both shear and dilatancy behaviour of joint. Moreover, good agreement in pre- and post-peak behaviour should be considered as a remarkable property of the assigned model. Since the CSDS model considers different loading conditions, joint geometry, dilatancy, scale effect and the influence of water pressure on the joint behaviour; it seems that it can be the best choice for predicting the joint shear and dilatancy behaviour.

CHAPTER 3 ARTICLE 1: MORPHOLOGICAL EVALUATION OF FRACTURES CREATED BY DIFFERENT LOADING MODES INTRODUCING THE MODIFIED SPLITTING TECHNIQUE

Arash Khosravi, Richard Simon, and Nooshin Falaknaz

This article was submitted to Canadian Geotechnical Journal in June 2016, under revision following comments from reviewers.

Abstract: The mechanical behaviour of a jointed rock mass is highly influenced by properties and geometry of rock joints. Amongst joint characteristics, the joint roughness plays an important role in both rock mass strength and deformation. Roughness may be influenced by loading conditions in which the rock joints are created. Depending on loading modes applied to the rock mass, rock joints can be created due to tensile, shear or both tensile and shear stresses. The influence of the loading modes on the joint roughness has not yet been thoroughly fully investigated and understood.

This paper consists of two types of analysis. First, a new 2D roughness profilommetry technique (2DRP) is presented on the basis of the contact profilommetry and image processing. Second, three types of fractures created by a modified splitting technique, uniaxial and triaxial compression tests (as representatives of the loading modes) are assessed based on the morphological point-of-view with help of the new technique (2DRP) and another non-contact profilommetry method.

Roughness profiles of the joint surface created by the modified splitting technique are studied in directions parallel and perpendicular to the loading axis. The results of this study show that the Joint Roughness Coefficient (*JRC*) values of the roughness profiles perpendicular to the loading axis are similar to each other with small variation between the profiles from one side of the specimen to another. In contrast, observation on the parallel profiles indicates a chaotic behaviour in the *JRC* values. Complementary microscopic studies on the roughness profiles were also carried out. A discussion follows on the contribution of grain size, loading modes and loading direction on the roughness distribution.

Keywords

Profilometry, Roughness, *JRC*, Fracturing mode, Confining stress, Fracture trajectory

3.1 Introduction

The principal types of discontinuities in rock masses are joints, which control the rock mass mechanical behaviour. Two main components that influence the shear strength of rock joint: the matrix strength and the geometrical parameters of fracture surfaces. The joint surface topography and spatial situation of two corresponding joint walls play a direct role in developing the shear strength. There are also several petrological properties and main effective factors that influence the morphological shape and strength of a fracture roughness, including mineral composition, degree of cementation, grain size and secondary minerals in the matrix (Kabeya, 1997). Additionally, many studies have been conducted to characterize and correlate the joint surface roughness with the joint mechanical behaviour (e.g. Mayers, 1962; Barton and Choubey, 1977; El-Soudani, 1978; Tse and Cruden, 1979; Maerz et al., 1990; Yu and Vayssade, 1991; Poon et al., 1992; Kulatilake et al., 1995; Belem et al., 2000; Grasselli, 2001; Yang et al., 2001; Kim et al., 2009; Tatone and Grasselli, 2010; and Jang et al., 2014).

The roughness of joint surfaces can be measured by two-dimensional (2D) and three-dimensional (3D) roughness profiling devices. The 2D devices require a contact with the rock surfaces, while 3D systems do not require a contact with the rock surface (e.g. Barton, 1972; Tse and Cruden, 1979; Maerz et al., 1990; Kim et al. 2009; Jang et al., 2014; Belem et al., 2000; Tatone and Grasselli, 2009). Typical 3D roughness quantification tools used are laser profilommetry and photogrammetry. These 3D roughness scanning tools enable us to obtain valuable point-to-point information of the surface topography either in laboratory or field scale with the maximum size of 1800×1800 mm^2 (Tatone and Grasselli, 2009, 2010, 2013). However, 3D terrestrial lighting method (LiDAR) can be used to recognize the presence of discontinuities in the rock mass in the area larger than mentioned (Otoo et al., 2011; Bistacchi et al., 2011).The accuracy and operation speed of 3D methods are superior to 2D methods, these modern and expensive instruments are not always available. In contrast, 2D roughness profiling devices, including stylus profilommeter, shadow profilommetry and profile comb are readily available, inexpensive and reliable alternative systems to provide the roughness profiles (Barton and Choubey, 1977; Poon et al., 1992; Maerz et al., 1990). Among these 2D devices, the profile comb is more commonly used in both field and laboratory, but provides lower accuracy. Using either 2D or 3D roughness profiles obtained from these methods and tools described can be used to calculate roughness parameters.

The first objective of this paper is to introduce a new simple 2D roughness profilommetry technique (2DRP) as an alternative 2D joint roughness characterization method for a joint size of equal or less than 100 mm. Although this new technique seems time-consuming, it provides an accurate method to obtain the *JRC* value compared to the subjective and visual comparison of the standard *JRC* profiles (Barton and Choubey, 1977) or to some of the contact profilommetry methods such as profile combs. The results of this new technique (2DRF) were verified using a 3D photogrammetry tool Advanced Topometric Sensor (ATOS) (Tatone and Grasselli, 2010, 2013).

The second objective of this study is to investigate the effect of loading modes on the fracture roughness profiles. A rock mass can be subjected to the combination of different loading modes. Based on different loading modes applied on the rock mass, different kind of fractures are created in terms of surface profile. Three different loading modes may occur in situ to create different fracture modes, including Mode I or opening as a tensile fracture; Mode II or in-plane shear and Mode III or out-plane shear (Brady and Brown, 1985). In the case of Mode I, the crack is initiated by a tensile load. In the other modes, fractures are created due to a combination of both tensile and shear loading stresses. Bobet and Enstein (1998) studied the effect of the loading modes on the crack initiation and propagation using uniaxial tensile test, uniaxial and triaxial compression tests on samples with a unique pattern of flaws. Their results indicate that the trajectory of the crack coalescence in the specimen with non-overlapped flaws changes when the confining pressure is applied to the specimen. Also, the results implicitly showed that the joint roughness decreases when a confining pressure increases. Therefore, the crack initiation, propagation and coalescence induced by different loading modes affect the roughness of fracture surface. Tang and Kou (1998) investigated the effect of loading modes on a pre-flawed sample using numerical code RFPA^{2D}. Three different loading modes I, II and combination of I and II were applied to a model to show the crack propagation mechanism. The results of this study were in good agreement with those obtained by Bobet and Enstein (1998). The effect of different loading modes on the roughness has also been investigated on rocklike materials (Amitrano and Schmittbuhl, 2002; Seredin et al., 2013). The results of their studies indicate that the roughness of the fractures induced by uniaxial tensile test is higher than those obtained using uniaxial and triaxial compression tests. They also concluded that the fracture roughness decreases with an increase of the confining pressure. Despite of interesting outcomes from these studies, these

results have not led to a comprehensive investigation on rock fracture surfaces affected by different loading modes. In this paper, the effect of different loading modes was investigated on three igneous rock types from coarse (gabbro) to intermediate (microgabbro) and fine-grained sizes (basalt). Furthermore, the regional roughness of the fracture surface created by the Modified Splitting Technique (representative of loading mode I) and the fracture (mode I) trajectory through the grains were investigated.

3.2 **Roughness parameters**

In order to quantify the morphological characteristics of a discontinuity surface, three categories of roughness parameters are used. The first group of roughness parameters employed the spatial information from the surface to show statistically the position of each point based on their amplitude and slope (Myers, 1962;; El-Soudani, 1978; Tse and Cruden, 1979; and Aydan et al. 1996 among others). The second group of roughness parameters, Joint Roughness Coefficient (*JRC*), was empirically established by Barton and Choubey (1977). The *JRC* was derived from a back calculation of the proposed relationship as a constitutive shear model for rock joints. The third group of roughness parameters is based on the fractal approach (Seidel and Haberfield, 1995; Zhou and Xie, 2003; Kulatilake et al., 2006) which is a mathematical model of rough surface inspired by the geometry of nature (i.e. coast line). In this paper, only statistical and empirical parameters are discussed.

3.2.1 Statistical roughness parameters

The statistical roughness parameters are identified based on amplitude and frequency of the asperities. The statistical roughness parameters commonly used in rock mechanics are summarized in Table 3.1. To assess the roughness of a fracture, only one statistical parameter is usually calculated. However, it is suggested to quantify fracture roughness based on at least two types of statistical parameters (Odling, 1994; and Hong et al., 2008). In this study, three roughness parameters (based on slope and wave length of asperities) are measured (Z_2, R_p and A_i) to make a comparison between the fracture surfaces obtained by different loading modes from morphological point of view. These parameters are defined as follows:

Z_2 is the root mean square of the tangent of the slopes of the lines that connect two neighbor points of the roughness profile depending on selected sampling span (interval) (Myers, 1962; Tse and Cruden, 1979):

$$Z_2 = \left[\frac{1}{N}\sum_{i=1}^{N}\frac{(y_{i+1}-y_i)^2}{(x_{i+1}-x_i)^2}\right]^{1/2} \quad (1)$$

Where, N is the number of sampling points; x_i and $x_{i+1}$are x coordinates of the i^{th} and $(i+1)^{th}$ sampling points; y_i and y_{i+1} are y coordinates of the i^{th} and $(i+1)^{\text{th}}$ sampling points. The higher the value of Z_2, the rougher the fracture surface is.

Table 3.1: Statistical roughness parameters used in rock mechanics.

Roughness based on frequency	**Roughness based on amplitude frequency**
Centreline average roughness (CLA) (AMS, 1955)	Profile roughness index (R_p) (Maerz et al., 1990)
Root mean square of roughness (RMS) (AMS, 1955)	Root mean square of the first derivative of the profile (Z_2) (Myers, 1962)
Maximum peak to valley (R_{max}) (El-Soudani, 1978)	RMS of the second derivative of the profile (Z_3) (Myers, 1962)
Mean standard variation of height (El-Soudani, 1978)	Profile average inclination angle (A_i) (El-Soudani, 1978)
Structure function (SF) (Sayles and Thomas, 1976)	Root mean square of inclination (RMS_i) (Aydan et al., 1996)
Auto-correlation function (AFC) (Bendet and Piersol, 1971)	

R_p is known as the Roughness Profile Index and is defined as the ratio of the true length of roughness profile to the projected length on the horizontal plane (El-Soudani, 1978):

$$R_p = \frac{1}{N-1}\sum_{i=1}^{N-1}\frac{\left[(x_{i+1}-x_i)^2+(y_{i+1}-y_i)^2\right]^{0.5}}{(x_{i+1}-x_i)} \quad (2)$$

A_i is a representative of spatial approach and known as the average inclination angle of the line, which connects two neighbor points on roughness profile with a particular sampling span:

$$A_i = \tan^{-1}\left[\frac{1}{L}\sum_{i=1}^{N-1}\left|\frac{y_{i+1}-y_i}{x_{i+1}-x_i}\right|\right] \quad (3)$$

where, L is the projected length of roughness profile.

3.2.2 Empirical roughness parameter (*JRC*)

JRC is likely the best known empirical roughness parameter derived from a back calculation of the joint shear strength with a proposed shear model. The *JRC* value can be obtained using a visual analogy between roughness profiles obtained from the fracture surface and the 10 standard *JRC* profiles. The observational nature of this method may lead to inaccurate discontinuities characterization and rock mass rating without sufficient experience. Depending on the rock joint compressive strength, a small error in the estimation of the *JRC* value can result in an unrealistic overestimation in the rock joint strength (Tse and Cruden, 1979; and Beer et al., 2002). Therefore, it is better to find an objective way to obtain an accurate *JRC* value. Many researchers proposed different equations to correlate *JRC* with two statistical roughness parameters of Z_2 and R_p (Tse and Cruden, 1979; Yu and Yayssade, 1991; Yang et al., 2001; Kim and Lee, 2009; Tatone and Grasselli, 2010; and Jang et al., 2014). However, it is worth noting that these two parameters are sensitive to the sampling interval (Myers, 1962). Table 3.2 summarizes the correlation between *JRC* and two statistical roughness parameters Z_2 and R_p with the sampling spans of 0.5 and 1 mm.

Table 3.2: Correlation between statistical ($Z_2$and R_p) and empirical (JRC) parameters.

Author	Relationships				Sampling span
	***JRC* and Z_2**	R^2	***JRC* and R_p**	R^2	
Tse and Cruden (1979)	$JRC = 32.2 + 32.47 \log Z_2$	0.986			1.27 mm
Maerz et al. (1990)			$JRC = 411(R_p - 1)$	0.984	≈0.6 mm
Yu and Vayssade (1991)	$JRC = 61.79\, Z_2 - 3.47$	0.973	$JRC = 92.07(R_p - 1)^{0.5} - 3.28$	0.974	0.5 mm
	$JRC = 64.22\, Z_2 - 2.31$	0.983	$JRC = 95.23(R_p - 1)^{0.5} - 2.62$	0.982	1 mm
Yang et al. (2001)	$JRC = 32.69 + 32.98 \log Z_2$	0.993			0.5 mm
Kim and Lee (2009)	$JRC = 63.4351\, Z_2 - 2.10976$	0.974	$JRC = 323.013 R_p - 319.788$	0.898	1 mm
Tatone and Grasselli (2010)	$JRC = 51.85\, {Z_2}^{0.60} - 10.37$	0.96	$JRC = \left(3.36 \times 10^{-2} + \frac{1.27 \times 10^{-3}}{\ln(R_p)}\right)^{-1}$	0.972	0.5 mm
	$JRC = 55.03\, {Z_2}^{0.74} - 6.10$	0.977	$JRC = \left(3.38 \times 10^{-2} + \frac{1.07 \times 10^{-3}}{\ln(R_p)}\right)^{-1}$	0.972	1 mm
Jang et al.(2014)	$JRC = 51.16\, {Z_2}^{0.531} - 11.44$	0.972	$JRC = 65.9(R_p - 1)^{0.302} - 9.65$	0.973	0.5 mm

In this study, Z_2 values were obtained for the roughness profiles with lengths of less than 100 mm. Then, the *JRC* values were calculated for each profile. To do so, a relationship was needed to consider the unevenness of the profiles which had the most effect on the joint shear behaviour. The relationship proposed by Tatone and Grasselli (2010) has been used in this study for the *JRC* calculations with an interval span of 0.5 mm. This equation is based on the realignment of the 10 standard JRC profiles resulted from their statistical best-fit lines.

3.3 **Fractures created in different modes**

In order to create a fracture in Modes I, II and III, two loading modes are required: tensile and a mixture of tensile and shear loads. The fracture obtained from the splitting method is considered as a Mode I fracture. Considering the stress distribution in a sample subjected to a splitting test, two compression zones are observed close to the loading contact areas. Therefore, the fracture surface is not fully created as a result of pure tension (Fairhurst, 1964; Xia and Zhou, 2010) and cannot technically be considered as a representative of tensile fracture. In this study, the Modified Splitting Technique was carried out on rock specimens with NQ size to create pure tensile fractures (Mode I).

In this technique, two grooves were cut along the length of the specimen with a width and depth of 3 mm on two opposite sides of the specimen. Then, the specimens were subjected to the axial loading with a round bar (used as a wedge) placed in the upper groove until the full fracture generated. This technique was hereinafter called as “Modified Splitting Technique”. Figure 3-1 shows a schematic view of the specimen and two grooves on two sides of the rock sample.

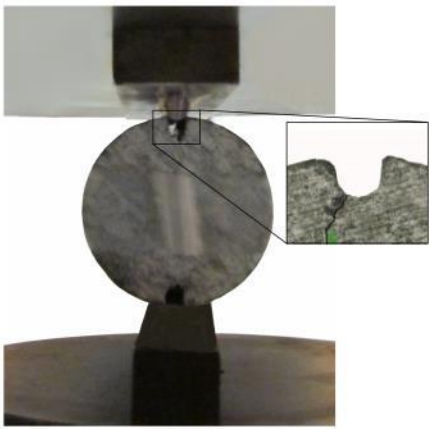

Figure 3-1: Modified Splitting Technique.

Furthermore, uniaxial and triaxial compression tests with three different confining stresses, i.e. σ_3=3 MPa, 8 MPa and 13 MPa, were conducted on the samples with NQ size and L/D ratio of 2 to 2.4 to create rock joints in Modes II and III. Based on Xia and Zhou (2010), the fracturing mode is changed with an increase in the confining stress due to an increase of shear/tensile fracture ratio. Therefore, the tests were carried out with a constant displacement rate of 0.1 mm/min using a Tinius Olsen testing machine with the capacity of 200 tons (400 000 lbs) at the Rock Mechanics Laboratory of École Polytechnique de Montreal. The loading was stopped as soon as the joint was created at peak strength. Normally, only a single failure plane is generated in the uniaxial compression tests, while there are likely more than one failure plane as a result of the triaxial compression tests. Figure 3-2 illustrates the examples of fracture patterns induced by the loading modes applied on three rock types in this study. In uniaxial and triaxial compression tests, the largest fracture plane was considered for further investigation. In total, 45 tests were conducted on three rock types as summarized in Table 3.3.

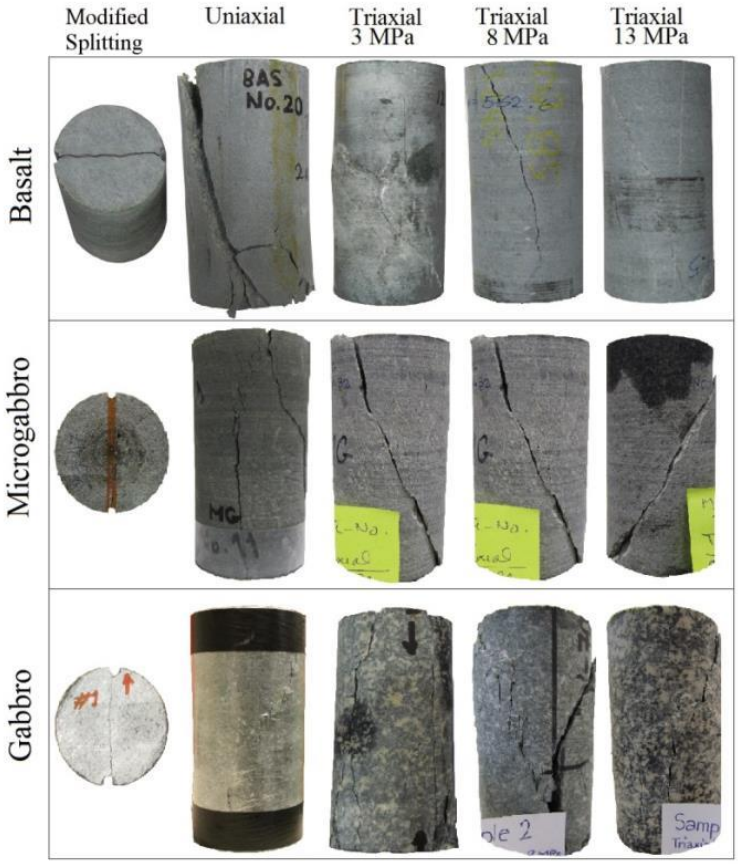

Figure 3-2: Fracture patterns obtained by different loading modes.

Table 3.3: Summary of the total number of tests.

Rock Type	Number of tests	Modified Splitting	Uniaxial compression	Triaxial compression	Confining stress (MPa)
Basalt	15	3	3	9	3, 8, 13
Gabbro	15	3	3	9	3, 8, 13
Microgabbro	15	3	3	9	3, 8, 13

3.4 New 2D roughness profilometery (2DRP)

To quantify the fracture roughness, a new experimental 2D roughness profilometry (2DRP) was developed in this study. This method is a non-contact technique in which a replica of the fracture surface is built. Then, a 2D image processing of the extracted section is established based on shadow photogrametry method proposed by Maerz et al. (1990). This new method is appropriated for the joint size less than 100 mm. The process is described in the following subsections.

3.4.1 Joint surface replication

In order to characterize the roughness profile in this study, a replica of the joint surface was created using modelling clay. In this study, the maximum joint surface area was 100 mm × 40 mm. Modelling clay is cheap, non-adhesive, non-shrinkable and easily available. Silicone rubber is a more accurate alternative to build the replica; however this material is expensive and its use is time consuming. For all subsequent measurements, a layer of the modeling clay with a thickness of 1.5 to 2 cm was spread out on the fracture surface as shown in Figure 3-3.

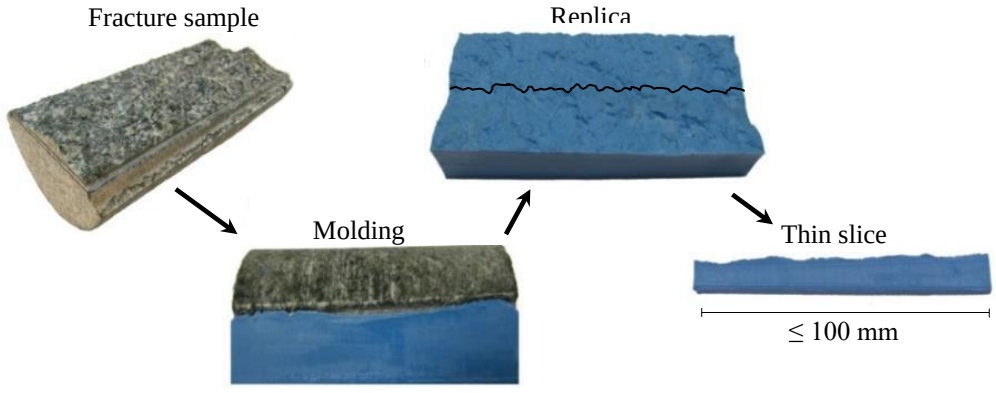

Figure 3-3: Schematic view of the procedure to obtain a thin slice of the replica representative of the roughness profile.

The joint surface was first lubricated with soap and water. Proper care was taken to avoid leaving soap bubbles on the joint when the modeling clay is placed. It would reduce adhesion between the modeling clay and joint surface which results in an inaccurate replica. The cast modeling clay was then carefully removed from the fracture surface right away. Then, a thin slice of the replica (with a minimum thickness of 10 mm) was cut with a sharp cutter knife in the direction of interest to obtain the desired roughness profile. This method can be repeated to obtain any desired profile along the replica's surface. It is recommended to lubricate the cutter knife with soap water before cutting the thin slice. Any slight adhesion between cutter knife and replica can deform the thin slice and create inaccuracies. If any deformation of the replica occurs, another replica can be built in short period of time. This feature is one of the advantages of this method compared with other techniques.

3.4.2 Photography, photo-analysis and digitizing

Following the joint surface replication, dimensions of the replicated slice of modelling clay were measured carefully. Then, 2D photos were taken from the thin slice as shown in Figure 3-4a. The thin slice was preferably illuminated in an acute angle of 45^{o} (Fig. 3-4a). The number of photos can vary based on the resolution and type of camera. To obtain good results, it is recommended to take multiple photos to avoid the picture distortion and elongation at the edges. In this study, at least 6 photos were taken of each thin slice (with length of approximately100 mm) so that only one part of the total length was seen in each photo (Fig. 3-4b). Afterwards, a central part of each photo was cropped from the original one and the cropped photos were superimposed with an image processing software (GIMP, Ver. 2.8) to create the total length of the thin slice.

GIMP 2.8 (Mattis Kimballl, 2013) is an open source software with a raster graphics editor and equipped with a filter named "Edge-Detect" to distinguish the contour of color transition (Fig. 3-4c). The profile can be saved as a new layer with any image format (e.g. jpg, tiff, bmp, etc) as shown in Fig. 3-4d. A digitizing software (Get Data Graph Digitizer 2.26, Fedorov, 2013) was then used to quantify the obtained roughness profile. This digitizing software has ability to auto-trace the roughness profile with accuracy and speed. In this study, the software accuracy was approximately 15 μm. Therefore, almost 6600 data points with coordinates (x, y) were obtained for a roughness profile with a length of 100 mm.

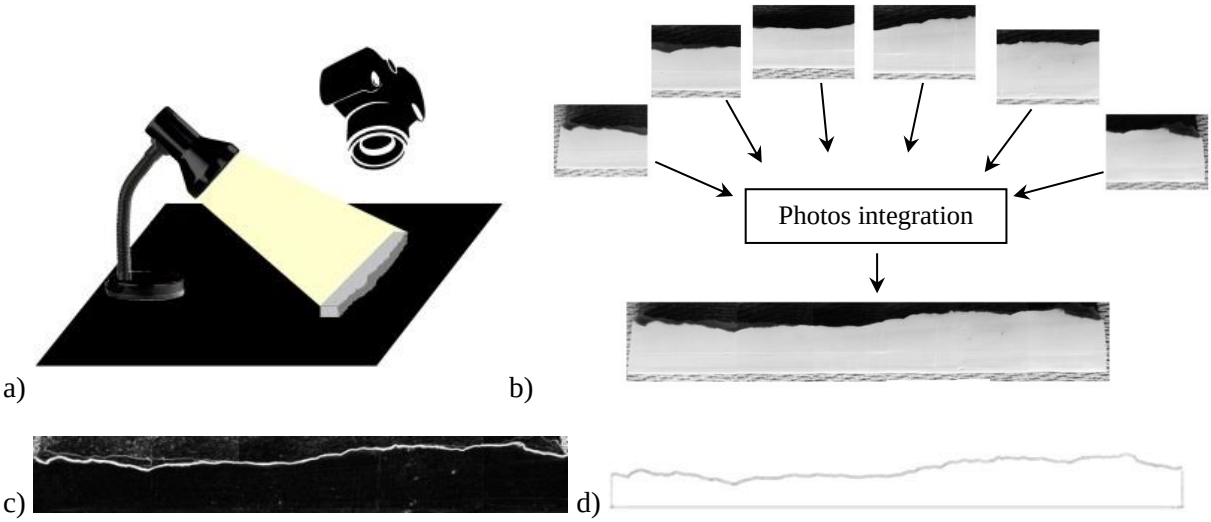

Figure 3-4: Replica photography and photo-processing.

3.4.3 Verification of the results

To validate the results of this new proposed technique (2DRP), the fracture surfaces used for the replication were digitized with the Advanced Topometric Sensor (ATOS II) as 3D roughness profilometer. The ATOS II system consists of a measurement head containing a central projector and two CCD cameras, and a high-performance Linux based PC to control the system as shown in Figure 3-5.

Figure 3-5: ATOS II system (adapted from Tatone and Grasselli, 2009).

This system measures 3D coordinates of the roughness profiles for the fracture surface via the projection of various structured white-light fringe patterns onto the surface. Images of these patterns are captured by the two CCD cameras. This system is able to capture a range of resolutions defined by a nominal point spacing of 0.044-1 mm (Tatone and Grasselli, 2010, 2013). Following digitization of the fracture surfaces, the roughness parameters (Z_2) was calculated using an Excel file with a sampling interval of 1 to 2 mm (for simplicity), for each roughness profile. These calculated parameters were then compared with those obtained by the proposed new technique (2DRP) presented in subsection 3.4 to validate the results.

Figure 6 shows a comparison between Z_2 calculated with ATOS II system data and those calculated with the new 2DRP method. This comparison is for the results of the roughness profiles created by the modified splitting method (Fig. 3-6a) and the uniaxial compression tests (Fig 3-6b). It can be seen that the results of the new technique correlate well with those obtained using ATOS II system with a correlation coefficient of R^2=0.988 and R^2=0.993 for the modified splitting method and for the uniaxial compression test, respectively. The difference between the values obtained by two methods is less than 5% in both fracture surfaces.

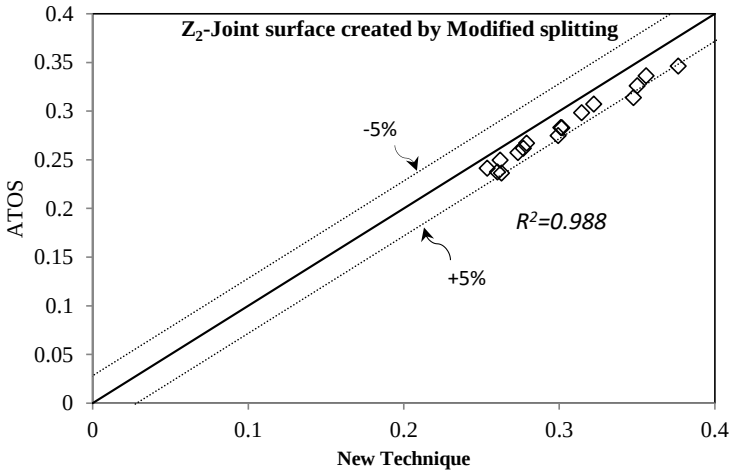

a)

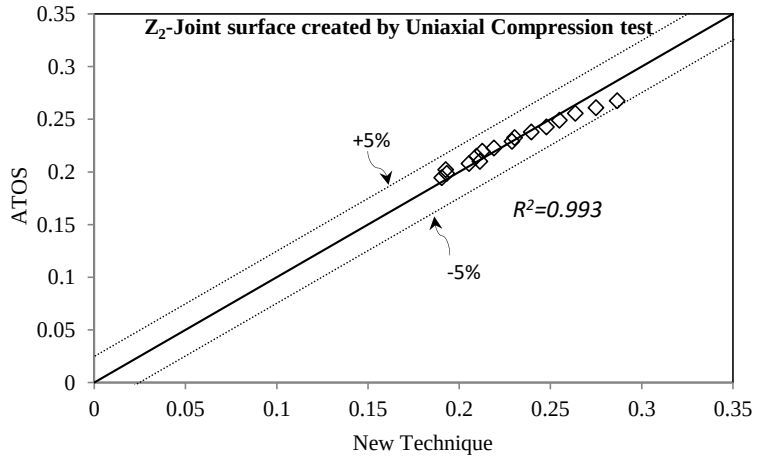

b)

Figure 3-6: Comparison between Z_2 obtained by ATOS II and the new proposed technique (2DRP) for the fractures created in gabbro by: a) the modified splitting technique; and b) uniaxial compression test.

3.5 **Roughness variation based on fracturing modes**

For this study, fracture planes were created in gabbro specimens by the modified splitting technique, uniaxial and triaxial (with a confinement stress of 3, 8 and 13 MPa) compression tests. The new proposed roughness profilometry (2DRP) was then used to characterize the fracture surfaces. Three roughness profiles were selected and studied in the middle part of each fracture surface as shown in Figure 3-7. The spacing between these profiles was ≈10 mm. In order to avoid any scale effect, a length of 70 mm was considered from the total length of the roughness profiles.

Figure 3-7: Roughness profiles selected in the middle part of the fracture surface.

In total, 45 roughness profiles were characterized for each rock type using this method. Three roughness parameters (Z_2, R_p and A_i) were then calculated for each roughness profile. Figure 3-8 displays the variations of the roughness parameters obtained in terms of different sampling span (0.3 to 2.0 mm) for gabbro specimens. As can be seen, the roughness parameters is interval dependent and they decrease with an increase in the sampling span. For instance, in the surface created by the uniaxial tests, the Z_2 value decreases by up to 40% from 0.36 to 0.22 when the sampling interval increases from 0.3 to 2.0 mm; this decrease is about 3% and 36 % for R_p and A_i, respectively. Among these parameters, R_p shows a chaotic behaviour at certain sampling interval more than 1.0 mm. The other two parameters show a smooth and steady decrease. The results also indicate that the fracture surface created by triaxial compression test with σ_3 = 13 MPa is rougher than those obtained under less confining stresses.

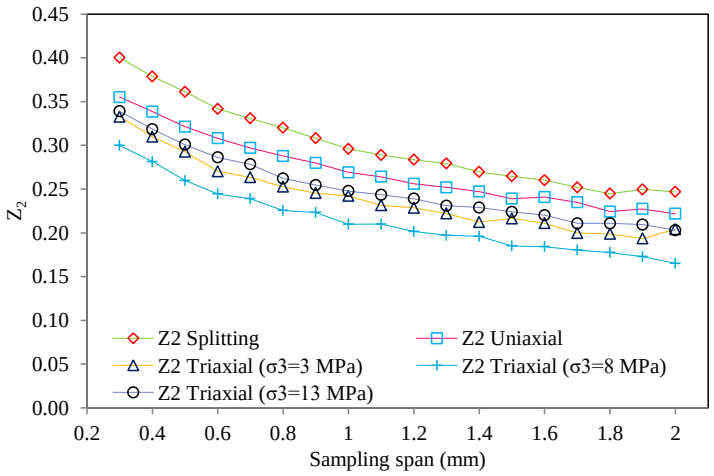

a)

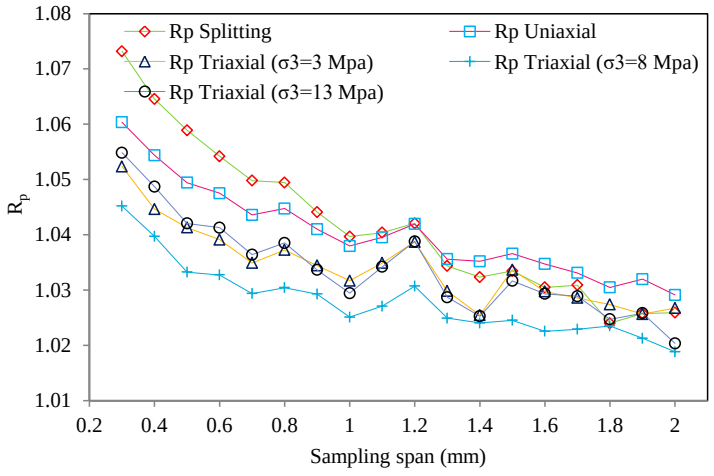

b)

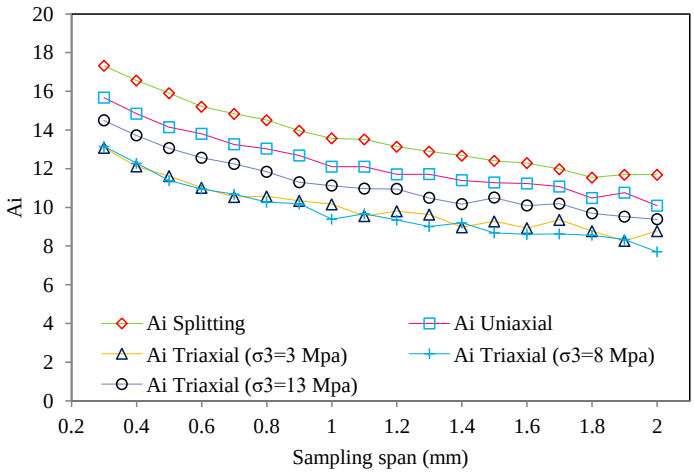

c)

Figure 3-8: Variation of the roughness parameters: a) Z_2; b) R_p and c) A_i of the fractures created in gabbro specimens by different loading modes with sampling span of 0.3 to2.0 mm.

Figure 3-9 presents the variation of three roughness parameters with different loading modes obtained in gabbro specimens for two sampling spans, 0.5 and 1.0 mm. It can be seen that the roughness parameters differs with these loading modes; the rougher surface is the surface created by the splitting method.

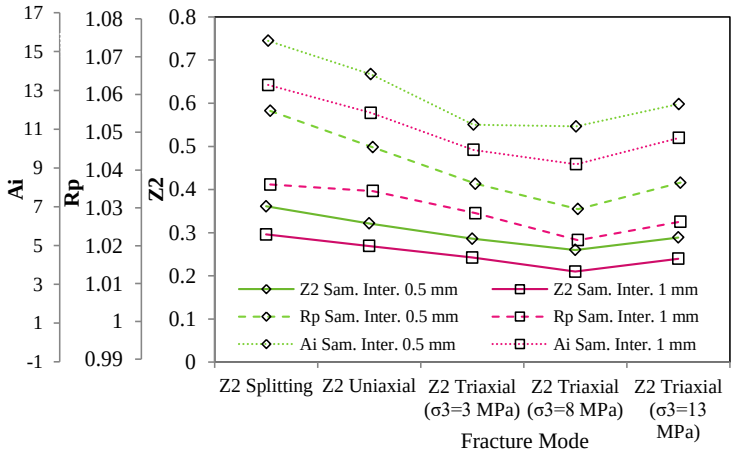

Figure 3-9: Variation of the roughness parameters in the sampling span of 0.5 and 1 mm with different loading modes (gabbro specimens).

For instance, when using a sampling interval of 0.5 mm, Z_2 decreases by up to 21%, from 0.36 for the surface created by splitting to 0.28 for the surface created by triaxial compression test with σ_3 = 3 MPa, and A_i decreases by up to 28%, from 16 to 11.5 for the same test respectively. Also

for the same sampling interval of 0.5 mm, the roughness parameters decrease with an increase in the confining stress from 3 to 8 MPa, by up to 9% for Z_2 and 1% for A_i, and then increase when the confining stress goes to 13 MPa, by up to 10% for both Z_2 and A_i (Fig. 3-9).

3.5.1 Effect of loading modes on the roughness variation

In the next step of this study, the *JRC* values were calculated for all 2D profiles. In doing so, the *JRC* value was calculated based on the equation proposed by Tatone and Grasselli (2010) to provide an objective estimate of roughness which can be comparable to the value of parameter rapidly estimated in the field. Figures 3-10a to 3-10c show the variation and the scattering of the *JRC* values for different loading modes and different rock types, gabbro (GAB), microgabbro (MG) and basalt (BAS).

Figure 3-10a shows for gabbro samples that the roughness parameters vary with the loading modes; a rougher surface is the surface created by the splitting method. The *JRC* value also varies with the loading mode from the splitting.

Different tendency can be seen in the JRC values of microgabbro and basalt specimens. Figure 3-10b shows for microgabbro that the *JRC* value is also influenced by the loading mode. Splitting surface showed a *JRC* value of 12, uniaxial surface a *JRC* of 9, and triaxial compression with σ_3 = 3 MPa a *JRC* value of 15. The results also illustrate that the *JRC* value decreases as a result of increasing in the confining stresses from 3 MPa with *JRC* = 15 to 13 MPa with *JRC* = 11. The same trend can be seen for the *JRC* values obtained for fracture surfaces created in basalt (Figure 3-10c). These two rock types, microgabbro and basalt, are similar in terms of the grain size and as expected show similar trends in *JRC* values with the loading modes. In contrast, gabbro is a coarse-grained rock and different trends are observed in the *JRC* values than those observed for microgabbro and basalt.

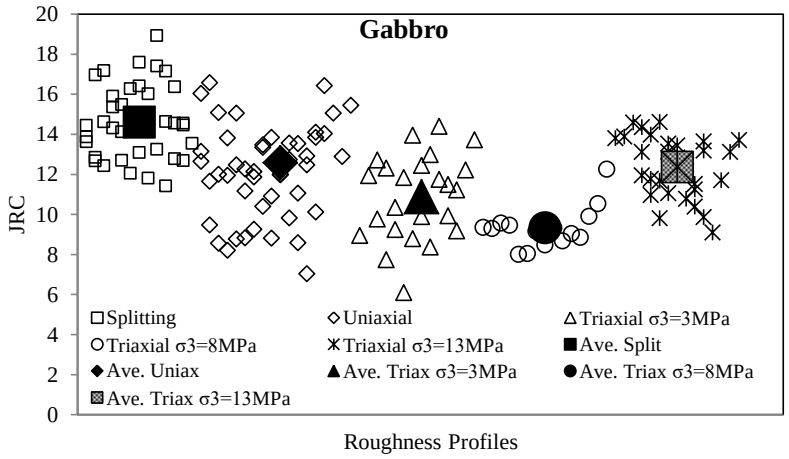

a)

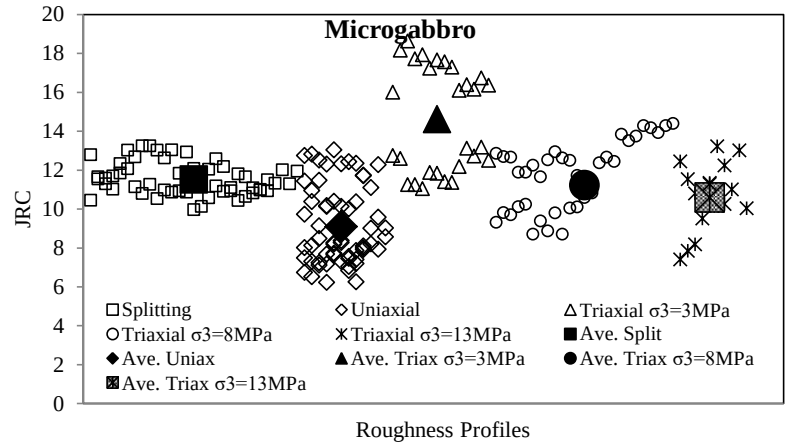

b)

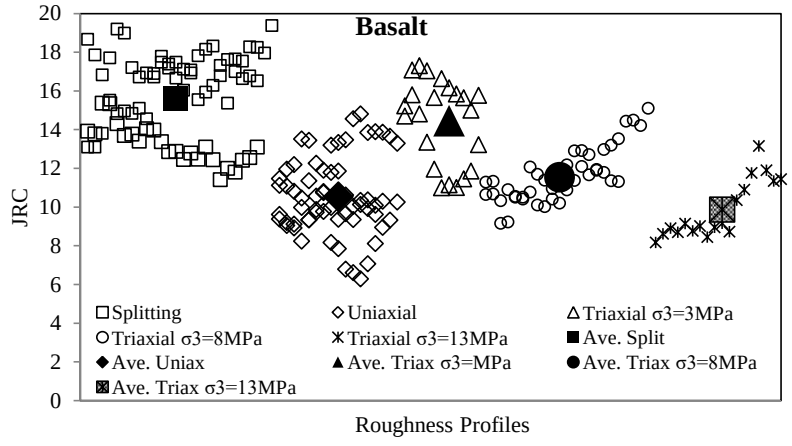

c)

Figure 3-10: Variation of the *JRC* values with different loading modes for: a) gabbro (GAB); b) microgabbro (MG); c) basalt (BAS).

3.5.2 Effect of loading direction on the roughness variation

To determine the effect of loading direction on the roughness variation, the fractures created with the Modified Splitting Technique were studied. To do so, the roughness profiles were analyzed parallel and perpendicular to the loading direction as shown in Figure 3-11. The spacing between each parallel profile was 10 mm, while the spacing of perpendicular profiles was 2.5 mm. Figure 3-11 also shows reference points for roughness measurement of the profiles parallel to the loading direction, Profile *A* on the left side of the specimens and Profile *B* on the right side of the specimens, and the profiles perpendicular to the loading direction, Profile *A′* at the bottom of the specimens and Profile *B′* at the top of the specimens. To study the effect of the segmental stress distribution, each roughness profile parallel to the loading axis was divided into three segments: upper, middle and lower as shown in Figure 3-11. To quantify the roughness of each segment, the *JRC* value was calculated from each profile.

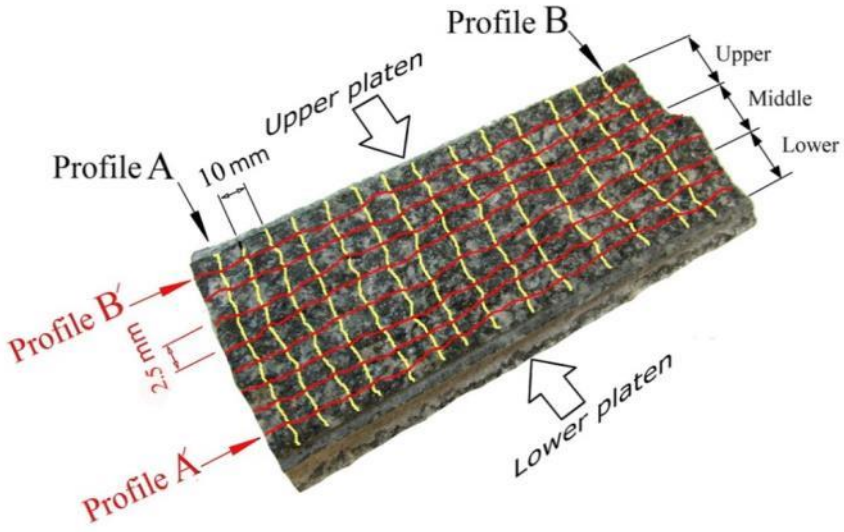

Figure 3-11: Schematic view of the roughness profiles perpendicular and parallel to the loading direction in the sample obtained from Modified Splitting Technique

Figure 3-12 shows the *JRC* values calculated for three segments along the profiles parallel to the loading axis. It is observed that the *JRC* values of all segments in the vicinity of loading areas are higher than those in the middle segment located at the core of the sample. The results also indicate that the average *JRC* values of the upper segments are higher than those obtained for the other segments (Figure 3-12a, b).

To analyze the variation of the *JRC* value with location of the roughness profiles, the *JRC* values were calculated for all the profiles parallel and perpendicular to the loading axis. The roughness (*JRC*) of the profiles parallel to the loading direction was measured from Profile *A* on the left side of the specimens to Profile *B* on the right side of the specimens as shown in Figure 3-13a.

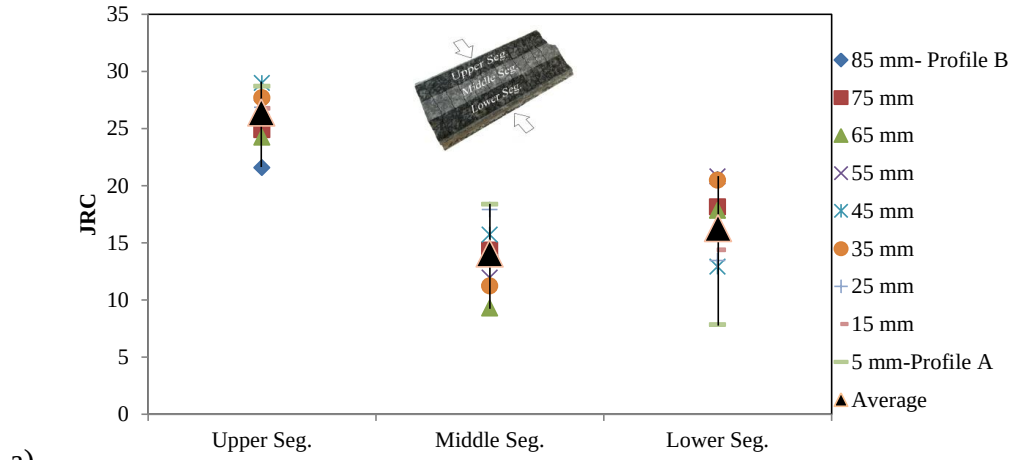

a)

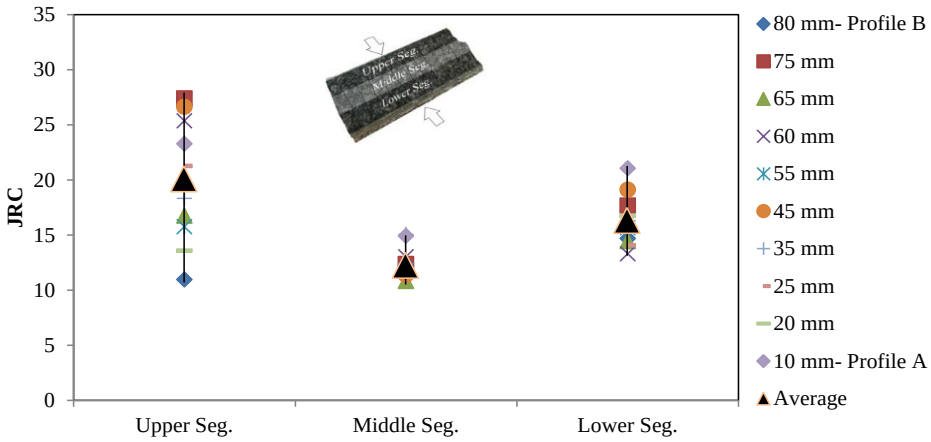

b)

Figure 3-12: The regional *JRC* distribution on the fracture surface created by the modified splitting technique; a) sample A; b) sample B.

Subsequently, each roughness parameter was imported to the Radar chart based on its spacing from the Profile *A*. As can be seen, the profile roughnesses in the middle of the specimens (from 37.5 mm to 60 mm) are close to each other. Also, the *JRC* variation shape in profiles parallel to the loading direction is unsteadily variable. The highest (JRC_{max}) and lowest (JRC_{min}) JRC values can also be observed for each rock type in Figure 3-13a. As can be seen, the JRC_{max}/ JRC_{min} ratio

is 1.56 for gabbro and 1.75 for microgabbro. The same procedure was used to calculate the roughness parameter of the profiles perpendicular to the loading direction.

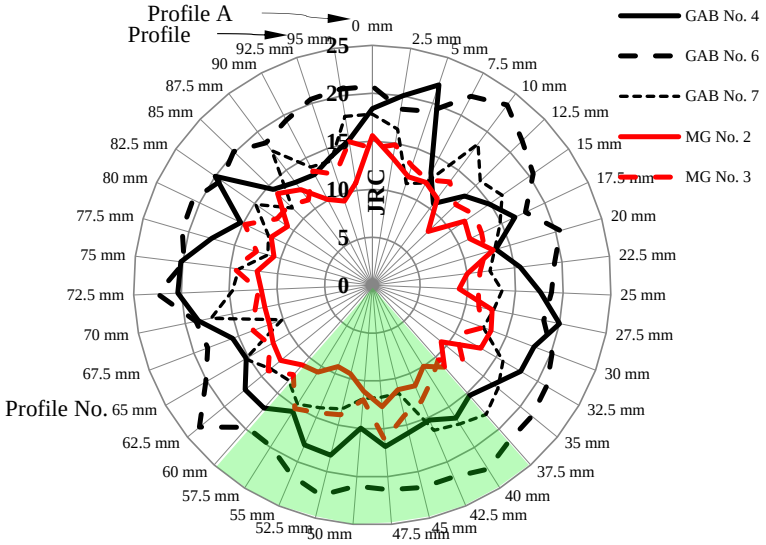

a)

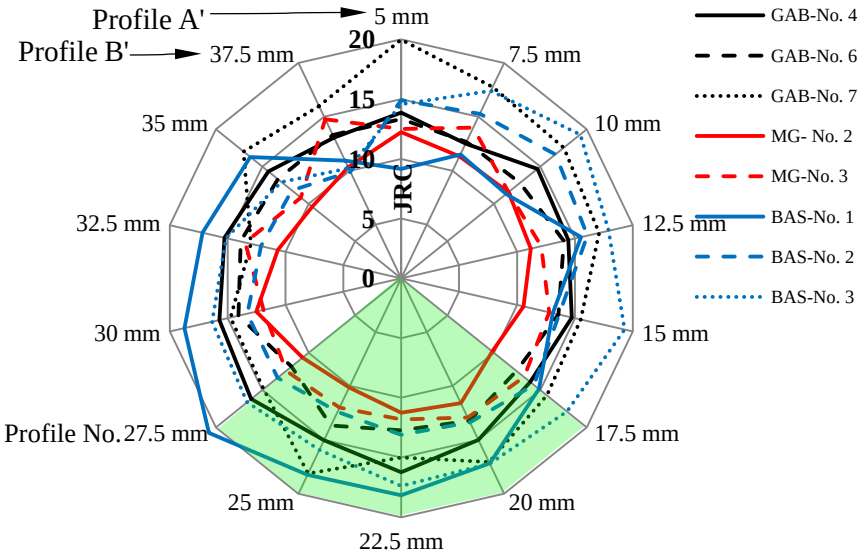

b)

Figure 3-13: Variation of the roughness in terms of the profiles direction for: (a) Profiles parallel to the loading axis –gabbro and microgabbro; (b) Profiles perpendicular to the loading axis-gabbro, microgabbro and basalt.

The roughness (*JRC*) of the profiles perpendicular to the loading direction was measured from Profile *A′* at the bottom of the specimens to Profile *B′* at the top of the specimens as shown in Figure 3-13b. The *JRC* variation shows an irregular elliptical shape for all perpendicular profiles.

This irregularity is reduced in the middle profiles, from 17.5 mm to 27.5 mm. The JRC_{max}/JRC_{min} ratio is different for each rock type, from 1.34 for gabbro to 1.33 for microgabbro and 1.94 for basalt.

3.6 **Fracture trajectory**

Several researchers investigated the fracture trajectory in rock samples based on the applied loads. Van de Steen et al. (2002) studied the crack path through grain boundaries, cleavage plane and fossil contents of rock materials by applying loading Mode I. The effect of loading rate on the fracture path was also studied by Roh (2000). The results indicated that the fracture trajectory in the cementitious material passed through the grain boundaries at low loading rate. It was also shown that the fracture passed sharply through the grains when the loading rate increased.

The objective of this part was to investigate the fracture trajectory through the matrix and crystals of the specimens subjected to the Modified Splitting Technique. Figure 3-14 shows an example of a gabbro specimen and its fracture trajectory. Gabbro is a dense and mafic intrusive igneous rock. From mineralogical point of view, gabbro contains pyroxene, plagioclase, and minor amounts of amphibole and olivine. To study the fracture trajectory of gabbro, two halves of the split specimen (by the Modified Splitting Technique) were glued together and the whole specimen was diametrically cut into three discs (Fig. 3-14a) along the length of the specimen. Figure 3-14b displays these three cuts in which the crystals of plagioclase were distinguished and highlighted (light rectangles). The red line (straight line) was along the loading axis that connected two loading points at the top and bottom of the specimen. This figure indicates how the fracture passes through the matrix and crystals in different regions of the sample. As can be seen, the fracture mainly passed through the matrix (predominantly pyroxene) and the tangent of the boundary of plagioclase crystals (points A). When fracture deviated from the loading axis and reached the plagioclase crystals, it inevitably passed through the crystals (points B). The latter phenomenon predominantly occurred in the mid-section of the cuts. Having a 90° cleavage in plagioclase created a stepwise breakage in the crystal when the fracture was forced to pass through it (Points C, the magnified portion of the setion).

3.7 Discussion

3.7.1 New 2D roughness profilometry method

A new simple 2D roughness profilommetry technique (2DRP) was introduced as an alternative method for characterizing 2D joint roughness. The results of this method were also validated with the ATOS II system. It was observed that the new technique's results correlated well with those obtained using ATOS II system. Although the 2DRP method is cheap and readily available, it is however time-consuming. A high level of skill is also needed for preparing the replica from the fracture surface if the fracture length is more than 100 mm. As a result, the measurement accuracy is affected by the length of the joint so that this technique can be used for a joint size of equal or less than 100 mm. Therefore, an alternative method should be used for longer fractures.

3.7.2 Loading modes and roughness parameter

The effect of different loading modes was investigated on three igneous rock types from coarse to fine-grained size (gabbro, microgabbro and basalt). The results of the Modified Splitting Method indicate that the roughness parameter was affected by both loading modes and grain size (rock type). As a result of combination of these influenced factors, different roughness variation was observed for these rocks. Since gabbro is a coarse-grained rock, the roughness parameters (i.e. JRC, Z_2, R_P, A_i) tended to decrease with the loading mode from the splitting to the triaxial with σ_3 = 8 MPa and then increased again when the confining stress reached to 13 MPa. Therefore, the fracture created by Modified Splitting Technique in gabbro specimens showed the highest roughness profiles. This trend was quite different for finer-grained rocks such as microgabbro and basalt. In these rock types, the JRC value decreased from splitting to the uniaxial and then increased when the loading mode changed to the triaxial compression with σ_3 = 3 MPa, then decreased as a result of increasing in the confining stresses to 13 MPa.

It is worth nothing that the results of this study are in good agreement with those obtained by Amitrano and Schmittbuhl (2002) and Seredin et al. (2013). In the former study, the effect of the confining stress on the roughness profiles was investigated in coarse-grained granite specimens. However, the effect of the grain size (rock type) was neglected.

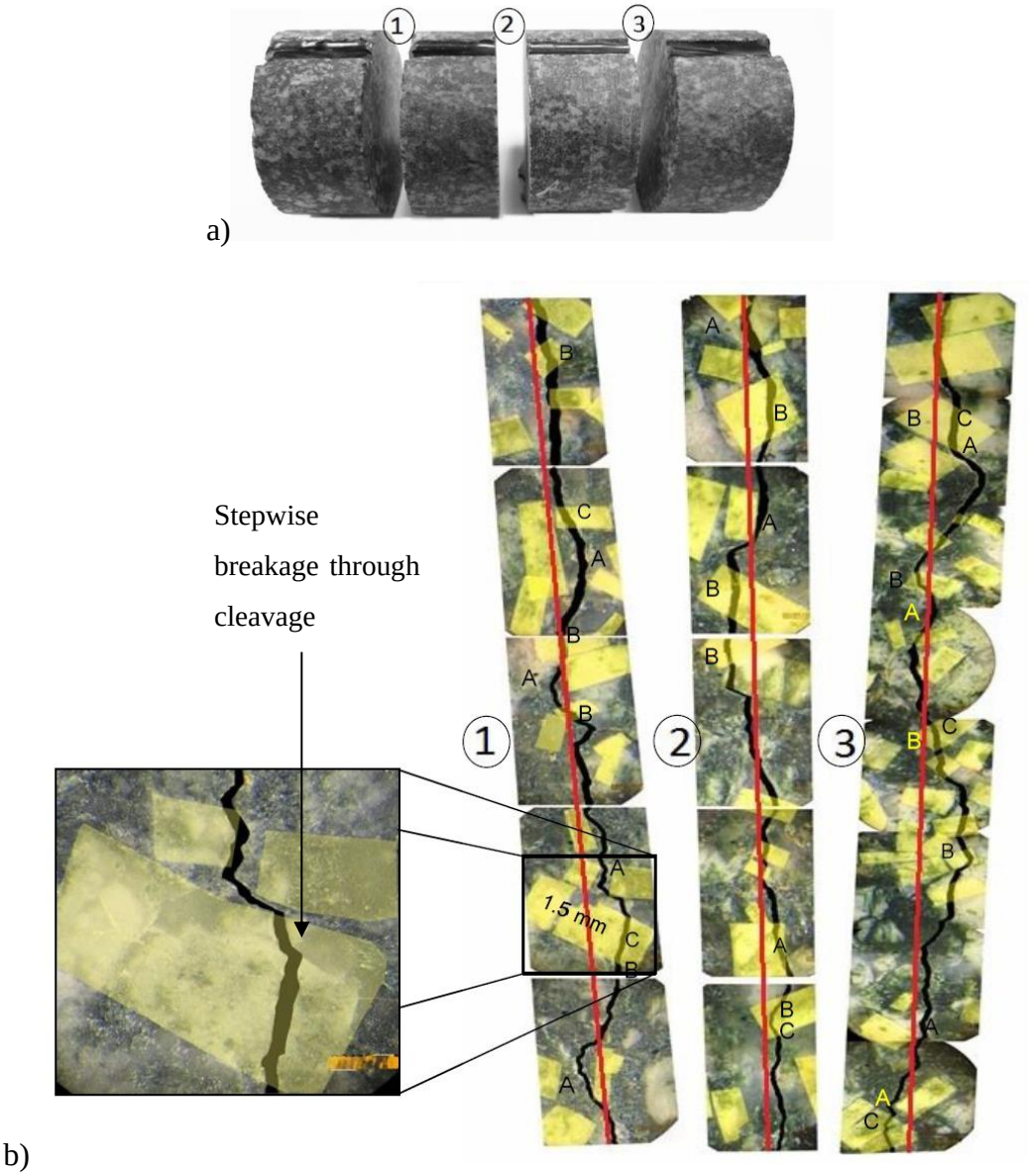

Figure 3-14: The fracture trajectory in the split specimen (gabbro).

Their results indicated that the roughness parameter initially decreased when the confinement stresses increased from 20 to 60 MPa, and then increased with an increase in the confining stress to 80 MPa. In the later study, Seredin et al. (2013) showed the effect of loading modes on the roughness parameter of rock-like materials. The outcomes of their study indicated that the roughness parameters decreased when the loading mode changed from tensile to uniaxial and triaxial. This discrepancy between the study of Seredin et al. (2013) and the current study can be attributed to the effect of the grain size (rock type) and mechanical properties of the specimens (rock-like material).

The results of fracture trajectory investigation confirmed that the coarse-grained formed roughness profiles with rougher unevenness compared to the fine-grained rocks. It was also observed that the number of the failure planes in the triaxial compression tests with 13 MPa confining stress was more than those created in lower confining stress. It can be inferred that the specimen might be destressed by forming minor failure planes before the major failure plane was created in triaxial compression with higher confining stress. Hence, the major failure plane might be less affected by the higher confining stress. As a result, the roughness parameter of failure plane obtained by confining stress at 13 MPa was higher than that obtained at 8 MPa. From microscopic point of view, two types of cracks, including tensile and shear might occur under compression. Shear cracks as secondary cracks generated in an acute angle along the crack orientation which was lower than the angle of tensile cracks. Furthermore, the ratio of shear/tensile cracks varied depending on the severity of loads. This ratio increased when the confining stress increased. It can be inferred that the shear cracks generated in lower angles were increased with the confining stress. This hypothesis is supported by the results of a study carried out by Xia and Zhou (2010) with PFC^{2D} for specimens under uniaxial and triaxial compression tests.

Also of note is that the roughness parameters in the current study were affected by a combination of loading mode and grain size that was not investigated in these researches. However, the question still remains as what is the influence of the confining stress on the roughness parameters. More microscopic studies should be conducted to realize the cracks initiation and propagation under loading condition. Computerized Tomography (CT) –as a new technology in the field of rock fracturing- could help a better understanding of fracture behaviour in further studies.

3.7.3 Effect of groove size on modified splitting results

In the current study, the Modified Splitting Technique was carried out on rock specimens to create pure tensile fractures (Mode I). The effect of the round bar and groove size on the tensile stress distribution along the axial diameter was studied using Phase^{2D} code (Rocscience, 2011). Mechanical properties of the rock and steel plates modelled in Phase^{2D} are summarized in Table 3.4. The diameter of the round bar was set to 1.5 times of the groove width, *b*. Figure 3-15 shows the stress distribution along the loading direction for three different groove sizes. This figure

indicates that the stress distribution tends to become fully tensile if the groove width increases from 1 to 3 mm. A small compressive zone can be seen close to the loading points when the groove size is smaller, i.e. 1 mm × 3 mm. Therefore, all modified splitting tests were conducted using a groove size of 3 mm × 3 mm.

Table 3.4: Mechanical properties required for Phase^{2D} models.

	Steel Plate	Rock sample
Unit weight (MN/m^3)	0.07	0.027
Young's Modulus (GPa)	200	65
Tensile Strength (MPa)	-	12
Friction Angles (Deg)	-	43

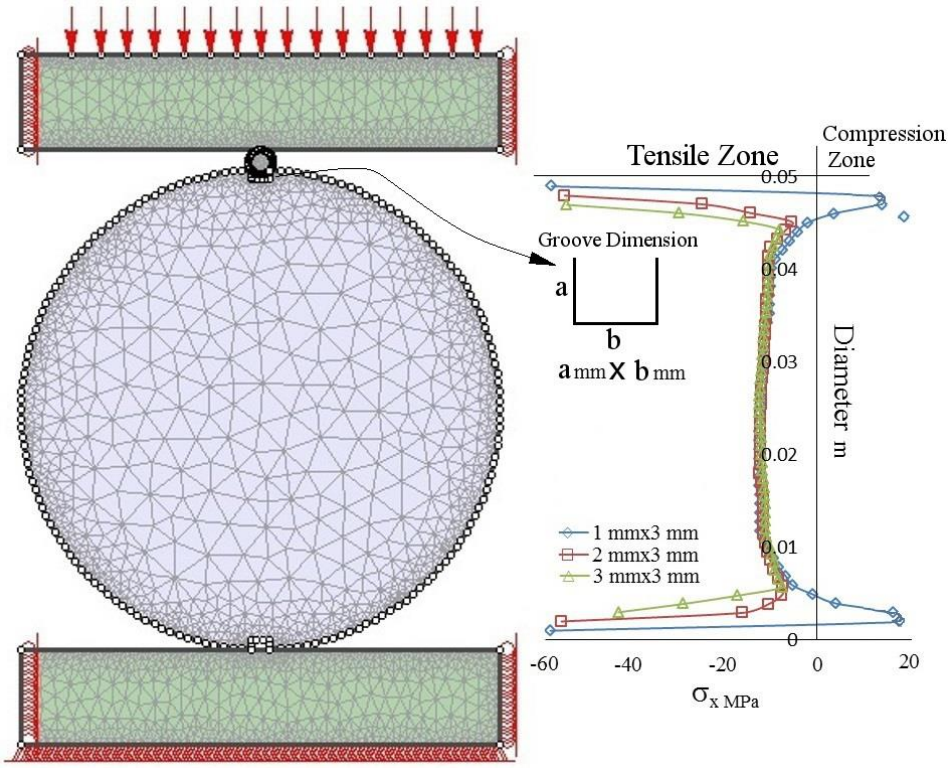

Figure 3-15: Tensile stress distribution obtained by the Modified Splitting Method with three different groove sizes (Phase^{2D}).

3.7.4 Loading direction in the modified splitting tests

The effect of loading direction on the roughness variation was also studied on the fractures created by the Modified Splitting Technique. The perpendicular and parallel profiles to the loading axis were considered for this purpose. The results indicate that the ratio of highest to

lowest *JRC* value of the profiles perpendicular to the loading axis was higher than those obtained for the profiles parallel to the loading axis. Furthermore, the roughness of profiles perpendicular to the loading axis showed almost uniform distribution with no considerable difference along the length of the specimens. This uniformity was not observed in the roughness profiles parallel to the loading axis (along the diameter length of the specimens). These results confirm that the roughness parameters can be significantly influenced by the loading direction.

The results further show that the *JRC* value of the profile was also affected by the distance from the loading points. The *JRC* values of the profiles in the vicinity of loading points were higher than those obtained from the middle portion of the specimens. This result is supported by the results obtained using Phase^{2D} models (Fig. 15) in which the tensile stress in the vicinity of the upper loading point (i.e. the groove with the round bar and size of 3 mm × 3 mm) is higher than that in the lower loading point. That is to say that when the axial loading is applied to the bar, the fracture initiates from the groove tip based on Mode I. This phenomenon also happens in the lower segment (a groove without the round bar) with a lesser intensity.

3.8 **Conclusion**

The main goal of the study presented here was to investigate the effect of loading modes on the fracture roughness created in different rock types. Based on the observations and analyses addressed in this paper, the major conclusion regarding to roughness parameters, loading modes and grain size of rock are as follows:

1- A new technique (2DRP) is proposed to characterize the roughness of the fracture surfaces. This method is simple, cheap and easily available for specimens less than 100 mm in length. It was shown that the results obtained by this method were in good agreement with those obtained using ATOS II system which employed a 3D profilometry technique.

2- The measured roughness parameters were affected by a combination of the loading modes and grain size of the rock. Fracture surfaces created by the Modified Splitting Technique (tensile fracture), uniaxial (both tensile and shear fractures) and triaxial (both tensile and shear fractures) can be classified as rougher, rough and smooth in gabbro samples, respectively. However, the results observed for microgabbro and basalt are quite different

than that in gabbro. In these rock types, the fracture created by the splitting test is rougher than that in the uniaxial, but not necessarily than that in the triaxial.

3- The roughness parameters decrease with an increase in the sampling interval in the rock types.
4- The roughness parameter generally decreases when the confining stress increases in triaxial compression test.
5- The roughness parameter of the fracture created using the Modified Splitting Technique is affected by the loading contact areas; the rougher are the portion of profiles located in the vicinity to the loading areas.
6- Variation of the *JRC* values in the roughness profiles parallel and perpendicular to the loading axis reveals the roughness anisotropy on the fracture surface. The *JRC* value in the profiles perpendicular to the loading axis is higher than that observed in the profiles parallels.

Acknowledgments

The authors would like to thank Professor G. Grasselli and Mr. B. Tatone at the University of Toronto for all their helps and supports in the scanning of the samples by ATOS II. The rock specimens were provided by Raglan mine (Glencore Group). This support is gratefully acknowledged.

Reference

Amitrano, D. and Schmittbuhl J. (2002). Fracture roughness and gouge distribution of a granite shear band. Journal of Geophysical Research: Solid Earth (1978–2012) 107(B12): ESE 19-11-ESE 19-16.

Aydan, Ö., Shimizu, Y. and Kawamoto, T. (1996). The anisotropy of surface morphology characteristics of rock discontinuities. Rock mechanics and rock engineering 29(1): 47-59.

Barton N.R. (1972). A model study of rock joint deformation Int. J. Rock Mech., 9, pp. 579–602

Barton, N. and Choubey V. (1977). The shear strength of rock joints in theory and practice. Rock mechanics 10(1-2): 1-54.

Beer, A., Stead, D. and Coggan, J.C. (2002). Technical note estimation of the joint roughness coefficient (JRC) by visual comparison. Rock mechanics and rock engineering 35(1): 65-74.

Belem, T., Homand-Etienne, F. and Souley, Ms. (2000). Quantitative parameters for rock joint surface roughness. Rock mechanics and rock engineering 33(4): 217-242.

Bendat J. S. and Piersol A. G. Random Data Analysis and Measurement Procedures, Wiley Interscience, Toronto (1971).

Bistacchi A., Griffith W.A., Smith S.A., Di Toro G., Jones R., and Nielsen S., 2011. Fault Roughness at Seismogenic Depths from LIDAR and Photogrammetric Analysis. Pure and Applied Geophysics, 168 (12), 2345-2363. doi: 10.1007/s00024-011-0301-7.

Bobet, A. and Einstein H. (1998). Fracture coalescence in rock-type materials under uniaxial and biaxial compression. International Journal of Rock Mechanics and Mining Sciences 35(7): 863-888.

Brady B. H. G. and Brown E. T. (1985). Rock Mechanics for Underground Mining, 1st Edn. Allen & Unwin, London.

El-Soudani, S. (1978). Profilometric analysis of fractures. Metallography 11(3): 247-336.

Fairhurst, C. (1964). On the validity of the 'Brazilian' test for brittle materials. International Journal of Rock Mechanics and Mining Sciences & Geomechanics Abstracts, Elsevier.

Fedorov S. (2013). Get Data Graph Digitizer.

Grasselli G. (2001). Shear strength of rock joints based on quantified surface description, Ph.D. thesis. Lausanne, Switzerland: Swiss Federal Institute of Technology (EPFL).

Hong, E. S., Lee, J-S. and Lee, I-M. (2008). Underestimation of roughness in rough rock joints. International journal for numerical and analytical methods in geomechanics 32(11): 1385-1403.

Jang H-S., K. S.-S., Jang B-A. (2014). Determination of joint roughness coefficient using roughness parameters. Rock Mech. Rock Eng. Online published on January 2014.

Kabeya K.K., Legge T.F.H. (1997). Relationship between grain size and some surface roughness parameters of rock joints. International Journal of Rock Mechanics and Mining Sciences 34(3-4): p. 146.

Kim, D.-Y. and Lee H.-S. (2009). Quantification of rock joint roughness and development of analyzing system. Proceedings of the international conference on rock joints & jointed rock masses, Tucson.

Kulatilake P.H.S.W., Shou G., Huang T.H., Morgan R.M. (1995). New peak shear strength criteria for anisotropic rock joints. Int J Rock Mech Min Sci Geomech Abstr, 32, pp. 673–697.

Kulatilake, P. H. S. W., Balasingam, P., Park, J., & Morgan, R. (2006). Natural rock joint roughness quantification through fractal techniques.Geotechnical & Geological Engineering, 24(5), 1181-1202.

Maerz, N., Franklin, J.A. and Bennett, C.P. (1990). Joint roughness measurement using shadow profilometry. International Journal of Rock Mechanics and Mining Sciences & Geomechanics Abstracts, Vol. 27, No. 5, pp. 329-343.

Mattis P. and Kimball S. (2013). GIMP 2.8

Myers, N. (1962). Characterization of surface roughness. Wear 5(3): 182-189.

Odling, N. (1994). Natural fracture profiles, fractal dimension and joint roughness coefficients. Rock mechanics and rock engineering 27(3): 135-153.

Otoo, J. N., Maerz, N. H., Duan, Y., & Xiaoling, L. (2011, January). LiDAR and optical imaging for 3-D fracture orientations. In 2011 NSF Engineering Research and Innovation Conference, Atlanta, Georgia.

Poon, C., Sayles, R.S and Jones, T.A. (1992). Surface measurement and fractal characterization of naturally fractured rocks. Journal of Physics D: Applied Physics 25(8): 1269.

Roh, Y.-S. (2000). Roughness characterization in the fracture of cementitious material. Ann Arbor, University of Colorado at Boulder.

Sayles R. S. and Thomas T. R. A Stochastic explanation of some structural properties of a ground surface. Int. J. Production Research 14, 641 (1976).

Seredin, V., Leibovich, L.O, Pushkareva, M.V., Kopylov, I.S. and Khrulev, A.S. (2013). Evolution of fracture surface morphology in rocks. Journal of Mining Science 49(3): 409-412.

Seidel, J. P., & Haberfield, C. M. (1995). Towards an understanding of joint roughness. Rock Mechanics and Rock Engineering, 28(2), 69-92.

Tang, C. and Kou S. (1998). Crack propagation and coalescence in brittle materials under compression. Engineering Fracture Mechanics 61(3): 311-324.

Tatone, B. S. and Grasselli G. (2009). A method to evaluate the three-dimensional roughness of fracture surfaces in brittle geomaterials. Review of Scientific Instruments 80(12): 125110.

Tatone, B. S. and Grasselli G. (2010). A new 2D discontinuity roughness parameter and its correlation with JRC. International Journal of Rock Mechanics and Mining Sciences 47(8): 1391-1400.

Tatone, B. S. and Grasselli G. (2013). An investigation of discontinuity roughness scale dependency using high-resolution surface measurements. Rock mechanics and rock engineering 46(4): 657-681.

Tse, R. and Cruden D. (1979). Estimating joint roughness coefficients. International journal of rock mechanics and mining sciences & geomechanics abstracts, Vol. 16, pp. 303-307.

Van de Steen B., Vervoort A., Sahin K. (2002). Influence of internal structure of crinoidal limestone on fracture paths. Engineering Geology 67(1): 109-125.

Xia, M. and Zhou K.-p. (2010). Particle simulation of the failure process of brittle rock under triaxial compression. International Journal of Minerals, Metallurgy, and Materials 17(5): 507-513.

Yang, Z., Lo, S.C. and Di, C.C. (2001). Reassessing the joint roughness coefficient (JRC) estimation using Z_2. Rock mechanics and rock engineering 34(3): 243-251.

Yu, X. and Vayssade B. (1991). Joint profiles and their roughness parameters. International journal of rock mechanics and mining sciences & geomechanics abstracts, Vol. 28, NO. 4, pp. 333-336.

Zhou, H. W., & Xie, H. (2003). Direct estimation of the fractal dimensions of a fracture surface of rock. Surface Review and Letters, 10(05), 751-762.

CHAPTER 4 ARTICLE 2: THE SHAPE EFFECT ON THE MORPHOLOGY OF THE FRACTURE SURFACE INDUCED BY THE BRAZILIAN TEST

Arash Khosravi, Richard Simon, and Patrice Rivard

This article was submitted to International Journal of Rock Mechanics and Mining Sciences in Feb. 2016, under revision following comments from reviewers.

Abstract: This paper presents a study on the effect of tensile stress distribution on the roughness of the fracture profile created by Brazilian tests on three rock types with different length to diameter (L/D) ratios. The roughness profiles were investigated in two directions: parallel and perpendicular to the loading axis. The results show that the roughness of the profiles perpendicular to the loading axis increases when the L/D ratio increases in all rock types. Furthermore, it was observed that the roughness of the profiles parallel to the loading axis decreases with an increase in the L/D ratio. This paper also shows the anisotropy of stress distribution along the length of the samples with different L/D ratios. Some of the implications and limitations of this investigation are also discussed.

Keywords

Roughness, Brazilian, Failure mode, Length-to-diameter ratio, Loading direction

4.1 Introduction

Fractures are one of the most important features affecting mechanical behaviour of rock masses. The degree of fracturing in a rock mass can be influenced by several factors: in situ stress, boundary conditions and geological history. Fractures are the main factor that must be taken into consideration in the control of thermo-hydro-mechanical behaviours. Two important physical characteristics of fracture that are used in rock mass classification systems are: the aperture and the roughness. Many studies have been conducted on these two components to show their relation with the mechanical behaviour (e.g. Barton and Quadros, 1997; Sharifzadeh et al., 2008; and Tatone and Grasselli, 2012). In applied rock mechanics, the shear strength of discontinuities is one of the most important parameter for stability analyses. To estimate the shear strength, the

surface roughness can be taken into account to model the shear behaviour of fractures (e.g. Barton, 1976; Kulatilake et al., 1995; Grasselli, 2001).

Fracture roughness has been quantitatively characterized based on morphological approaches, such as empirical (Barton and Choubey, 1977), statistical (Reeves, 1985; Maerz et al., 1990) and fractal approaches (Seidel and Haberfield, 1995; Zhou and Xie, 2003; Babadagli and Develi, 2003). Each of these approaches uses parameters that quantify the fracture topography. Among them, empirical approaches are the most commonly used in rock mechanics. The Joint Roughness Coefficient (JRC) –as an empirical approach- is a widely used roughness parameter (Barton 1973). Since JRC is a subjective parameter that is estimated by comparing the roughness profile with ten standard roughness profiles (ISRM 1978), relationships have been proposed between the JRC value and various roughness parameters used in statistical approaches. These relations quantitatively express the roughness parameters (Tse and Cruden, 1979; Yu and Vayssade, 1991; Yang et al., 2001; Kim and Lee, 2009; Tatone and Grasselli, 2010; Jang et al., 2014).

Brady and Brown (1985) showed that fractures occur in three conditions or modes: shear, tensile or a combination of both. Mode I defines the fracture created in tension, while Mode II and III are the fractures induced by both tensile and shear stresses (Mode II as in-plane shear and Mode III as out of plane tear, Fig. 4-1). These fracture modes can be created in laboratory using direct or indirect tensile, uniaxial and triaxial compression tests. The fracture surface induced by an indirect tension test (Brazilian test) is created in Mode I.

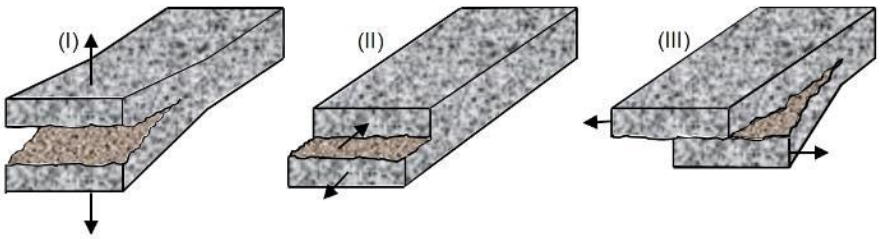

Figure 4-1: Loading and displacement modes of fractures: (I) tensile opening; (II) in-plane shear; (III) out-of-plane tearing (Modified from Brady and Brown 1985).

There are many experimental and numerical studies for the stress and strain distribution in the samples split by Brazilian tests (Hondros, 1959; Fairhurst, 1964; ASTM, 1984; ISRM, 1978; Wang et al., 2004; Markides et al., 2012; Erarslan et al., 2012; Li and Wang, 2013). More

recently, several investigations have been conducted on the cracking patterns of foliated and pre-notched samples with different arrays (Chen et al., 1998; Al-Shayea, 2005; Tavallali et al., 2007; Tavallali and Vervoort, 2010; Ghazvinian et al., 2013; Vervoort et al., 2014). Stirling et al. (2013) performed Brazilian tests based on ASTM, ISRM and Flattened loading methods and identified the location of crack initiation and fracture patterns. They showed that the onset location of cracking is clearly at the center; however, the crack propagation could not be captured by Digital Image Correlation (DIC) in these tests.

Apart from the ultimate stress applied on samples submitted to Brazilian tests of different L/D ratio, the strain variation along the loading direction was also investigated by Stirling et al. (2013). Accordingly, the degree of the deformation perpendicular to the loading axis increases across the diameter as L/D ratio decreases. This may be due to the confinement induced by the length of the specimen. The results of this study showed that the effect of the strain distribution in terms of the L/D ratio is more tangible on the fracture surface along the loading direction.

To date however, little work has been done on the relationship between the fracture roughness and loading modes. Seredin et al. (2013) also conducted laboratory tests on rocklike material to create fractures in different modes. The results of this study showed a variation of roughness in fractures created by different loading modes. This investigation indicated that the roughness of the fracture created using uniaxial tension is higher than those created using other loading modes. They also concluded that the roughness decreases when the confining pressure (in triaxial mode) increases.

Khosravi et al. (2014) also investigated the influence of the fracture modes on the roughness by conducting splitting, uniaxial and triaxial compression tests on gabbro. The observed results were in good agreement with the results obtained by Seredin et al. (2013). However, in this case, the roughness obtained using splitting test was higher than those obtained from other loading modes. Figure 4-2 shows the schematic view of the splitting test and the results obtained using different loading modes.

Feng et al. (2014) carried out an investigation on the fracture surface morphology obtained from Brazilian tests on granite samples with a L/D ratio of 0.4. Three fracture roughness profiles were selected parallel to the loading axis. The results showed that the three segments (s1, s2 and s3) along the profiles (with 60% overlap) do not have identical roughness parameters (Fig. 4-3).

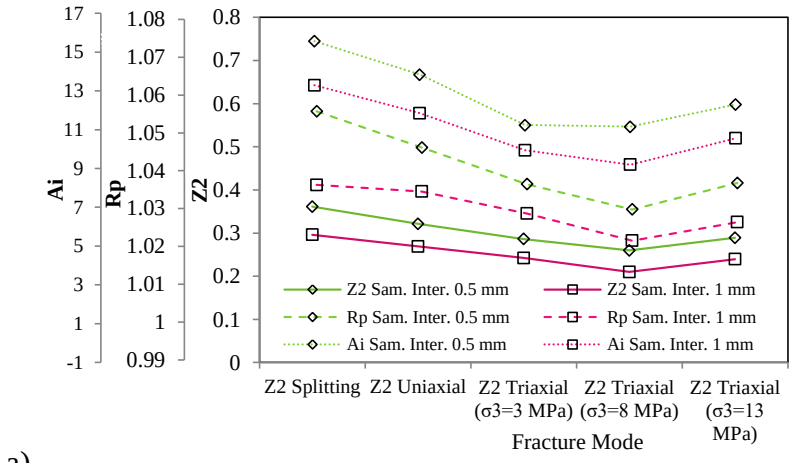

a)

b)

Figure 4-2: a) Roughness of the fracture obtained from different loading modes on Gabbro samples (Khosravi et al. 2014); b) Cylindrical sample with notches and round bar on the top.

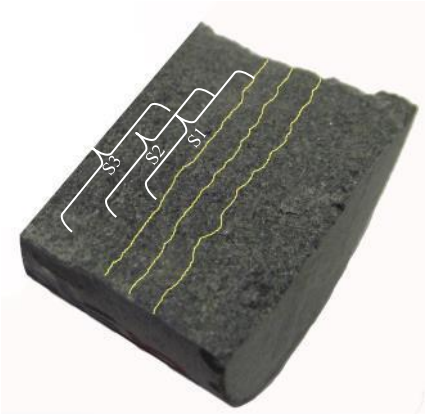

Figure 4-3: Schematic diagram of roughness profiles and three overlapped sections (after Feng et al. 2014).

A similar study was conducted by Khosravi and Simon (2014) on tensile induced fractures in gabbro samples. Different roughness profiles parallel to the loading axis were selected. The

results indicated that the roughness parameters calculated for three non-overlapping segments were not similar. Khosravi and Simon (2015) also investigated the roughness profile of the fractures created using Brazilian tests on the samples with different L/D ratio. The results showed that the roughness of the profiles parallel to the loading axis decreases when the L/D ratio increases (Fig. 4-4).

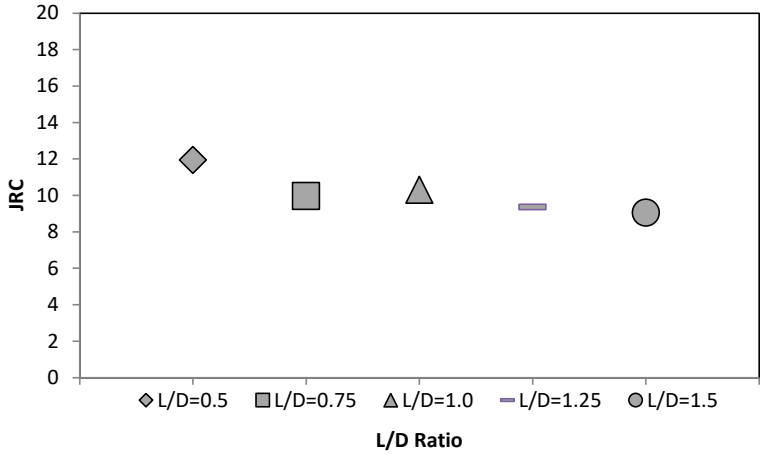

Figure 4-4:Variation of the JRC value with L/D ratio obtained from the parallel roughness profiles in gabbro sample (Khosravi and Simon, 2015).

In this paper, the roughness parameter (JRC) of the tensile fracture surfaces induced by Brazilian test was studied considering the loading direction and the size and rock type of the samples. The variation of roughness parameters along the roughness profiles parallel and perpendicular to the loading axis was investigated for different rock types. The results illustrate how the shape and loading direction of the samples can affect the fracture roughness. The roughness variation of three rock types with different grain sizes is also compared.

4.2 **Methodology and experimental procedure**

This study comprised of four steps including: (1) Samples with different L/D ratios were subjected to Brazilian tests. A total of 5 samples were tested for each L/D ratio; (2) At least 2-3 non-damaged fracture surfaces were scanned using a 3D laser scanner to evaluate the roughness profiles in the direction parallel and perpendicular to the loading axis.; (3) The root mean square (RMS) of the first derivative of the roughness profiles was calculated using approach proposed by Myers (1962); and (4) The variation of the roughness parameter was studied for each induced fracture surface with respect to the loading direction and the size of the specimens.

4.2.1 Specimen type and Size

This study was carried out on three rock types: gabbro, microgabbro and basalt. The gabbro tested was a coarse-grained rock with a grain size ranging from 1-5 mm. Half of the gabbro samples mainly contained pyroxene (mainly clinopyroxene) and olivine as dark-coloured minerals and the other half of the samples contained grey-coloured plagioclase feldspar (up to 90%) in the form of rectangular crystals. Less than 5% of the gabbro was composed of quartz. The microgabbro tested was a plutonic intrusive igneous rock with intermediate sized grains ranging between 0.5-1.0 mm. The crystals in the microgabbro were smaller than those of the gabbro and were formed in an environment in which the magma cooled faster. It was composed of plagioclase crystals (≈ 60%), clinopyroxene (≈ 30%) and olivine (≈ 10%). The basalt tested was a fine-grained igneous (volcanic) rock mainly containing olivine, plagioclase and pyroxene with grain sizes ranging from approximately 0.3-0.5 mm. Olivine was a significant constituent in this basalt, which made the color greenish. Some other secondary minerals were found, such as calcite, quartz and chlorite. In summary, the gabbro, microgabbro and basalt samples were relatively similar in chemical composition but differed in grain sizes.

For this study, Brazilian tests were conducted on cylindrical NQ rock samples and different lengths (i.e., 23.75, 35.6, 47.5, 59.4 and 71.25 mm). A total of 89 specimens were prepared for Brazilian tests.

4.2.2 Brazilian tests

To study the effect of sample shape on the roughness parameters, Brazilian tests were conducted on 89 NQ sized specimens (47.5 mm diameter) using a Tinius Olsen testing machine with the capacity of 200 tons at the Rock Mechanics Laboratory, at the University of École Polytechnique de Montréal (Fig. 4-5). In this study, all tests were carried out based on ASTM (1984) method by applying a line load induced by two flat platens and two cardboard cushions between the sample and platens. At least 5 samples were loaded for each L/D ratio using a loading rate of 0.3 MPa/s.

Figure 4-5: Testing machine Tinius Olsen 200 tons at École Polytechnique de Montréal.

Figure 4-6 shows some of the split samples with different L/D ratios after the Brazilian tests. It should be noted that only 41 samples with undamaged surface were obtained after the Brazilian tests. Therefore, the L/D ratios of microgabbro samples were limited to 0.5, 0.75, and 1.0 due to sample availability and damaged samples.

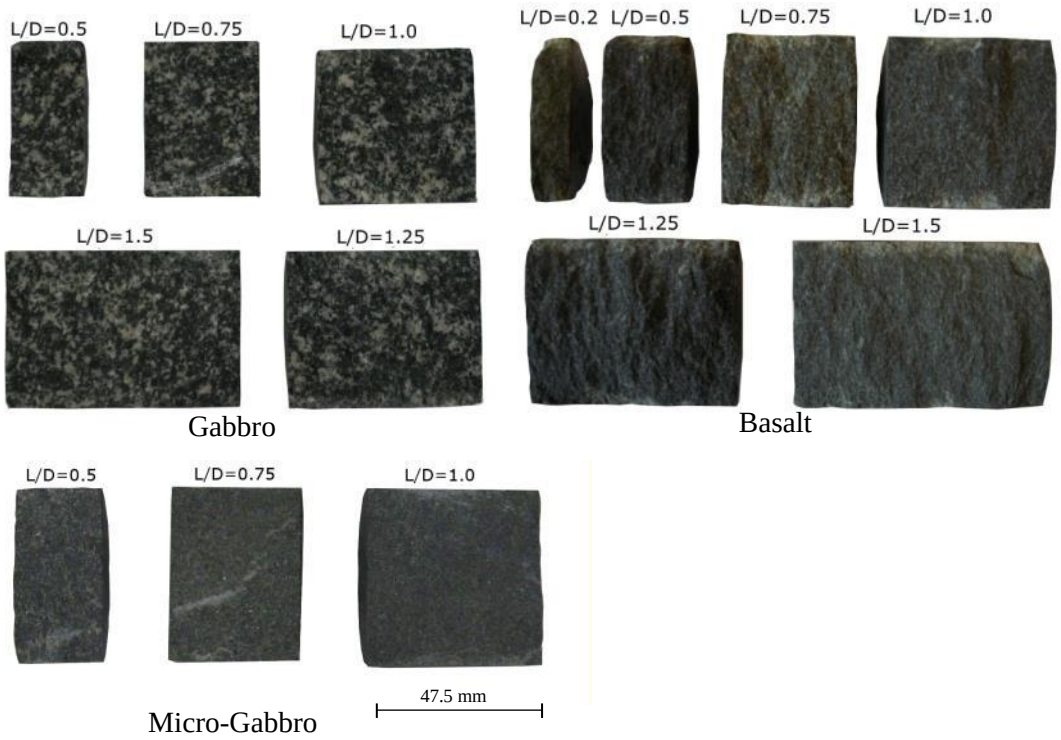

Figure 4-6: Specimens with variety of L/D ratios split by the Brazilian test.

Figure 4-7 shows the average ultimate loads and stresses in terms of L/D ratio. A linear trend of the ultimate load can be seen for the samples with different L/D ratios when the L/D ratio ≤ 1.0. The results also show an increase in the tensile strength from gabbro (coarse grained) to basalt (fine grained) by up to 1.4 times for L/D of 1.0. It can be seen that the tension stress and the ultimate load in microgabbro are approximately 10% less than those obtained for basalt for L/D ratio equal to 1 which can be due to the similarity of the grain size.

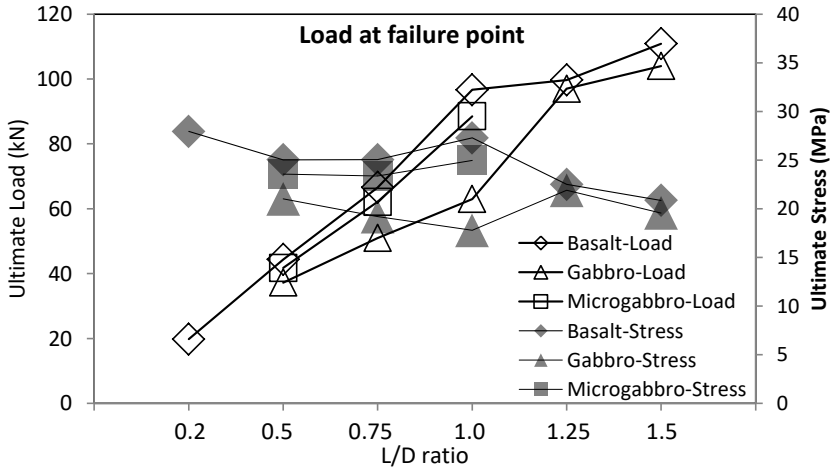

Figure 4-7: Variation of average ultimate loads and stresses at failure point with L/D ratio in three rock types.

4.2.3 Equipment

In this study, a laser profilometer (Kreon Zephyr© 25) was used to obtain 3D coordinates of the fracture surfaces (Fig. 4-8). The maximum resolution of this scanner was 72 μm for the x and y axes, and 16 μm in the z axis. The fracture surfaces were scanned after each Brazilian test. A high data density can be obtained using the profilometer in the form of a cloud of points. In this study, about 10,000,000 points for each sample were scanned and reduced by gridding to obtain the roughness parameters. The sampling interval of 0.1 mm (distance a data-point to the adjacent point) was taken into account in gridding the cloud of points.

Figure 4-8: 3D laser profilommeter used for this study.

4.2.4 Roughness characterization

This part of the study focused on the roughness characterization of the induced tensile fractures created in Brazilian tests. In most of the split samples, one half of the split sample was affected by a secondary fracture in the compression zone at the loading area(s). The other half was usually undamaged. Based on the cracking pattern and the degree of damage, about 2 or 3 specimens for each L/D ratio were selected after the Brazilian tests, so that the fracture surfaces did not include debris and secondary fractures. The results were obtained from two halves of the fracture that were entirely matched. For example, over 6-7 basalt samples were split with a L/D ratio equal to 1.5 to obtain 1-2 undamaged fracture surfaces. The selected fracture surfaces were scanned with the 3D laser profilometer with a sampling interval of 0.1 mm to obtain roughness profiles parallel and perpendicular to the loading axis as shown in Figure 4-9. The distance between two adjacent profiles was scanned with a spacing of 0.1 mm, but a distance of 0.5 mm is used here due to large volume of data points. The total number of roughness profiles obtained using the profilometer is summarized in Table 4.1.

4.2.5 Joint roughness parametrization

It is well known that the shear strength of a rock joint depends on its roughness. Joint roughness parameters determinations can be classified into three categories: statistical, empirical and fractal. Statistical roughness parameters are defined based on two approaches: roughness amplitude and slope. The JRC (Barton and Choubey, 1977) -as a statistical parameter- is the most widely used

empirical roughness parameter in applied rock mechanics using subjective visual estimation which can be erroneous. Furthermore, a rough surface can be quantitatively described in terms of the concept of fractal geometry.

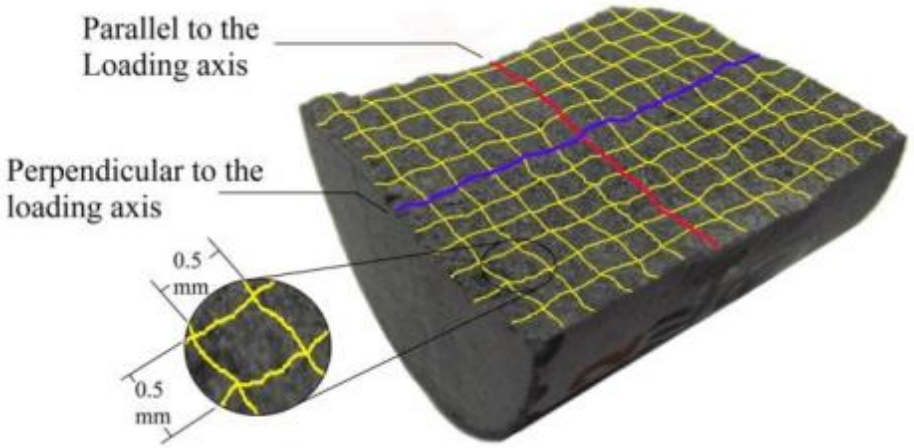

Figure 4-9: Roughness profiles parallel and perpendicular to the loading axis.

Table 4.1: Summary of total number of roughness profiles obtained with profilommeter.

L/D ratio	Number of roughness profiles		Total number of profiles	Sampling intervals (mm)
	Perpendicular to the loading axis	Parallel to the loading axis		
0.2	47	9	3430	0.5
0.5	47	22		
0.75	47	34		
1	47	45		
1.25	47	57		
1.5	47	68		

To reduce the error in determining the JRC value, which may give rise to an overestimation of the joint shear strength (Tse and Cruden, 1979; Beer et al., 2002), statistical parameters have been used for the past four decades. The most widely used statistical roughness parameters in the field of rock mechanics are: Root Mean Square (*RMS*), *RMS* of the first derivative of the profile height (Z_2) (Mayers, 1962), Structure function value (Sayles and Thomas, 1977) and Roughness profile index (R_p) (El-Soudani, 1978).

In this study, the roughness parameter Z_2 was calculated for all 2D profiles perpendicular and parallel to the loading axis. Although Z_2 is limited to the sampling span of the data point, one particular sampling span for all roughness profiles was considered to avoid any discrepancies in the results. For a 2D profile, Z_2 is given by:

$$Z_2 = \frac{1}{L}\int_{x=0}^{x=L}\left(\frac{dy}{dx}\right)^2 \approx \frac{1}{M(Dx)^2}\sum_{i=1}^{M}\left(y_{i+1} - y_i\right)^2 \qquad (1)$$

Where L is the length of the roughness profile, Dx and $y_{i+1} - y_i$ are adjacent points distance on x- and y-coordinates, respectively. M is the number of straight line segments connecting the adjacent points to form the profile. The joint roughness is used in several rock mass classification systems (i.e., RMR, GSI, and Q) or in shear strength criteria (Bieniawski, 1989; Hoek et al., 1995; Barton et al., 1974). JRC is one of the parameters used in the Barton-Bandis shear strength criterion (Barton and Choubey, 1977; Barton and Bandis, 1990) to estimate discontinuity shear strength in engineering practice. Many researchers proposed correlations between JRC and the Z_2 values for two sampling spans of 0.5 mm and 1 mm as summarized in Table 4.2. A good correlation can be seen between these two parameters.

Table 4.2:Correlation between *JRC* and Z_2.

Author	Relationship	Sampling Span	R^2
Tse and Cruden [1979]	$JRC = 32.2 + 32.47 \log Z_2$	1.27 mm	0.986
Yu and Vayssade [1991]	$JRC = 61.79\, Z_2 - 3.47$	0.5 mm	0.973
	$JRC = 64.22\, Z_2 - 2.31$	1 mm	0.983
Yang et al. [2001]	$JRC = 32.69 + 32.98 \log Z_2$	0.5 mm	0.993
Kim and Lee [2009]	$JRC = 63.4351\, Z_2 - 2.10976$	1 mm	0.974
Tatone and Grasselli [2010]	$JRC = 51.85\, {Z_2}^{0.60} - 10.37$	0.5 mm	0.96
	$JRC = 55.03\, {Z_2}^{0.74} - 6.10$	1 mm	0.977
Jang et al.[2014]	$JRC = 51.16\, {Z_2}^{0.531} - 11.44$	0.5 mm	0.972

In this study, JRC was calculated for each profile based the equation proposed by Tatone and Grasselli (2010) with an interval span of 0.5 mm to maximize the influence of measurement resolution. This equation is based on the realignment of the 10 standard JRC profiles to their best fit lines.

4.3 **Results**

4.3.1 Fracturing patterns in terms of L/D ratio

The fracture pattern was studied in the samples of different lengths (shape effect). A total number of 89 Brazilian tests were carried out in this study. Figure 4-10a indicates two fracture types,

including tensile (primary) and shear/tensile (secondary) fractures observed in the split samples. The notch (secondary fracture) is a fracture created in both shear and tension (primarily shear). These notches occur during and after the main tensile fracturing parallel to the primary fractures due to compression at the loading area(s).

Figure 4-10b shows the fracture patterns of three rock types with different L/D ratios after each test. The V or U shape fractures can be observed as a result of asymmetrical notches (secondary fractures) at the top and/or bottom of the split samples. These secondary fractures are connected to the primary (tensile) fractures at right and acute angles creating wedges as shown in Figure 4-10b. It can be seen that the specimen length influences the size of these wedges. For gabbro and microgabbro, the size of the wedge induced by the compression zone near the loading plate increases with an increasing L/D ratio. It should be noted that the wedge sizes are not the same at both end surfaces of the specimen. In some samples, the wedge occurs in only one end surface, specifically in the specimens with a L/D ratio > 1.0 as shown in Figure 4-11.

4.3.2 Variation of the fracture surface morphology

The fracture surface morphology was also investigated for the split samples by Brazilian test. For this purpose, the roughness variation was studied for the profiles parallel and perpendicular to the loading axis (Figure 4-9). The roughness parameters (Z_2, JRC) were calculated using the method described in section 2.5 for all the profiles. The distance between the roughness profiles was 0.5 mm.

a)

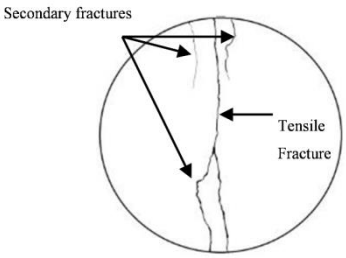

b)

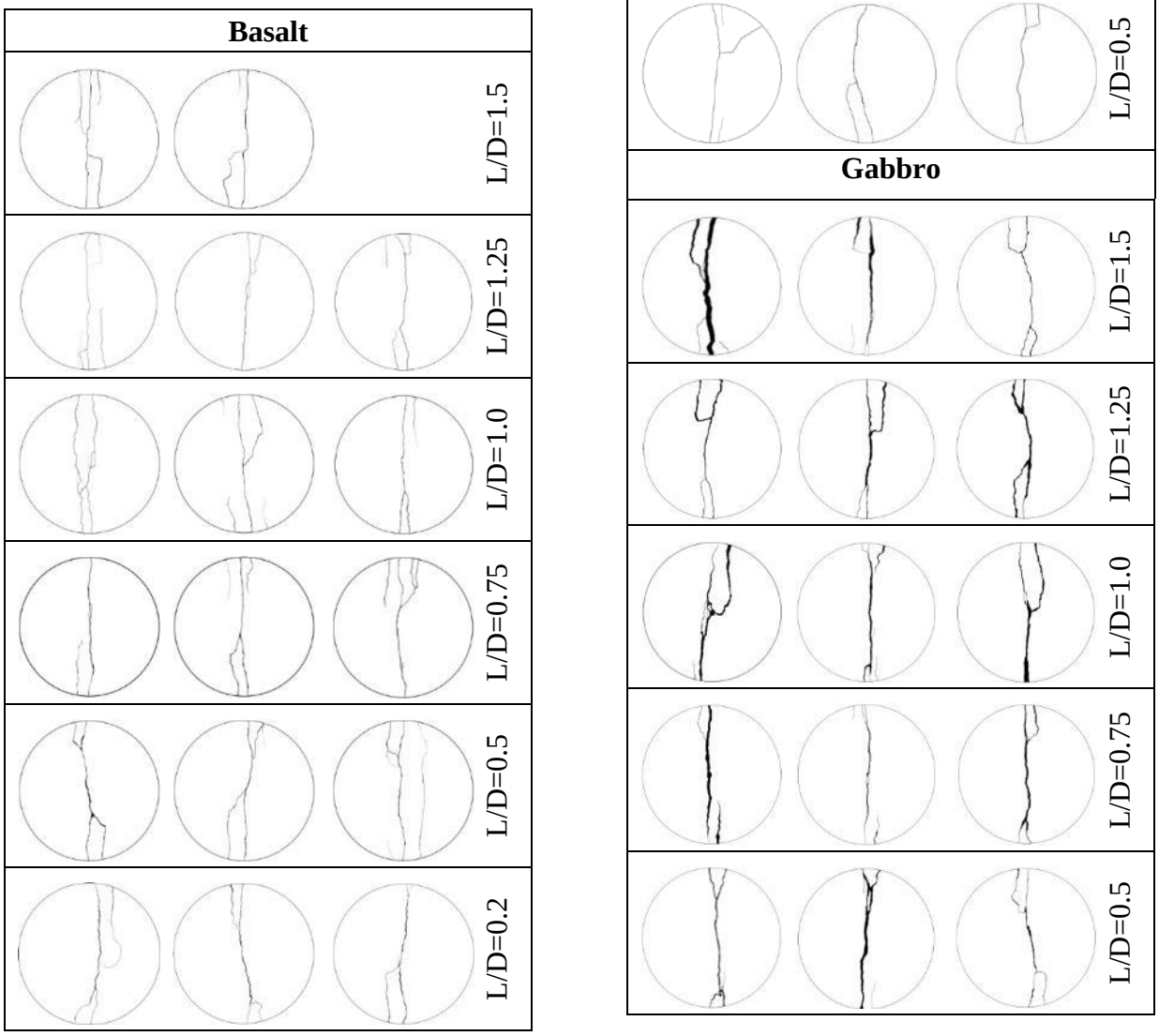

Figure 4-10: a) Fracture types observed in the split samples; b) Fracture pattern of the three rock types with different L/D ratios.

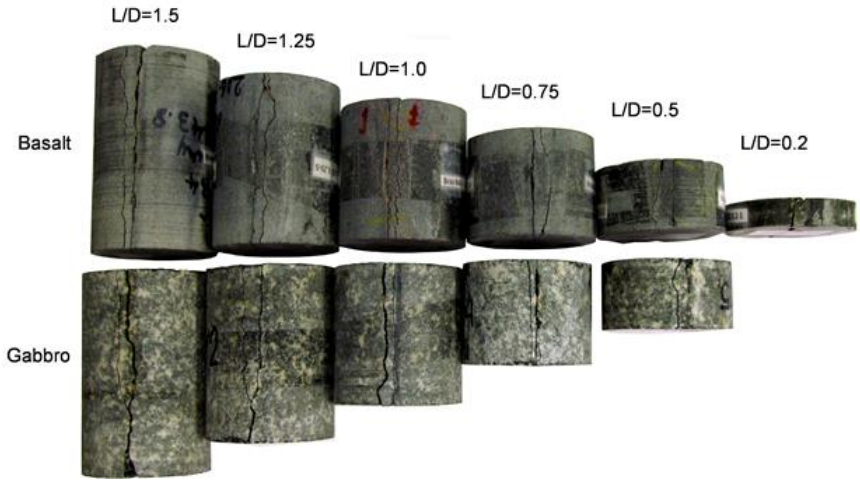

Figure 4-11: The size of wedge along the length of the specimens (gabbro and basalt).

4.3.2.1 Roughness profiles parallel to the loading axis

Roughness profiles parallel to the loading axis have almost the same length for all L/D ratios. The length of these profiles is slightly shorter than the sample diameter to avoid the effect of the compression zones induced by loading points on the roughness profiles. Roughness profiles were selected with an interval span of 0.5 mm between two adjacent data points. Figure 4-12 shows the variation of the roughness parameter parallel to the loading axis in the specimens with different L/D ratios. The results indicate that the roughness scattering in basalt is more than that in other rock types in terms of L/D ratio (Fig. 4-12c). For instance, the difference between the minimum and maximum JRC, associated with a L/D ratio equal to 1.0, is approximately 12 in basalt, while this difference is about 8.5 for microgabbro and 11 for gabbro. It can be seen that the scattering of the JRC values in microgabbro is less than that observed in the other rock types. Moreover, no typical trend or behaviour is observed for the JRC values when the L/D ratio changes.

Based on Yu et al. (2006) results, roughness profiles at mid-length of samples are influenced by a homogeneous stress distribution. Therefore, one third of the roughness profiles were selected at the mid-length of each sample (Figure 4-13) to demonstrate the trend of JRC variation in three rock types in terms of L/D ratios.

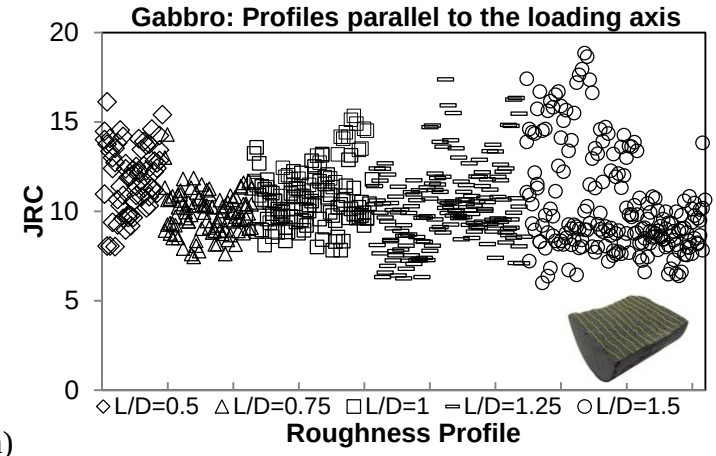

a)

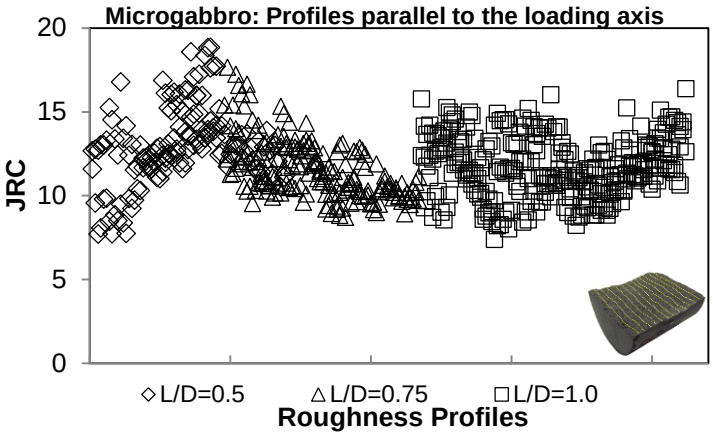

b)

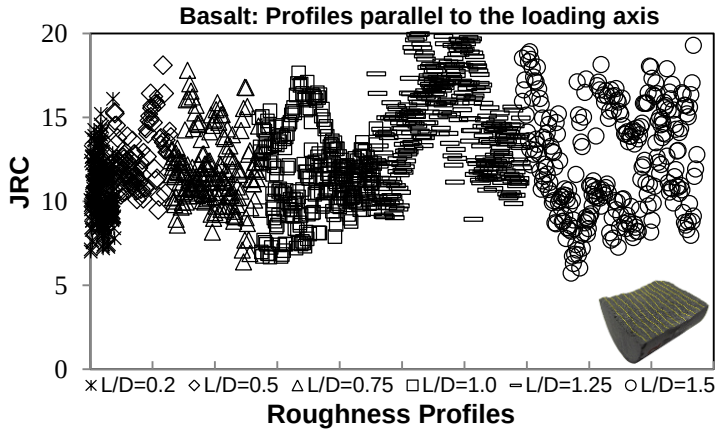

c)

Figure 4-12: Variation of the roughness in the profiles parallel to the loading direction with L/D ratio.

Figure 4-14 shows the JRC values calculated at mid-length of the samples. It is seen that the average JRC value decreased with increasing L/D ratio in gabbro by up to 20% (from 11.42 to

9.18) and microgabbro by up to 5% (from 12.3 to 11.7) (Fig 4-14a, b), while the roughness of basalt increased slightly with an increase of L/D ratio from L/D = 0.2 to 1.25, and then decreases when L/D ≥ 1.25 (Fig. 4-14c). The roughness variance for gabbro was in the range of 1.12 to 2.58 and for microgabbro, it was between 0.62 and 2.63. For basalt samples, the variance was between 1.43 and 13.37, which was much higher than the variance calculated for the other two rock types.

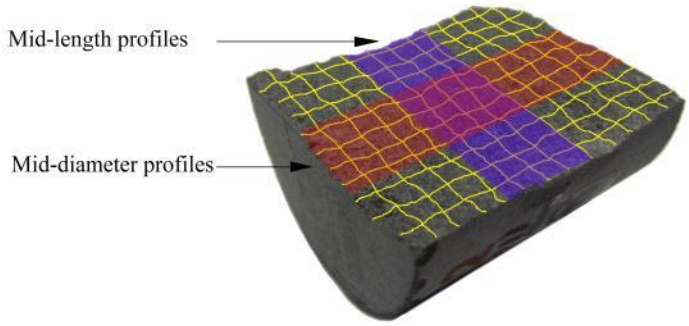

Figure 4-13: Mid-length and mid-diameter profiles of a specimen.

4.3.2.2 Roughness profiles perpendicular to the loading axis

The lengths of the roughness profiles perpendicular to the loading direction were approximately: 23.50, 35.63, 47.5, 59.38 and 71.25 mm. Consequently, the JRC values were calculated for all L/D ratios considering the scale effect correction to avoid the effect of different lengths of the profiles on the results. The relationship proposed by Barton and Bandis (1982) was used to consider the roughness scale effect as follows.

$$JRC_n = JRC_0 \left[\frac{L_n}{L_0}\right]^{-0.02JRC_0} \quad (2)$$

Where JRC_n is the JRC value of the roughness with the length of L_n; L_n is the length of the longest profiles; and JRC_0 is the JRC value measured for the roughness with the basic length of L_0. Figure 4-15 displays the variation of the roughness for the profiles perpendicular to the loading axis in terms of L/D ratio. The results show that the JRC value increases with an increase in the L/D ratio. A positive scale effect was observed in the roughness profiles of all three rock types when the length of the profiles increases.

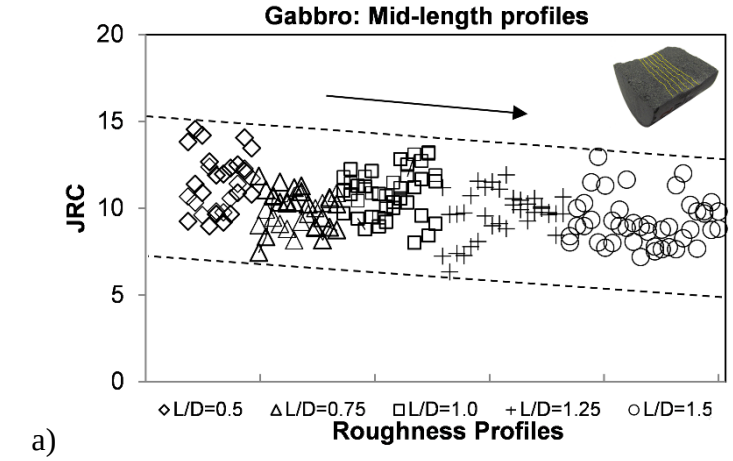

a)

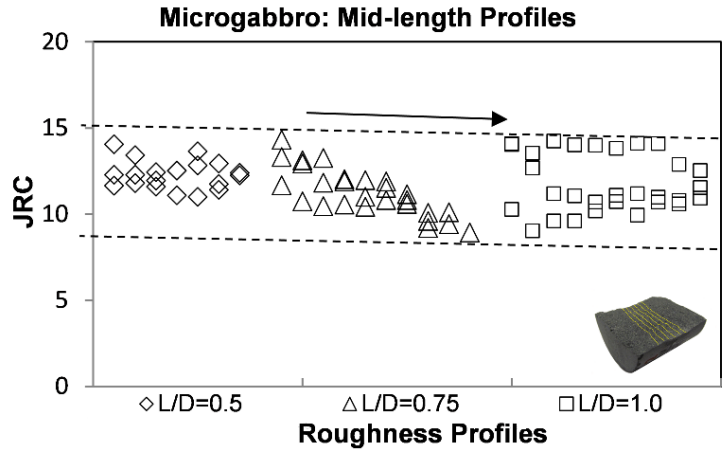

b)

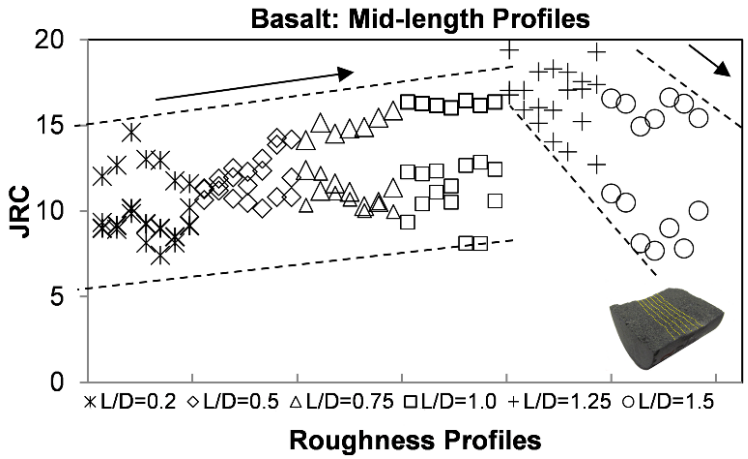

c)

Figure 4-14: Variation of the roughness parallel to the loading direction in the mid-length of the samples with L/D ratio.

The results also indicate that the roughness scattering in basalt was more than that in other rock types in terms of L/D ratio (Fig. 4-15c). The roughness of the profiles in the samples with a L/D

ratio ≤ 1.0 varied in a narrow window. For instance, the roughness variation of basalt, microgabbro and gabbro with a L/D ratio = 0.5 was in the range of 8 to 10, 6.8 to 11 and 7.7 to 11.7, respectively. In this case, the variation of roughness perpendicular to the loading axis was associated with the grain size of the rocks, contrary to what was observed for the variation of roughness parallel to the loading axis. It is worth noting that the JRC values in the vicinity of two loading platens were close to each other for all L/D ratios. For instance, the average JRC value was 10 for the profiles close to the upper and lower platen in basalt, while it was 10.5, 11 for microgabbro and gabbro, respectively.

Figure 4-16 illustrates the variation of the JRC values perpendicular to the loading axis in terms of L/D ratio. It can be observed that the JRC values in the samples with a L/D ratio=0.2 varied along a convex shape so that the JRC values in the core of the sample were lower than those in the vicinity of the loading platens. This trend changed to a wavy shape for L/D ratio=0.5 and 0.75. In the samples with a L/D ratio equal to 1.0, the JRC variation showed a concave shape, so that the JRC values of the roughness profile in the sample core were greater than those in the vicinity of both loading platens. It can also be seen that the concave focal length decreased with an increase in L/D ratio. A similar trend can be seen in the other rock types with coarser grain sizes (microgabbro and gabbro); however, the curvature of the concave shape was milder when L/D ratio increases.

Figure 4-17 shows the JRC values of one third of the roughness profiles selected in the mid-diameter of each sample (as shown in Figure 4-13). Therefore, homogenous stress distribution induced at the mid-diameter gives rise to a small range of the JRC variation in each L/D ratio compared to the whole roughness profiles shown in Figure 4-15. It can be seen that the profile roughness (at the mid-diameter) increased with an increase of L/D ratio for all three rock types. Data scattering also increased when the L/D ratio increases (Fig. 4-17a and 4-17c). The roughness values formed a narrow window with approximately width of 5 on the JRC scale for all three rocks. This window was smaller than that obtained from the whole roughness profiles along the sample diameter (Fig. 4-15).

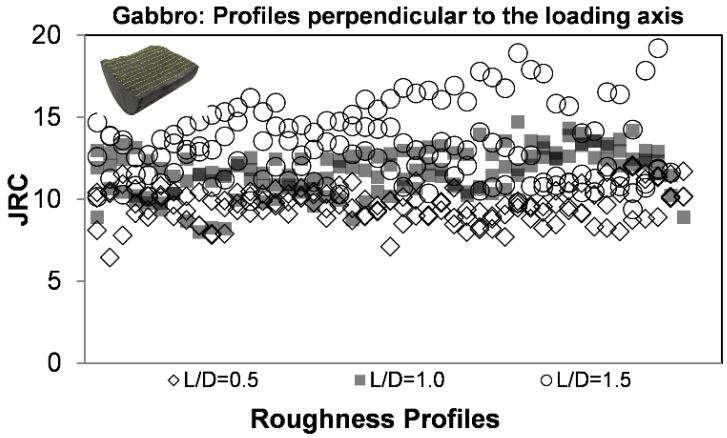

a)

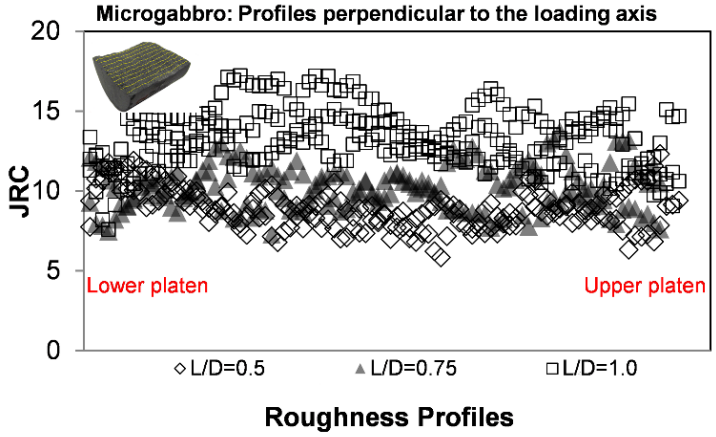

b)

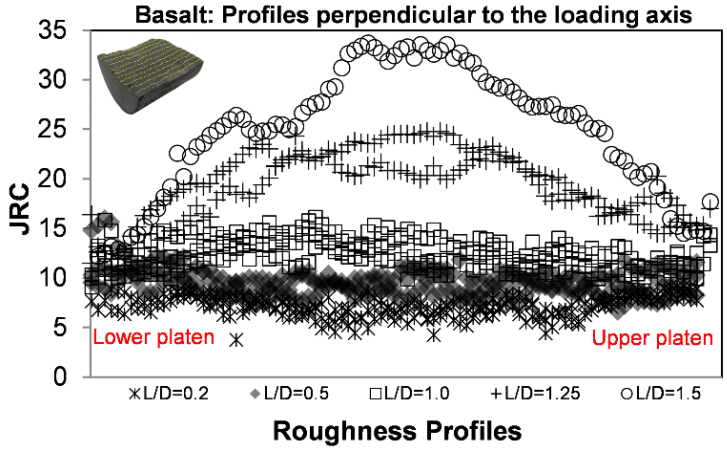

c)

Figure 4-15: Variation of the roughness perpendicular to the loading axis with L/D ratio.

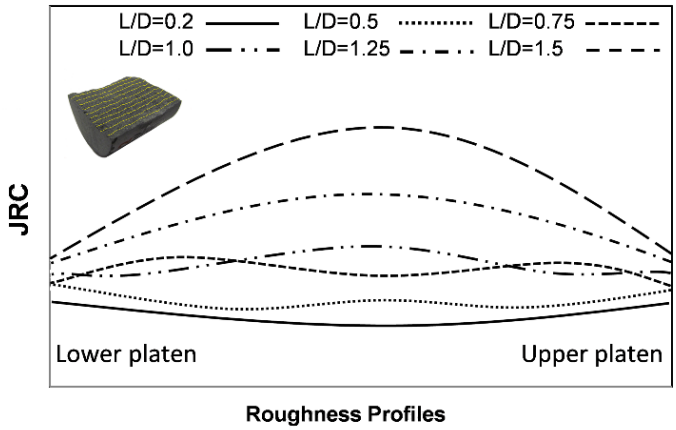

Figure 4-16: Schematic variation of the roughness perpendicular to the loading axis and with L/D ratio.

4.4 Discussion

The experimental results presented above constitute a step forward in the evaluation of fracture roughness in different loading conditions. The results presented above illustrate how the roughness parameter can be affected by the loading direction considering rock type and shape effect. It is thus worth commenting on the results obtained using Brazilian tests for different rock types and shapes. Other aspects that may influence the experimental results are also discussed briefly.

4.4.1 Stress distribution and roughness

In this paper, the variation of roughness was assessed according to the loading direction in the Brazilian test on samples with different L/D ratios. The roughness of the profiles parallel to the loading direction decreased with increasing L/D ratio in gabbro, microgabbro. In basalt specimens, the JRC value increases with an increase in the L/D ratio from 0.2 to 1.0; however, it decreases as the L/D ratio increases from 1.25 to 1.5. However, the roughness of the profiles perpendicular to the loading direction seems to increase with an increase in the L/D ratio. It can be inferred that the roughness parallel and perpendicular to the loading direction measured at the mid-length and mid-diameter of the specimens varies due to changes in the induced confining stress perpendicular to the two circular surfaces.

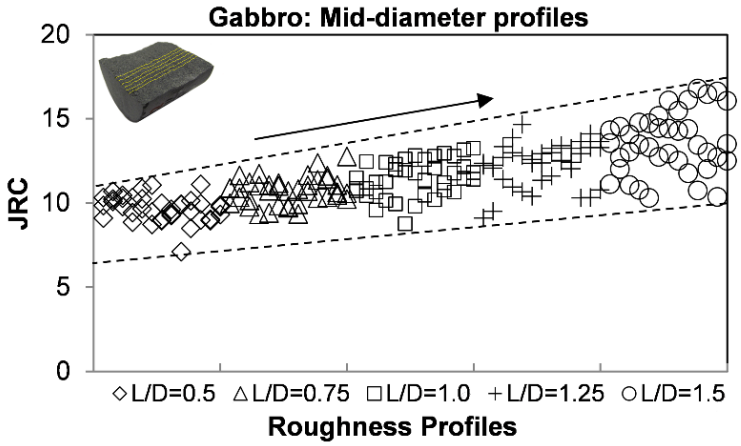

a)

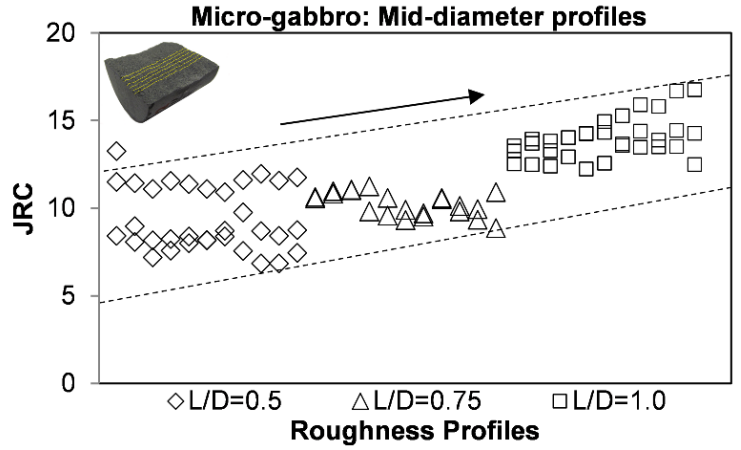

b)

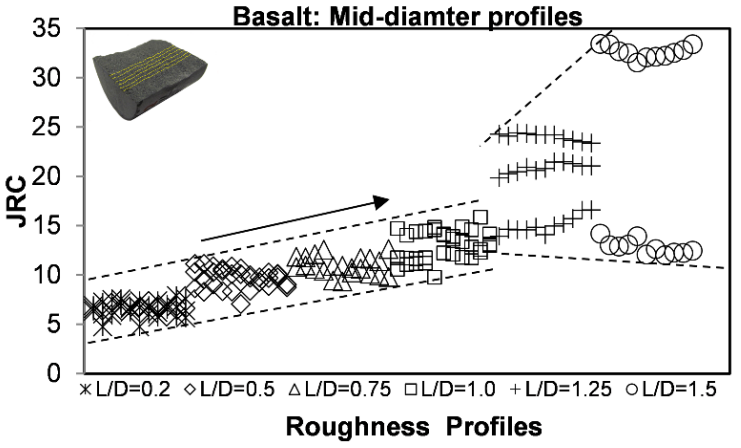

c)

Figure 4-17: Variation of the roughness perpendicular to the loading axis in mid-diameter of the samples with L/D ratio.

A plane stress condition can be assumed at small L/D ratios so that the confining pressure is negligible perpendicular to the two end-surfaces. When the L/D ratio increases, the differential stress between the two circular surfaces and center of the samples increases. This hypothesis is supported by the results of two numerical investigations of Brazilian tests carried out by Yu et al. (2006) and Von Dinh (2011). In these studies, they conducted 3D FEM analyses to study the tensile stress distribution in the disc specimens with the same diameter and different length (L/D ratio equal to 0.2, 0.5 and 1.0). Due to linear loading applied on the disc specimen, the analysis carried out by Yu et al. (2006) is representative of the ASTM procedure (Fig. 4-18), while the one conducted by Von Dinh (2011) is representative of the ISRM testing outline. The tensile stresses obtained from the 3D FEM analyses at the end-surface (circular surface) and at the center of the samples are listed in Table 4.3. It can be seen that the differential tensile stress between the circular surface and the center of the sample decreases with decreasing L/D ratio. For instance, the differential tensile stress between the circular surface and the center is 5.500 MPa for the sample L/D=1.0, while it is 0.250 MPa in the specimen L/D = 0.2 (Table 4.3). These numerical results can be compared with the experimental observations in the profiles parallel to the loading direction in which the roughness value decreased with an increase of the L/D ratio.

Comparison between the above-mentioned numerical investigations and the current experimental results obtained from Brazilian tests showed that the roughness variation appears to be affected by the stress distribution and shape effects. The experimental results presented here pave the way for the development of comprehensive numerical simulations to help better understand the roughness variation with the stress distribution and loading direction. Further numerical simulations are required to determine the relation between fracture roughness and loading direction.

4.4.2 Roughness scattering

The experimental results presented herein showed the roughness scattering in the profiles parallel and perpendicular to the loading direction. The results indicate that roughness scattering of the profiles parallel to the loading axis is higher than that in the profiles perpendicular to the loading axis. Although basalt is the most homogeneous rock in terms of the grain size, the roughness scattering of the profiles parallel to the loading direction in this rock type is more than that in the other rocks.

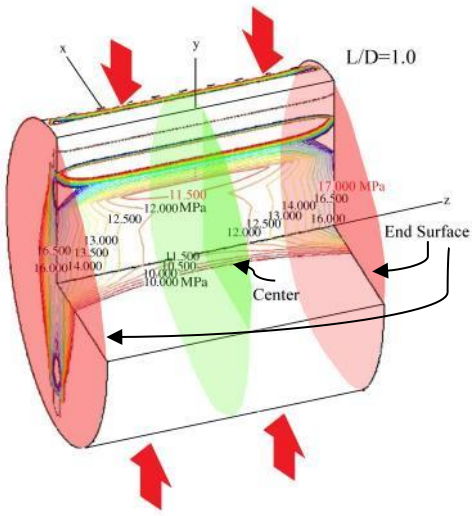

Figure 4-18: Tensile stress distribution in the specimen with L/D=1.0 obtained by 3D FEM analysis (adapted from Yu et al., 2006).

Table 4.3: Tensile stress values at the center and end surface of the Brazilian samples as function of L/D ratio (Yu etl., 2006; Von Dinh, 2011).

	L/D=0.2			L/D=0.5			L/D=1.0		
ASTM Yu et al. (2006)	End Surface	Center	Diff.	End Surface	Center	Diff.	End Surface	Center	Diff.
	13.000	12.750	0.250	14.500	11.500	3.000	17.000	11.500	5.500
	L/D=0.25			**L/D=0.5**			**L/D=1.0**		
ISRM Von Dinh (2011)	End Surface	Center	Diff.	End Surface	Center	Diff.	End Surface	Center	Diff.
	16.236	15.796	0.440	16.270	14.429	1.841	16.339	14.052	2.287

At present, there are a few investigations carried out on the influence of loading direction on the roughness scattering. Kabeya (2002) investigated the influence of grain size on the surface roughness by the splitting test. He concluded that roughness is influenced by the grain size and that larger grain size leads to rougher surfaces. Babadagli and Develi (2003) studied fractal properties of rock fracture surface created using Brazilian tests with different loading rates. All rock samples had the same dimensions. The fractal dimensions of 32 profiles were calculated parallel and perpendicular to the direction of loading. Their results showed that there was no correlation between the scattering of fractal dimension (roughness) of the profiles parallel to the loading direction and the grain size. However, more scattered fractal dimensions were observed

for the larger grain size in the profiles perpendicular to the loading direction. These results are in agreement with those obtained in the current study.

4.4.3 Limitation

The general approach and experimental results presented herein may contribute to a better understanding of the loading mode of the existing fractures in surface or underground excavation projects. But despite the new and original insights provided by these results further investigations should be considered. The effect of the loading direction on the roughness parameter and scattering can be studied on different rock types such as sedimentary and metamorphic rocks. More microscopic studies should also be carried out to better capture the grain size influence on the tensile fracture surface roughness scattering. The effect of the loading direction on the fracture roughness can also be investigated using other rock mechanics tests such as triaxial and uniaxial compression tests. Additional work is underway to deal with these aspects.

4.5 Conclusion

This paper presented the main results of an investigation on the fracture surface created by tension (Mode I) on three igneous rocks with different grain sizes. Among the split samples, undamaged fracture surfaces for each L/D ratio and rock type were selected to be scanned by a 3D laser profilommeter. The roughness profiles were extracted parallel and perpendicular to the loading direction with a 0.5 mm spacing. The results showed a relationship between the sample length and roughness of the fracture surface.

The results indicated that the sample shape and loading direction could affect the fracture roughness induced by Brazilian testing. The results also showed that the size of the wedge induced by the compression zone implicitly decreases with a decrease in the L/D ratio. This induced wedge is not observed in basalt at two circular surfaces when the L/D ratio is equal to 1.25 and 1.5.

The investigation of the fracture topography revealed that the roughness of the profiles parallel to the loading axis decreased with increasing in the L/D ratio in gabbro and microgabbro, while the roughness of basalt increased slightly with an increase of the L/D ratio from L/D = 0.2 to 1.25, and then decreased when the L/D ratio was greater than or equal to 1.25. It was also shown that the roughness of the profiles perpendicular to the loading axis increased with increasing in the

L/D ratio. The variation of the roughness for the profiles perpendicular to the loading axis showed a unique trend between two loading platens. Moreover, the roughness distribution for the profiles perpendicular to the loading axis was a convex shape for the lower L/D ratio; this suggests that the roughness in the core of sample is less than that in the vicinity of the loading platens. This convex shape gradually turns into a concave shape for the samples with a higher L/D ratio, meaning that the roughness of the profiles at the core of the sample is higher than that in the vicinity of the loading platens. The study presented herein is an important step in moving forward for further studies on the fracture surfaces considering different loading modes. Finally, it should be noted that additional investigations are under way using triaxial tests to assess the effect of the loading mode on the roughness parameters of the fractures.

Acknowledgement

The authors would like to acknowledge Raglan Mine (Glencore Group) for providing the rock cores (basalt and microgabbro) used in this study. Scanning of the fracture surfaces in this study was performed at the Department of Civil Engineering of University of Sherbrooke. This support is gratefully acknowledged. The corresponding author greatly acknowledges Dr. Nooshin Falaknaz for her help and endless support.

References

Al-Shayea NA (2005) Crack propagation trajectories for rocks under mixed mode I–II fracture. Eng Geol ;81:84–97.

ASTM C496 (1984) Standard test method for splitting tensile strength of cylindrical concrete specimens. In Annual Book of ASTM, Standards, vol. 0.042. Philadelphia: ASTM; pp. 336–41.

Babadagli T., & Develi K. (2003). Fractal characteristics of rocks fractured under tension. Theoretical and applied fracture mechanics, 39(1), 73-88.

Barton N (1976) The shear strength of rock and rock joints. Int. J. Rock Mech.Min. Sci. and Geomech. Abstr. 13:255-279.

Barton N.R (1973) Review of a new shear strength criterion for rock joints. Engng. Geol. 7: 287-332.

Barton N, Bandis S (1982) Effects of block size on the shear behaviour of jointed rock. Proceedings of the 23rd U.S. symposium on rock mechanics, Goodman and Heuze (eds) 739-760.

Barton N, Bandis S (1990) Review of predictive capabilities of JRC-JCS model in engineering practice. In: Barton N, Stephansson O (eds) Rock Joints; Proceedings of the International Symposium on Rock Joints, Loen, Norway, 4–6 June 1990. A. A Balkema, Rotterdam, pp 603–610

Barton N and Choubey V (1977) The shear strength of rock joints in theory and practice. Rock mechanics 10(1-2): 1-54.

Barton N, de Quados EF (1997) Joint aperture and roughness in the prediction of flow and groutability of rock masses. Proc., NY Rocks '97, Linking Science to Rock Engineering, New York, USA, 907–916.

Barton N, Lien R, Lunde J (1974) Engineering classification of rock masses for the design of tunnel support. Rock Mech Rock Eng 6(4):189–236

Beer A, Stead D and Coggan JC (2002) Technical note estimation of the joint roughness coefficient (JRC) by visual comparison. Rock mechanics and rock engineering 35(1): 65-74.

Bieniawski, Z. T. (1989) Engineering rock mass classifications: A complete manual for engineers and geologists in mining, civil, and petroleum engineering. New York: Wiley.

Brady BHG and Brown ET (1985) Rock Mechanics for Underground Mining, 1st Edn. Allen & Unwin, London.

Chen C-S, Pan EN, Amadei B (1998) Determination of deformability and tensile strength of anisotropic rock using Brazilian tests. Int J. Rock Mech Min Sci; 35:43–61.

EI-Soudani S. M. (1978) Profilometric analysis of fractures. Metalography. 11 247-336 .

Erarslan, N and Williams D J (2012) Experimental, numerical and analytical studies on tensile strength of rocks. International Journal of Rock Mechanics and Mining Sciences 49: 21-30.

Fairhurst C (1964) On the validity of the 'Brazilian' test for brittle materials. Int J Rock Mech Min Sci Geomech Abstr 1(4): 535–546.

Feng Z, Pan X, Dai G and Liu H (2014) Research on Rock Fracture Surface Morphology Characterization under Brazilian Test. Abstract and Applied Analysis. Vol. 2014. Hindawi Publishing Corporation.

Grasselli G (2001) Shear strength of rock joints based on quantified surface description. Ph.D. thesis. Lausanne, Switzerland: Swiss Federal Institute of Technology (EPFL).

Ghazvinian A, Nejati HR, Sarfarazi V, Hadei MR (2013) Mixed mode crack propagation in low brittle rock-like materials. Arab J Geosci; 6:4435–44.

Hoek E, Kaiser PK, Bawden WF (1995) Support of Underground Excavations. A. A Balkema, Rotterdam

Hondros G (1959) Evaluation of Poisson Ratio and the Modulus of Materials of Low Tensile Resistance by the Brazilian (Indirect Tensile) test with particular reference to concrete. Aust J Appl Sci;10:243–68.

ISRM (1978) Suggested methods for the quantitative description of discontinuities in rockmasses. Int. J. Rock Mech. Min. Sci. Geomech. Abstr. 15, 319–368.

Jang H-S, K S-S, Jang B-A (2014). Determination of joint roughness coefficient using roughness parameters. Rock Mech. Rock Eng. Online published on January 2014. pp.2061-2073.

Kabeya, K. K. (2012). Grain size distribution as a determinant of rock joints roughness. PhD dissertation, Rand Afrikaans University, Johannesburg.

Khosravi, A, Simon R, Falaknaz N (2014) Evaluation of roughness parameters of rock fractures created by different loading modes. Georegina2014, Regina, Sask, Canada28 September-1 October 2014.

Khosravi A, Simon R (2015) The effect of sample size on the created fracture surface by the splitting (Brazilian) test. The 13th international ISRM congress 2015Montreal, Canada. 10-13 May,

Kim, D-Y and Lee H-S (2009) Quantification of rock joint roughness and development of analyzing system. Proceedings of the international conference on rock joints & jointed rock masses, Tucson.

Kulatilake PHSW, Shou G, Huang TH, Morgan RM (1995) New peak shear strength criteria for anisotropic rock joints. Int J Rock Mech Min Sci Geomech Abstr, 32, pp. 673–697.

Li D, Wong LNY (2013) The Brazilian disc test for rock mechanics applications: review and new insights. Rock Mech Rock Eng 46(2):269–287.

Maerz N., Franklin J.A. and Bennett C.P. (1990). Joint roughness measurement using shadow profilometry. International Journal of Rock Mechanics and Mining Sciences & Geomechanics Abstracts, 1990;27(5), :329-343.

Markides, CF and Kourkoulis S (2012) The stress field in a standardized Brazilian disc: the influence of the loading type acting on the actual contact length. Rock mechanics and rock engineering 45(2): 145-158.

Myers N (1962) Characterization of surface roughness. Wear 5(3): 182-189.

Rocco C, Guinea GV, Planas J, Elices M (1999) Size effect and boundary conditions in the Brazilian test: experimental verification. Mater Struct; 32:210–7.

Reeves, M. J. (1985) Rock surface roughness and frictional strength. International Journal of Rock Mechanics and Mining Sciences & Geomechanics Abstracts, vol. 22, no. 6, pp. 429-442. Pergamon, 1985.

Sayles R. S. and Thomas R. R. (1977) The spatial representation of surface roughness by means of the structure functions, a practical alternative to correlation. Wear 42, 263-276.

Seredin V, Leibovich LO, Pushkareva MV, Kopylov IS and Khrulev AS (2013) Evolution of fracture surface morphology in rocks. Journal of Mining Science 49(3): 409-412.

Sharifzadeh M, Mitani Y, Esaki T (2008) Rock joint surfaces measurement analysis of aperture distribution under different normal, shear loading using GIS. Rock Mech Rock Eng; 41:299–323.

Seidel J. P., & Haberfield C. M. (1995). Towards an understanding of joint roughness. Rock Mechanics and Rock Engineering, 28(2), 69-92.

Stirling RA, Simpson DJ and Davie CT (2013) The application of digital image correlation to Brazilian testing of sandstone. Int J Rock Mech Min Sci; 60: 1-11.

Tatone BSA and Grasselli G (2010) A new 2D discontinuity roughness parameter and its correlation with JRC. International Journal of Rock Mechanics and Mining Sciences 47(8): 1391-1400.

Tatone BSA and Grasselli G (2012) Quantitative measurements of fracture aperture and directional roughness from rock cores. Rock Mech Rock Eng 45(4): 619–629.

Tavallali A, Debecker B, Vervoort A (2007) Evaluation of Brazilian tensile strength in transversely isotropic sandstone. In: proc 11th Int Cong Rock Mech, Lisbon; p. 269–72.

Tavallali A, Vervoort A (2010) Effect of layer orientation on the failure of layered sandstone under Brazilian test conditions. Int J Rock Mech Min Sci; 47: 313–22

Tse R and Cruden D (1979) Estimating joint roughness coefficients. International journal of rock mechanics and mining sciences & geomechanics abstracts, Vol. 16, pp. 303-307.

Vervoort A, Min K-B, Konietzky H, Cho J-W, Debecker B, Dinh Q-D, Frühwirt T and Tavallali A (2014) Failure of transversely isotropic rock under Brazilian test conditions. Int J Rock Mech Min Sci; 70: 343–352.

Von Dinh, Q. D. (2011). Brazilian Test on Anisotropic Rocks: Laboratory Experiment, Numerical Simulation and Interpretation. PhD dissertation. Institut für Geotechnik. Freiberg.

Wang QZ, Wang XM, Jia SQ, et al. (2004) The flattened Brazilian disc specimen used for testing elastic modulus, tensile strength and fracture toughness of brittle rocks: analytical and numerical results. Int J Rock Mech Min Sci; 41: 245–253.

Yang Z, Lo SC and Di CC (2001) Reassessing the joint roughness coefficient (JRC) estimation using Z2. Rock mechanics and rock engineering 34(3): 243-251.

Yu Y, Yin JM, Zhong ZW, (2006) Shape effects in the Brazilian tensile strength test and a 3D-FEM correction. Int J Rock Mech Min Sci; 43: 623–7.

Yu, X and Vayssade B (1991) Joint profiles and their roughness parameters. International journal of rock mechanics and mining sciences & geomechanics abstracts, Vol. 28, NO. 4, pp. 333-336.

Zhou H. W., & Xie H. (2003). Direct estimation of the fractal dimensions of a fracture surface of rock. Surface Review and Letters, 10(05), 751-762.

CHAPTER 5 ARTICLE 3: EFFECT OF PRE-PEAK LOADING CONDITION ON POST-PEAK BEHAVIOUR OF BRITTLE ROCKS

Arash Khosravi and Richard Simon

This article was submitted to International Journal of Rock Mechanics and Mining Sciences in June 2016, under revision following comments from reviewers.

Abstract: Understanding of post-peak (post-failure) behaviour of intact rocks can be useful predict violent pillar instability or rockbursts as well as optimize the design phase of underground openings. It is always difficult to obtain the post-peak behaviour of brittle rocks due to the excess energy release and the sudden collapse of rock samples at their ultimate strengths.

In this paper, a stiff servo-controlled testing machine was used to obtain the post-peak curves of hard rocks. A new loading procedure with incremental cyclic loading and axial displacement rate was applied to rock specimens. Brittleness and fracture pattern of rock samples were then evaluated. The results of uniaxial compression tests using the proposed damage-controlled method are presented for two brittle rock types. A discussion follows on the key (critical) characteristics of the stress-strain curves and limitations of the proposed method.

Keyword: Post-peak, Brittle rock, Uniaxial compression, Testing procedure, Brittleness

5.1 Introduction

The design of an underground opening requires the understanding of the mechanical behaviour of rocks under different loading conditions. In many cases, a rock engineer encounters conditions where the induced stresses exceed the ultimate strength of the rock mass. These conditions result in fracturing of the rock mass surrounding the excavation. A portion of the surrounding rock mass may behave in a brittle manner that is defined by the descending portion of the strain-stress curve (Aubertin et al., 1994; Aubertin and Simon, 1997). Rockburst is one of the phenomena that occurs in deep underground structures due to high stress conditions. This phenomenon is a result of brittle fracturing of the rock mass where the potential energy of the whole system is released in a violent manner. Investigation of the post-peak behaviour of brittle materials can be helpful in characterizing rockburst. A good understanding of the post-failure behaviour helps engineers to

estimate the load-bearing capacity of underground openings beyond the peak strength during the strain softening phase. Generally, it is difficult to obtain the post-peak phase in laboratory due to the excess energy released by the loading system and rapid disintegration of the rock samples at their ultimate strength. This brittle failure of samples under compression cannot be considered as an intrinsic property of intact rocks (Rummel & Fairhurst, 1970; Wawersik & Fairhurst, 1970). The pre- and post-peak behaviour of rocks have been investigated by many researchers using laboratory compression tests on brittle rock samples. In these studies, different loading procedures were applied to obtain the complete stress-strain curve. There are two methods applicable in order to obtain a complete stress-strain curve: a) by reducing the amount of strain energy stored in the system with an increase of the rigidity of the testing machine; and b) by applying a particular loading procedure with a slow displacement (strain) rate. Cook (1965) carried out uniaxial compression tests on marble and granite in order to analyse the resilience of the loading system, the violence of fracture, and the slope of the stress-strain curve. In this study, the resilience of the testing machine was increased during the tests. It was concluded that large amounts of energy can be dissipated during failure by converting the elastic energy into surface energy. Rummel and Fairhurst (1970) investigated the post-peak behaviour of marble specimens by applying a constant strain rate. The results of this study showed that deformations in the post-peak load region were developed slowly if a sufficiently slow strain rate was applied during the test. Wawersik and Fairhurst (1970) also conducted uniaxial and triaxial tests to obtain a complete stress-strain curve by applying the axial strain rate along with rapid unloading on different rock types. They distinguished two classes of rock behaviour based on fracture development in rock samples. Based on this study, Class I represented stable fracture propagation in specimens in which a residual strength is retained even after compressive strength has been exceeded. Class II represented the rock behaviour where failure was self-sustaining as shown in Figure 5-1.

Salamon (1974) used a stiff testing machine, to obtain the post-peak curve of a brittle rock by applying a very small strain rate in an uniaxial compression tests. He showed that the post-peak behaviour could be captured when the absolute value of the post-failure modulus of the sample was smaller than that of the testing machine. Martin (1993) and Martin and Chandler (1994) conducted damage-controlled laboratory tests on granite, limestone and potash specimens to investigate the influence of crack volume on the crack damage stress. In this investigation, the

axial stress was increased using an axial strain rate control. After the axial stress reached 75% of the rock specimens anticipated peak strength, the load unload cycles were performed using axial-strain control. Their results demonstrated that the crack initiation stress was independent of the accumulated damage in the sample. However, the crack damage stress was dependent on the amount of accumulated damage.

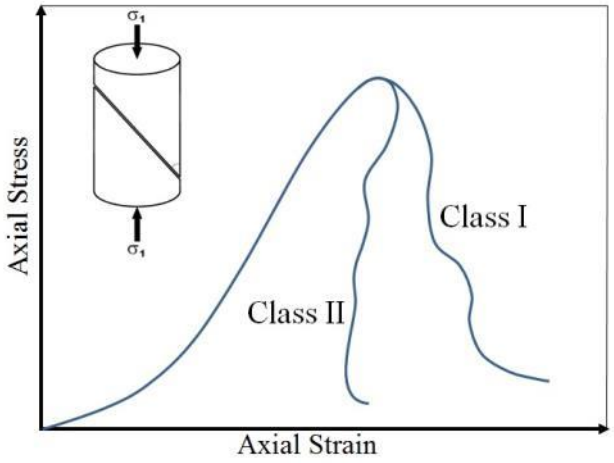

Figure 5-1: Two classes of post-peak behaviour in uniaxial compression (Adapted from Wawersik and Fairhurst 1970).

Based on aforementioned studies, homogeneous fracture development is highly associated with the controlled strength loss caused by the low rate dissipation of energy, which is spread gradually out of the whole sample. Dissipation of a portion of the elastic energy stored in the sample by destressing it within the pre-peak region can help fractures to stop due to the stable local fracture propagation. Since the behaviour of intact rocks is not the same as that of ideal elastic materials, they are loaded to failure by applying a slow strain rate to obtain a controlled, continuous and progressive breakdown. In other words, a low deformation rate results in releasing the excess energy at a lower rate.

Many interesting conclusions have been obtained from these experimental studies. However, the previous efforts to obtain the post-peak behaviour of rocks in compression are based on an increase of the rigidity of the testing machine or by applying a particular loading procedure with a slow displacement (strain) rate. In the current study, the same approach was chosen, although partial unloading cycles were performed to obtain a complete post-peak curve. Using this specific procedure, a series of uniaxial compression tests were carried out on two hard rocks

(microgabbro and basalt) in order to obtain the complete stress-strain curves. Following the description of the loading technique used in this study, the characteristics of the stress-strain curve, the fracture patterns and the deformation stages during compression tests will be addressed.

5.2 Uniaxial compression test

In order to study the behaviour of rocks under compression and also have a better understanding of rockburst mechanism as a brittle fracturing phenomenon, uniaxial compression tests are carried out on brittle rocks. A complete stress-strain curve is obtained for each test in order to study the post-peak behaviour of the rocks. As the boundary condition influences the compressive behaviour of rocks, the post-peak phase can be obtained by using specified loading boundary conditions. Other factors can also influence the behaviour of rock samples under compression including: sample anisotropy, size of the sample, platen friction, loading rate and stiffness of the testing machine (Jaeger 1966). In order to obtain a complete stress-strain curve, a loading procedure should be customized based on the load and strain rate control. The following subsections describe both procedures used to obtain the complete stress-strain curves for hard rocks.

5.2.1 Draft ISRM suggested method for the complete stress-strain curve: a review

A complete stress-strain curve cannot only be obtained by using a proper stiff and servo-controlled loading machine. The testing procedure plays an equally important role in obtaining successful uniaxial compression test. Fairhurst and Hudson (1999) proposed an alternative controlled testing procedure where the axial and circumferential strain control or computed feedback control were used to obtain the complete stress-strain curve. In order to reduce the elastic energy accumulation in the system, the spacers and rotating support were not recommended to locate in the loading setup.

In this method, a small pre-load was applied to the specimen in force control to seat the specimen on the loading platens. Once seated, the control mode was switched to the axial strain control mode. The loading was initially set at an axial rate of 0.001 mm/mm/s and continued at this rate until 70% of the expected strength was obtained. The strain control mode was then switched to a

circumferential strain control at the rate of 0.0001 mm/mm/s. With this low rate, the applied load was dropped gradually to 50% of the peak load. Once obtained, the strain loading was switched back and maintained at 0.001 mm/mm/s axial strain rate until the residual strength of the sample was obtained. Due to this methods lengthy load reduction procedure, many microscopic fractures may have occurred during the testing process.

5.2.2 Damage-controlled loading method

The damage-controlled loading method was proposed by Martin and Chandler (1994) in order to obtain a complete stress-strain curve. A stiff and servo-controlled testing machine was used to apply the confining pressure and the axial stress with a rate of 0.75 MPa/sec. The axial stress was then increased with the axial strain rate control equivalent to 0.75 MPa/sec until approximately 75% of the expected ultimate strength of the specimen was reached. The load-unload cycles were conducted at 40 MPa increments. Specific care was needed in order to prevent abrupt failure of the sample when the peak strength was reached. For this purpose, the load-unload cycles were carried out at 0.063 mm increments of circumferential deformation using axial-strain control. This method took approximately 8 hours to be completed. Since the unstable cracking in the brittle materials began at approximately 70-80% of their peak strength (Martin, 1993; Aubertin and Simon, 1997; Eberhardt et al., 1998), the cyclic loading was releasing a portion of the accumulated energy of the system in the damage-controlled loading method (Martin, 1993).

5.3 New damage-controlled cyclic loading method

In the current study, a simple procedure is proposed by the authors in order to obtain the complete post-peak curve using pre-peak damage-controlled method along with cyclic loading. The loading procedure is based on the combination of axial force and displacement rate control. At first, the loading begins with a force control rate (0.5 kN/sec) until approximately 60-70% of the expected peak strength is obtained (zone 1 in Fig. 5-2). The loading phase then continues with the axial displacement rate of 4×10^{-5} μm/min until approximately between 70-80% of ultimate strength of the sample is reached (zone 2 in Fig. 5-2). Afterwards, the axial rate decreases to 10^{-5} μm /min and it maintained at this rate until the test is completed (zone no. 3 in Fig. 5-2). In this step, the load-unload cycles are applied with a maximum overall unloading of 40 MPa for each unload cycle. The load-unload cycles are performed using an axial displacement control at the

rate of 10^{-5} μm /min. In addition to the load-unload cycles, the loading procedure is able to halt loading as pause. Pausing in the procedure at the loading level helps the cracks to coalesce and propagate due to the excess energy of the system. Each test takes a maximum of 2.5 hours to be completed. A typical force-time curve obtained by the new method is shown in Figure 2.

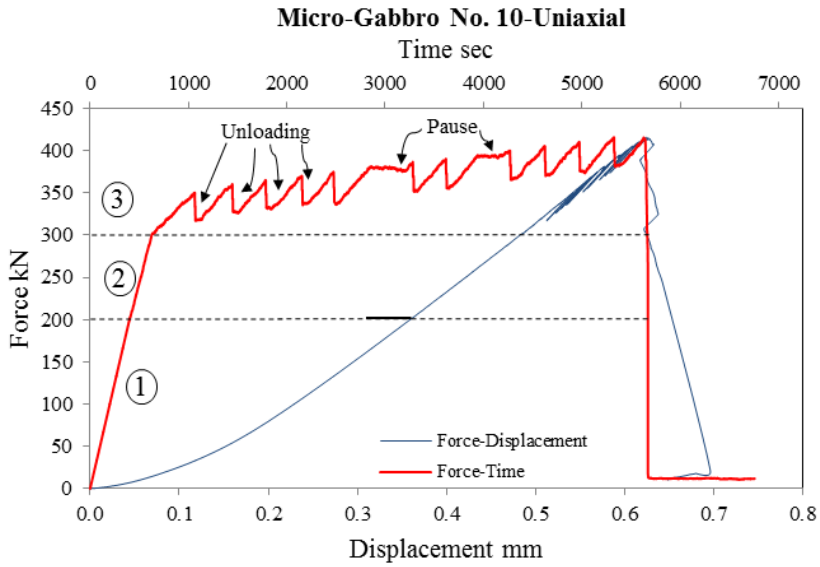

Figure 5-2: An example of the procedure applied to obtain the complete force-displacement curve.

5.4 Sample preparation and equipment

Two rock types were used in the uniaxial compression tests, including basalt and microgabbro. These rocks are classified as very hard and brittle. Basalt is a fine-grained igneous (volcanic) rock comprised of plagioclase and pyroxene. Microgabbro is a plutonic intrusive igneous rock with medium sized grains comprised of plagioclase, clinopyroxene and olivine. Basalt and microgabbro are very low porosity rocks that show brittle behaviours. The uniaxial compression tests were conducted on cylindrical NQ-size rock samples with a length-to-diameter ratio in the range of 2 to 2.4. A total of 31 specimens were subjected to the uniaxial compression.

Special care was taken in the parallelism of the circular surfaces in the samples to meet the standard tolerance of ≤ 25 μ (ASTM D4543-08). The uniaxial compression tests were conducted using a servo-controlled MTS testing machine with an axial force capacity up to 2670 kN as shown in Figure 5-3. The proposed procedure specified for brittle rocks in section 3 was used to

obtain the complete stress-strain curve. To avoid any excessive accumulated energy in the loading system no rotating or any other support was located between the sample and the loading platens. Two axial and one radial extensometer with an accuracy of 0.127 mm were used to measure the axial and radial displacements.

Figure 5-3: MTS testing machine with an axial force capacity of 2670 kN used for this study at University of Sherbrooke.

5.5 **Experimental results**

The UCS value was in the range of 270 MPa to 320 MPa for basalt and 150 MPa to 220 MPa for microgabbro samples. Table 1.1 summarized the results of the test using the new damage-controlled cyclic method. Stress-strain curves derived from the uniaxial compression tests of basalt and microgabbro samples are shown in Figure 5-4. The post-peak shape of the stress-stain curve for basalt samples was not quite similar to that of microgabbro samples. It can be seen that the post-peak behaviour of basalt samples corresponds to class II failure behaviour while the post-peak behaviour of microgabbro sample corresponds to class I failure behaviour. The results also indicate that the damage-controlled cyclic method can be developed as a successful approach to achieve the post-peak behaviour of brittle material based on a slow axial rate control. According to Figure 4, no violent disintegration at peak stress occurred in the samples subjected to the proposed damage-controlled cyclic method.

Table 5.1: Summary of sample number and rock mechanics tests.

Rock Type	L/D	Number of uniaxial compression tests	UCS (MPa)	Density	Tensile Strength
Basalt	2-2.4	19	270-320	3.00	25
Microgabbro	2-2.4	12	150-220	2.97	23.5

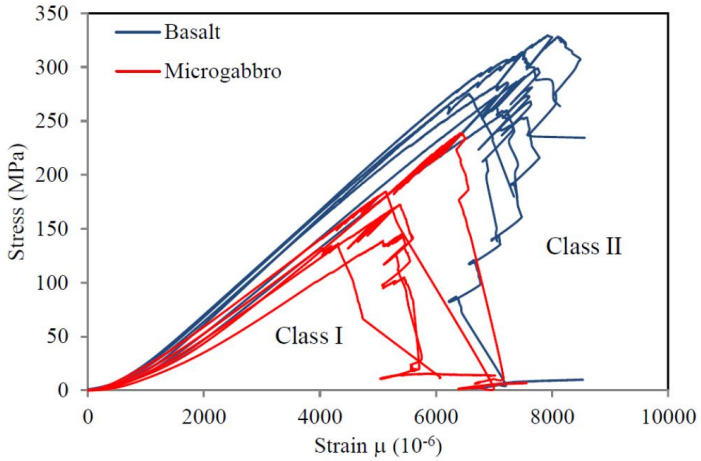

Figure 5-4: Complete stress-strain curve obtained by damage-controlled cyclic loading method.

Figures 5-5 and 5-6 are depicted the fracture patterns in three samples of basalt and microgabbro samples after the uniaxial compression tests. Figures 5-5a and 5-6a show two examples of the failed samples with a sudden loss of strength at failure using a standard axial compression test. In this case, the post-peak behaviour of the samples was not obtained. A major inclined fracture was created along with axial secondary fractures in these samples.

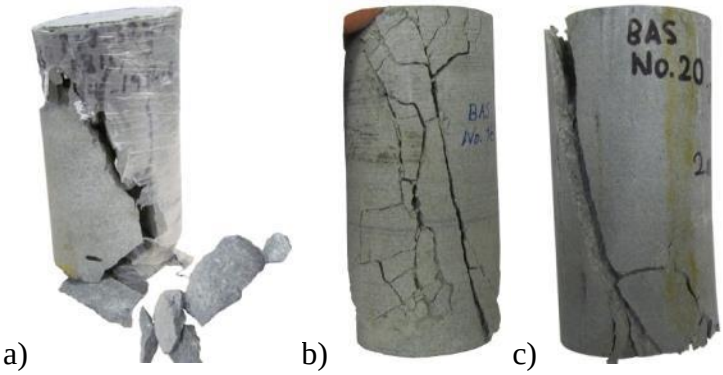

a) b) c)

Figure 5-5: Fracture pattern of basalt samples subjected to uniaxial compression test: a) unstable and violent failure with the entire loss of strength; b) stable fracturing due to damage-controlled cyclic method; c) partial loss of strength in the post-peak phase followed by a total loss.

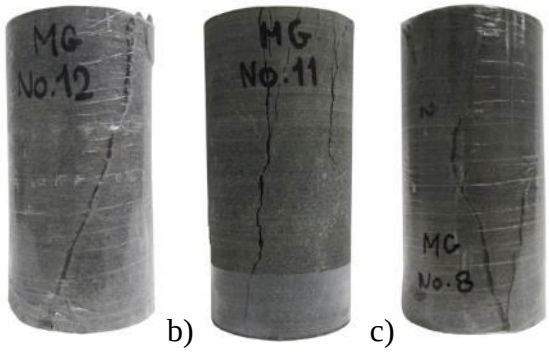

a) b) c)

Figure 5-6: Fracture pattern of microgabbro samples subjected to uniaxial compression test: a) unstable and violent failure with entire loss of strength; b) stable fracturing due to damage-controlled cyclic method; c) partial loss of strength in the post-peak phase continuing with total loss.

Figures 5-5b and 5-6b represent the smooth loss of strength in the two samples due to the application of the damage-controlled cyclic method. The post-peak stress-strain curves were obtained for these samples. In these cases, the homogenous fracture network was distributed in the whole body rather than local concentrations resulted in forming a single failure plane. Figures 5c and 6c illustrate two samples in which the post-peak were started with a partial loss of strength followed by a total loss. A major failure plane was resulted in failure of the samples along with micro-fractures localized in an area close to one of the platens.

Figure 5-6b shows the axial and low angle cracks in microgabbro samples after the uniaxial compression test. By controlling the post-peak phase, shear fractures could occur as inclined fractures to the loading direction. The inclined shear fractures tended to propagate and convert to a single fracture leading the loading phase to the residual phase and finally to the complete loss of the resistance. The shear fractures are consistent with those reported by Wawersik and Fairhurst (1970) and Lajtai (1974).

The damage-controlled cyclic method also influenced the fracturing pattern of the samples which can be seen in the axial stress-radial displacement curve. Figure 5-7 displays a complete stress-strain curve derived from a uniaxial compression test on a microgabbro specimen. The radial displacement shows a stepwise sample expansion in the pre-peak and post-peak. In this figure, the stepwise radial displacement is started at onset of the axial displacement rate of 4×10^{-5} μm /min at which the micro-cracks unstably propagate. Each horizontal section of the curve indicates

that the fracture was opened in a controlled manner. The expansion curve shows a snap back in the radial displacement with a partial loss of the stress level as soon as the axial displacement was switched to 10^{-5} µm /min (*). The sample expansion continued slowly when the cyclic loading was applied.

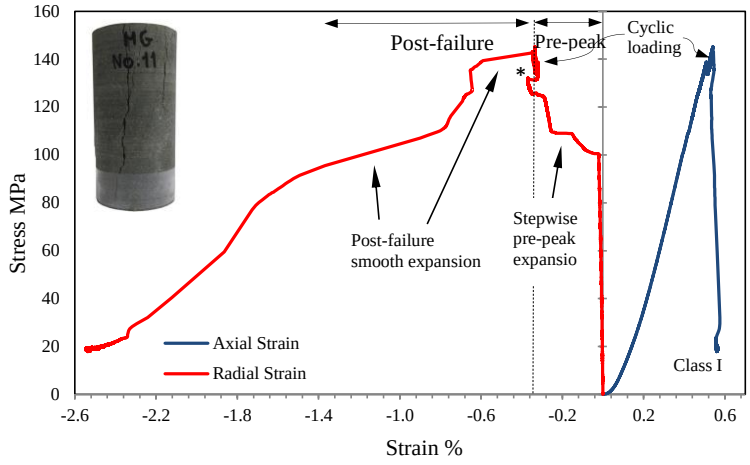

Figure 5-7: An example of a successful complete stress-strain curve with a smooth radial displacement.

5.6 Discussion

5.6.1 Applied procedure and fracture patterns

In this study, the post-peak behaviour of two different rocks, basalt and microgabbro, was studied. Brittle intact rocks usually behave in a very unstable fashion in the post-peak region. In order to determine the post-peak behaviour, the pre-peak behaviour of brittle rocks should be considered to study. To do so, a new damage-controlled method was used to obtain the stress-strain curves. Figure 5-8 shows a stress-strain curve of a microgabbro specimen subjected to the uniaxial compression test. Four deformation stages can be identified in this figure in the pre-peak phase of compressive loading in terms of cracking phenomenon. The pre-peak behaviour of brittle rocks subjected to axial compression tests was also described in many publications (Wawersik and Brace, 1971; Gill et al., 1993; Martin, 1993; Martin and Chandler, 1994; Aubertin and Simon, 1997; Eberhardt et al., 1999 among others).

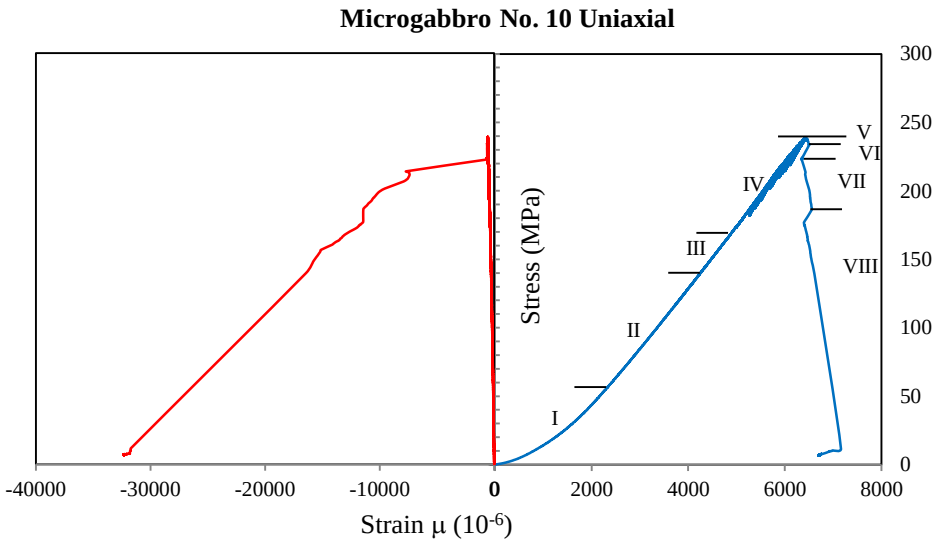

Figure 5-8: Axial and radial deformation in pre- and post-peak stages of a microgabbro sample.

As can be seen in Figure 5-8, stage I is associated with micro-cracks closure at the onset of loading demonstrated as a non-linear section of the curve. This stage is common in all rock types; however, the curvature of this non-linear section in hard and brittle rocks with low porosity (basalt and microgabbro) is less than that in rock types with higher porosity such as sandstone. Stage II is a linear elastic deformation representing the elastic properties of the sample. Cracking is initiated in stage III which is associated with a stable crack growth as a result of accelerating the radial straining at 30-50% of the peak strength. Rapid acceleration of the micro-cracking events is the characteristic of stage IV, which starts at the axial stress between 50% and 90% of the UCS. The micro-cracks opening are associated with the noises that can be easily heard. Although these four steps for microgabbro samples were identified based on similar deformation stages described by Martin and Chandler (1994) and Aubertin et al. (1997), in the damage-controlled cyclic procedure proposed herein, more focus was given on the stage IV to make a pause and load-unload cycles. Each pause in this stage helped the sample keep cracking at a decreasing rate in the load.

A significant amount of micro-brittle damage occurred during the period of the constant load (pause) for four minutes. The same conclusion was addressed by Eberhardt et al. (2000) using acoustic emission. In addition, the unload cycles allowed the sample to release small amount of accumulated energy in the system. This released energy balanced the stiffness of the damaged sample and testing machine as closely as possible. In this stage, the loading rate affected the

loading curve, ultimately the strength of the sample, and the cracking network. The fracturing pattern of the sample was also influenced by the slow loading rate. With a low loading rate, the cracking process in the pre-peak region was started with cracks parallel to the direction of loading and propagated with low angle growing towards the center of the sample. These cracks made an inclined main fracture at the peak strength. The low axial displacement rate and damage-controlled procedure helped the crack initiation, coalescences and propagation to be gently distributed within the entire specimen.

In stage V, a large number of cracks occurred parallel to the loading direction. Based on Diederichs (2004), the post-failure phase was also accompanied by intensified seismic activities due to huge volume of cracking phenomenon. As a result of crack coalescence, a larger crack was gently formed which resulted in a load drop (snap back) in stage VI. Since some amount of energy was released by applying the damage-controlled cyclic method in the pre-peak phase, the number of cracks formed in stage VI was not enough to cause complete disintegration of the sample. Stage VI might be the most important portion of the post-peak. Stage VI can be repeated in the post-peak phase with accumulating cracks and opening a new fracture. The sample kept losing its integrity in stage VII along with a controlled release of energy and increase in axial and radial strain. The cracking network was propagated in the whole specimen in stages V, VI and VII. The crack propagation continued in stage VIII until the applying load exceeded the residual compressive strength of the cracked sample. In fact, stage VIII is a combination of stages VI and VII in which a network of cracks was propagated. These crack networks resulted in a major fracture followed by the sample failure (Fig. 5-8). As can be seen in this figure, the sample failed smoothly with a gradually load drop.

5.6.2 Brittleness

Brittleness is a characteristic of geo-materials having inner heterogeneous stress distributions resulting in violent failure potential in rocks. The brittleness affects the development of local and progressive failure of geo-materials. To characterize and quantify the brittleness, many indices were proposed. Brittleness indices represent the severity of strength loss beyond peak strength. It also reflects the ability of a material to withstand inelastic deformations before the failure occurs. Some brittleness indices can be obtained using a stress-strain curve while the others can be calculated from mechanical properties of rocks. BIM (Brittleness Index Modified) is an example

of a brittleness index obtained from the pre-peak portion of the stress-strain curve (Aubertin and Gill, 1988; Aubertin et al., 1994). B_4 is a brittleness index calculated from the compressive (σ_c) and tensile strength (σ_t) of brittle material (Altindag, 2010). Figure 5-9 shows a schematic view of the BIM concept. A higher BIM value is related to a greater amount of energy dissipated before failure and less energy available for violent failure.

$$BIM = \frac{A_2}{A_1} \quad (1)$$

$$B_4 = \sqrt{\frac{\sigma_c \times \sigma_t}{2}} \quad (2)$$

In the current study, these brittleness indices were obtained from the pre-peak stress-strain curve and the compressive and tensile strength of rock specimens. Table 5.2 indicates the magnitudes of the brittleness indices for microgabbro and basalt (BIM and B_4) and the intensity of the brittle phenomenon. It can be seen that both rocks are categorized in high bursting liabilities with higher chance of violent failure.

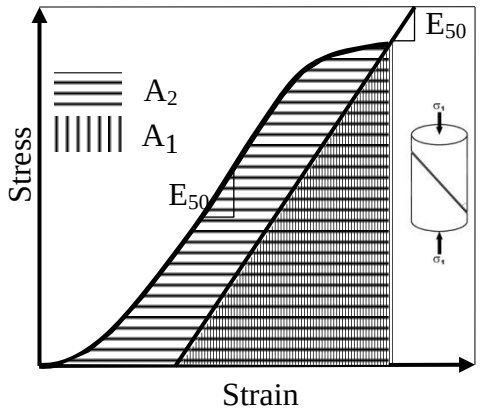

Figure 5-9: Schematic conception of the BIM (Adapted from Aubertin and Gill, 1988; Aubertin et al., 1994).

Table 5.2: Classification of the brittleness indices for microgabbro and basalt.

	BIM	**Class**	**B_4**	**Class**
Basalt	1.03-1.15	High	44-68	Extremely high
Microgabbro	1.02-1.15	High	41-60	Extremely high

Aubertin et al. (1994) also proposed a correlation between BIM and the pre-peak modulus, E, and the post-peak modulus, E', based on the literature data as follows:

$$BIM = 0.42|E/E'| + 0.98 \qquad (R^2 = 0.53) \quad (3)$$

Where E' is the slope of the steepest portion of stress-strain curve in the post-peak phase. This parameter was found from the complete stress-strain curves in the previous studies (Aubertin et al. 1994). This correlation can be used for the preliminary calculation of E' for intact rocks. In this study, the correlation between BIM and $|E/E'|$ was verified for basalt and microgabbro based on the stress-strain curves as shown in Figure 5-10.

Considering the experimental data used by Aubertin et al. (1994), the correlation obtained based on the current study is consistent with that proposed by Aubertin et al. (1994). However, this correlation was relatively low with a correlation coefficient of 0.52. When the graph was modified based on the results of fine-grained rocks with lower porosity, the data scattering was in a narrower window. A new correlation between *BIM* and $|E/E'|$ was also obtained with a higher correlation coefficient (R^2=0.82) as shown in Figure 5-11.

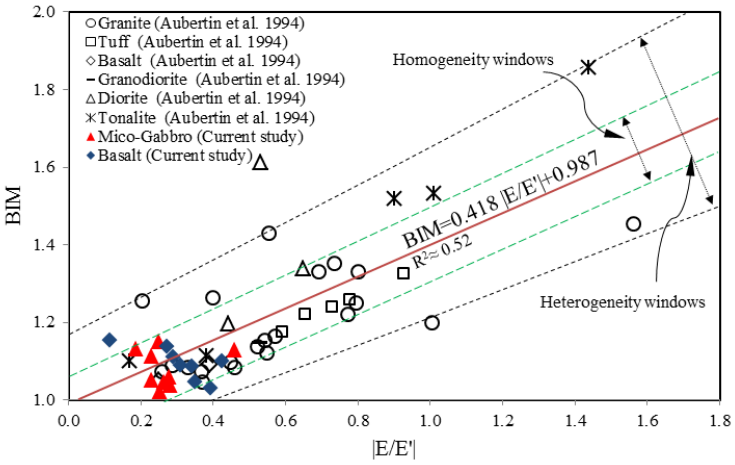

Figure 5-10: Empirical correlation between BIM and |E/E'| including basalt and microgabbro.

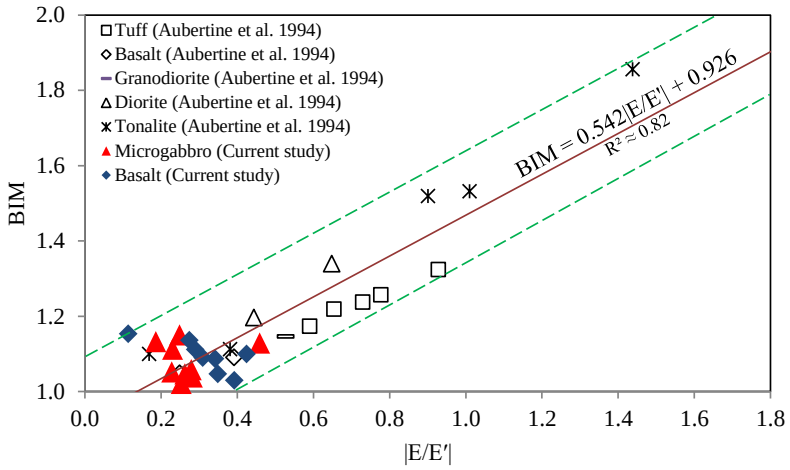

Figure 5-11: Empirical correlation between BIM and |E/E'| for fine-grained rocks.

5.6.3 Energy concept

As already mentioned, the damage-controlled cyclic method helps the loading system to balance the accumulated and dissipated energies. The area under the stress-strain curve corresponds to the elastic energy stored in the pre-peak region based on energy concept. According to study carried out by Wawersik and Fairhurst (1970), extraction of the elastic energy stored in the material is one way to control fracturing after sample is failed. The elastic energy in the pre-peak region can be diminished by the damage-controlled method through a low loading rate as well as cyclic loading. To investigate the elastic energy stored in the specimens during the application of the proposed damage-controlled cyclic method, two stress-strain curves obtained from the standard uniaxial test (dashed line) and the damage-controlled cyclic procedure (solid line) were compared for basalt samples. Figure 5-12a shows two areas under the curves which correspond to the elastic energy. A_1 is the area (elastic energy) related to the standard UCS test while A_2 corresponds to the damage-controlled cyclic procedure. In the latter method, the stress-strain curve departed from linearity at 70% of the compressive strength once the displacement rate was applied. In this case, a large number of cracks were unstably growing in a controlled manner resulting in a decreasing of the pre-peak slope of the curve. For the standard method, this departure from linearity was observed at almost 95% of the compressive strength.

This differential elastic energy of two loading curves $(A_1 - A_2)$ indicates the energy was dissipated. The larger the differential energy, the higher is the possibility of capturing the post-

peak region. The area under the curve obtained with the new loading procedure is less than that obtained from the standard uniaxial compression test. It indicates that an amount of the energy dissipated during the test with the new procedure was approximately 13%.

The effect of the loading rate on the stress-strain curve was also investigated by Hashiba et al. (2006). They studied the effect of the loading rate on pre- and post-peak behaviour of marble, sandstone and andesite.

Figure 5-12b shows the variation of the stress-strain curve while the loading rate changes from a higher rate 1 to lower rate 2. As can be seen in this figure, the area under curve 1, A_1, (i.e. rate 1) is larger than that in curve 2, A_2 (i.e. rate 2). They concluded that the peak strength and strain obtained by the higher loading rate were higher than those with the lower loading rate. These observations correspond well to the results obtained in the current study as shown in Figure 5-12a.

5.6.4 Effect of loading rate and unload cycles on the results

Based on the damage-controlled loading used by Martin and Chandler (1994), a large number of full unloads cycles applied in pre- and post-peak. The tests took approximately 8 hours to be completed. In this method, the large number of load-unload cycles may cause fatigue problem in the sample. Mechanical behaviour of brittle rocks is time-dependent. In the other hand, long term testing can also lead to plastic straining (creep). Numerous unload cycles and duration of the test significantly impacts the mechanical behaviour of rocks.

In the draft ISRM suggested method, the low circumferential strain rate applied in this process can help the procedure meet its objective; however, the duration of the tests is too long. The low circumferential strain rate can cause the brittle samples to lose strength through inducing the micro-cracks in entire body of the sample. This method may cause a creeping phenomenon in the sample due to the extended duration of the test.

In the damage-controlled cyclic method proposed in this study, the duration of tests were not prolonged due to the limited unload cycles (maximum 40 MPa) and loading rate. The duration of the tests carried out by this method was maximum 2.5 hours. Therefore, the creep phenomenon might not be occurred. In the other hand, limited number of short unload cycles eliminated the risk of fatigue problem significantly.

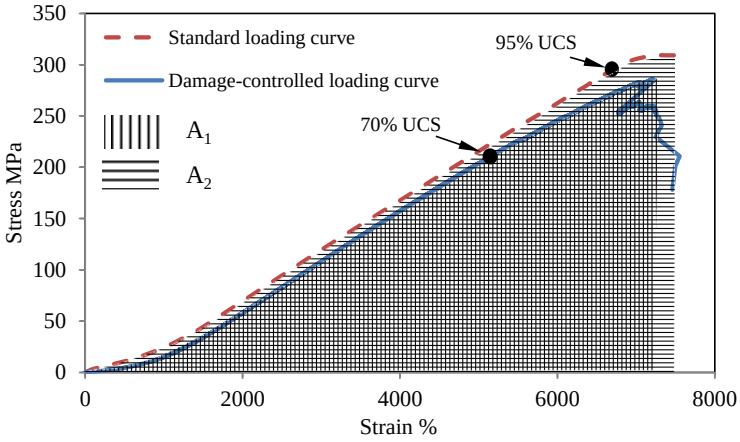

a)

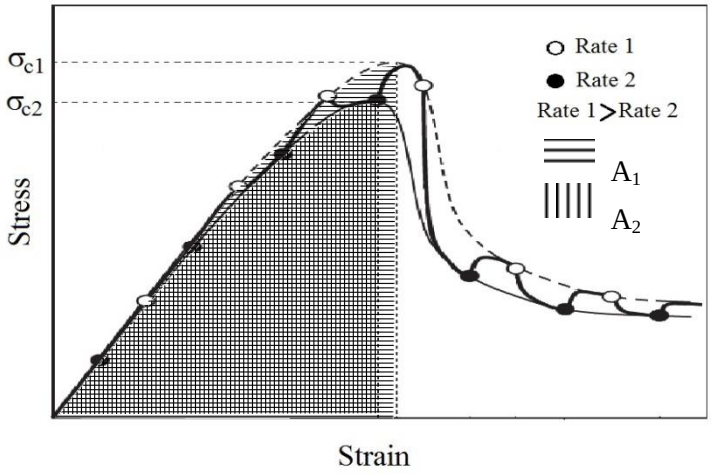

b)

Figure 5-12: Effect of loading rate and loading cycles on stress-strain curve in hard rock; a) Comparison between elastic energy obtained from a standard uniaxial test and the proposed damage-controlled cyclic loading test on a basalt specimen; b) Schematic stress-strain curve adapted from Hashiba et al. (2006).

5.6.5 Limitations

In this study, a damage-controlled cyclic method was used to capture the post-peak behaviour of hard rocks. Generally, all rocks appeared to behave similarly during the procedure, however, noticeable differences were obsereved in some specimens as shown in Figure 5-13. In this figure, an abrupt drop of strength can be seen at peak point.

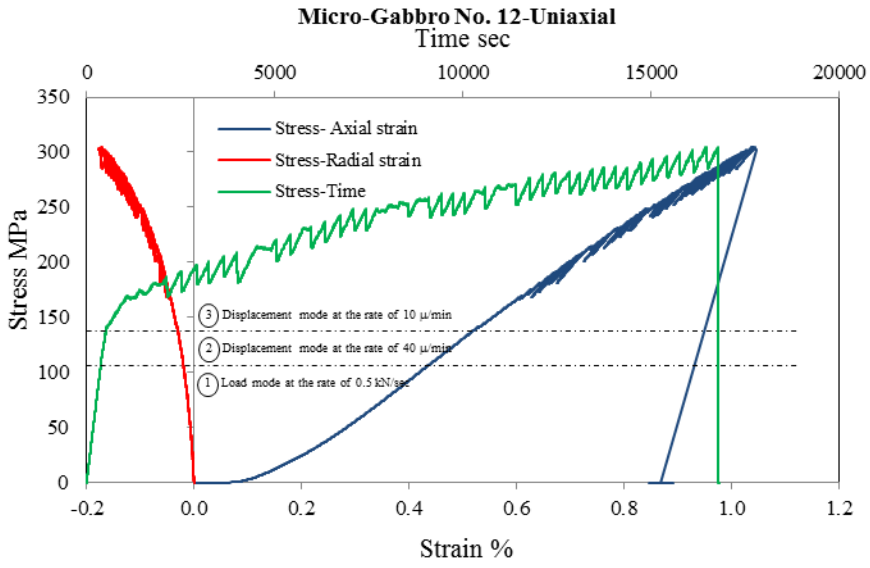

Figure 5-13: Strain hardening of microgabbro due to the large number of cyclic loadings in the pre-peak region.

In this test, the cyclic loading was started at a stress level of 170 MPa which was approximately 90% of the expected peak strength. Also, a total of 34 load-unload cycles were applied in the pre-peak phase. The peak compressive strength occurred at 305 MPa which was approximately 30% higher than the maximum compressive strength recorded for microgabbro samples in this study (i.e. 240 MPa). The results indicate that the samples failed at a stress level much higher than that expected. Based on the actual peak compresive strength of this specimen, i.e. 305 MPa, the cyclic loading applied on the sample was started at the stress level of ≈ 55% of the compressive strength instead of 80-100%. Applying the cyclic loading below the crack damaged threshold, i.e. stress level of 55%, can cause a reduction of crack coalescence. The internal breakdown of the material stiffness occurs when the crack size and density reach a specific state. At this state, a large crack and coalescence can occur. Therefore, the point at which the loading cycles started can affect the loading curve, the ultimate strength of the sample, and the resulting cracking network.

It should be emphasized that the damage-controlled cyclic method proposed herein, is generally limited to determining the level of loading (%) in which the loading rate should be switched from one loading mode to another. In addition, it is hard to assign an absolute value to the compressive strength to all specimens. These are the main factors that should be considered during application of the proposed damage-controlled cyclic method.

5.7 **Conclusion**

In this study, two hard and brittle rock types, basalt and microgabbro, were subjected to the uniaxial compression test through conducting damage-controlled cyclic method. A specific procedure with a combination of axial load and displacement rate was applied in order to obtain a complete stress-strain curve. The test was started with force control rate of 0.5 kN/sec until the loading level reached 60-70% of the expected compressive strength. Afterward, the axial displacement rate (4×10^{-5} μm/min) was applied until a stress level of 70-80% of the expected peak strength was achieved at which the displacement rate was switched to a lower rate (10^{-5} μm/min). In this low displacement rate stage, the load-unload cycles were also applied. Cyclic loading in pre-peak can create damages at a microscopic scale. This means that the crack initiation occurs as uniformly as possible along with gentle crack coalescence and propagating in the form of vertical cracks. These are followed by low angle cracks penetrating in the body of the sample to form a crack network. Development of the crack network indicates that the elastic energy dissipation is in an imperceptible manner, which can lead the test to the post-peak region. The damage-controlled cyclic method enables us to control the unstable cracking phenomenon in hard rocks under compression. Therefore, the complete stress-strain curve can be obtained by this method in order to investigate the post-peak behaviour of brittle rocks and estimate the post-peak stiffness. In this study, the correlation between BIM and $|E/E'|$ was also modified by the post-peak modulus obtained from the stress-strain curves. Knowing that the post-peak stiffness can help us a better understanding of the post-peak phenomena such as rockbursts, the complete stress-stain curve obtained by damage-controlled cyclic method can be used as a calibration tool of the experimental or analytical models for prediction of the post-peak behaviour of intact rocks.

Acknowledgement

The authors would like to give our very special thanks to the engineering faculty of University of Sherbrooke. Our sincere gratitude also to Mr. Danick Charbonneau, the laboratory technician for his time and efforts. We would also like to thank Dr. Nooshin Falaknaz for her precious advice. The rock samples were provided by Raglan mine (Glencore group). This support is gratefully acknowledged.

Reference

Altindag R. (2010). Assessment of some brittleness indexes in rock-drilling efficiency. Rock mechanics and rock engineering 43(3): 361-370.

ASTM D 4543-08 (2008). Preparing rock cores as cylinderical test specimens and verifying conformance to dimension and shape, ASTM International, West Conshohocken, PA, USA.

Aubertin, M. and Gill, D.E. (1988). Une methodologie d'evaluation du potentiel de coups de terrain dans les mines d' abitibi. Proc. Colloque sur Ie ContrOle de Terrain (AMMQ),Val d'Or, 47-77.

Aubertin M., Gill D. and Simon R.. (1994). On the use of the brittleness index modified (BIM) to estimate the post-peak behavior of rocks. 1st North American Rock Mechanics Symposium, American Rock Mechanics Association.

Aubertin M. and Simon R. (1997). A damage initiation criterion for low porosity rocks. International Journal of Rock Mechanics and Mining Sciences 34(3): 17. e11-17. e15.

Cook, N.G., 1965, December. The failure of rock. In International Journal of Rock Mechanics and Mining Sciences & Geomechanics Abstracts (Vol. 2, No. 4, pp. 389-403). Pergamon.

Diederichs, M. S. (2007). The 2003 Canadian Geotechnical Colloquium: Mechanistic interpretation and practical application of damage and spalling prediction criteria for deep tunnelling. Canadian Geotechnical Journal, 44(9), 1082-1116.

Eberhardt E. et al. (1999). Quantifying progressive pre-peak brittle fracture damage in rock during uniaxial compression. International Journal of Rock Mechanics and Mining Sciences 36(3): 361-380.

Eberhardt E. et al. (1998). Identifying crack initiation and propagation thresholds in brittle rock. Canadian Geotechnical Journal 35(2): 222-233.

Eberhardt E. et al. (2000). Laboratory Testing Of Stress-Induced Brittle Fracture Damage Through Incremental Loading. ISRM International Symposium, International Society for Rock Mechanics.

Fairhurst C. and Hudson J. (1999). Draft ISRM suggested method for the complete stress-strain curve for intact rock in uniaxial compression. International Journal of Rock Mechanics and Mining Sciences 36(3): 279-289.

Gill, D. E., et al. (1993). A practical engineering approach to the evaluation of rockburst potential. Rockburst and Seismicity in Mines. Balkema, Rotterdam: 63-68.

Hashiba K. et al. (2006). A new testing method for investigating the loading rate dependency of peak and residual rock strength. International Journal of Rock Mechanics and Mining Sciences 43(6): 894-904.

Jaeger J. (1966). Brittle fracture of rocks. The 8th US Symposium on Rock Mechanics (USRMS), American Rock Mechanics Association.

Lajtai E. (1974). Brittle fracture in compression. International Journal of Fracture 10(4): 525-536.

Martin C. and Chandler N. (1994). The progressive fracture of Lac du Bonnet granite. International Journal of Rock Mechanics and Mining Sciences & Geomechanics Abstracts, Elsevier.

Martin C. D. (1993). The strength of massive Lac du Bonnet granite around underground openings, University of Manitoba Manitoba.

Rummel F. and Fairhurst C. (1970). Determination of the post-failure behavior of brittle rock using a servo-controlled testing machine. Rock mechanics 2(4): 189-204.

Salamon M. (1974). Rock mechanics of underground excavations. Advances in rock mechanics, Proc. 3rd Cong. ISRM., Denver B 1: 951-1009.

Wawersik W. and Brace W. (1971). Post-failure behavior of a granite and diabase. Rock mechanics 3(2): 61-85.

Wawersik W. and Fairhurst C. (1970). A study of brittle rock fracture in laboratory compression experiments. International Journal of Rock Mechanics and Mining Sciences & Geomechanics Abstracts, Elsevier.

CHAPTER 6 ARTICLE 4: POST-PEAK BEHAVIOUR OF HARD AND BRITTLE ROCKS: ESTIMATION AND VERIFICATION USING THE CSDS MODEL FOR ROCK JOINTS

Arash Khosravi and Richard Simon

This article was submitted to International Journal of Geomechanics in June 27th, 2016, under revision following comments from reviewers.

Abstract: Determination of post-peak behaviour of hard and brittle rocks can help engineers evaluate and predict potential instabilities in underground openings. Rockbursts are one type of instability that has long been studied and evaluated using different approaches. One approach is based on stiffness comparison between the post-peak behaviour of the failed rock and the pre-peak behaviour of the surrounding rock. To predict the post-peak behaviour of hard rock, Simon et al. (2003) proposed a methodology based on the CSDS constitutive model for rock joint surfaces. To date, the CSDS model has only been validated using data from the literature. This paper aims to verify the model using axial compression and direct shear tests. The required model properties are obtained using the results compression and direct shear tests. The model properties are established for evaluating the shear behaviour of the rock joint induced by uniaxial compression. The results show that the approach can be used to estimate the post-peak behaviour of medium to hard rocks. A comparison is also made between the model properties obtained from axial compression and those obtained using the direct shear test, and the discrepancy between some of the parameters is subsequently discussed.

Keywords

Post-peak behaviour, Axial compression, The CSDS model, Rockburst, Initial asperity angle, Failure plane angle

6.1 Introduction

Underground openings are prone to various hazards. The most feared ones are those that occur unexpectedly and are associated with some forms of violence in hard brittle rocks, such as rockbursts, coal bumps and rockfalls (Salamon, 1993). A rockburst is an instantaneous failure of

rock due to huge accumulated elastic energy in the system that can occur in all depth (Petukhov, 1972; Kidyinski, 1981; Singh, 1989; Yi and Kaiser, 1993; Wu and Zhang., 1997; Tang et al., 2000; Whyatt et al., 2002; Lee et al., 2004; Mitri, 2007; Wang et al., 2010). Many Canadian underground mines suffered this hazardous phenomenon (Kaiser et al., 1995).

Rockbursts can be caused by two distinct phenomena that are associated with states of unstable equilibrium causing either a slip along major discontinuities as fault-slip burst or a breakdown of a portion of the rock mass as strain-burst (Stiller et al., 1983; Cook, 1987; Johnston 1988, Gill and Aubertin, 1988; Gill et al., 1993; McGarr, 1993; Zhang and Wang, 2006; Li et al., 2008; Cai et al., 2012; Sainoki and Mitri, 2014). Predicting burst-prone areas of underground openings is extremely important at the design phase, and there is an important need for improved knowledge of the mechanical behaviour of the rock mass subjected to compression to enable engineers to quantitatively predict the system response. A methodology for assessing the rockburst potential in underground excavations is therefore needed.

In the last two decades, many attempts have been made to predict rockbursts based on different approaches. Crack growth mechanisms, seismicity, strain energy accumulation, artificial neural network, numerical modeling, Gaussian process, fuzzy modelling and random forest are the concepts that were mainly used to predict the rockbursts (e.g., Dyskin and Germanovich, 1993; De Beer and Mendecki, 1998; Haijun et al., 2003; Wiles, 2005; Jian et al., 2009; Su et al., 2009; Adoko et al., 2013 and Dong et al., 2013). These concepts are mainly based on statistical and mathematical approaches where the mechanical properties of the surrounding rock mass are generally not well considered. Strain energy accumulation and mechanical properties of rock in the loading phase (pre-peak) have also been used to evaluate burst prone areas in terms of the brittleness indices as simple and cost effective methodologies. These indices can be obtained through conducting hardness, penetration, point loading, tensile and uniaxial tests (Reichmuth, 1967; Hucka and Das, 1974; Aubertin et al., 1994; Qiao and Tian, 1998; Wang and Park, 2001; Hajiabdolmajid and Kaiser, 2003; Yagiz, 2009; Altindag, 2010; Meng et al. 2015). Since rockburst phenomenon is related to the energy release in the post-peak phase of intact rock, the post-failure was studied by many researchers using uniaxial and triaxial laboratory tests on different rock types (Cook 1965; Hudson et al., 1970; Hudson, 1989; Rummel and Fairhurst 1970; Salamon 1974; Aubertin and Simon 1997; Tarasov and Potvin, 2013). These studies resulted in a significant improvement of our understanding of mechanism of the post-peak behaviour and the

influence of the loading rate, stress level, confining stress and the stiffness of the testing machine on the complete stress-strain curve.

In order to capture the complete stress-strain curve by a stiff and servo-controlled testing machine, the loading procedure and control variables are very important. Therefore, a few specific loading procedures were proposed to capture the post-peak of medium to hard rocks in which the load was applied based on axial and/or circumferential displacement rate control (Wawersik and Fairhurst, 1970; Martin and Chandler, 1994; Fairhurst and Hudson, 1999; Khosravi, 2016). The post-peak curve can be also obtained by applying the confining stress in triaxial compression test; however, the post-peak behaviour of intact rocks in uniaxial compression is completely different (Santarelli and Brown, 1989; Hakami, 1988; Martin and chandler, 1994; Hoek and Brown, 1997; Tiwari and Rao, 2006).

The effect of the loading variable (axial strain or lateral strain rate control) on the post-peak behaviour was also investigated by Mirsha and Nie (2013). It was shown that the post-peak behaviour can be changed by the loading variable. Although the stiff servo-controlled testing machine can capture the post-peak curve, indirect approaches can be also used to estimate a complete stress-strain curve when a qualified servo-controlled machine is not available. As a consequence, Simon et al. (2003) proposed an indirect analytical approach using triaxial compression tests and the CSDS constitutive model (Complete Stress-Displacement Surface-Simon, 1999) model for rock joints to predict the post-peak behaviour of brittle rocks under uniaxial compression. Since discontinuity controls the post-peak behaviour of intact rock, the CSDS model was used to estimate the post-peak behaviour of hard rocks among other constitutive shear models developed for predicting the shear behaviour of joints (Patton, 1966; Ladany-Archambault, 1970; Barton et al., 1973; Saeb-Amadei, 1992), In these models, the surface morphology has also been taken into consideration. Characterizing the discontinuity morphology can improve the estimation of the post-peak behaviour of rocks.

Despite many interesting outcomes obtained by Simon et al. (2003) for prediction of the post-peak of rocks using an indirect approach, no verification has been conducted using hard brittle rocks. Therefore, the proposed approach cannot be applied for further engineering applications without sufficient experimental results on hard rocks.

The objective of the current study is therefore twofold. First, it aims to perform direct shear, uniaxial and triaxial compression tests on hard rocks and also a morphological study of fracture surfaces to verify the proposed indirect approach. Therefore, the influence of the joint surface characterization on the CSDS model parameters is explicitly investigated. Second, it was also postulated that the model properties required to estimate the uniaxial post-peak behaviour could be obtained from direct shear tests instead of triaxial tests. The shear behaviour of rock joints in direct shear tests was therefore compared to the shear behaviour of failure planes induced by triaxial compression tests using the CSDS model (Simon, 1999).

6.2 The CSDS constitutive model for rock joints: a review

Certain some shear strength criteria are indicative the peak shear strength of a dilatant rock joint subjected to a monotonic shear force and a constant or variable normal load (Saeb and Amadei, 1992; Grasselli and Egger, 2003 among others). The CSDS model was developed as a constitutive model (Simon, 1999) to model rock joint behaviour in the post-peak region. This model is reviewed in the following sections.

6.2.1 Shear stress-shear displacement

In the CSDS model, shear stress is modeled in terms of shear displacement based on an exponential relationship. In this model, both peak and residual displacements are considered to be constant for a given joint. A relationship is defined as follows:

$$\tau = F(u) = a + bexp(-cu) - dexp(-eu) \qquad (6\text{-}1)$$

where: τ is the shear stress (MPa); u is the shear displacement (mm); and a to e are model parameters with a specified imposed conditions: $c < e$, and $a, b, c, d, e > 0$. By making certain assumptions about shear conditions for different shear displacements, the following equations are used to obtain the model parameters (Simon, 1999):

$$a = \tau_r \qquad (6\text{-}2)$$

$$b = d - a \qquad (6\text{-}3)$$

$$c = {}^{5}/_{u_r} \qquad (6\text{-}4)$$

$$\frac{deu_r}{5(d-\tau_r)} - exp\left[u_p\left(e - \frac{5}{u_r}\right)\right] = 0 \qquad (6\text{-}5)$$

$$d = \frac{\tau_p - \tau_r\left[1 - exp\left(-\frac{5u_p}{u_r}\right)\right]}{exp\left(-\frac{5u_p}{u_r}\right) - exp(-eu_p)} \qquad (6\text{-}6)$$

where: τ_r and τ_p are the residual and peak shear strengths and u_p and u_r are the peak shear displacement and the displacement at the onset of τ_r. To determine the values of d and e, equations 6-5 and 6-6 must be solved simultaneously with standard iterative methods in which the condition $c < e$ must be met.

Residual shear strength can also be obtained from relationships developed by Goodman (1976) or the Coulomb criterion:

$$\tau_r = \tau_p\left(B_0 + \frac{1-B_0}{\sigma_T}\sigma_n\right) \qquad when \quad \sigma_n < \sigma_T \qquad (6\text{-}7)$$

or

$$\tau_r = \sigma_n \tan\phi_r \qquad (6\text{-}8)$$

where: σ_n is normal stress applied to the rock joint; σ_T represents the compressive strength of the rock; B_0 is the ratio of residual to peak shear strength at very low normal stress ($0 \leq B_0 \leq 1$); and ϕ_r is the residual friction angle of the rock joint surface. The LADAR peak shear criterion (Ladanyi and Archambault, 1970) as modified by Saeb (1990) is used to calculate the shear strength at peak (τ_p). The peak shear strength is then given as:

$$\tau_p = \sigma_n(1 - a_s)\tan(i + \phi_u) + a_s S_r \qquad (6\text{-}9)$$

where: a_s is the fraction of the joint surface on which shearing through asperities takes place; i is the angle of dilatancy; ϕ_u is the friction angle for sliding along the asperities; and S_r represents the shear strength of the asperities (herein called the "Coulomb criterion"). According to Ladanyi and Archambault (1970):

$$i = arctan\left[\left(1 - \frac{\sigma_n}{\sigma_T}\right)^4 tani_o\right] \qquad (6\text{-}10)$$

$$\mathrm{a}_s \simeq 1 - \left(1 - \frac{\sigma_n}{\sigma_T}\right)^{1.5} \qquad (6\text{-}11)$$

Saeb (1990) has used the Mohr-Coulomb strength criterion for the shearing of rock asperities as follows:

$$S_r = S_o + \sigma_n \tan \phi_o \quad (6\text{-}12)$$

where: i_o is the initial asperity angle; S_o represents the cohesion; and ϕ_o is the internal friction angle obtained from the Mohr circles.

6.2.2 Normal -shear displacement (dilation)

In the CSDS model, normal displacement also corresponds to shear displacement on discontinuity. Simon (1999) proposed an exponential equation to describe the normal displacement (v) behaviour of the rock joint during the shearing course:

$$\mathrm{v} = \beta_1 - \beta_2 \exp(-\beta_3 u) \quad (6\text{-}13)$$

where β_1, β_3 and β_4 are model parameters and can be determined from the following equations:

$$\beta_1 = u_r \left(1 - \frac{\sigma_n}{\sigma_T}\right)^4 \tan i_0 + \frac{\sigma_n \, V_m}{k_{ni} \, V_m - \sigma_n} \quad (6\text{-}14)$$

$$\beta_2 = \beta_1 - \frac{\sigma_n \, V_m}{k_{ni} \, V_m - \sigma_n} \quad (6\text{-}15)$$

$$\beta_3 \cong \frac{1.5}{u_r} \quad (6\text{-}16)$$

where V_m is the maximum closure of the rock joint and k_{ni} is the initial normal stiffness.

6.3 Post-peak behaviour of brittle rocks: approach review

The behaviour of brittle hard rock subjected to compression can be classified into five stages as shown in Figure 6-1: (1) crack closure, (2) linear elastic deformation, (3) crack initiation and stable crack growth, (4) critical energy release and unstable crack growth, and (5) failure and post-peak behaviour (Martin, 1993; Aubertin et al., 1998; Eberhardt et al., 1998). The post-peak stage takes place as soon as the specimen starts to lose integrity. Basically, the capacity to follow the behaviour in this stage depends upon the response of the loading system and the loading condition (i.e., loading rate) (Hakami, 1988; Martin, 1993). The post-peak behaviour of brittle rocks is associated with a rapid release of elastic energy release, and a very steep slope is

therefore expected for the post-peak portion of the curve. The slope of the post-peak portion tends to decrease with an increase in confining stress on the specimen.

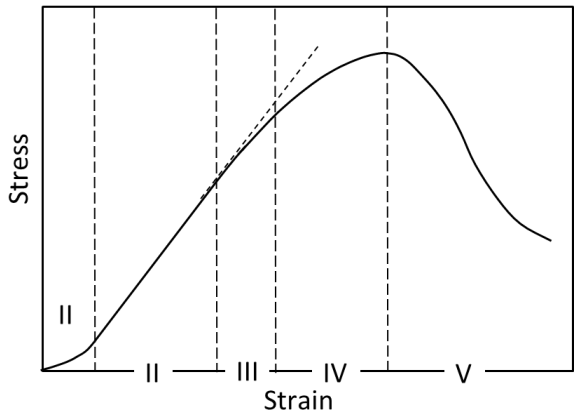

Figure 6-1: Deformation behaviour of rock under compression.

6.3.1 Stress-strain components in post-peak behaviour

The post-peak behaviour of intact rock is highly dependent on the mechanical properties of the failure plane. Figure 6-2 illustrates an idealized single failure plane created by triaxial compression. The post-peak phase starts once of the crack propagation phenomenon is complete and creates of a failure plane in the sample subjected to the triaxial compression.

The shear and normal stresses on the failure plane can be calculated by the following equations:

$$\sigma_n = \tfrac{1}{2}(\sigma_1+\sigma_3) - \tfrac{1}{2}(\sigma_1-\sigma_3)\cos 2\beta \qquad (6\text{-}17)$$

$$\tau = \tfrac{1}{2}(\sigma_1-\sigma_3)\sin 2\beta \qquad (6\text{-}18)$$

where σ_1 and σ_3 are the major and minor stresses applied on the specimen; and β is the failure plane angle measured after the specimen is retrieved at the end of the test. In the post-peak phase, the axial strain is due to the strain components induced by the material compaction and shearing process on the failure plane. These strain components are as follows (Simon et al., 2003):

1) The axial strain component induced by the shear displacement (u) on the failure plane ($\Delta\varepsilon_t$),

2) The axial strain component induced by the normal displacement (v) of the failure plane ($\Delta\varepsilon_n$) and

3) The axial strain component due to the rock matrix compaction (taken as elastic strain) ($\Delta\varepsilon_e$).

Therefore, the total axial strain (ε) in the post-peak phase can be given as:

$$\varepsilon = \varepsilon_p + \Delta\varepsilon_t + \Delta\varepsilon_n + \Delta\varepsilon_e = \varepsilon_p + \frac{\Delta u \cos\beta}{L} - \frac{\Delta v \sin\beta}{L} + \frac{\Delta\sigma_1}{E} \quad (6\text{-}19)$$

where: ε_p is the axial strain at peak; L is the length of the specimen; and E is the secant elastic modulus taken at 50% of the peak strength.

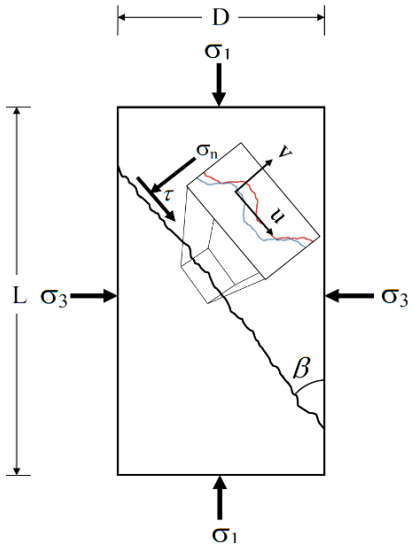

Figure 6-2: Shear stress-strain components of the failure plane in a sample subjected to triaxial compression test (adapted from Simon et al., 2003).

6.3.2 Determination of the shear behaviour of rock joints based on triaxial compression tests

Simon et al. (2003) proposed a procedure by which the shear and normal displacements of the failure plane induced by triaxial compression can be obtained. The shear stress-shear displacement curve is derived using a complete triaxial compression test curve, and the material properties are then determined by establishing the CSDS model parameters as follows:

1) The shear displacement (u) and normal displacement (v) on the failure plane are extracted from the total strain in the post-peak phase by subtracting the elastic and peak strains (Eq. 6-19).

2) The normal displacement (v), which is a function of the shear displacement (Eq. 6-13), can be isolated using an iterative technique. To do so, the first normal displacement is set as zero to

calculate the first u from Eq. 6-19. V_m is also considered zero at the onset of the shearing course. Since the variation of v is taken into account v(u=0)=0, equations 6-14 is modified to:

$$\beta_1 = u_r \left(1 - \frac{\sigma_n}{\sigma_T}\right)^4 \tan i_0 \qquad (6\text{-}20)$$

Then, Eq. 6-13 is calculated considering the initial value of u using the starting values of the CSDS model parameters. The iteration process continues until it yields a constant u. The experimental shear stress-displacement curve of the failure plane is then obtained.

3) The CSDS model parameters can be obtained by the curve-fitting method using the experimental shear stress-displacement curve (a, b, c, d, e, β_1, β_2 and β_3).

The validity of the model properties (i_o, u_p, u_r, B_0, ϕ_o, ϕ_u, ϕ_r, σ_T and S_o) are strongly dependent on the tests results. Any sudden release of the accumulated energy in the post-peak phase can lead to unreliable model properties and difficulty in curve fitting process.

6.3.3 Prediction of post-peak behaviour

In this step, the aforementioned process is back-analyzed by considering the model properties determined using the CSDS model. To estimate the post-peak behaviour of axial compression (the axial stress-strain curve), the following steps can be taken (Simon et al., 2003):

1) The shear (τ) and normal stress (σ_n) imposed on the failure plane are calculated considering the post-peak phase of each triaxial compression test (Eq. 6-17 and 6-18).

2) The CSDS model parameters (a, b, c, d, e, β_1, β_2 and β_3) are calculated for corresponding values of τ, σ_n and the measured model properties in Section 3.2.

3) The shear displacement (u) is also calculated. This value must be isolated from Eq. 6-1 while the CSDS model parameters are determined from the former step. Since two u values are isolated from Eq. 6-1, including one before peak strength and one for the post-peak phase, the accepted value is the one meets the condition of $u > u_p$. This process can be performed by Solver tools in Excel.

4) The normal displacement (v) is then calculated from the obtained u values using Eq. 6-13 considering β_1 given in Eq. 6-20.

5) The axial strain in the post-peak phase is ultimately calculated by Eq. 19 considering the shear and normal displacements on the failure plane.

6.4 Experimental procedure

In this study, a series of rock mechanics tests were carried out in order to: 1) determine the mechanical properties of the specimens; and 2) use the post-peak data points for verifying the CSDS model. Several direct shear and triaxial and uniaxial compression tests were therefore conducted on two rock types: microgabbro (MG) and basalt (BAS).

Microgabbro is a plutonic intrusive igneous rock comprised of grains with intermediate size ranging from 0.5 to 1.0 mm. The crystals in microgabbro are usually formed in an environment in which the magma is cooled down quickly. It was mainly comprised of plagioclase crystals (≈ 60%), clinopyroxene (≈ 30%) and olivine (≈ 10%). Basalt is a fine-grained igneous (volcanic) rock with grain size ranging from approximately 0.3 to 0.5 mm, containing mainly silica (45-50%), olivine, plagioclase and pyroxene (50-55%). Olivine is a significant constituent in basalt, giving it a greenish color. Other, secondary minerals might be found, such as calcite, quartz and chlorite.

6.4.1 Triaxial compression tests

Triaxial compression tests can be used to obtain the material strength properties and the post-peak portion of the stress-strain curve. A series of triaxial compression tests were therefore carried out on the two rock types using a servo-controlled Tinius Olsen testing machine with the capacity of 400,000 lbs at the rock mechanics Laboratory of École Polytechnique de Montréal, as shown in Figure 6-3. Specimens were prepared according to standard practice (ASTM) on NQ sized cylindrical core with a diameter of 47.5 mm. The length-to-diameter (L/D) ratios of the specimens were in the range of 2 to 2.4. Three confining stresses were applied to the specimens: 15, 20 and 24 MPa.

The triaxial tests were carried out on the basis of the force and axial displacement rate control adapted from Fairhurst and Hudson (1999). In this procedure, the loading phase was started with the force rate of 0.5 kN/sec until 70% of the expected peak force was approximately reached (≈ 300 kN). Then, the loading procedure was switched to an axial displacement rate of 0.04

mm/min. The displacement rate was reduced to 0.02 mm/min at 80-85% of the ultimate strength and remained constant until the complete stress-strain curve was obtained. The axial displacement was measured by two high performance LVDTs with an accuracy of 0.01 attached to the samples in the triaxial Hoek cell.

a) 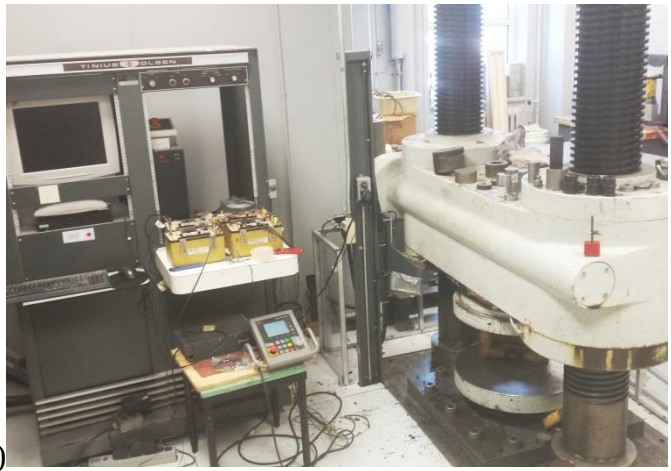 b) 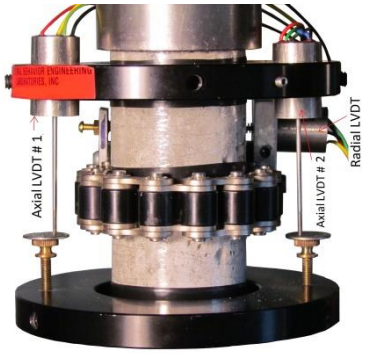

Figure 6-3: Triaxial compression test: a) 200 tons Tinius Olsen machine at Polytechnique Montréal; b) sample and LVDTs.

Figure 6-4 shows the rock specimens after the triaxial tests. The specimens, boundary conditions and rock mechanics properties obtained from the triaxial compression tests are listed in Table 6.1. The complete stress-strain curves obtained from the triaxial compression tests are shown in Figure 6-5.

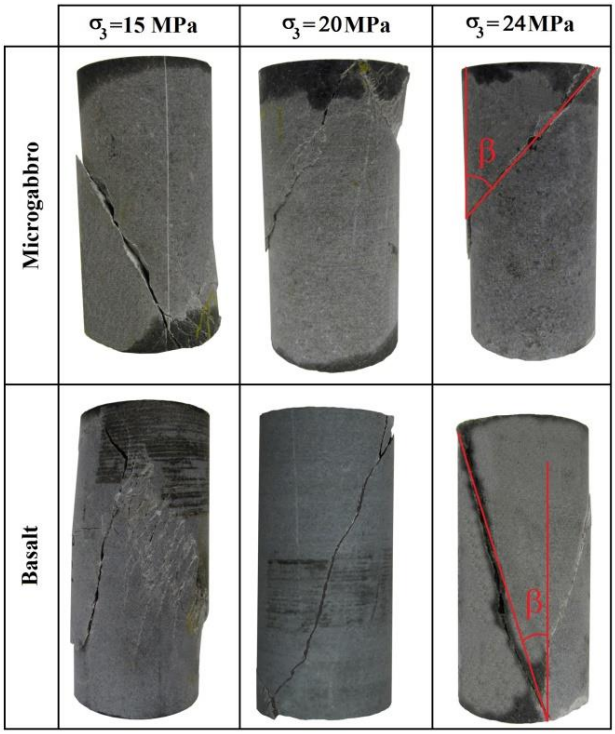

Figure 6-4: Typical results after triaxial compression tests.

Table 6.1: Summary of the triaxial compression tests and the mechanical properties of the samples.

Rock type	Sample No.	Peak strength σ_1 (MPa)	Confining stress σ_3 (MPa)	Angle of failure plane β (°)	Friction angle ϕ_o (°)	Cohesion S_o (MPa)
Microgabbro	MG-Triax-19	234	15	25.5	47	27
	MG-Triax-20	203	15	25.5		
	MG-Triax-14	202	20	31		
	MG-Triax-16	250	20	21		
	MG-Triax-31	372.6	20	21		
	MG-Triax-32	366.6	20	22		
	MG-Triax-15	190	24	32		
	MG-Triax-17	250	24	24		
	MG-Triax-30	306.7	24	30		
Basalt	BAS-Triax-14	355.5	15	15	52	33
	BAS-Triax-17	350	15	14		
	BAS-Triax-19	384.3	15	14		
	BAS-Triax-30	381.8	15	13.5		
	BAS-Triax-22	282.8	20	20		
	BAS-Triax-23	321.7	20	22		
	BAS-Triax-27	315.7	20	24		
	BAS-Triax-29	397.8	24	17		

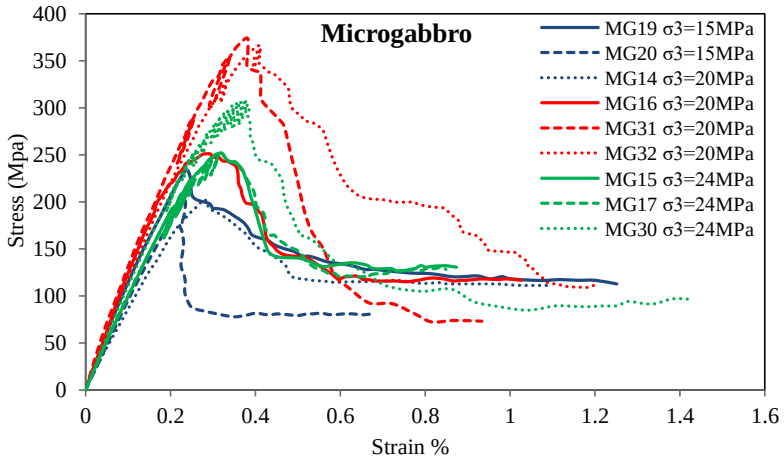

a)

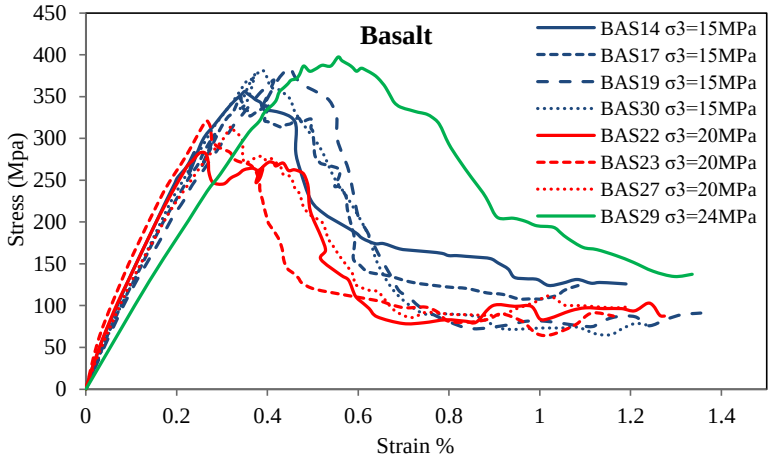

b)

Figure 6-5: Complete stress-strain curves obtained from the triaxial compression tests on microgabbro and basalt with σ_3 = 15, 20 and 24 MPa.

6.4.2 Uniaxial compression tests

Using the CSDS model and the proposed approach, the uniaxial post-peak behaviour of medium strength rocks can be predicted from the complete stress-strain curve of triaxial compression tests (Simon et al., 2003). In order to verify this approach for hard rocks, a total of 28 uniaxial compression tests (ASTM, 2008) were also conducted on the two rock types, 17 for basalt rock and 11 for microgabbro specimens, using a 600,000 lbs MTS servo-controlled testing machine at the University of Sherbrooke to obtain the post-peak phase. The uniaxial tests were carried out on cylindrical NQ rock samples with a diameter of 47.5 mm and an L/D ratio of in the range of 2 to 2.4.

The loading procedure is based on a combination of axial force and strain rate in pre- and post-peak phases (see details in Khosravi, 2016). In this method, loading is started by applying an axial force rate of 0.5 kN/sec until the applied load reached approximately 60-70% of the expected peak force. The loading mode is then switched to an axial strain rate of 4×10^{-5} µm/min. This rate remains constant until 70-80% of the expected ultimate load is obtained, at which the axial strain rate is reduced to 1×10^{-5} µm/min. This rate is kept constant until the complete stress-strain curve is obtained. Figure 6-6 shows typical specimens after the uniaxial compression tests, and the stress-strain curves obtained using the uniaxial tests are shown in Figure 6-7. Table 6.2 summarizes the mechanical properties obtained from the uniaxial tests. .

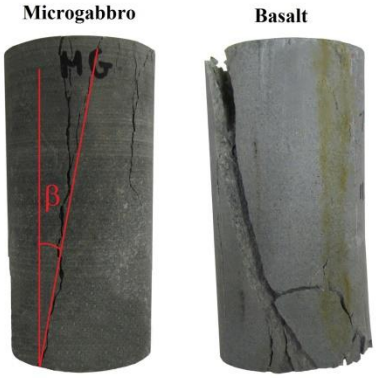

Figure 6-6: Typical results after uniaxial compression tests.

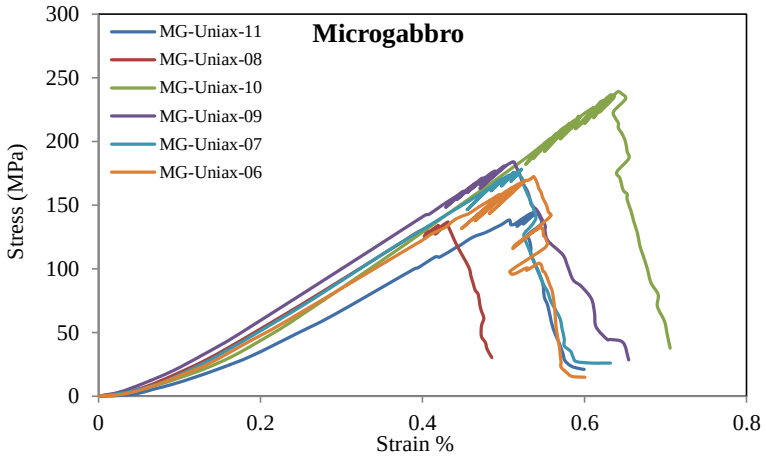

a)

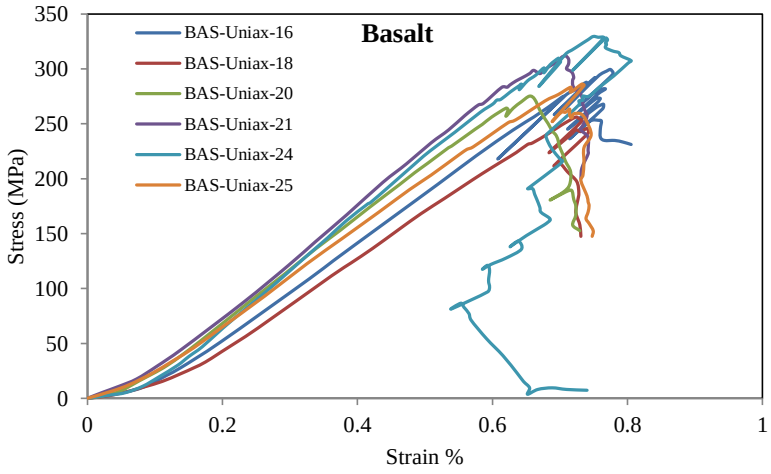

b)

Figure 6-7: Complete stress-strain curves obtained using the uniaxial compression test and strain control rate method for: a) microgabbro; and b) basalt .

Table 6.2: Summary of the uniaxial compression test results.

Rock type	Sample No.	Compressive strength (MPa)	Angle of failure plane β (º)	Elastic modulus (GPa)	Average Compressive strength (MPa)
Microgabbro	MG-Uniax-04	164.5	18	39	180
	MG- Uniax -05	230	16		
	MG- Uniax -06	172.3	9.5		
	MG- Uniax -07	177.7	14.5		
	MG- Uniax -08	136.4	17		
	MG- Uniax -09	184.33	11		
	MG- Uniax -10	238.8	14		
	MG- Uniax -11	144.9	17		
	MG- Uniax -12	304.9	9.5		
Basalt	BAS- Uniax -12	156.3	14.7	45.4	280
	BAS- Uniax -13	313.5	22		
	BAS- Uniax -16	299	20		
	BAS- Uniax -18	256	13		
	BAS- Uniax -20	275.1	15		
	BAS- Uniax -21	312.8	16		
	BAS- Uniax -24	330	12		
	BAS- Uniax -25	285.9	16		
	BAS- Uniax -26	305.3	18		
	BAS- Uniax -27	251	27		
	BAS- Uniax -28	287.6	18		

6.4.3 Direct shear tests

Two series of direct shear tests were carried out on rock joints created artificially by splitting the cylindrical specimens along their axes. The objective of these tests was to determine the strength

properties of the specimens. The shear behaviour of the rock joint in the direct shear test was also compared to the shear behaviour of the failure plane induced by the triaxial compression tests using the CSDS model. It was also postulated that the direct shear tests could be used to predict the uniaxial post-peak behaviour. The tests were conducted under constant normal load (CNL) boundary condition. The normal stresses applied to the microgabbro and basalt was in the range of 10-17 MPa and 3-8 MPa, respectively. The joint specimens were cast in shear boxes according to ASTM D6507-08 (2008). The molding material used for the basalt samples was Hydro-stone (USG) with a uniaxial compressive strength of 6.9 MPa in dry condition. The material used to mold the microgabbro specimens was SikaGrout212, which has a uniaxial compressive strength of 26 MPa after 24 hours; however, some of the tests failed due to compaction of the SikaGrout212 during the shear test, and the molding material for the microgabbro was changed to Sika® Pronto 11, which has a strength of 56 MPa after 24 hours. The shear tests were conducted at the University of Sherbrooke using a servo-controlled testing machine with a loading capacity of 300 tons (MTS) and the shearing loading rate of 0.25 mm/min, as shown in Figure 6-8.

Figure 6-8: 300 tons MTS testing machine at University of Sherbrooke.

Normal and shear displacements were measured using two extensometers (run of 25.00±0.05 mm) with high-precision repeatability. The tests were run until the residual shear strength was obtained. The test conditions and mechanical parameters for the two rock types are summarized in Table 6.3. Figure 6-9 shows the shear stress-shear displacement curves obtained from the shear tests on the microgabbro and basalt along with a sheared specimen.

Table 6.3: Summary of shear tests and obtained mechanical properties.

Rock type	Normal stress (MPa)	No. of specimens	Peak shear displ. u_p (mm)	Residual shear displ. u_r (mm)	Peak friction angle ϕ_u (^{o})	Residual friction angle ϕ_r (^{o})
Microgabbro	10	3	0.66	5	45	43
	14	3	0.87	5		
	17	4	0.93	6		
Basalt	3	2	0.31	5.5	48	46
	5	2	0.35	6		
	8	2	0.44	6		

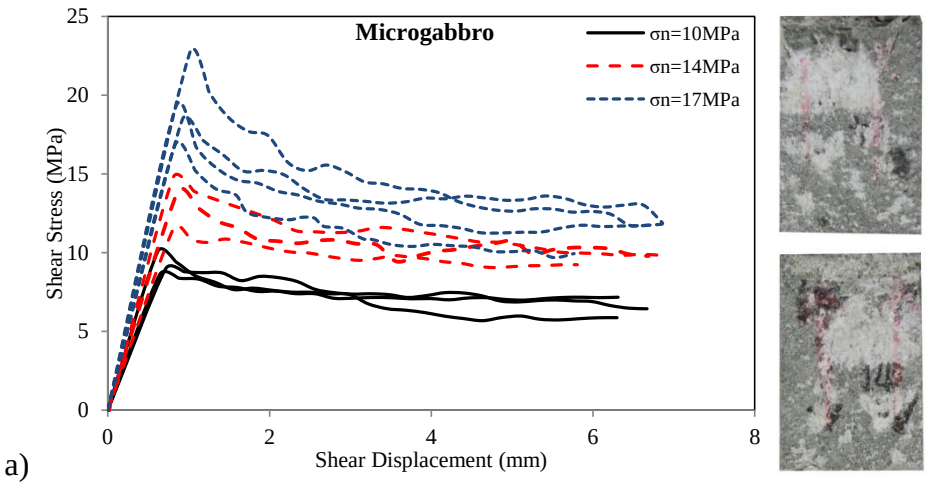

a)

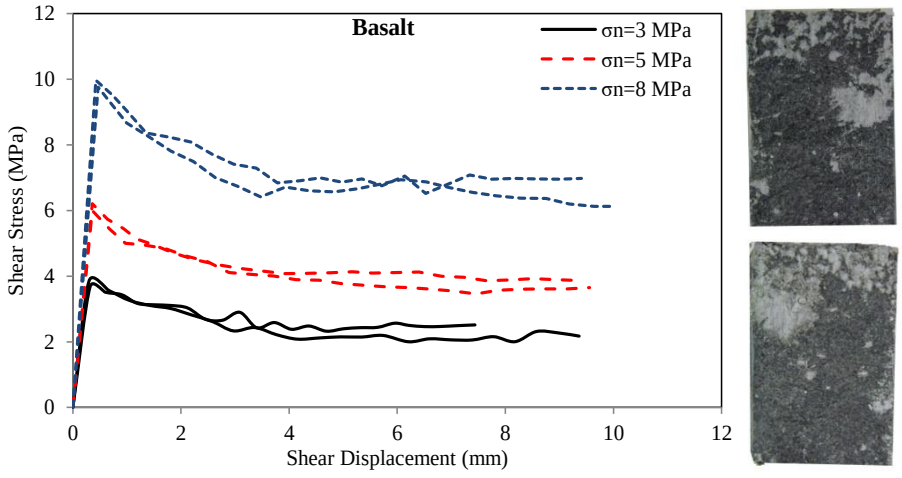

b)

Figure 6-9: Results of direct shear tests and sheared joints on: a) microgabbro; and b) basalt.

6.5 Post-peak estimation using the new approach

6.5.1 Application to triaxial compression tests

The proposed approach (Simon et al., 2003) can be used to obtain the post-peak behaviour of rocks under triaxial compression. To do so, the results of triaxial compression tests on two rock types were used to determine the shear behaviour of the induced failure plane. The CSDS model properties were also obtained from the shear behaviour of the failure plane, based on the proposed approach described in Sections 3.1 to 3.3. The larger the number of triaxial tests, the more accurate the CSDS model properties obtained, and accordingly, the better the estimation of post-peak behaviour. Table 6.4 presents the CSDS model properties determined for each test by curve fitting. In the table, σ_T is the uniaxial compressive strength and E is the elastic modulus obtained from the uniaxial compression tests. The failure plane angle, β, was also measured from the triaxial tests. Other CSDS properties were adjusted so that the model (solid lines) was fitted on the τ-u curves of the available triaxial tests (data points), as shown in Figures 6-10a and 6-10c.

Table 6.4: CSDS model properties obtained from triaxial compression tests on microgabbro and basalt.

Specimen	σ_3 (MPa)	E (GPa)	β (°)	u_p (mm)	u_r (mm)	i_o (°)	σ_T (MPa)	S_o (MPa)	ϕ_u (°)	ϕ_0 (°)	ϕ_r (°)
Microgabbro											
MG- Triax-19	15	39	25.5	0.005	2.5	28	180	27	48	52	46
MG- Triax -20	15	39	25.5	0.005	2.5	28	180	27	45	50	39
MG- Triax -14	20	39	31	0.005	2.7	28	180	27	41	50	39
MG- Triax -16	20	39	21	0.005	2.5	28	180	27	45	50	41
MG- Triax -31	20	39	21	0.005	2.5	28	180	27	43	50	42
MG- Triax -32	20	39	22	0.005	2.5	28	180	27	44	53	42
MG- Triax -15	24	39	32	0.005	2.5	25	180	27	42	47	39
MG- Triax -17	24	39	24	0.005	2.5	25	180	27	45	48	41
MG- Triax -30	24	39	30	0.005	2.5	25	180	27	43	47	41
Average		39		0.005	2.5	27	180	27	44	50	41
Basalt											
BAS- Triax -14	15	45.4	15	0.005	3	31	280	33	49	53	46
BAS- Triax -17	15	45.4	14	0.005	3	31	280	33	48	53	46
BAS- Triax -30	15	45.4	14	0.005	4.2	33	280	33	49	53	46
BAS- Triax -23	20	45.4	22	0.005	3	33	280	33	47	53	46
BAS- Triax -27	20	45.4	24	0.005	3.2	33	280	33	47	53	46
BAS- Triax -29	24	45.4	17	0.005	3	33	280	33	48	53	46
Average		45.4		0.005	3.2	32	280	33	48	53	46

The post-peak behaviour of the samples subjected to the triaxial loading was then estimated using the CSDS model. Figures 6-10b and 6-10d show the post-peak curves obtained for the two rock types using this approach. Three confining stresses were applied: 15, 20 and 24 MPa. It can be seen that the slope of the post-peak portion decreases with an increase in confining pressure on the specimens. Also, curve fitting was better curve for the microgabbro, with lower UCS values, than for the basalt, with higher UCS.

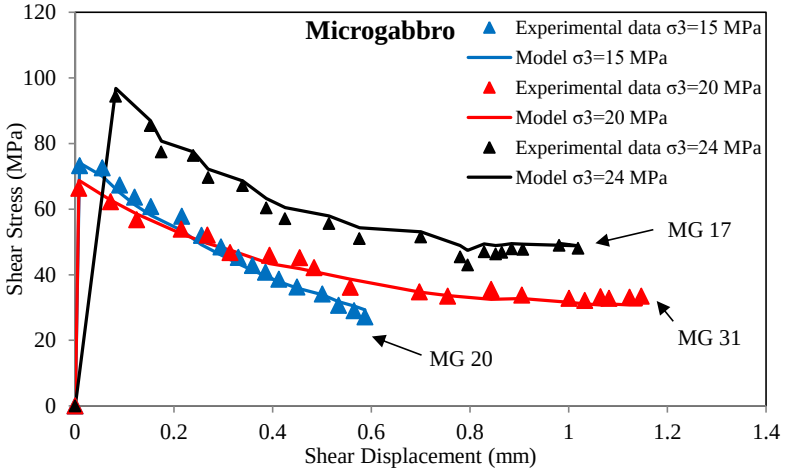

a)

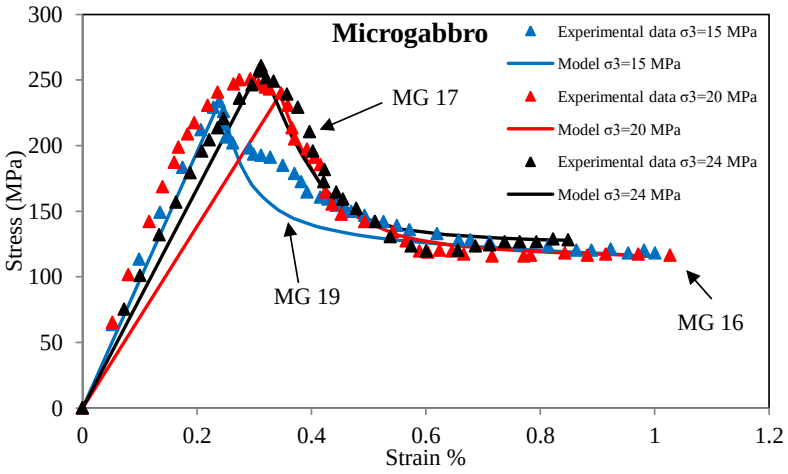

b)

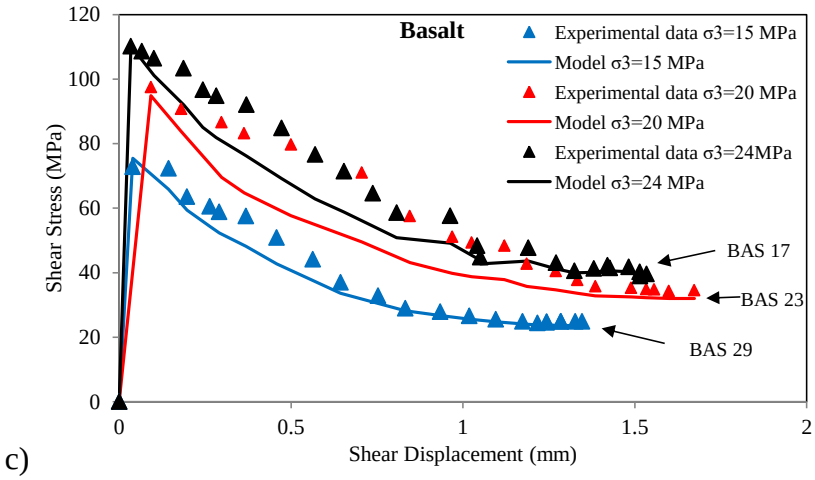

c)

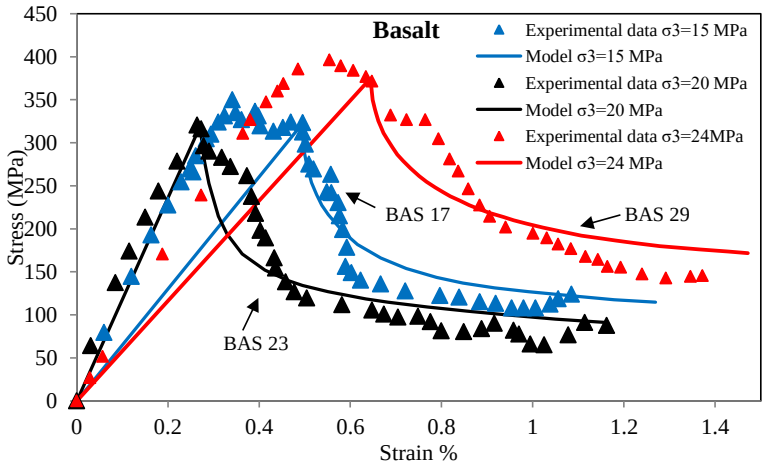

d)

Figure 6-10: Application of the proposed approach (Simon et al. 2003) to obtain shear stress-displacement curves for: (a) microgabbro, (b) basalt; and complete triaxial compression stress-strain curves for: (c) microgabbro, (d) basalt

The results also indicate that the experimental post-peak stress-strain curves are closely approximated by the modeled curves obtained using the proposed approach.

6.5.2 Application to uniaxial compression tests

The same approach can be also used for the uniaxial test results on hard rock specimens. To do so, the results of uniaxial compression tests on basalt and microgabbro were analysed. Table 6.5 shows the CSDS model properties, including the elastic modulus, E, and the uniaxial compressive strength, $\sigma_{T,}$ determined for each uniaxial compression test. The failure plane angle, β, was also measured for each uniaxial test.

Table 6.5: The CSDS model properties used for the prediction of the post-peak behaviour of the uniaxial compression tests.

Specimen	E (GPa)	β (°)	u_p (mm)	u_r (mm)	i_o (°)	σ_T (MPa)	S_o (MPa)	ϕ_u (°)	ϕ_0 (°)	ϕ_r (°)
Microgabbro										
MG-Uniax-07	39	14.5	0.006	5	37	180	27	45	50	42
MG-Uniax-10		14	0.006	5	37	180	27	47	50	43
Average			0.006	5	37	180	27	46	50	42.5
Basalt										
BAS-Uniax-25	45.4	16	0.006	5	35	280	33	49	53	46
BAS-Uniax-21		16	0.006	5.2	36	280	33	49	53	46
Average			0.006	5.1	35.5	280	33	49	52	46

Other CSDS model properties were obtained for each test using curve fitting method. It can be seen that the values of i_o and u_r are higher than those obtained using curve fitting on the triaixal tests. Other model properties are fairly similar to those obtained for the triaxial post-peak curves.

Figure 6-11 shows the uniaxial post-peak curves obtained for the microgabbro and basalt specimens using the proposed approach. It can be seen that the estimated post-peak curves based on the proposed approach (solid line) are in good agreement with those obtained experimentally (data points).

6.6 Estimation of the CSDS model properties using the shear test

It was postulated that the CSDS model properties could be also obtained by fitting the CSDS model to the experimental results of direct shear tests. Consequently, direct shear tests were conducted on rock joints artificially created by the splitting method (Figure 6-9). Table 6.6 presents the CSDS model properties determined for each test using curve fitting. Again, the values of σ_T and elastic modulus, E, were taken from the uniaxial compression tests. A significant difference can be seen between the model properties obtained from the direct shear tests and those obtained from the triaxial compression tests (Table 6.4).

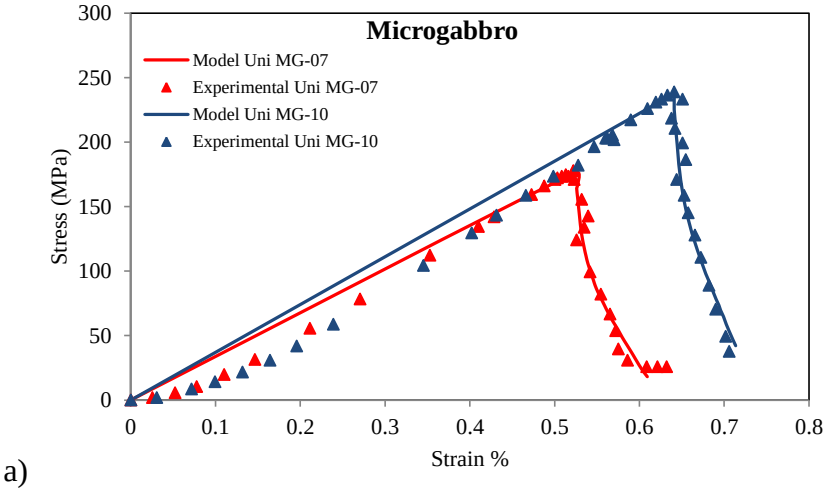

a)

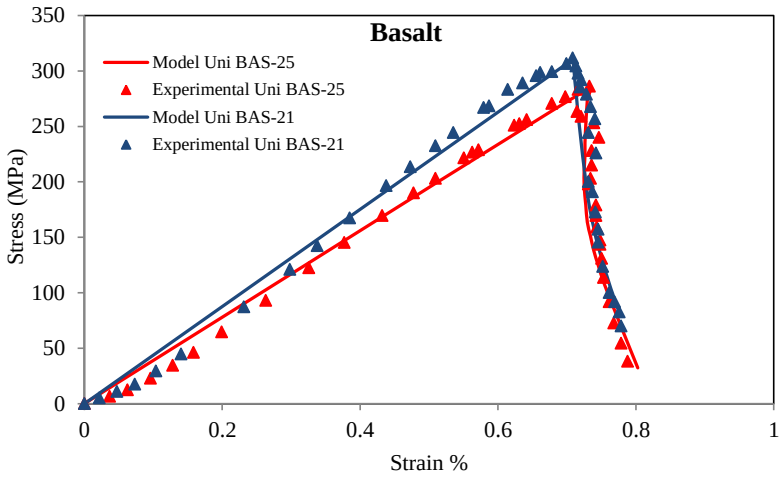

b)

Figure 6-11: Application of the proposed approach to predict the post-peak behaviour of specimens subjected to the uniaxial compression test for: a) microgabbro; and b) basalt.

For instance, a 100% difference is observed between the average values of residual shear displacement, u_r, and a 285% difference can be observed in the average values of the asperity angle, i_o, obtained using curve fitting on the triaxial and direct shear test results. Figure 6-12 shows the curves fitted to the result of the direct shear tests (data points) for the basalt and microgabbro specimens using the proposed approach (solid lines). Good agreement can be seen between the post-peak shear behaviour of the rock joints determined using the CSDS model and that determined using the experimental data.

Table 6.6: The CSDS model properties obtained from the result of direct shear tests on microgabbro and basalt.

Specimen	σ_n (MPa)	u_p (mm)	u_r (mm)	i_o (°)	σ_T (MPa)	S_o (MPa)	ϕ_u (°)	ϕ_0 (°)	ϕ_r (°)
Microgabbro									
MG-Shear-12	10	0.6	6	5	180	27	32	35	32
MG-Shear-13	10	0.5	5	5	180	27	33	36	33
MG-Shear-15	10	0.6	5	6	180	27	33	36	30
MG-Shear-06	14	0.5	6	10	180	27	34	37	31
MG-Shear-07	14	0.6	5	8	180	27	33	36	32
MG-Shear-08	14	0.6	5.5	9	180	27	34	36	33
MG-Shear-01	17	0.6	5	8	180	27	34	36	29
MG-Shear-16	17	0.6	5	6	180	27	38	39	36
MG-Shear-18	17	0.6	5	9	180	27	38	39	36
Average		0.6	5.3	7	180	27	34	37	32
Basalt									
BAS-Shear-01	3	0.3	6	6	280	33	43	44	43
BAS-Shear-02	3	0.3	5.5	6	280	33	42	43	42
BAS-Shear-03	5	0.3	6	6	280	33	40	43	37
BAS-Shear-04	5	0.3	5.5	6	280	33	41	43	38
BAS-Shear-05	8	0.35	6	6	280	33	42	43	42
BAS-Shear-06	8	0.4	6	6	280	33	42	43	38
Average		0.32	5.8	6	280	33	42	43	40

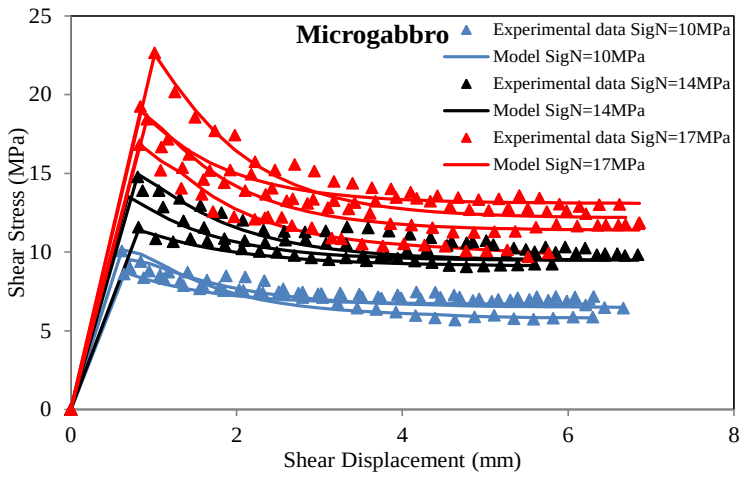

a)

b)

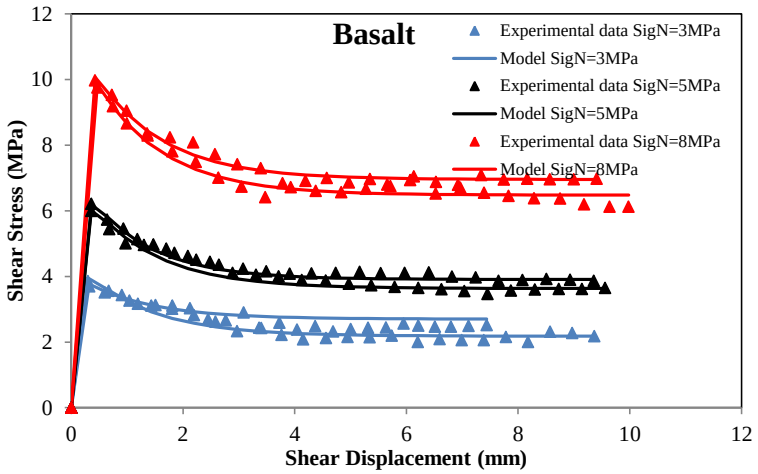

Figure 6-12: Comparison between the results of the CSDS model and direct shear tests (CNS): a) Microgabbro specimens with σ_n= 10, 14 and 17 MPa; and b) Basalt specimens with σ_n= 3, 5 and 8 MPa.

6.7 **Initial asperity angle**

In the current study, the application of the CSDS model is highly dependent on the accuracy of the model properties. One of the CSDS model properties, initial asperity angle (i_o), can be measured by characterizing the fracture surface. Initial asperity angle is one of the most important parameters in the CSDS model. i_o corresponds to the initial asperity angle over which the shearing process is mobilised at very low normal load, $i_{0\,max}$is the highest asperity angle in a given sampling interval (Figure 6-13a), and $i_{0\,ave}$ is the average value of the asperity angles along the shearing direction in terms of the sampling interval. Figure 6-13b shows the variation in asperity angle over the roughness profile in the shearing. In the case of low normal load on a joint surface, the joint slides on the steepest asperities at the onset of the shearing process as seen in Figure 6-13c. The asperities will be sheared off under high normal load, with the shearing process depending on the mechanical properties of the joint surface. This parameter therefore plays an undeniable role in the shear behaviour of the rock joint.

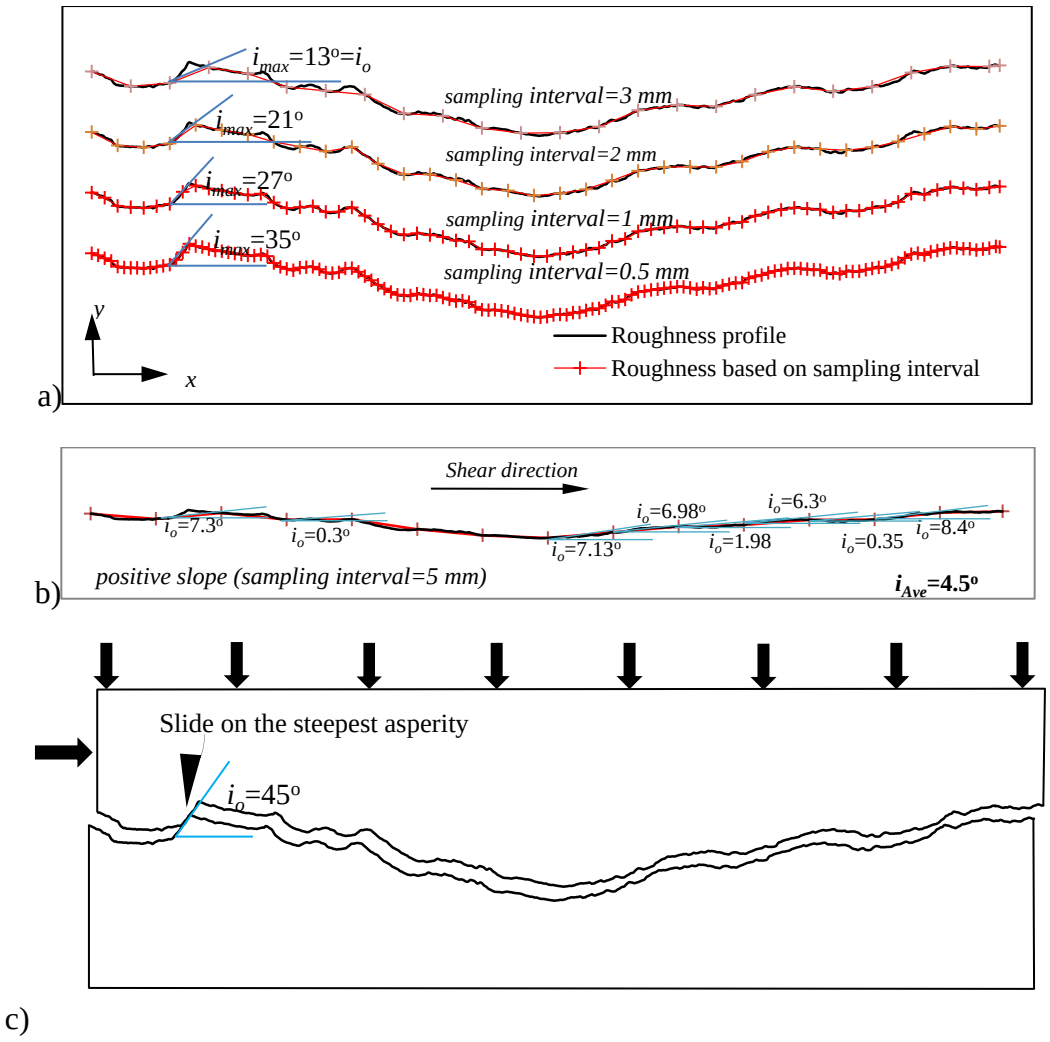

Figure 6-13: Asperity angle of a rock joint: a) maximum asperity angle in terms of sampling intervals; b) average asperity angle in shearing direction; c) the role of initial asperity angle on the joint sliding.

In this part of the study, the variation of the asperity angle over fractures was also investigated. The asperity angles were obtained from the fracture surfaces created using splitting, uniaxial compression tests and triaxial compression tests at σ_3 = 3, 8 and 13 MPa. The fractures were retrieved from uniaxial and triaxial compression test as soon as they were created. The tests were carried out with a displacement rate of 1 µm/sec on 30 cylindrical NQ rock samples (see details in Khosravi 2016). The fracture surfaces were then characterized using a 3D laser profilommeter (Kreon Zephyr© 25) to obtain the asperity angle in 2D. In order to avoid any scale effect, a 70 mm section was chosen from the total length of the roughness profiles in all fracture samples.

Figure 6-14 shows the variation of the maximum and average asperity angles for the fracture surfaces in the microgabbro and basalt, at a sampling interval of 0.5 to 5 mm.

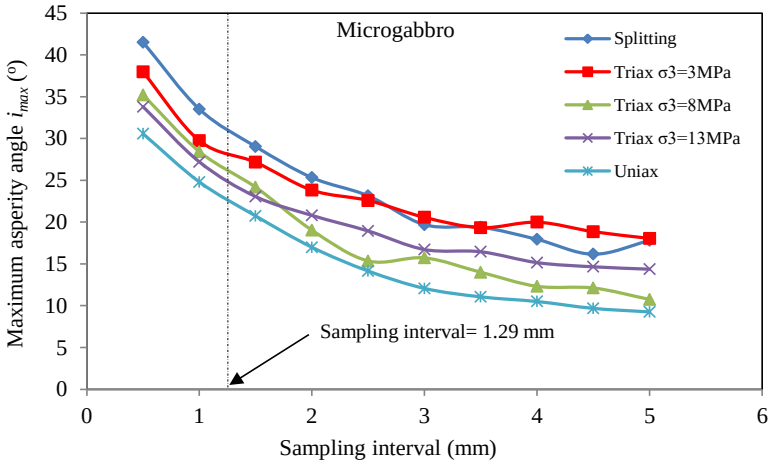

a)

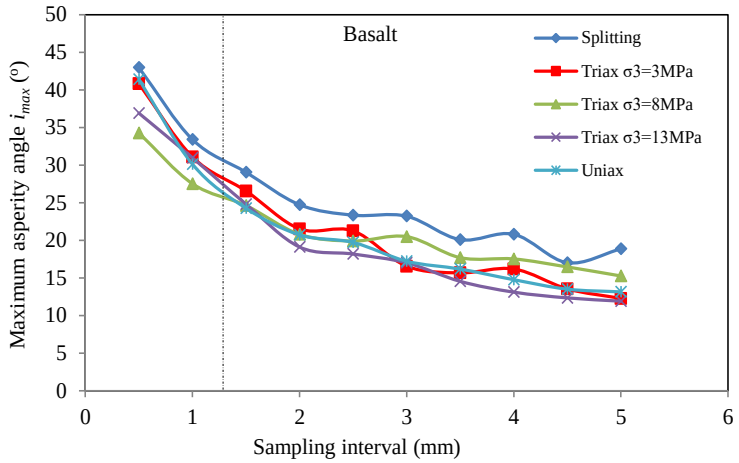

b)

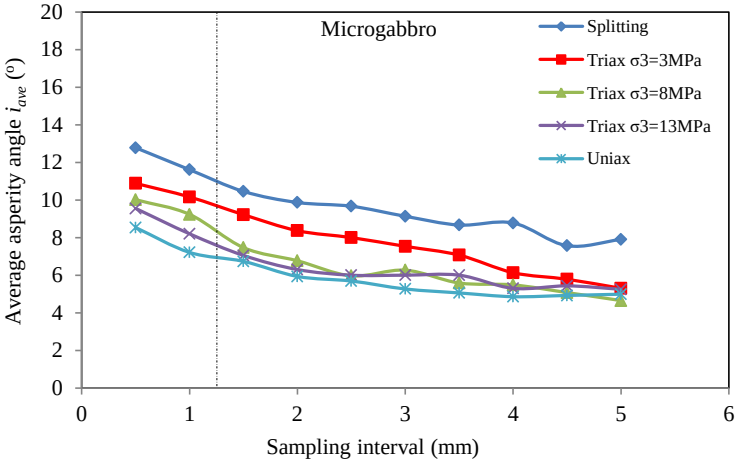

c)

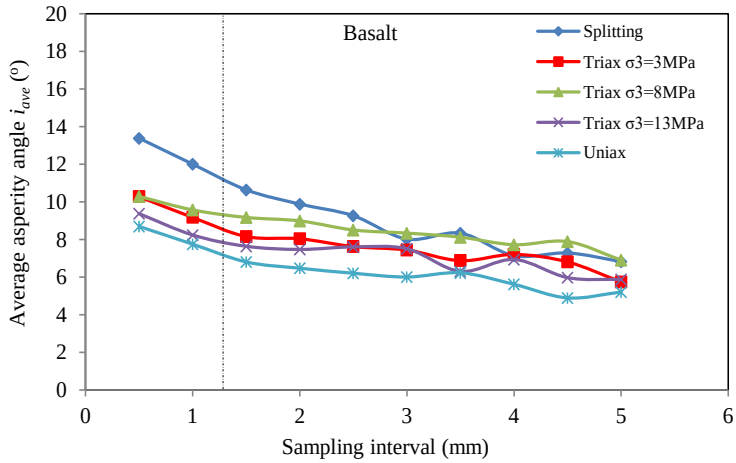

d)

Figure 6-14: Variation of: maximum asperity angle (i_{max}) with the sampling interval for (a) microgabbro and (b) basalt; and variation of: average asperity angle (i_{ave}) for (c) microgabbro; and (d) basalt.

An optimized sampling interval of 1.29 mm, equal to 1.85% of the joint length of 70 mm (Deng et al. 2004), was considered to measure the asperity angle. This sampling interval is displayed in Figure 6-14 by a vertical dashed-dotted line. It can be seen that the maximum and average asperity angles decrease with sampling intervals.

Based on the CSDS approach, the model properties are obtained from the result of triaxial compression tests. For this reason, the triaxial test conducted under the confining stress of 13 MPa was chosen for the investigation. In the fracture surface created by triaxial compression testing with the confining stress of 13 MPa, the maximum asperity angle decreases by up to 58% (from 35° to 14.4°) in the microgabbro and 67% (from 36.9° to 11.9°) in the basalt. The average asperity angle also decreases by up to 45% (from 9.5° to 5.25°) in the microgabbro and 37% (from 9.4° to 5.9°) in the basalt. The asperity angle decreases until a particular sampling interval is reached (stationary threshold) beyond which the trend line becomes horizontal. Figure 6-14 shows that the stationary threshold occurs at a sampling interval higher than 5 mm.

At a sampling interval of 1.29 mm, the maximum asperity angles in triaxial testing (with σ_3 = 13 MPa) on the microgabbro and the basalt were approximately 23^o and 28^o, respectively. The average asperity angle was 7^o for both the microgabbro and the basalt at the same sampling interval of 1.29 mm.

Furthermore, the asperity angle of the fractures shows a specific trend at each sampling interval. At a sampling interval of 1.29 mm, the fractures obtained from splitting, triaxial tests (σ_3 = 3, 8, 13 MPa) and uniaxial tests can be categorized from steepest to smoothest surface.

6.8 Discussion

6.8.1 Brittleness

One of the most important rock properties is brittleness. The concept of rock brittleness is based on the strain-dependent mobilization of cohesion and friction of rock. Rock brittleness characterizes a rock's potential for violent failure (Aubertin et al., 1994; Hajiabdolmajid and Kaiser, 2003; Altindag, 2010). Brittleness can be used to assess the stability of underground excavations. The severity of strength loss in hard brittle rocks can be evaluated using brittleness indices. The Brittleness Index Modified (BIM) is a brittleness measure based on the analysis of elastic energy in the pre-peak phase of the stress-strain curve (Aubertin and Gill, 1988). The BIM value can be related to the $|E/E'|$ ratio, where E and E' are the pre-peak and post-peak moduli of the stress-strain curve (Aubertin et al., 1994). E' is the maximum negative slope of the stress-strain curve. Figure 6-15 shows the correlation between BIM and $|E/E'|$ based on the results obtained for the microgabbro and basalt. Based on the BIM values, these two rock types can be classified as very brittle material in which a violent failure occurs at peak strength. Also, it can be seen that the BIM values and equation obtained for these rock types are in the same range as those depicted by Aubertin et al. (1994).

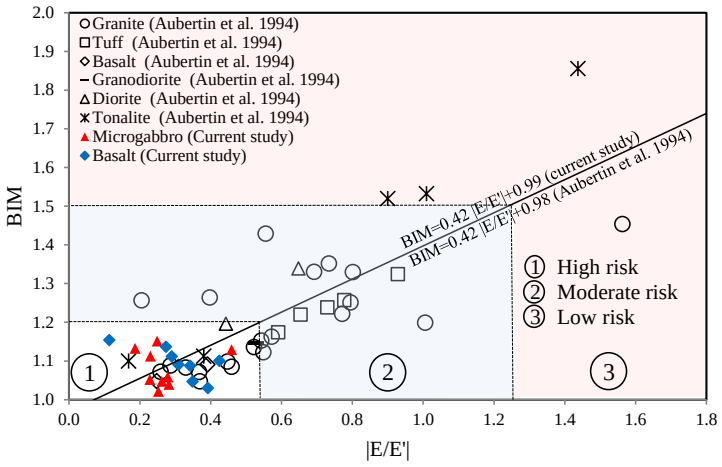

Figure 6-15: Relation between brittleness (BIM) and |E/E′| for the current study.

High brittleness can affect the post-peak behaviour of very hard rock. In this study, the influence of brittleness can be observed by estimating the shear behaviour of the failure plane in the triaxial compression of the basalt (Fig. 6-10c). It indicates that the quality of the post-peak curve in triaxial compression testing is critical to obtaining a good result.

6.8.2 CSDS model properties obtained from laboratory tests

Table 6.7 summarizes the average CSDS model properties obtained using the curve fitting method on the uniaxial and triaxial compression, and direct shear tests. A discrepancy can be observed in some of the model properties obtained by curve fitting to the various test results, most notably the asperity angle, i_o, and the peak and residual shear displacements, u_p and u_r, as shown in Table 6.7.

Table 6.7: The average CSDS model properties based on curve fitting method on uniaxial, triaxial, and direct shear test results.

Tests	Specimens	β (°)	u_p (mm)	u_r (mm)	i_o (°)	σ_T (MPa)	S_o (MPa)	ϕ_u (°)	ϕ_0 (°)	ϕ_r (°)
Uniaxial	Microgabbro	14	0.006	5	37	180	27	46	50	42.5
	Basalt	16	0.006	5.1	35.5	280	33	49	52	46
Triaxial	Microgabbro	-	0.005	2.5	27	180	27	44	50	41
	Basalt	-	0.005	3.2	32	280	33	48	53	46
Direct shear	Microgabbro	-	0.6	5.3	7	180	27	34	37	32
	Basalt	-	0.32	5.8	6	280	33	42	43	40

6.8.2.1 Results of triaxial compression and direct tests

Table 6.7 shows a difference between the model properties estimated based on the triaxial compression and direct shear test results (i_o, u_p, u_r, β, ϕ_o, ϕ_u and ϕ_r) using the curve fitting method. The shear tests were conducted under constant normal load conditions, while the shearing process in the triaxial tests occurred in variable normal stiffness. As since the loading boundary condition on the failure planes is quite different in triaxial and direct shear tests, the post-peak behaviours are not similar in those tests. It can be inferred that loading boundary conditions significantly influence the CSDS model properties.

-Influence of loading conditions on peak shear displacement (u_p)

Table 6.7 shows the peak shear displacement, u_p, obtained by the CSDS model using the curve fitting method. It can be seen that the u_p value obtained from the direct shear and triaxial

compression tests are 0.6 and 0.005 mm, respectively, for microgabbro and 0.32 and 0.005 mm for the basalt specimens. In direct shear tests, the rock joints were fully matched, and the peak shear displacements of 0.6 mm and 0.32 mm are therefore due to compacting of the two halves of the joint by the normal stress and instantaneous damage of the unevenness asperities at the mobilization threshold. The u_p value obtained by the CSDS model for the direct shear tests is in good agreement with the experimental data (Table 6.3). The very small peak shear displacement of 0.005 mm for the triaxial compression tests is due to immediate mobilization of the asperities during the fracturing process.

-Influence of loading conditions on residual shear displacement (u_r)

Table 6.7 shows important variation between the residual shear displacements (u_r) obtained by the CSDS model for the triaxial compression tests and the direct shear tests. It can be seen that the u_r values for the direct shear tests are approximately 5.3 mm for the microgabbro and 5.8 mm for the basalt. These values are almost 1.8 to 2.1 times those obtained for the triaxial compression tests, i.e., 2.5 for the microgabbro and 3.2 mm for the basalt. This discrepancy may be due to different applied loading boundary condition. The normal stress on the induced failure plane is initially much higher in the triaxial compression than in the direct shear test, and then decreases until it reaches the residual strength. In the direct shear test, the normal stress is kept constant in the pre- and post-peak phase. In the triaxial compression tests, the asperities are therefore sheared off at the onset of mobilization due to high normal stress.

Figure 6-16 illustrates the two fracture surfaces created by a triaxial compression test with a confining stress of 20 MPa and a direct shear test with a normal stress of 17 MPa on the microgabbro specimens. It is worth noting that the initial normal stress in the triaxial compression test was 68.4 MPa at the onset of mobilization while the normal stress was almost 44.5 MPa at residual displacement. These normal stresses in the pre- and post-peak phases are much higher than those applied in the direct shear test (17 MPa). After filtering the contact area in the two specimens (highlighted area in Fig. 6-16), one can see that almost 75% of the surface was sheared off in the triaxial compression test, while, this area was approximately 50% in the direct shear test. Furthermore, residual shear displacement takes place over a shorter distance in the triaxial compression test than in the direct shear test due to shearing off a higher percentage of asperities in the triaxial compression test.

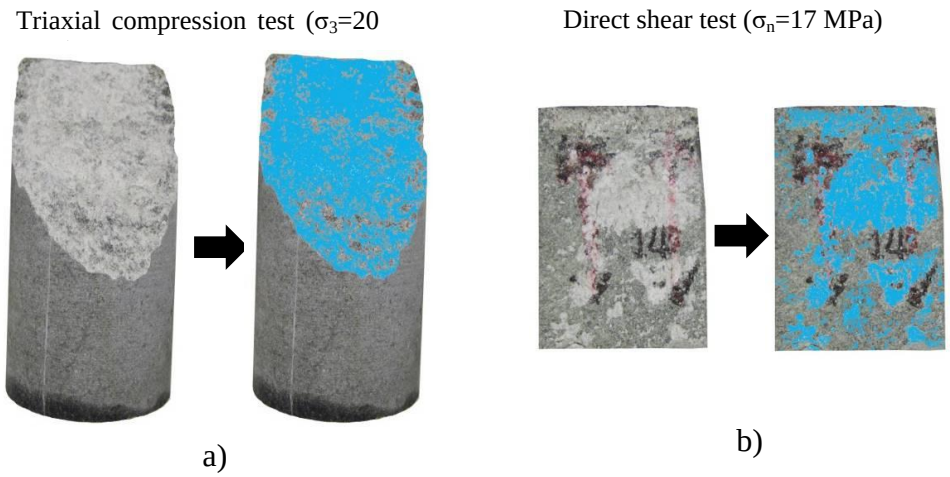

Figure 6-16: Contact area on the failure surface of microgabbro specimens in a) triaxial compression test (σ_3=20 MPa); and b) direct shear test (σ_n=17 MPa).

-Influence of loading conditions on initial asperity angle (i_0)

Initial asperity angle (i_0) is an important parameter of the fracture surface that affects both shear and normal behaviour of the joint. A considerable difference was observed between the initial asperity angles obtained using the CSDS model (curve fitting method) on the direct shear test and the triaxial compression test (Tab. 6.7). For instance, the asperity angle obtained using the CSDS model based on the direct shear test are 7˚ and 6˚ for the microgabbro and basalt while these are 27˚ and 32˚ from the triaxial test results.

The maximum asperity angle, $i_{0\,Max}$, of the failure plane created by the triaxial tests was also measured as shown in Figures 6-14a and 6-14b. It can be seen that the maximum measured asperity angles in a sampling interval of 1.29 mm are 24° for the microgabbro and 28° for the basalt when σ_3 = 13 MPa.

In addition, the average asperity angle, $i_{0\,Ave}$, measured in the same confining stress and the sampling interval is approximately 8° for both basalt and microgabbro as shown in Figures 6-14c and 6-14d. After comparing the curve fitting results (the CSDS model) with the measured values, it was inferred that the asperity angle derived from the CSDS model using the direct shear test results is close to the average asperity angle (≈ 8°) measured using the results of triaxial testing with σ_3 =13 MPa. In addition, the asperity angles derived from the CSDS model on the

triaxial test results, i.e., 27° for the microgabbro and 32° for the basalt, are almost the same as to the maximum asperity angles measured in the triaxial tests with σ_3 =13 MPa (Fig. 6-14).

The difference between the initial asperity angles obtained from the direct shear tests and the triaxial compression tests can be related to the roughness anisotropy of the fracture surface in terms of the normal stress on the failure plane. To study the impact of roughness anisotropy on the initial asperity angle, three fracture surfaces created by splitting, uniaxial compression tests and triaxial compression tests (at confining stresses of 3, 5 and 8 MPa) on the microgabbro were characterized. To do so, the roughness profiles extracted from these fracture surfaces were divided into three sections, left, middle and right as shown in Figure 6-17.

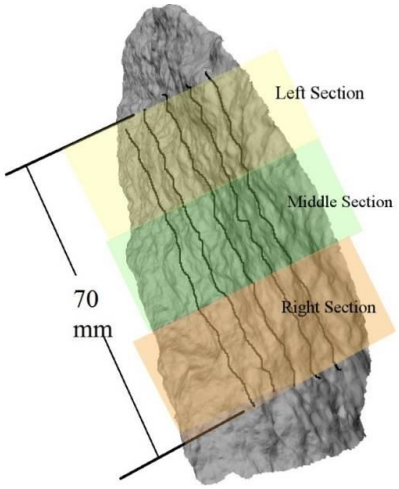

Figure 6-17: Three sections of roughness profiles on the fracture surface.

Two measurements of $i_{o\,max}$ and $i_{o\,ave}$, were obtained for each section on at least three roughness profiles. Fracture surfaces induced by splitting and uniaxial and triaxial compression tests were then compared in terms of the average and maximum asperity angles along the sections at a sampling interval of 1.0 mm, as shown in Figure 6-18.

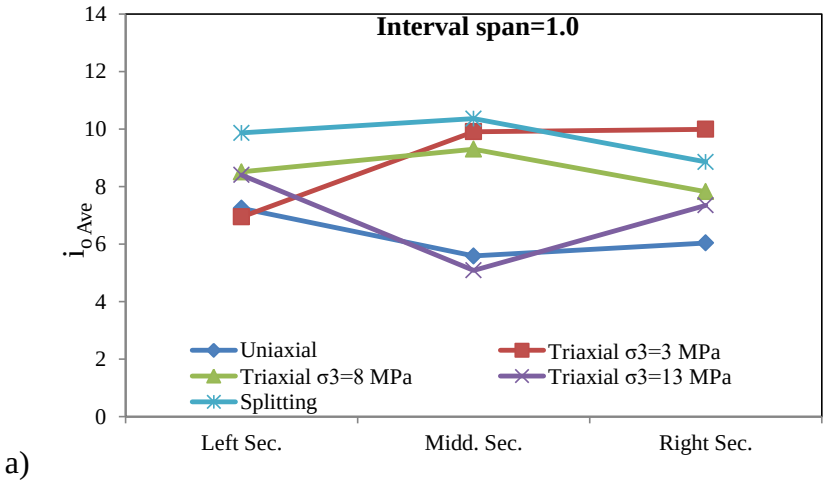

a)

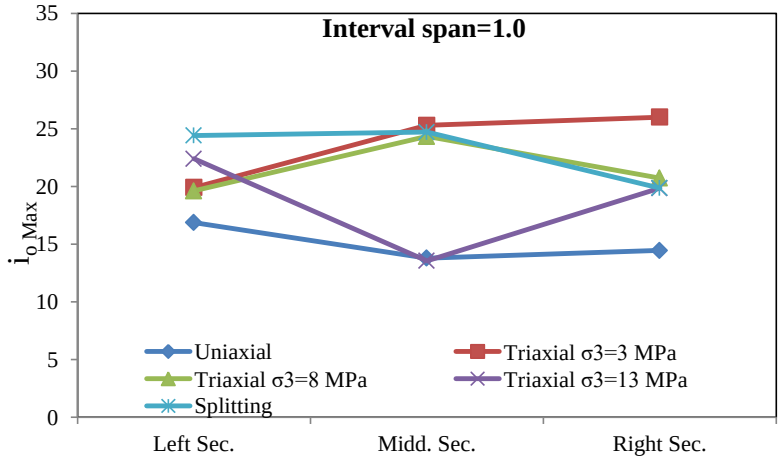

b)

Figure 6-18: Sectional variation of the asperity angle: a) $i_{o\ ave}$ and b) $i_{o\ max}$.

As can be seen, the variation of the asperity angle is not considerable from the left section to the right one in the fractures induced by splitting and uniaxial compression. For instance, the variation from the left to the right section is less than 1° for $i_{o\ ave}$ in both the splitting and uniaxial fractures and 2° and 5° for $i_{o\ max}$ is in the splitting and uniaxial fractures, respectively. In addition, both the average and maximum asperity angles for the middle section of the splitting fracture are higher than for the other two sections. In the uniaxial compression test fracture, those values are lower for the middle section than for two other sections. In the fractures created by the triaxial test with confining stresses of 3 and 8 MPa, the average and maximum asperity angles for the middle section are higher than for the other two sections. When the confining stress is increased to 13 MPa, the value of these measurements is lower for the middle section than for the other two sections. For instance, the value of $i_{o\ ave}$ for the middle section of the fractures created

by splitting, uniaxial compression and, triaxial compressions (σ_3=3, 8 and 13 MPa) are 10.3°, 5.6°, 9.9°, 9.2° and 5.1°, respectively. Also, the variation trend of the asperity angle for the middle section is significantly different than the trend for the other two sections. As can be seen, with σ_3 = 13 MPa, the average asperity angle is 5.1° for the middle section but 8.4° and 7.3° for the left and right sections, respectively. It can be inferred that at higher confining stresses, the asperity angle for the middle section is smoother than for the other sections. It can be also concluded that the middle section of the specimen is considerably influenced by the applied normal stress and may control the initial shearing process of the failure plane. Since the middle section is one third of the fracture area, it is recommended that the scale effect on the asperity angle parameter of the model be considered.

- *Angle of the failure plane induced by axial compression (β)*

The failure plane angle (β) is a key parameter in triaxial compression test results. The magnitude of the normal and shear stresses acting on the failure plane are significantly influenced by the failure plane angle (β). This angle can be visually measured after each test. A simple method for estimating is based on the *L/D* ratio of the specimen (Simon et al., 2003). For instance, for a standard *L/D* ratio of 2-2.5, β is in the range of 21-27°. However, a different failure plane angle (i.e. 20° to 40°) can be observed based on parameters such as rock type (Hakami, 1988). In this study, the measured failure plane angles for the triaxial compression tests were in the range of 20.5° to 32° for the microgabbro and 13.3° to 24° for the basalt specimens. Figure 6-4 displays the fracturing patterns and the failure plane angles for the microgabbro specimens.

6.8.2.2 Triaxial and uniaxial compression tests results

Determination of the post-peak stiffness of hard rock under uniaxial compression is always difficult due to a sudden failure. In the approach proposed by Simon et al. (2003), the post-peak behaviour of a hard rock can be predicted based on the results of triaxial tests. The CSDS model properties obtained from triaxial test results could thus probably be used to predict the post-peak uniaxial curve of hard rock (σ_3 = 0 MPa). To test this hypothesis, the average values of the model properties determined from the triaxial test results were used to estimate the post-peak curve of uniaxial compression (Table 6.4). Figure 6-19 illustrates the complete uniaxial post-peak curves estimated using the proposed approach.

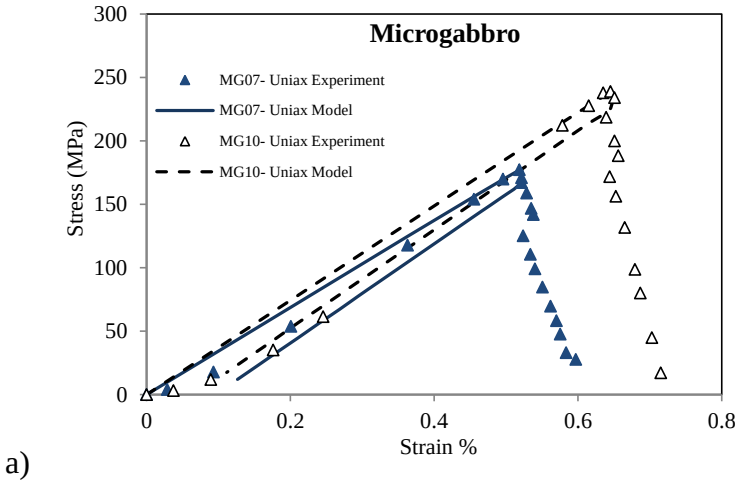

a)

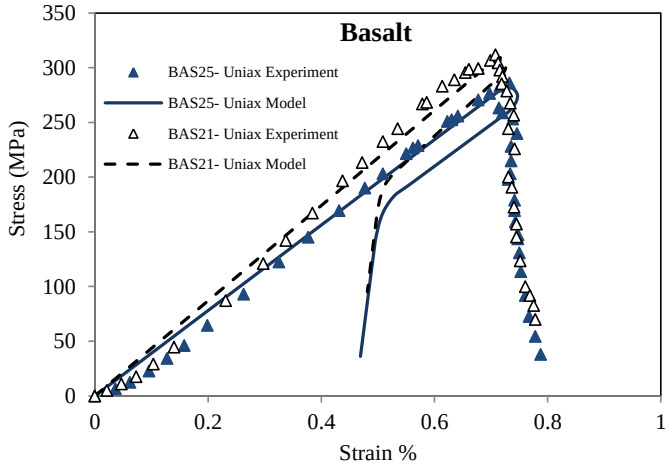

b)

Figure 6-19: Estimation uniaxial post-peak curve using the CSDS model properties obtained from triaxial tests; a)microgabbro; and b)basalt.

As can be seen, the curves estimated using the proposed approach are not in agreement with the data points obtained from the tests, indicating that the model properties obtained from triaxial tests are not well suited to obtaining the post-peak phase for uniaxial tests. The discrepancy between the CSDS model properties (i_o,u_r and β) obtained from the triaxial tests and used to predict the post-peak uniaxial curve and those obtained from the uniaxial tests (back analysis) is shown in Table 7 and discussed below:

-Initial Asperity Angle (i_o)

Table 6-7 shows a considerable difference between the initial asperity angles obtained using the CSDS model on the uniaxial compression results and those obtained based on the triaxial test

results. For instance, for the microgabbro, there is a 27% difference between the average i_o values of 37° for uniaxial tests and 27° for the triaxial tests, while for the basalt, there is a 10% difference between the average i_o values of 35.5° for the uniaxial tests and 32° for the triaxial tests. These results indicate that the initial asperity angle obtained based on the CSDS model from the triaxial tests is underestimated compared to the initial asperity angle required to predict the uniaxial post-peak curve for hard rocks with UCS > 180 MPa. This observation is not consistent with those made by Simon et al. (2003) for a granite specimen with the medium strength of 95 MPa. Based on the experimental results on hard rocks, it would thus appear that the model properties required to estimate the post-peak curve of the uniaxial tests for medium-strength rocks cannot be obtained as proposed by Simon et al. (2003).

Figure 6-14 shows the measured average asperity angle, $i_{0\,Ave}$, and maximum asperity angle, $i_{0\,Max}$, of the failure plane created by uniaxial and triaxial (σ_3=13 MPa) compression tests at a sampling interval of 1.29 mm. As can be seen, the measured $i_{0\,Ave}$ is 7° for the uniaxial tests on both the microgabbro and the basalt, and approximately 8° for the triaxial tests on both rocks. On the other hand, the maximum asperity angles, $i_{0\,Max}$, measured for the uniaxial tests are 23° and 26° for the microgabbro and basalt specimens, respectively, compared to 25° and 27° for the triaxial tests (Figure 6-14). Thus, these values are way lower than the initial asperity angles obtained from the CSDS model (37° and 35.5° for the microgabbro and basalt, respectively-see Table 6.7). If the sampling interval is decreased from 1.29 mm to 0.5 mm, $i_{0\,Max}$ measured for the triaxial tests are 35° for the microgabbro and 37° for the basalt, fairly close to the average value of i_o obtained from the CSDS model (Table 6.7).

-Residual shear displacement (u_r)

Table 6.7 displays the average residual shear displacement, u_r, derived from the CSDS model using the uniaxial test results (back analysis). As shown in this table, the u_r value obtained from triaxial tests are 2.5 mm for the microgabbro and 3.2 mm for the basalt, are much lower than the values of 5 mm and 5.1 mm obtained for the uniaxial tests. This discrepancy was not observed for the medium strength rock results derived from the literature (Simon et al. 2003).

Figure 6-20 shows the failure plane obtained from a uniaxial compression test on a basalt specimen. The highlighted contact area reveals that only 20% of the surface located near the upper loading platen was involved in the shearing process. In contrast, one can see that

approximately 75% of the failure surface was sheared off in the triaxial compression test as shown in Figure 6-16.The residual shear displacement takes place over the shorter distance in the triaxial compression test than in the uniaxial test, due to shearing off of a higher percentage of the asperities and the variable normal stresses. Additional laboratory tests using a modern stiff testing machine are required to evaluate the shearing behaviour of the failure plane induced by uniaxial compression.

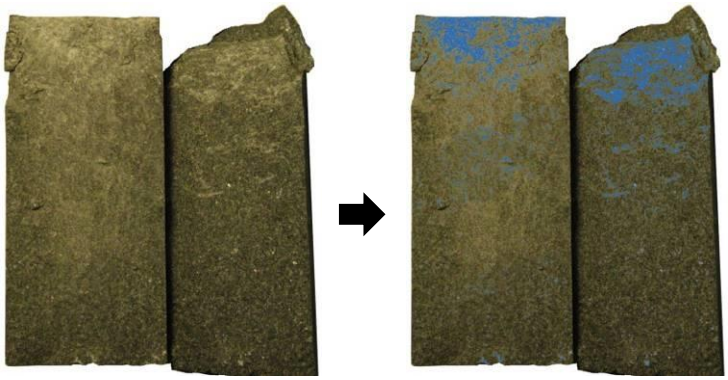

Figure 6-20: Contact area on the failure plane induced by a uniaxial compression test on basalt.

- *Angle of the failure plane induced by axial compression (β)*

The angle of the induced failure plane (β) can influence the friction between the loading platens and the two circular surfaces of the specimen which plays a very important role in the calculation of the CSDS model parameters. Figure 6-6 shows the failure plane angle (β) for the basalt and microgabbro specimens. The measured failure plane angle (β) for the uniaxial compression tests were in the range of 9.5° to 18° for the microgabbro and 12° to 22° for the basalt. Moreover, different fracture patterns can be seen in Figure 6. The results indicate that the number failure planes and their angle may vary with rock type and strength. It would thus seem that more than one failure plane can be created in uniaxial compression tests. However, the experimental observations suggest that only one of the induced failure planes is involved in the post-peak shearing phase.

6.8.3 Proposed CSDS model properties for estimating the uniaxial post-peak behaviour of hard rocks

Prior to the current study, Simon et al. (2003) proposed a new approach based on the CSDS model to predict the uniaxial post-peak behaviour of medium strength rocks based on triaxial test

results. Similar model properties were used in both uniaxial and triaxial applications. The results of the current study on hard rocks with UCS> 180 MPa, showed that the model properties used to estimate the uniaxial post-peak behaviour of hard rocks cannot be captured solely by the triaxial compression test results. In order to determine the CSDS model properties, direct shear tests and fracture surface characterization must be carried out with an appropriate normal stress and sampling interval. Table 6.8 presents a list of suggested laboratory tests for obtaining each CSDS model properties, and shows the CSDS model properties used in this study to estimate the post-peak curve of uniaxial compression testing. It can be seen that a sampling interval of 0.5 mm was used to obtain the measured maximum asperity angle $i_{0\,Max}$, from the triaxial tests on the microgabbro and the basalt.

Table 6.8: Source of the model properties for estimation of post-peak uniaxial compression behaviour.

β (°)	**u_p (mm)**	**u_r (mm)**	**i_o (°)**	**σ_T (MPa)**	**S_o (Mpa)**	**ϕ_u (°)**	**ϕ_0 (°)**	**ϕ_r (°)**
Estimated by empirical and experimental methods	CSDS approach on Triaxial tests	Direct shear test	Fracture surface characterization	Uniaxial compression test	Triaxial compression test	Direct shear test	Triaxial compression test	Direct shear test
The CSDS model properties obtained from the laboratory test in this study in order to obtain the uniaxial post-peak curve								
Microgabbro								
-	0.005	5.3	35	180	27	44	50	41
Basalt								
-	0.006	5.8	37	280	33	48	53	46

Figure 6-21 illustrates a complete uniaxial compression stress-strain curve predicted based on the proposed approach using the triaxial test results. The uniaxial compression test post-peak curve was estimated from the model properties obtained from fracture surface characterization, triaxial compression tests and direct shear tests (Tab. 8). The uniaxial compression test post-peak curve fits well with the model properties given.

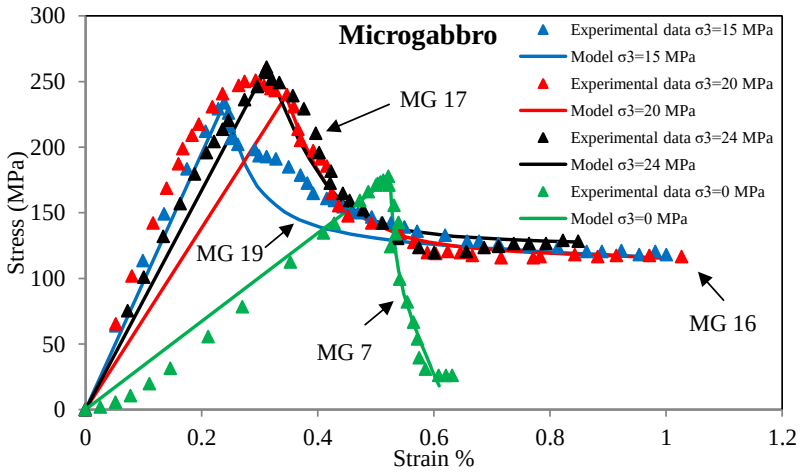

Figure 6-21: Experimental and model results of triaxial and uniaxial compression (microgabbro).

6.9 **Final remarks**

Simon et al. (2003) proposed an approach to estimate the post-peak behaviour of rocks based on triaxial compression test results. This approach showed that the CSDS parameters obtained from triaxial tests can be used to predict the post-peak behaviour of medium strength rocks. A comparison of the CSDS model parameters from triaxial tests and those calculated from back analysis of uniaxial tests indicated that the proposed approach tends to underestimate the asperity angle and residual shear displacement required to predict the uniaxial post-peak curve for hard rocks with UCS $\geq$ 180 MPa. The CSDS model properties obtained from the direct shear tests also showed that those results alone cannot be used to estimate the model properties required for further studies. However, the residual shear displacement obtained from direct shear tests, along with the friction angles obtained from triaxial compression tests, can be used to evaluate the post-peak behaviour in uniaxial compression. Further laboratory tests are required on different rock types to better capture the correlation between the model properties obtained from uniaxial, triaxial and direct shear tests.

In triaxial compression tests, peak strength usually occurs at a single peak point. However, the fracturing pattern, which is affected by the loading rate conditions, could delay the creation of a major failure plane. As a result of the continuous cracking phenomenon, a curved shape in the vicinity of the peak point can be seen when the confining stress increases as shown in Figures 10b and 10d. It is therefore difficult to determine the point at which the failure plane is

completed. In this study, the peak point was considered to be the onset of the steepest portion of the post-peak phase.

In this study, the uniaxial and triaxial compression tests were conducted by two testing machines. The pre-peak curves of the tests can be influenced by the stiffness of the testing apparatus. However, the post-peak behaviour of the specimens under the uniaxial compression was not affected by pre-peak stiffness.

6.10 **Conclusion**

This paper has validated the use of the CSDS constitutive model (Simon et al. 2003) to estimate the post-peak behaviour of intact hard rocks subjected to compression. The approach was established on the basis of normal and shear displacement of the failure plane induced by the axial compression. A series of direct shear, uniaxial compression and triaxial compression tests were carried out on two rock types -microgabbro and basalt- to obtain the CSDS model properties (i_o, u_p, u_r, ϕ_o, ϕ_u, ϕ_r, σ_T and S_o). To verify the complete stress-strain curves obtained by the proposed approach, the uniaxial and triaxial compression tests were carried out applying a low displacement rate.

The results indicated that the approach can be used to estimate of the post-peak behaviour of intact hard rocks. To do so, the model properties were obtained from uniaxial and triaxial compression tests, direct shear tests and fracture surface characterization as follows:

- The internal friction angles and cohesion of the intact rock (ϕ_o and S_o) were obtained from the triaxial compression tests.
- The peak and residual friction angles of the rock joint (ϕ_u and ϕ_r) and residual shear displacement (u_r) were obtained from the direct shear test.
- The ultimate compressive strength (σ_T) and elastic modulus (E) were derived from the standard uniaxial compression tests.
- The peak shear displacement (u_p) can be obtained by applying the proposed approach to the results of the triaxial compression tests.
- The asperity angle (i_o) can be obtained from the maximum asperity angle ($i_{0\,max}$) measured from the failure plane in triaxial compression. This model property can be

obtained from fracture surface characterization at a sampling interval of 0.5 mm instead of 1.29 mm.

- Except for i_o and u_p, the other model properties can be estimated with the curve fitting method by applying the proposed approach to the result of triaxial compression tests.

According to the results, the fracture surface created by the triaxial compression test has anisotropy in terms of asperity angle (roughness) with the asperity angle in the mid-length of the fracture surface created by the triaxial compression test decreasing as the confining stress increased. This indicates that the loading boundary conditions are not identical on the fracture surface. The amount of load on the mid-length of the fracture surface was higher than on the upper and lower part of the surface when the confining stress increased. Due to the high level of load in the mid-length, the asperities were generated at low angles. The result highlights the role of the asperity angle in the shearing process.

This paper presents an insight into the prediction of post-peak behaviour of intact rocks. Additional investigations are recommended to generate further findings for rocks in different ranges of unconfined strength and brittleness. The findings can be developed to predict rockburst behaviour. Consequently, this paper aims to contribute to a better understanding of post-failure control in underground projects.

Acknowledgement

The authors would like to acknowledge Raglan mine (Glencore group) for providing the rock cores (basalt and microgabbro) used in this study. The scanning on the fracture surfaces and direct shear tests in this study were performed at Department of Civil Engineering of University of Sherbrooke. This support is gratefully acknowledged.

Reference

Adoko, A.C. et al. (2013). Knowledge-based and data-driven fuzzy modeling for rockburst prediction. International Journal of Rock Mechanics & Mining Sciences 61 (2013) 86–95.

Altindag, R. (2010). Assessment of some brittleness indexes in rock-drilling efficiency. Rock Mech. Rock Eng. V. 43, 361–370.

ASTM D 5607-08 (2008). Standard Test Method for Performing Laboratory Direct Shear Strength Tests of Rock Specimens Under Constant Normal Force, ASTM International, West Conshohocken, PA,.

Aubertin, M., Gill, D.E. and Simon, R. (1994). On the use of the brittleness index modified (BIM) to estimate the post-peak behavior of rocks. NARMS' 94, Proc., First North American Rock Mech. Symp., Austin Uni., 945-952.

Aubertin, M., & Simon, R. (1997). A damage initiation criterion for low porosity rocks. International Journal of Rock Mechanics and Mining Sciences, 34(3), 17-e1.

Aubertin, M., Julien, M.R., Li, L. (1998). The semi-brittle behavior of low porosity rocks. Keynote Lecture, In: NARMS'98, Proceedings of 3rd North American Rock Mechanics Symposium, Vol. 2, Cancun, June. SMMR/ICA/ISRM. 1998. p. 65-90.

De Beer, W., & Mendecki, A. J. (1998). Rockburst prediction-case studies using a kinematics of failure approach. Journal-south african institute of mining and metallurgy, 98, 65-74.

Cai, M., Kaiser, P. K., & Duff, D. J. (2012, January). Rock support design in burst-prone ground utilizing an interactive design tool. In 46th US Rock Mechanics/Geomechanics Symposium. American Rock Mechanics Association.

Cook, N.G.W. (1965). A note on rockburst considered as a problem of stability. J. South Afr. Int. Min. Metallurgy 65, 437-446.

Cook, N.G.W. (1966) .The basic mechanics of rockbursts. J. South African Inst. Mining and Metallurgy, vol. 66, 56--70.

Cook N.G.W. (1987). Coupled processes in geomechanics. In: Tsang (ed.). Coupledprocesses associated with nuclear waste repositories. Academic Press Inc. London. pp. 39-66.

Deng, D., Simon, R. amd Aubertin, M. (2004). A geometrical approach for the estimation of scale effects in rock joint behaviour. 57th Canadian geotechnical conference, Quebec, P33-40.

Dong, L. J., Li, X. B., & Kang, P. E. N. G. (2013). Prediction of rockburst classification using Random Forest. Transactions of Nonferrous Metals Society of China, 23(2), 472-477.

Dyskin, A. V. and L. N. Germanovich (1993). Model of rockburst caused by cracks growing near free-surface. Rotterdam, A a Balkema.

Eberhardt, E. (1998). Brittle rock fracture and progressive damage in uniaxial compression. Phd thesis, University of Saskatchewan, Canada, 362p.

Fairhurst, C.E., Hudson, J.A. (1999). Draft ISRM suggested method for the complete stress-strain curve for intact rock in uniaxial compression. International Journal of Rock Mechanics and Mining Sciences 36(3): 279-289

Gill, D.E. and Aubertin, M. (1988). Évaluation du potentiel de coups de terrain dans les mines d'Abitibi. Rapport de recherche de l'URSTM présenté à l'Institut de Recherche en Santé et Sécurité du Travail (IRSST).

Gill, D. E., M. Aubertin, et al. (1993). Practical engineering approach to the evaluation of rockburst potential. Proceedings of the 3rd International Symposium on Rockbursts and Seismicity in Mines, Aug 16 - 18 1993, Kingston, Ont, Canada, Publ by A.A. Balkema.

Goodman, R.E. (1976). Methods of Geological Engineering in Discontinuous Rock, p. 472. West, New York.

Grasselli G, Egger P. (2003). Constitutive law for the shear strength of rock joints based on three-dimensional surface parameters. Int J Rock Mech Min Sci., 40:25–40.

Haijun, C., Nenghui, L., Dexin, N., & Yuequan, S. (2003). Prediction of rockburst by artificial neural network. Chinese journal of rock mechanics and engineering, 22(5), 762-768.

Hajiabdolmajid, V. & Kaiser, P. (2003). Brittleness of rock and stability assessment in hard rock tunnelling. Tunnelling and Underground Space Technology V. 18, 35–48.

Hakami, H. (1988). Post-failure Behaviour of Brittle Rock. Doctoral Thesis, LuleA University of Technology, Sweden.

Hoek, E., and Brown., E.T. (1997) Practical estimates of rock mass strength, International Journal of Rock Mechanics and Mining Sciences & Geomechanics Abstracts, 34,8, pp 1165-1186.

Hucka V, Das B (1974) Brittleness determination of rocks by different methods. Int J rock Mech Min Sci Geomech Abstr 11:389–392.

Hudson, J.A. (1989). Rock mechanics principles in engineering practice. London, Butterworths, 67p.

Hudson, J.A., Brown, E.T. & Fairhust, C. (1971) Optimizing the control of rock failure in servo-controlled laboratory test.Journal of Rock Mechanics, 3, 217 – 224.

Johnston, J. C. (1988). A survey of mining associated rockbursts, Master Thesis. Massachusetts Institute of Technology.

Kaiser, P., Morrison, D., Swan, G., McCreath, D., Tannant, D., Neumann, M., Kazakadis, V. And Talebi, S. (1995). Mining Research Directorate- The Canadian Rockburst Research Program 1990-1995. CAMIRO Mining Division, 2 Vol.s.

Khosravi A. (2016). Investigation of post-peak behaviour of hard rocks. PhD thesis. To be published.

Kidybiński, A. (1981). Bursting liability indices of coal. InInternational Journal of Rock Mechanics and Mining Sciences & Geomechanics Abstracts (Vol. 18, No. 4, pp. 295-304). Pergamon.

Ladanyi, B., Archambault, G. (1970). Simulation of the shear behaviour of a jointed rock mass. The 11th Symposium on Rock Mechanics, Berkeley, pp. 105–125.

Lee, S.M., Park, B.S., Lee, S.W., (2004). Analysis of rockbursts that have occurred in a waterway tunnel in Korea. Int. J. Rock Mech. Min. Sci., 41(3), 545.

Li, Z.-H., L.-M. Dou, et al. (2008). Study on fault induced rock bursts. Journal of China University of Mining and Technology 18: 321-326.

Martin, C.D. (1993). Strength of massive Lac du Bonnet granite around underground openings. Ph.D. thesis, Department of Civil and Geological Engineering, University of Manitoba, Winnipeg, 278pp.

Martin, C. D., & Chandler, N. A. (1994). The progressive fracture of Lac du Bonnet granite. In International Journal of Rock Mechanics and Mining Sciences & Geomechanics Abstracts (Vol. 31, No. 6, pp. 643-659). Pergamon.

McGarr, A. (1993). Keynote address: Factors influencing the strong ground motion from mininginduced tremors. Proc. 3rd Int. Symp. on Rockbursts and Seismicity in Mines, ed. Young, Balkema, pp. 3-12.

Meng, F., Zhou, H., Zhang, C., Xu, R., & Lu, J. (2015). Evaluation methodology of brittleness of rock based on post-peak stress–strain curves.Rock Mechanics and Rock Engineering, 48(5), 1787-1805.

Mishra, B., & Nie, D. (2013). Experimental investigation of the effect of change in control modes on the post-failure behavior of coal and coal measures rock. International Journal of Rock Mechanics and Mining Sciences, 60, 363-369.

Mitri, H. S. (2007). Assessment of horizontal pillar burst in deep hard rock mines. International Journal of Risk Assessment & Management 7(Copyright 2007, The Institution of Engineering and Technology): 695-707.

Petukhov, I. (1972). Rock Bursts in Coal Mines. Nedra, Moscow.

Qiao, C.S., Tian, Z.Y. (1998). Study of the possibility of rockburst in Dong-gua-shan Copper Mine. Chinese J. Rock Mech. Eng. Žexp. 17, 917_921.

Reichmuth D.R. (1967). Point load testing of brittle materials to determine tensile strength and relative brittleness. The 9th US Symposium on Rock Mechanics (USRMS). American Rock Mechanics Association, pp 134–159

Rummel, F., & Fairhurst, C. (1970). Determination of the post-failure behavior of brittle rock using a servo-controlled testing machine. Rock mechanics,2(4), 189-204.

Saeb S. and Amadei B. (1992) Modelling rock joints under shear and normal loading. Int J Rock Mech Min Sci Geomech Abstr; 29: 267–78.

Sainoki, A., & Mitri, H. S. (2014). Dynamic behaviour of mining-induced fault slip. International Journal of Rock Mechanics and Mining Sciences, 66, 19-29.

Salamon, M.D.G. (1974). Rock mechanics of underground excavations. , Advances in rock Mechanics, Proc. 3rd Cong. Int. Soc. Rock. Mech., vol.1-B, 1974. 951–1099.

Salamon, M.D.G. (1993). Keynote address: Some applications of geomechanical modelling in rockburst and related research. Rockbursts and Seismicity in Mines, Young (ed.) 1993 Balkema, Rotterdam, ISBN 905403205, 297-309.

Santarelli, FJ., and Brown, E.T. (1989). Failure of three sedimentary rocks in triaxial and hollow cylinder compression tests, International Journal of Rock Mechanics and Geomechanics Abstracts, 26,5, pp 401 - 413.

Simon, R. (1999). Analysis of fault-slip mechanisms in hard rock mining. Phd Thesis, McGill University, Montreal, Canada.

Simon, R., Aubertin, M., & Deng, D. (2003). Estimation of post-peak behaviour of brittle rocks using a constitutive model for rock joints. In 56th Canadian Geotechnical Conference.

Singh, S.P. (1989). Classification of mine workings according to their rockburst proneness. Mining Science and Technology, V 8, 253-262.

Stiller, H., Hurtig, E., Grosser, H. and Knoll, P. (1983). On the Nature of Mining Tremors. Earthq. Predict. Res. 2, pp. 57-63.

Su, G-S. et al. (2009). Rockburst prediction using Gaussian process machine learning. Computational intelligence and software engineering, CiSE.

Tang, C.A., Tham,L.G., Lee, P.K.K., Tsui,Y. and Liu, H. (2000). Numerical studies of the influence of microstructure on rock failure in uniaxial compression Ð Part II: constraint, slenderness and size effect. International Journal of Rock Mechanics and Mining Sciences 37, 571-583.

Tarasov BG, Potvin Y (2013) Universal criteria for rock brittleness estimation under triaxial compression. Int J Rock Mech Min Sci 59:57–69.

Tiwari, R. P., & Rao, K. S. (2006). Post failure behaviour of a rock mass under the influence of triaxial and true triaxial confinement. Engineering Geology, 84(3), 112-129.

Wang, J. A. & Park, H.D. (2001). Comprehensive prediction of rockburst based on analysis of strain energy in rocks. Tunnelling and Underground Space Technology, V. 16, 49-57.

Wang, P., F.-X. Jiang, et al. (2010). The stress incremental forecasting method of rock burst. Meitan Xuebao/Journal of the China Coal Society 35: 5-9.

Wawersik, W. R., & Fairhurst, C. (1970, September). A study of brittle rock fracture in laboratory compression experiments. In International Journal of Rock Mechanics and Mining Sciences & Geomechanics Abstracts (Vol. 7, No. 5, pp. 561IN7565-564IN14575). Pergamon.

Whyatt, J.K., Blake, W., Williams, T.J., White, B.G. (2002). 60 years of rockbursting in the Coeur D'Alene District of Northeastern Idaho, USA: lessons learned and remaining issues. In: Proceedings of the 109th Annual Exhibit and Meeting, Society for Mining, Metallurgy, and Exploration, February 25–27, Phoenix, AZ. Preprint 02-164, 1–10.

Wiles, T.D. (2005). Rockburst prediction using numerical modelling-realistic limits for failure prediction accuracy. Sixth international symposium, on rockburst and seismicity in mines, Australia.

Wu, Y. and Zhang, W. (1997). Evaluation of the bursting proneness of coal by means of its failure duration. Rockbursts and Seismicity in Mines, Gibowicz & Lasocki, Balkema, Rotterdam.

Yagiz S (2009) Assessment of brittleness using rock strength and density with punch penetration test. Tunn Undergr Sp Tech 24(1):66–74.

Yi, X. & Kaiser, P. K. (1993). Mechanisms of rockmass failure and prevention strategies in rockburst conditions. Rockbursts and Seismicity in Mines. 141-145 Balkema. Rotterdam.

Zhang, L. and Wang, Z. (2006). Rock Failure under Unloading Conditions and Application for Rock Burst. Soil and Rock Behavior and Modeling, Proceedings of the GeoShanghai conference, Geotechnical Special Publication, n 150, p 235-240.

CHAPTER 7 SUMMARY AND GENERAL DISCUSSION

7.1 Main results

One of the most dangerous instability problems in Canadian underground mines is rockburst. Rockburst is a sudden and violent failure of intact rock in underground opening (strainburst) or a violent slip along a pre-existing discontinuity (fault-slip burst). In the strainburst phenomenon, a failure plane occurs as a result of failure. The post-peak behaviour, which is affected by the rockburst severity, can be determined by understanding the loading boundary condition on the failure plane induced by compression. This failure plane controls the hydro-mechanical behaviour of the rock mass. Therefore, an accurate prediction of the post-peak behaviour of induced fractures can improve the stability of underground openings in the design phase.

Many studies were performed trying to predict rockbursts based on statistical and mathematical methods where the mechanical properties of rock mass are not well considered (e.g., Dyskin, and Germanovich, 1993; Beer and Mendecki, 1998; Haijun et al., 2003; Wiles, 2005; Adoko et al., 2013 and Dong et al., 2013). Brittleness indices were also proposed to evaluate the burst proneness in deep mines. These indices are based on strain energy accumulation and mechanical properties of rock in the loading phase (Aubertin and Gill, 1988; Aubertin et al., 1994; Wang and Park, 2001).

Another approach to study the rockburst phenomenon is the analysis of the energy released at the post-peak phase of rock mass using experimental methods (Cook, 1965; Rummel and Fairhurst, 1970; Wawersik and Fairhurst, 1970; Salamon, 1974; Gill et al., 1993; Aubertin and Simon, 1997; Xiao et al., 2010). The damage-controlled approach (Martin, 1993; and Martin and Chandler, 1994) and the ISRM method (Fairhurst and Hudson, 1999) were proposed to obtain the post-peak behaviour of rocks. Simon et al. (2003) also proposed an indirect analytical approach based on triaxial compression tests and a constitutive model for rock joint- the CSDS model (complete stress-displacement surface) - to estimate the post-peak behaviour of hard rock.

Since the strain-type rockburst occurs in intact rock under compression, the shear mechanical behaviour of the created joint plays an important role in the severity of the process regarding to the applied boundary condition in the post-peak phase. Many investigations were carried out to characterize the joint surface roughness parameters (e.g. Mayers, 1962; Barton and Choubey,

1977; El-Soudani, 1978; Tse and Cruden, 1979; Maerz et al., 1990; Yu and Vayssade, 1991; Poon et al., 1992; Kulatilake et al., 1995; Belem et al., 2000; Grasselli, 2001; Yang et al., 2001; Kim et al., 2009; Tatone and Grasselli, 2010; and Jang et al., 2014). In recent years, much effort has been devoted to study the effect of different loading modes on the roughness parameters using laboratory tests (Tang and Kou, 1998; Bobet and Enstein, 1998; Amitrano and Schmittbuhl, 2002; Seredin et al., 2013). However, there are still many neglected factors that should be considered in the prediction of the post-peak phase of intact rocks. For instance, most of these investigations neglected the influence of the loading modes and loading direction on the roughness parameters of different rock types considering the length of samples and their grain size. Also, the model properties proposed by Simon et al. (2003) were obtained from curve fitting rather than actual measured values.

The goal of this thesis was to validate the proposed indirect approach for the prediction of the post-peak behaviour (stiffness) of rock and the rock burst proneness in underground excavations considering the fracture surface quantification and characterization.

In order to reach this goal, a series of laboratory tests, including splitting, uniaxial, triaxial compression and Brazilian tests were carried out on hard rocks: gabbro, microgabbro and basalt. The created joints were then characterized using 2D and 3D profilommetry devices. In the next step, the effect of loading direction and the L/D ratio in the Brazilian tests on the joint roughness parameters was also assessed for the rocks. A new procedure, called the damage-controlled cyclic method, was used to obtain the post-peak curve of the rocks. The results of the uniaxial and triaxial and direct shear tests obtained using the new damage-controlled method, direct shear tests results and the results of the joint surface characterization were used to estimate the CSDS model properties and the post-peak behaviour of the hard rocks based on the proposed approach. The discussion presented in this section refers to the results presented in this study.

Morphology of the fractures induced by different loading boundary conditions

The shear mechanical behaviour of the created joint plays an important role in the severity of the rockburst regarding to the applied boundary condition in the post-peak. In order to characterize and quantify the fracture surfaces, a series of Modified Splitting, uniaxial and triaxial compression tests with a confining pressure of 3, 5 and 8 MPa, were carried out to obtain fractures in tensile and tensile/shear modes. Three hard rocks: gabbro, microgabbro and basalt

were chosen for this study. A simple 2D Roughness Profilometry (2DRP) method was proposed for scanning the fracture surfaces. The main results have shown that:

- The roughness parameters obtained from the proposed method (2DRP) were validated with the results of a 3D laser profilommeter (ATOS II system). It was observed that the results of 2DRP are well correlated with those obtained using ATOS II system.
- The results of the Modified Splitting Technique indicate that the roughness parameter is affected by both loading modes and grain size (rock type). As a result of combination of these influenced factors, different roughness variations are observed for these rocks.
- It is seen that for a coarse-grained rock (gabbro), the roughness parameters decrease with the loading mode from the splitting to the triaxial with σ_3 = 8 MPa and then increased when the confining stress goes up to 13 MPa. Therefore, the roughest fracture is the one created by the Modified Splitting Technique in gabbro specimens. This trend was different for the finer-grained rocks (microgabbro and basalt) where the *JRC* value decreased from Modified Splitting to the uniaxial and then increased when the loading mode changed to the triaxial compression with σ_3 = 3 MPa. The *JRC* value then decreased as a result of increasing in the confining stresses to 13 MPa.
- These results imply that the roughness parameters can be significantly influenced by the loading direction so that the ratio of highest to lowest *JRC* value of the roughness profiles perpendicular to the loading axis is lower than those obtained for the profiles parallel. Furthermore, the roughness values of the profiles perpendicular to the loading axis show almost uniform distribution along the length of the specimens. This uniformity is not observed in the roughness profiles parallel to the loading axis.
- The results further show that the *JRC* value of the profile is also affected by the loading contact areas. The *JRC* values of the profiles in the vicinity of loading points are higher than those obtained from the middle portion of the specimens.
- The results indicated that the roughness parameters decreased with an increase in the sampling interval.

The loading and shape effect on the morphology of the fractures created by the Brazilian test

In this part of the research, the loading and the shape effect on the fracture surface morphology were studied. To do so, Brazilian tests were conducted on three rock types with different length-to-diameter (L/D) ratios to create the tensile fracture surfaces. The fracture surfaces were then scanned by a 3D laser profilometer and the roughness profiles were obtained parallel and perpendicular to the loading direction. The main outcomes of this study indicate that:

- The roughness variation in the Brazilian tests appears to be affected by the stress distribution and shape effects. The roughness of the profiles parallel to the loading direction decreases with an increase of the L/D ratio for the rock types except for basalt samples with the L/D ratios of 0.2 to 1.0. It is shown that the roughness of the profiles perpendicular to the loading direction increases with an increase in the L/D ratio. It can be inferred that the roughness parallel and perpendicular to the loading direction measured at the mid-length and mid-diameter of the specimens varies due to changes in the induced confining stress perpendicular to the two circular surfaces of the samples.
- The results illustrate that the roughness scattering of the profiles parallel to the loading axis is higher than that in the profiles perpendicular to the loading axis.
- The roughness distribution of the profiles perpendicular to the loading axis shows a convex shape for the lower L/D ratio which implies a lower roughness in the core of the sample. This convex shape gradually turns into a concave shape for the samples with a higher L/D ratio, meaning that the roughness of the profiles at the core of the sample is higher than that in the vicinity of the loading platens.
- The results also show that the size of the wedge created by the compression zone implicitly increases with an increase in the L/D ratio.

Effect of the pre-peak loading condition on the post-peak behaviour

In order to study the behaviour of rocks under compression and also to have a better understanding of rockburst mechanism as a brittle fracturing phenomenon, uniaxial compression tests were carried out on brittle rocks. A stiff servo-controlled testing machine with a particular testing procedure was used to obtain the post-peak curve of two intact rocks: basalt and microgabbro. This proposed loading procedure was called the damage-controlled cyclic method. The main findings of this investigation are as follows:

- The post-peak phase of the axial stress-strain curve can be obtained by using the damage-controlled cyclic loading procedure by which the axial load is applied on the specimen with a combination of axial load and displacement rate control along with load-unload cycles.
- In the new loading procedure, the displacement rate control must be started at 60-70% of the predicted UCS, which corresponds to the cracking initiation phase. Otherwise, the procedure may lead to strain hardening in the pre-peak phase. When it is the case, it is harder to obtain the post-peak curve.
- The results obtained by the new damage-controlled cyclic method show that the post-peak behaviour of basalt -as a very hard rock- can be classified as class II behaviour, while the post-peak behaviour of microgabbro corresponds to class I behaviour.
- The elastic energy accumulated in the specimens by applying the damage-controlled cyclic method is less than that in the standard loading method due to the low loading rate and cyclic loading. A portion of the energy in the pre-peak phase is released by applying the new method, which leads the specimen to develop the cracking network and to lose gradually its integrity by shearing along main and secondary cracks.
- The Brittleness Index Modified (BIM) obtained from the pre-peak stress-strain curve is in good agreement with those calculated based on other testing procedure results. It can be also seen that both rocks are categorized in high bursting liabilities with higher chance of a violent failure.

Post-peak behaviour of hard and brittle rocks estimation and verification using The CSDS model for rock joints

In deep mining operation, rockburst is a critical issue that must be addressed in order to control the risk for the safety of workers and equipment. The determination of the post-peak behaviour of hard rocks can lead us to estimate the rockburst potential in the design phase. An indirect approach based on triaxial compression tests and a constitutive model for rock joint- the CSDS model- was proposed (Simon et al. 2003) to predict the post-peak behaviour of the failure plane induced by the axial compression. In this study, this approach was verified using the results of compression and direct shear tests on two hard rocks. The CSDS model parameters were then obtained using the results of the laboratory tests and fracture surface characterization and

quantification. The CSDS model parameters obtained from the triaxial tests were compared with those obtained from the uniaxial and direct shear tests. The results indicate that:

- Application of the proposed approach in the uniaxial, triaxial compression and the direct shear tests show that this approach can be used to predict the post-peak behaviour of hard rocks.
- The CSDS model properties obtained based on the curve fitting method may vary from one test to another due to different boundary conditions applied in different tests. Peak shear displacement (u_p), residual shear displacement (u_r) and initial asperity angle (i_o) are the challenging model properties. For instance, the value of u_p, u_r obtained from the direct shear tests are higher than those obtained using the triaxial and uniaxial tests while the value of i_o is lower in the direct shear tests than the ones from the triaxial and uniaxial tests.
- Maximum and average asperity angles of the fracture induced by the Modified Splitting Technique are highest compared to those induced by the uniaxial and triaxial compression tests. In the triaxial compression, the maximum and average asperity angles decrease with an increase in the confining stress.
- Asperity angles, calculated based on the fracture surface characterization, show the different values rather than those obtained using a curve fitting method. It can be seen that the asperity angle from the CSDS model on direct shear test results is close to the measured average asperity angle from the triaxial test (with σ_3 = 13 MPa) in the sampling interval of 1.29 mm, while the asperity angles from the CSDS model on the triaxial test results are almost similar to the measured maximum asperity angles from the triaxial tests with σ_3 = 13 MPa in the same sampling interval. The results also indicate that the measured maximum asperity angle from the uniaxial tests becomes fairly close to the average value of i_o obtained from the CSDS model if the sampling interval decreases from 1.29 to 0.5 mm.
- The roughness anisotropy of the fracture surfaces plays an important role in the asperity angle variation. The maximum asperity angle measured from the middle section of the fractures is higher than the borders. Furthermore, the higher confining stress results in smoother asperity angles in the middle section.

- The angle of the failure plane, β, observed from the uniaxial and triaxial tests is usually lower than the theoretical failure angle obtained from the analytical solution proposed by Simon et al. (2003).
- The CSDS model properties needed for estimating the post-peak curve of the uniaxial compression test can be obtained by the triaxial compression tests, direct shear tests and fracture surface characterization.
- Verification of the approach by conducting the laboratory tests is highly dependent on the quality of tests and equipment. Equipment and test procedure are key factors to obtain high resolution results which lead to accurate estimation of the post-peak behaviour.

7.2 Discussion

This thesis presents the verification of the CSDS approach by which the post-peak behaviour of hard and brittle rocks under uniaxial compression can be estimated. A comprehensive investigation has been conducted on the morphology of the fracture surface induced by different loading boundary conditions. In this dissertation, the relationship between roughness parameters, loading condition and post-peak behaviour was studied.

In order to characterize fracture surfaces with a length of $\leq$ 100 mm, a new 2D roughness profilommetry method (2DRP) was developed. The results of the roughness characterization carried out by the 2DRP method show a good agreement with those obtained from a high resolution 3D laser profilommeter (ATOS II). This 2DRP method can be used in the lab or in the field when other roughness profilommetry methods are not available. In order to obtain fracture surfaces induced by different boundary conditions, Modified Splitting, uniaxial and triaxial compression tests were used. These fractures are created in tensile mode or a combination of tensile and shear. The results indicated that the fractures induced by the Modified Splitting, uniaxial and triaxial compression can be classified as rougher, rough and smooth surfaces for gabbro samples as a coarse grain rock type. This classification cannot be observed in microgabbro and basalt as medium and fine-grain sized rocks. The results of this study correspond well with those obtained by Amitrano and Schmittbuhl (2002) and Seredin et al. (2013). A remarkable finding for all rock types in this research is that the roughness of the fractures induced by the triaxial compression decreases while the confining stress increases.

In order to understand the relationship between the loading direction and roughness of the induced fracture, a series of the Brazilian tests were conducted on three rock types with different L/D ratios to create the tensile fractures. The results show that the roughness of the mid-length profiles parallel to the loading axis decreased with an increase in the L/D ratio in gabbro and microgabbro; however, the basalt samples showed a different trend for the L/D ratios of 0.2 to 1.0. The results further indicated that the roughness of the profiles perpendicular to the loading axis increased while the L/D ratio increased.

The post-peak behaviour was studied using a new loading procedure based on a damage controlled technique in the pre-peak phase named as "damage-controlled cyclic method". To estimate the post-peak, an approach was used based on the CSDS constitutive model on the failure plane induced by the triaxial compression tests using the new damage-controlled method.

The results showed that the CSDS model properties can be obtained by the triaxial compression tests, direct shear tests and fracture surface characterization.

Despite the additional information and insight provided by the results presented in this thesis, it should be recalled that some of these results are based on some operational laboratory limitations. For instance, the 2DRP method is applicable for fractures less than 100 mm. Also, this method is time consuming compared to laser profilommetry; however, it is more accurate compared to the comb profilommeter. The effect of loading modes on the roughness parameter was also investigated using the modified splitting technique, uniaxial and triaxial tests with confining stress up to 13 MPa. Recent studies by Amitrano and Schmittbuhl (2002) and Seredin et al. (2013) were conducted on granite specimens and rock-like materials with a higher confining stresses. The effect of the higher confining stresses (σ_3 > 13 MPa) was neglected in the current study due to the limited capacity of the loading system. In this research, a limited number of microscopic studies were carried out to investigate the fracture trajectory based on the applied loads. Therefore, additional microscopic studies could be performed to realize the crack initiation and propagation under different loading conditions.

In this thesis, variation of roughness was assessed according to the loading condition in the Brazilian test on the samples with different L/D ratios. An important outcome of this assessment was that the roughness of the profiles parallel to the loading direction decreased with an increase of the L/D ratio, while increased in the profiles perpendicular to the loading direction. These

results were supported using the numerical simulations carried out by Yu et al. (2006) and Von Dinh (2011). Although the results shown in this thesis are the first dealing with the loading direction in the Brazilian tests, numerical investigation in 3D gives a better understanding of the stress distribution in the specimens due to different loading conditions and its effect on the roughness parameters. More work is required to cover this aspect. The roughness scattering was also considered in this study. Although basalt is the most homogeneous rock in terms of grain size, the roughness scattering of the profiles parallel to the loading direction in this rock type is more than that in the other rocks. At present, a few investigations were carried out on the influence of loading direction on the roughness scattering. Babadagli and Develi (2003) showed that there is no correlation between the roughness scattering of the profiles parallel to the loading direction and the grain size. However, more scattered roughness was observed for the largest grain size in the profiles perpendicular to the loading direction in their studies. These results are in good agreement with those obtained in the current study. Based on Kabeya (2002), roughness obtained from a fine-grained material is less than that in the coarse-grained. Further investigation is required to assess the roughness scattering due to variation in the loading condition.

Martin and Chandler (1994) and Fairhurst and Hudson (1999) proposed two loading procedures in order to obtain the post-peak behaviour of rocks. These methods took approximately 8 hours per tests due to load-unload cycles and small axial and radial loading rate. The large number of full load-unload cycles and small loading rate may cause fatigue and creep phenomena in the samples. Fatigue and creep problems cannot be occurred by conducting a damage-controlled cyclic method with partial load-unload cycles and low loading rate. A new damage-controlled cyclic method was proposed in this study to capture the post-peak curves of hard rocks. This procedure was a combination of load and displacement rates control along with pauses and partial load-unload cycles with a certain amount of increments of the load in each cycle. The low displacement rate control in the cyclic loading can lead cracks to be propagated in a steady state manner. Otherwise, a violent fracturing of the sample may occur. Each pause and load-unload cyclic applied on the sample helped the system to be destressed and to release a slight amount of the stored elastic energy. This slightly released energy influenced the loading curve in the pre-peak phase. Therefore, the elastic energy underneath the loading curve in the pre-peak phase tended to decrease compared to the curve obtained by a standard loading procedure (with higher loading rate). The small amount of decreased energy significantly influenced the post-peak curve

of a sample subjected to the axial compression to be obtained by a standard testing machine. The energy released by cyclic loading could be reflected in the cracking patterns of the samples. Applying the cyclic loading below the crack damaged threshold, i.e. stress level of 55% of the UCS, can cause a reduction of crack coalescence. The internal breakdown of the material stiffness occurs when the crack size and density reach to a specific state. At this state, a large crack and coalescence can occur. Therefore, the point at which the loading cycles started can affect the loading curve, ultimate strength of the sample, and cracking network. It should be noted that the damage-controlled cyclic method is generally limited to determining the level of loading (%) in which the loading rate should be switched from one loading mode to another. In addition, it is hard to assign an absolute value to the compressive strength of all specimens. These are the main factors that should be considered during the application of the proposed damage-controlled cyclic method.

Simon et al. (2003) established an approach to predict the post-peak behaviour of granite samples with $UCS = 95$ MPa based on the triaxial test results and the CSDS model. In the current study, the ultimate strength of the rock types was between 180 to 280 MPa. These rocks can be classified as very hard rocks that the post-peak curve is very difficult to obtain by a stiff-machine. In order to obtain the post-peak curves in the triaxial and uniaxial tests, two different servo-controlled machines were used due to the operational laboratory limitations. However, the post-peak curves cannot be influenced by the stiffness of the servo-controlled machine; this suggests that additional tests should be conducted with the same loading systems to validate the obtained post-peak curves. Also, the results with a higher resolution can evidently be obtained if a modern stiff and servo-controlled testing machine is used in which a fast response of a sudden fracture in the sample can be provided.

CHAPTER 8 CONCLUSIONS AND RECOMMENDATIONS

This doctoral thesis presents the verification of an approach that was developed to estimate the post-peak behaviour of hard rocks. This verification was carried out using the results of the direct shear, uniaxial and triaxial compression and Brazilian tests. A comprehensive investigation was conducted to characterize the fractures induced by different loading conditions. These fractures were obtained from the Modified Splitting, uniaxial and triaxial compression tests with confining stresses of 3, 8 and 13 MPa.

To characterize the fracture surfaces induced by the applied loading conditions, a 2D roughness profilommetry method (2DRP) was proposed in this thesis. This method is easy to use in the field or in laboratory on small scale surfaces and when no reliable device is available. The results obtained using 2DRP method was compared with a widely known 3D profilommeter (ATOS II). A good correlation was observed between the results of these two methods.

The results of the fracture surface characterization for three rock types show a descending order in the roughness from the Modified Splitting to the uniaxial and the triaxial compression with confining stress of 3 and 8 MPa in gabbro; however, the roughness increases in triaxial compression with confinement of 13 MPa. The results observed for microgabbro and basalt are quite different than those in gabbro. In these rock types, the fracture created by Modified Splitting is rougher than that in uniaxial compression, but not necessarily rougher than that in the triaxial tests. It can be concluded that the roughness of the splitting fracture is higher than that in the uniaxial in all three rock types. Variation of the *JRC* values in the roughness profiles parallel and perpendicular to the loading axis reveals the roughness anisotropy on the fracture surface so that the *JRC* value in the profiles perpendicular to the loading axis is higher than that observes in the parallel profiles.

A microscopic study on the fracture created by Modified Splitting Technique represents the role of the coarse grains in roughness profiles of gabbro sample parallel to the loading axis. The morphological study on the fracture surfaces induced by Brazilian tests (fracture created in mode I) shows a relationship between the loading direction and the roughness variation on the fracture surface in terms of the L/D ratio of the specimens. The investigation of the fracture topography reveals that the roughness of the profiles parallel to the loading axis decreases with increasing the

L/D ratio in gabbro and microgabbro, while the roughness of basalt increases slightly with an increase of L/D ratio from L/D = 0.2 to 1.25, and then decreases when the L/D ratio was larger than 1.25. It is also shown that the roughness of the profiles perpendicular to the loading axis increases with an increasing L/D ratio. The roughness scattering in the profiles parallel to the loading direction is higher than that in the roughness profiles perpendicular to the loading direction.

In order to better understanding the behaviour of brittle rocks, rock samples were subjected to compression tests. To estimate the post-peak behaviour of hard rocks a new damage-controlled cyclic method was proposed. The loading procedure in this method is a combination of the axial force and displacement rate. In the procedure, the displacement rate control must be started at a level corresponding to the cracking initiation (60-70% of UCS). In this method, the crack initiation occurs as uniformly as possible along with gentle crack coalescence and propagation in the form of a crack network. Development of the crack network indicates the elastic energy dissipation in an imperceptible way, which can lead the test to the post-peak region.

The damage-controlled cyclic method enables to control the unstable cracking phenomenon in hard rocks submitted to compression. Therefore, the complete stress-strain curve can be obtained by this method in order to investigate the post-peak behaviour of brittle rocks and also to estimate the post-peak stiffness. The results show that the elastic energy accumulated in the specimens by applying the damage-controlled cyclic method is less than that in the standard loading method due to the low loading rate and cyclic loading and the secondary cracks generated in the body of the specimen. The correlation between Brittleness Index Modified (BIM) and post-peak stiffness obtained from the complete stress-strain curve are in good agreement with those calculated in the literature by other testing equipment and procedures. It is seen that both rocks are categorized as high bursting liabilities with higher chance of a violent failure.

The results of uniaxial and triaxial compression tests obtained using the damage-controlled cyclic method and the results of direct shear tests were used to estimate the model properties of the CSDS constitutive model. A proposed approach (Simon et al. 2003) was also used to predict the post-peak behaviour of brittle rocks subjected to the uniaxial compression based on the results of triaxial tests. The results indicate that the CSDS model properties obtained based on the curve fitting method may vary from one test to another due to different boundary conditions applied in

different tests. Peak shear displacement (u_p), residual shear displacement (u_r) and initial asperity angle (i_o) are the most challenging properties among the other parameters. It can be seen that the value of u_p, u_r obtained from the direct shear tests are higher than those obtained using the triaxial and uniaxial tests while the value of i_o in the direct shear tests is lower than the ones from the triaxial and uniaxial tests. It can be seen that the asperity angle from the CSDS model on the results of the direct shear test is close to the measured average asperity angle from the triaxial test (with $\sigma_3 = 13$ MPa) in the sampling interval of 1.29 mm, while the asperity angles from the CSDS model on the triaxial test results are almost similar to the measured maximum asperity angles of the fracture surface created by triaxial tests with $\sigma_3 = 13$ MPa and the same sampling interval.

The results also indicate that the measured maximum asperity angle from the uniaxial tests becomes fairly close to the average value of i_o obtained from the CSDS model if the sampling interval decreases from 1.29 to 0.5 mm. The angle of the failure plane, β, observed from the uniaxial and triaxial tests is usually lower than the theoretical failure angle obtained from the analytical solution proposed by Simon et al. (2003). It can be concluded that the CSDS model properties needed for estimating the post-peak curve of uniaxial compression test can be obtained by uniaxial compression test (ultimate compressive strength and elastic modulus) triaxial compression tests (internal friction angle, cohesion), direct shear tests (peak and residual friction angle; and residual shear displacement) and fracture surface characterization (asperity angle).

8.1 Original contributions and practical applications

The methodology presented in this thesis can be used in prediction of rockburst phenomenon in deep underground mines. The purpose of this investigation was to obtain the post-peak curve of hard rocks. This thesis is comprised of different tasks that mainly focus on the fracture characterization and the post-peak estimation in hard intact rocks. The results of this study can have various positive impacts for the mining industry. The main contribution of this research can be summarized as follows:

1. A simple method (2DRP) was proposed to characterize small scale rock fracture surfaces ($\leq$ 100 mm). This method can be used in laboratory or in the field.
2. For the first time, the fracture surfaces obtained by different loading conditions were characterized from a morphology point of view. Three rock types were used in this study

with different grain size in order of large, medium and fine. The laboratory tests conducted to obtain the fractures are: Modified Splitting, uniaxial and triaxial compression tests with three confining stresses. These test results lead to:

- A classification of the fracture surfaces based on the loading modes.
- An evaluation of roughness anisotropy in the profiles parallel and perpendicular to the loading direction.
- An evaluation of the influence of the loading contact areas on the roughness parameter.

3. A unique evaluation was carried out on the relationship between the loading direction and the surface roughness by selecting tensile fractures obtained from the samples with different L/D ratios subjected to Brazilian tests. The result of this part of the study allowed:
    - An evaluation of the roughness variation in profiles parallel and perpendicular to the loading direction considering the shape effect and the grain size.
    - An assessment of the roughness scattering in different loading directions.
    - The determination of wedge size created in different L/D ratio.
4. A novel study was conducted on the relationship between the loading direction, the roughness parameter and the sample shape (L/D ratio in the Brazilian tests)
5. A new damage-controlled cyclic method was proposed in this work to obtain the post-peak curve of hard rocks (the complete stress-strain curve) by using an ordinary standard testing machine. The results of this study lead to:
    - A new approach - damage controlled cyclic method- to capture the post-peak curves of hard rocks.
    - A classification of rock behaviour based on the new procedure results.
    - An evaluation of the brittleness index of hard rocks.
6. This study verified that the CSDS approach can estimate the parameters required for the prediction of the post-peak behaviour of hard intact rocks using triaxial tests. The two parameters including residual shear displacement and asperity angle can be obtained using the direct shear tests and the fracture surface characterization. The results of this part of the study allowed:
    - A determination of the CSDS model properties based on different laboratory tests.

- An improved model properties based on the results of triaxial and uniaxial compression and direct shear test.
- A tool for the prediction of rockbursts as a post-failure phenomenon that occurs violently in the burst-prone areas.

8.2 **Recommendations**

In addition to the results presented in this thesis, several aspects need further research to better capture the rock burst behaviour. Some of these aspects can be summarized as follows:

1. It is beneficial to conduct a comprehensive characterization of fracture surfaces created by different loading modes (Modified Splitting, uniaxial and triaxial compression tests) on different rock types such as sedimentary and metamorphic rocks. Investigation of the effect of different rock types with particular granularities and mechanical strength can help better understand the relationship between loading modes and roughness.
2. It is recommended carrying out triaxial tests with higher confining stresses to assess the roughness parameters of the fractures surface at these stresses.
3. Microscopic studies would be useful to investigate the fracture trajectories.
4. It is also valuable to subject the fractures retrieved from different loading modes to direct shear test to directly study the shear behaviour of the fractures.
5. In this thesis, the variation of roughness parameter of tensile fractures created by Brazilian test was studied on the samples with different L/D ratio. It would be valuable to conduct the same study on the samples with the same L/D ratios but different diameters (scale).
6. 3D numerical modelling of laboratory tests with different scales subjected to Brazilian test should also be carried out to obtain a relationship between the stress distribution and roughness of the profiles in parallel and perpendicular to the loading direction.
7. It would be useful to assess the roughness scattering due to variation in the loading conditions.
8. It is recommended conducting a sensitivity analysis on the strain rate to find an optimized value by which the post-peak phase can be obtained.
9. It is also suggested to carry out the damage-controlled cyclic method on other rock types to capture the post-peak curve of rocks. It is also recommended that the loading phase in

damage-controlled cyclic method switches to radial strain control rather than the small axial displacement control to better capture the post-peak curve.

10. Additional tests on other rock types with different UCS are recommended to estimate the CSDS model properties for various rocks.
11. An important validation is to obtain the CSDS model properties and post-peak curves with a highly stiff servo-controlled testing machine equipped with fast response signal. Accordingly the results should be compared with the post-peak curves obtained by an ordinary standard testing machine through using the damage-controlled cyclic method.

References

Adoko, A. C., Gokceoglu, C., Wu, L., & Zuo, Q. J. (2013). Knowledge-based and data-driven fuzzy modeling for rockburst prediction. International Journal of Rock Mechanics and Mining Sciences, 61, 86-95.

Altindag, R. (2010). Assessment of some brittleness indexes in rock-drilling efficiency. Rock Mech. Rock Eng. V. 43, 361–370.

Amadei, B., Saeb, S. (1990). Constitutive models of rock joints. International Symposium on Rock Joints. A.A. Balkema, Leon, Norway.

Amitrano, D. and Schmittbuhl J. (2002). Fracture roughness and gouge distribution of a granite shear band. Journal of Geophysical Research: Solid Earth (1978–2012) 107(B12): ESE 19-11-ESE 19-16.

Asadollahi P, Tonon F. (2010). Constitutive model for rock fractures: revisiting Barton's model. Engineering Geology 113(1–4):11–32.

Asadollahi, P. (2009). Stability analysis of a single three dimensional rock block: effect of dilatancy and high-velocity water jet impact, PhD Dissertation, University of Texas at Austin.

Aubertin, M. and Gill, D.E. (1988). Une methodologie d'evaluation du potentiel de coups de terrain dans les mines d' abitibi. Proc. Colloque sur le Controle de Terrain (AMMQ), Val d'Or, 47-77.

Aubertin M, Julien MR, Li L. (1998). The semi-brittle behaviour of low porosity rocks. Keynote Lecture, In: NARMS'98, Proceedings of 3rd North American Rock Mechanics

Aubertin, M., Gill, D.E. and Simon, R. (1994). On the use of the brittleness index modified (BIM) to estimate the post-peak behaviour of rocks. NARMS' 94, Proc., First North American Rock Mech. Symp., Austin Uni., 945-952.

Bandis, S., A C. Lumsden and N. Barton (1981). "Experimental studies of scale effects on the shear behaviour of rock joints." Int. J. Rock Mech. Min. Sci. & Geomech. Abstr. 18: 1-21.

Bardet, J.P. (1989). Finite element analysis of rockburst as surface instability. Computers and Geotechnics 8 (1989) 177-193.

Barton, N. (1971). Estimation of in situ shear strength from back analysis of failed rock slopes. Int. Symp. Rock Mech. Rock Fracture. Paper II-27, Nancy.

Barton, N., (1973). Review of a new shear strength criterion for rock joints. Eng. Geol. 7,287–332.

Barton, N., Bandis, S. (1982). Effects of block size on the shear behaviour of jointed rock. 23rd U.S. Symp. on Rock Mechanics, Berkeley, CA, 739-760.

Barton, N., Bandis, S.C., Bakhtar, K. (1985). Strength, deformation and conductivity coupling of rock joints. Int. J. Rock Mech. Min. Sci. & Geomech. Abstr. 22 (3), 121–140.

Barton, N., Choubey, V. (1977). The shear strength of rock joints in theory and practice. Rock Mech. 10, 1–54.

Bath, M. (1984). Rockburst Seismology in Gay, N.C., Wainwright, E.N. (eds), Rockbursts and Seismicity in Mines, South African Institute of Mining and Metallurgy, Symposium No.6, pp. 7-16.

De Beer, W., & Mendecki, A. J. (1998). Rockburst prediction-case studies using a kinematics of failure approach. JOURNAL-SOUTH AFRICAN INSTITUTE OF MINING AND METALLURGY, 98, 65-74.

Beer, A., Stead, D. and Coggan, J.C. (2002). Technical note estimation of the joint roughness coefficient (JRC) by visual comparison. Rock mechanics and rock engineering 35(1): 65-74.

Belem, T., Homand-Etienne, F., & Souley, M. (2000). Quantitative parameters for rock joint surface roughness. Rock mechanics and rock engineering, 33(4), 217-242.

Blake, W. (1972) Rockburst mechanics. Quarterly of the Colorado School of Mines, 67, 1-64.

Blake, W. and Hedley, D.G.F. (2003). Rockbursts: Case Studies from North American Hard-Rock Mines. SME Publication.

Bobet A, and Einstein H.H. (1998). Fracture coalescence in rock material under uniaxial and biaxial loading. Int. J. Rock Mech. Min. Sci. Vol. 35, No. 7, pp. 863-888.

Brummer RK, Rorke AJ. (1990). Case studies on large rockbursts in South African gold mines. In: Proceedings of the Second International Symposium on Rockbursts and Seismicity in Mines. Minneapolis 1988. A.A. Balkema, 1990. p. 323-330.

Carr, J. R., & Warriner, J. B. (1987). Rock mass characterization using fractal dimesion. In Rock Mech., Proc. 28th US Symp. on Rock Mech. pp. 73-80.

Castelli M, Re F, Scavia C, Zaninetti A (2001) Experimental evaluation of scale effects on the mechanical behavior of rockjoints. In: Sarkka P, Eloranta P (eds) Rock mechanics—a challenge for society; proceedings of Eurock 2001, Espoo, Finland, 4–7 June 2001. A.A. Balkema, Rotterdam, pp 205–210.

Chapuis, R.P. (1990). A constitutive equation for granular materials from consideration of their internal structure. Yielding, Damage, and Failure of Anisotropic Solids, EGF5, Boehler (ed.), Mechanical Engineering Publications, 277-287.

Chen, H., N. Li, et al. (2003). Prediction of rockburst by artificial neural network. Yanshilixue Yu Gongcheng Xuebao/Chinese Journal of Rock Mechanics and Engineering 22: 762-768.

Cook N.G.W. (1987). Coupled processes in geomechanics. In: Tsang (ed.). Coupledprocesses associated with nuclear waste repositories. Academic Press Inc. London. pp. 39-66.

Cook, N.G.W. (1963). The basic mechanics of rockbursts. J.S. Afr. Inst. Min. Metal., vol. 64. 71-81.

Cook, N.G.W. (1965). A note on rockburst considered as a problem of stability. J. South Afr. Int. Min. Metallurgy 65, 437_446.

Cook, N.G.W. (1966) .The basic mechanics of rockbursts. J. South African Inst. Mining and Metallurgy, vol. 66, 56--70.

Cook, N.G.W. (1978). An Industry Guide to the Amelioration of Hazards of Rockbursts and Rockfalls, Chamber of Mines of South Africa.

Cook, N.G.W. (1983). Origin of rockbursts. Proc. Rockburst Prediction and Control, IMM, London, 1-9.

Cotterell, B. (1971). Brittle fracture in compression. International Journal of Fracture 8(2): 195-208.

Cravero M, Iabichino G, Ferrero AM (2001) Evaluation of joint roughness and dilatancy of schistosity joints. In: Sarkka P, Eloranta P (eds) Rock mechanics—a challenge for society;

proceedings of Eurock 2001, Espoo, Finland, 4–7 June 2001. A.A. Balkema, Rotterdam, pp 217–222.

Deng, D., Simon, R. and Aubertin, M. (2004). A geometrical approach for the estimation of the scale effects in rock joint behavior. Proceeding of 57th Canadian Geotechnical Conferente and 5th joint CGS-IAH Conference, Quebec City, Canada.

Dight P. M. and Chiu H. K. (1981). Prediction of shear behavior of joints using profiles. Int. J. Rock. Mech. Min. Sci. & Geomech. Abstr. 18, 369-386.

Dong, L. J., Li, X. B., & Kang, P. E. N. G. (2013). Prediction of rockburst classification using Random Forest. *Transactions of Nonferrous Metals Society of China*, *23*(2), 472-477.

Dyskin, A. V. and L. N. Germanovich (1993). Model of rockburst caused by cracks growing near free-surface. Rotterdam, A a Balkema.

Eberhardt, E. (1998). Brittle rock fracture and progressive damage in uniaxial compression. Phd thesis, University of Saskatchewan, Canada, 362p.

Eberhardt, E., Stead, D., Stimpson, B., & Read, R. S. (1998). Identifying crack initiation and propagation thresholds in brittle rock. Canadian Geotechnical Journal, 35(2), 222-233.

El-Soudani, S. (1978). Profilometric analysis of fractures. Metallography 11(3): 247-336.

Fairhurst, C. (1964). On the validity of the Brazilian test for brittle materials. Int. J. Rock Mech. Min. Sci., 1, 535-546.

Fairhurst, C. E., & Hudson, J. A. (1999). Draft ISRM suggested method for the complete stress-strain curve for intact rock in uniaxial compression. International Journal of Rock Mechanics and Mining Sciences, 36(3), 279-289.

Fardin N, Stephansson O, Jing L (2001). The scale dependence of rock joint surface roughness. Int J Rock Mech Min Sci 38(5):659–669.

Fardin N (2008) Influence of structural non-stationarity of surface roughness on morphological characterization and mechanical deformation of rock joints. Rock Mech Rock Eng 41(2):267–297.

Fortin, M., Archambault, G., Aubertin, M., Gill, D.E. (1988): An algorithm for predicting the effect of a variable normal stiffness on shear strength of discontinuities. Proc. 15th Can. Rock Mech. Symp., 109-117.

Fredrich. J.T. , Evans. B. and Wong, T-F. (1990). Effect of grain size on brittle and semi-brittle strength: Implications for micromechanical modeling of failure in compression. Journal of Geophysical Research. 95 (B7): 10907-10920.

Frid, V. (1997). Rock-burst hazard forecast by electromagnetic radiation excited by rock fracture. J. Rock Mech. Rock Eng. 30 (4), 229– 236.

Frid, V. (2000). Electromagnetic radiation method water-infusion control in rockburst-prone strata. Journal of Applied Geophysics 43(1): 5-13.

Frid, V. (2001). Calculation of electromagnetic radiation criterion for rockburst hazard forecast in coal mines. Pure and Applied Geophysics 158(5-6): 931-944.

Gill, D. E., M. Aubertin, et al. (1993). Practical engineering approach to the evaluation of rockburst potential. Proceedings of the 3rd International Symposium on Rockbursts and Seismicity in Mines, Aug 16 - 18 1993, Kingston, Ont, Canada, Publ by A.A. Balkema.

Gill, D.E. and Aubertin, M. (1988). Évaluation du potentiel de coups de terrain dans les mines d'Abitibi. Rapport de recherche de l'URSTM présenté à l'Institut de Recherche en Santé et Sécurité du Travail (IRSST).

Goodman, R.E. (1976). Methods of geological engineering in discontinuities rocks. West Publishing Co., Minnesota.

Goodman, R.E. and Boyle, W. (1985): Non-linear analysis for calculating the support of a rock block with dilatant joint faces. Presented at the 34th Geomechanics Colloquy, Salzburg, Austria.

Grasselli G, Egger P. (2003). Constitutive law for the shear strength of rock joints based on three-dimensional surface parameters. Int J Rock Mech Min Sci., 40:25–40.

Griffith, A.A. (1920). The phenomena of rupture and flow in solids. Philosophical Transactions of the Royal Society of London, Series A. Mathematical and Physical Sciences. 221 (587): 163-198.

Haberfield, C. M., Johnston, I. W. (1994): A mechanistically based model for rough rock joints. Accepted for publication Int. J. Rock Mech. Min. Sci. Geomech. Abstr.

Haijun, C., Nenghui, L., Dexin, N., & Yuequan, S. (2003). Prediction of rockburst by artificial neural network. *岩石力学与工程学报*, *22*(5), 762-768.

Hajiabdolmajid, V. (2001). Mobilization of Strength in Brittle Failure of Rock, Ph.D. Thesis, Queen's University, Kingston, Canada.

Hedley, D.G.F., (1992). Rockburst Handbook for Ontario Hard rock Mines. CANMET Special Report SP92-1E.

Heunis, R. (1980). The development of rock-burst control strategies for South African gold mines. J. S. Afr. Ins. of Min. Metall. April, 139-150.

Hoek, E., Brown, E.T. (1980). Underground Excavation in Rock. The Institution of Mining and Metallurgy, London. pp. 155–156, pp. 137–154.

Homand F, Belem T, Souley M. (2001). Friction and degradation of rock joint surfaces under shear loads. Int J Numer Anal Methods Geomech 25:973–99.

Hong, E. S., Lee, J-S. and Lee, I-M. (2008). Underestimation of roughness in rough rock joints. International journal for numerical and analytical methods in geomechanics 32(11): 1385-1403.

Huang, S. L., Oelfke, S. M., & Speck, R. C. (1992, March). Applicability of fractal.characterization and modelling to rock joint profiles. In International journal of rock mechanics and mining sciences & geomechanics abstracts (Vol. 29, No. 2, pp. 89-98). Pergamon.

Huang, X., Haimson, B. C., Plesha, M. E. and Qiu, X. (1993). An investigation of the mechanics of rock joints-Part I: Laboratory investigation, Znt. J. Rock Mech. Min. Sci. & Geomech. Abstr. 30(3), 257-269.

ISRM. (1978). Suggested methods for the quantitative description of discontinuities in rockmasses. Int. J. Rock Mech. Min. Sci. Geomech. Abstr.;15:319–368.

Jang H-S., K. S.-S., Jang B-A. (2014). Determination of joint roughness coefficient using roughness parameters. Rock Mech. Rock Eng. Online published on January 2014.

Jeager, J.C., Cook, N.G.W. (1979). Fundamentals in Rock Mechanics, Third ed. Chapman and Hall. 176–201.

Jian, S., W. Lian-guo, et al. (2009). Application of fuzzy neural network in predicting the risk of rock burst. Procedia Earth and Planetary Science 1: 536-543.

Jiang, Q., Feng, X., Xiang, T. and Su, G. (2010). Rockburst characteristics and numerical simulation based on a new energy index: a case study of a tunnel at 2,500 m depth. Bull Eng Geol Environ V. 69, 381–388.

Johnston, J. C. (1988). A survey of mining associated rockbursts, Master Thesis. Massachusetts Institute of Technology.

Joughin, N.C., and Jaeger, A.J. (1983). Fracture of rock at stope faces in South African gold mines. Proceedings Symposium on Rockbursts- Prediction and Control. London, Institution of Mining and Metallurgy.

Kaiser, P., Morrison, D., Swan, G., McCreath, D., Tannant, D., Neumann, M., Kazakadis, V. And Talebi, S. (1995). Mining Research Directorate- The Canadian Rockburst Research Program 1990-1995. CAMIRO Mining Division, 2 Vol.s.

Kaiser, P.K. and Maloney, S.M. (1997). Scaling Laws for the Design of Rock Support, Pure appl. geophys. 150, 415–434.

Kidybinski, A. (1981). Bursting Liability Indices of Coal. Int. J. Rock Mech. Min. Sci. & Geomech. Abstr. V. 18, 295-304.

Kim, D.-Y. and Lee H.-S. (2009). Quantification of rock joint roughness and development of analyzing system. Proceedings of the international conference on rock joints & jointed rock masses, Tucson.

Khosravi, A, Simon R, Falaknaz N. (2014). Evaluation of roughness parameters of rock fractures created by different loading modes. Georegina2014, Regina, Sask, Canada 28 September-1 October 2014.

Kranz, R. L. (1983). Microcracks in rocks: a review. Tectonophysics, 100(1-3), 449-480.

Kulatilake P.H.S.W., Shou G., Huang T.H., Morgan R.M. (1995). New peak shear strength criteria for anisotropic rock joints. Int J Rock Mech Min Sci Geomech Abstr, 32, pp. 673–697.

Ladanyi, B., Archambault, G. (1970). Simulation of the shear behaviour of a jointed rock mass. The 11th Symposium on Rock Mechanics, Berkeley, pp. 105–125.

Lajtai, E. (1974). Brittle fracture in compression. International Journal of Fracture 10(4): 525-536.

Lajtai, E. Z. (1971). A theoretical and experimental evaluation of the Griffith theory of brittle failure. Teclonophysics 11, 129-15.

Lanaro F, Jing L, Stephansson O (1999) Scale dependency of roughness and stationarity of rock joints. In: Vouille G, Berest P (eds) Proceedings of the 9th congress of ISRM, Paris, France, 25–28 August 1999, pp 1391–1395.

Leal-Gomes M.J.A. (2003). Some new essential questions about scale effects on the mechanics of rock joints. In: Handley M (ed) Proceedings of the 10th ISRM Congress: Technology roadmap for rock mechanics. Sandton, South Africa, South African Institute of Mining and Metallurgy, pp 721–727.

Lee, S. W., Hong, E. S., Bae, S. I., et al. (2006). Modelling of Rock Joint Shear Strength Using Surface Roughness Parameter, Rs. Tunnelling and Underground Space Technology, 21(3–4): 239.

Lee, Y. H., Carr, J. R., Barr, D. J., & Haas, C. J. (1990). The fractal dimension as a measure of the roughness of rock discontinuity profiles. In International journal of rock mechanics and mining sciences & geomechanics abstracts (Vol. 27, No. 6, pp. 453-464). Pergamon.

Lee, S.M., Park, B.S., Lee, S.W., (2004). Analysis of rockbursts that have occurred in a waterway tunnel in Korea. Int. J. Rock Mech. Min. Sci., 41(3), 545.

Linkov, A. M. (1996). Rockbursts and the instability of rock masses. International journal of rock mechanics and mining sciences & geomechanics abstracts 33: 727-732.

Lippmann, H. (1990). Keynote lecture. Mechanical considerations of bumps in coal mines. Proceedings of the International Symposium on Rockbursts and Seismicity in Mines: 279-279.

Maerz NH, Franklin JA (1990) Roughness scale effects and fractal dimension. In: Pinto Da Cunha A (ed) Scale effects in rock masses; proceedings of the first international workshop on scale effects in rock masses, Loen, Norway, 7–8 June 1990. A.A.Balkema, Rotterdam, pp 121–125.

Maerz, N., Franklin, J.A. and Bennett, C.P. (1990). Joint roughness measurement using shadow profilometry. International Journal of Rock Mechanics and Mining Sciences & Geomechanics Abstracts, Vol. 27, No. 5, pp. 329-343.

Maksimovic, M. (1996). A family of nonlinear failure envelopes for non-cemented soils and rock discontinuities. The Electronic Journal of Geotechnical Engineering, 1, 1-15.

Mandelbrot, B. B. (1989). Multifractal measures, especially for the geophysicist. In Fractals in geophysics (pp. 5-42). Birkhäuser Basel.

Martin, C.D. (1993). Strength of massive Lac du Bonnet granite around underground openings. Ph.D. thesis, Department of Civil and Geological Engineering, University of Manitoba, Winnipeg, 278pp.

Martin, C. D., & Chandler, N. A. (1994). The progressive fracture of Lac du Bonnet granite. In International Journal of Rock Mechanics and Mining Sciences & Geomechanics Abstracts (Vol. 31, No. 6, pp. 643-659). Pergamon.

Martin, C. D. and Maybee, W. G. (2000). The strength of hard-rock pillars. Int. J. Rock Mech. Min. Sci., 37(8):1239–1246.

McClintock, F. A., and J. B. Walsh, (1962). Friction on Griffith cracks under pressureP, roc. U.S. Natl. Congr.A ppl. Mech., 4th, 1015-1021.

McMahon, T., & Mines, U. S. B. O. (1988). Rock burst research and the Coeur d'Alene District: US Dept. of the Interior, Bureau of Mines.

Mitri, H. S. (2007). Assessment of horizontal pillar burst in deep hard rock mines. International Journal of Risk Assessment & Management 7(Copyright 2007, The Institution of Engineering and Technology): 695-707.

Mitri, H.S., Hassani, F.P., and Kebber, R. (1993). A strain energy approach for the prediction of rockburst potential in underground hard rock mines. Proc. First Can. Symp. on Numerical Modelling Applications in Mining and Geomech., McGill University, 228–239.

Morrison, R. G. K. (1942), Report on the rockburst situation in Ontario mines, Transactions of theCanadian Institute of Mining and Metallurgy and of the Mining Society of Nova Scotia XLV, 225-272.

Muehlhaus, H. B. (1990). Exfoliation phenomena in pre-stressed rock. Proceedings of the International Symposium on Rockbursts and Seismicity in Mines: 101-101.

Muralha, J., & Pinto da Cunha, A. (1990). Analysis of scale effects in joint mechanical behaviour. In Proceedings of the Scale Effects in Rock Masses Symposium (pp. 191-200).

Murrell, S. and P. Digby (1970). "The theory of brittle fracture initiation under triaxial stress conditions—I." Geophysical Journal of the Royal Astronomical Society 19(4): 309-334.

Myers, N. (1962). Characterization of surface roughness. Wear 5(3): 182-189.

Nemat-Nasser S, Horii H. (1982). Compression-induced non-planar crack extension with application to splitting, exfoliation and rockbursts. J. Geophys. Res. 1982; B87:6805-21.

Neyman, B., Szecowka, Z., Zuberek, W. (1972). Effective methods for fighting rock burst in Polish collieries. Proc. 5th Int. Strata Control Conf., 23.1-23.9.

Odling, N. (1994). Natural fracture profiles, fractal dimension and joint roughness coefficients. Rock mechanics and rock engineering 27(3): 135-153.

Ohnishi Y, Yoshinaka R (1995) Laboratory investigation of scale effect in mechanical behaviour of rock. In: Myers LR, Tsang CF, Cook NGW, Goodman RE (eds) Proceedings of the conference on fractured and jointed rock masses, Lake Tahoe, CA, 3–5 June 1992. A.A. Balkema, Rotterdam, pp 465–477.

Ortlepp W. D. (2001). Thoughts on the rockburst source mechanism based on observations of the mine-induced shear rupture.

Ortlepp, W. D. (2000). Observation of mining-induced faults in an intact rock mass at depth, Elsevier Ltd.

Ortlepp, W. D. and Stacey, T. R. (1994). Rockburst mechanisms in tunnels and shafts. Tunnelling and Underground Space Technology, Vol. 9, No. 1, pp. 59-65.

Ortlepp, W.D. (1978). The mechanism of a rockburst. Proc. 19th U.S.Symp. on Rock Mech., Reno, NV.

Park, C.H. and Bobet, A. (2010). Crack initiation, propagation and coalescence from frictional flaws in uniaxial compression. Engineering Fracture Mechanics 77 (2010) 2727–2748

Patton, F.D. (1966). Multiple modes of shear failure in rock. The 1st Congress of the International Society of Rock Mechanics, Lisbon, pp. 509–513.

Peng, Syd. S. (1986). Coal Mine Ground Control, 2nd Ed., Wiley Interscience, 491 pages.

Petukhov, I. (1972). Rock Bursts in Coal Mines. Nedra, Moscow.

Piteau, D. R. (1970). Geological factors significant to the stability of slopes cut in rock. South African Institute of Mining and Metallurgy.

Pratt, H.R., Black, A.D., and Braze, W.F. (1974). Friction and deformation of jointed quartz diorite. In: Proceedings of 3rd ISRM conference, Denver, USA, 2A, pp 306–310

Qiao, C.S., Tian, Z.Y., 1998. Study of the possibility of rockburst in Dong-gua-shan Copper Mine. Chinese J. Rock Mech. Eng. Žexp. 17, 917_921.

Ramasey, J.G. (1967). Folding and fracturing of rocks. McGraw-Hill, London, p 289.

Rasouli, V., & Harrison, J. P. (2001). Is the observational method of roughness determination trustworthy. In Proceedings of ISRM international symposium. Eurock. pp. 277-282.

Reyes, O. & Einstein, H.H. (1990). Failure mechanism of fractured rock –A Fracture coalescence model. Proceedings 7th International Congress of Rock Mechanics 1: 333-340.

Ryder, J. A. (1988). Excess Shear Stress In The Assessment Of Geologically Hazardous Situations. Journal of the South African Institute of Mining and Metallurgy 88: 27-39.

Ryder, J.A. (1986). Excess Shear Stress' assessment of geologically hazardous situations. Colloquium, Mining in the Vicinity of Geological and Hazardous Structures, South African Institute of Mining and Metallurgy.

Saeb S, Amadei B. (1992) Modelling rock joints under shear and normal loading. Int J Rock Mech Min Sci Geomech Abstr; 29: 267–78.

Saeb, S. (1990). A variance on the Ladanyi and Archambault's shear strength criterion. Rock Joints, Barton & Stephansson (eds), Balkema, 701-705.

Salamon, M.D.G. (1970). Pillar stability/instability and design of pillar workings., Int.J. Rock Mech. Min. Sci. vol. 7. 613–631.

Salamon, M.D.G. (1974). Rock mechanics of underground excavations. , Advances in rock Mechanics, Proc. 3rd Cong. Int. Soc. Rock. Mech., vol.1-B, 1974. 951–1099.

Salamon, M.D.G. (1983). Rockburst hazard and the fight for its alleviation in South African gold mines. In Rockbursts: prediction and control, London. The Institution of Min. Metall, 11-52.

Salamon, M.D.G. (1984). Energy considerations in rock mechanics: fundamental results. J.S. Afr. Inst. Min. Metall., V.84, pp. 233-246.

Salamon, M.D.G. (1993). Keynote address: Some applications of geomechanical modelling in rockburst and related research. Rockbursts and Seismicity in Mines, Young (ed.) 1993 Balkema, Rotterdam, ISBN 905403205, 297-309.

Seredin, V., Leibovich, L.O, Pushkareva, M.V., Kopylov, I.S. and Khrulev, A.S. 2013. Evolution of fracture surface morphology in rocks. Journal of Mining Science 49(3): 409-412.

Simon, R. (1999). Analysis of fault-slip mechanisms in hard rock mining. Phd Thesis, McGill University, Montreal, Canada.

Singh, S. P. (1987). Influence of rock properties on the occurrence and control of rockbursts. Mining science & technology 5: 11-18.

Singh, S. P. (1988). Burst Energy Release Index. Rock Mechanics and Rock Engineering 21: 149-155.

Singh, S.P. (1989). Classification of mine workings according to their rockburst proneness. Mining Science and Technology, V 8, 253-262.

Souley, M., Hommand, F. And Amadei, B. (1995). An extension to the Saeb and Amadei constitutive model for rock joints to include cyclic loading paths. Int. J. Rock Mech. Min. Sci. And Geomech. Abstr. Vol. 32, 2, pp 101-109.

Tang, B. (2000). Rockburst Control Using Destress Blasting. PhD Thesis, McGill University, Montreal, Canada.

Tatone, B. S. and Grasselli G. (2009). A method to evaluate the three-dimensional roughness of fracture surfaces in brittle geomaterials. Review of Scientific Instruments 80(12): 125110.

Tatone, B. S. and Grasselli G. (2010). A new 2D discontinuity roughness parameter and its correlation with JRC. International Journal of Rock Mechanics and Mining Sciences 47(8): 1391-1400.

Tatone, B. S., & Grasselli, G. (2013). An investigation of discontinuity roughness scale dependency using high-resolution surface measurements. Rock mechanics and rock engineering, 46(4), 657-681.

Tremblay, D., Simon, R. and Aubertin, M. (2007). A constitutive model to predict the hydromechanical behavior of rock joints. Proceding of Geo 2007, Ottawa, Canada.

Tse, R. and Cruden D. (1979). Estimating joint roughness coefficients. International journal of rock mechanics and mining sciences & geomechanics abstracts, Vol. 16, pp. 303-307.

Turk, N., Greig, M. J., Dearman, W. R., & Amin, F. F. (1987). Characterization of rock joint surfaces by fractal dimension. In The 28th US Symposium on Rock Mechanics (USRMS). American Rock Mechanics Association.

Vardoulakis, I. (1984). Rock bursting as a surface instability phenomenon. International Journal of Rock Mechanics and Mining Sciences 21: 137-144.

Wakabayashi, N., & Fukushige, I. (1992). Experimental study on the relation between fractal dimension and shear strength. In Paper for the ISRM Symp. Fractured and Jointed Rock Masses. Lake Tahoe.

Wang, B. (1992). A block-spring model for jointed rocks. Ph.D. Thesis, University of Ottawa, Canada, 204 p.

Wang, J. A. & Park, H.D. (2001). Comprehensive prediction of rockburst based on analysis of strain energy in rocks. Tunnelling and Underground Space Technology, V. 16, 49-57.

Wang, P., F.-X. Jiang, et al. (2010). The stress incremental forecasting method of rock burst. Meitan Xuebao/Journal of the China Coal Society 35: 5-9.

Wawersik, W. R. and Fairhurst, C. (1970). Study of brittle rock fracture in laboratory compression experiments. International Journal of Rock Mechanics and Mining Sciences 7: 561-575.

Weissbach, G. (1978). A new method for the determination of the roughness of rock joints in the laboratory. In International Journal of Rock Mechanics and Mining Sciences & Geomechanics Abstracts (Vol. 15, No. 3, pp. 131-133). Pergamon.

Whyatt, J.K. (2000). Influence of geologic structures on stress variation and the potential for rockbursting in mined with particular reference to the lucky friday mine, Idaho. Ph.D. Thesis, University of Minnesota, 203p.

Whyatt, J.K., Blake, W., Williams, T.J., White, B.G. (2002). 60 years of rockbursting in the Coeur D'Alene District of Northeastern Idaho, USA: lessons learned and remaining issues. In: Proceedings of the 109th Annual Exhibit and Meeting, Society for Mining, Metallurgy, and Exploration, February 25–27, Phoenix, AZ. Preprint 02-164, 1–10.

Wiles, T.D. (2002). Loading System Stiffness-A Parameter to Evaluate Rockburst Potential. First international seminar on deep and high stress mining. Australia.

Wong RHC, Chau KT. (1998). Crack coalescence in rock-like material containing two cracks. Int Rock Mech Min Sci 35(2):147–64.

Wong RHC, Tang CA, Chau KT, Lin P. (2002). Splitting failure in brittle rocks containing pre-existing flaws under uniaxial compression. Engng Fract Mech. 69:1853–71.

Wong, L.N.Y., Einstein, H.H. (2009).Crack coalescence in molded gypsum and Carrara Marble: Part1—macroscopic observations and interpretation. Rock Mech. Rock Eng. 42(3):475–511.

Wu, Y. and Zhang, W. (1997). Evaluation of the bursting proneness of coal by means of its failure duration. Rockbursts and Seismicity in Mines, Gibowicz & Lasocki, Balkema, Rotterdam.

Xie, H. P., & Pariseau, W. G. (1994). Fractal esti mate of rock fractureroughness (JRC). Science in China: Series D, 24(5), 524-532.

Xia, M. and Zhou, K. (2010). Particle simulation of the failure process of brittle rock under triaxial compression. International Journal of Minerals, Metallurgy and Materials 17/5, 507-513.

Yang, Z., Lo, S.C. and Di, C.C. (2001). Reassessing the joint roughness coefficient (JRC) estimation using Z_2. Rock mechanics and rock engineering 34(3): 243-251.

Yi, X. & Kaiser, P. K. (1993). Mechanisms of rockmass failure and prevention strategies in rockburst conditions. Rockbursts and Seismicity in Mines. 141-145 Balkema. Rotterdam.

Yu, X. and Vayssade B. (1991). Joint profiles and their roughness parameters. International journal of rock mechanics and mining sciences & geomechanics abstracts, Vol. 28, NO. 4, pp. 333-336.